

Spontaneous Imbibition Studies in Shale Gas Reservoirs: Insight into Origins of High Salinity
Flowback Water

by
Clara Palencia

A dissertation submitted to the Department of Petroleum Engineering,
Cullen College of Engineering
in partial fulfillment of the requirements for the degree of

Doctor of Philosophy
in Petroleum Engineering

Chair of Committee: Lori Hathon PhD

Committee Member: Michael Myers PhD

Committee Member: Christine Ehlig - Economides PhD

Committee Member: Carlos Torres Verdin PhD

Committee Member: Thomas Lapen PhD

University of Houston
December 2021

DEDICATION

To my beloved parents Manuel Palencia Caratt and Clara Lucia Hernandez for their passion about teaching young people. To my husband, Boris Castro, for all his love and for making my life so much fun.

ACKNOWLEDGMENTS

I want to express my gratitude to God, for every moment of my PhD, it is truly being an honor. To Boris, my husband, for his confidence, love and support during these years, to my mom and my sisters for giving me the strength to make this possible, to my advisors, Dr. Lori Hathon and Dr. Michael Myers, for changing my life, making me a better person, for their patience, encouragement, trust and love, and to my friends at UH for helping me, and making this journey a happy one.

ABSTRACT

Although hydraulic fracturing fluid is typically fresh water, in shale gas reservoirs, produced water or flowback, is often very saline. This observation suggests that flowback water is gaining salt from the formation. It is not currently known whether the recovered salt comes from dissolution of mineral salts, or interaction between bound water and frac fluid. In the absence of flowback water data, spontaneous imbibition experiments, can provide insight into the physics that governs the principal controls on flowback water salinity. This is the primary objective of this research. In addition, imbibition experiments can be related to clay mineral content (brittleness), total porosity, the relative volume of mineral hosted (water wet) and organic matter hosted (hydrocarbon wet) pore systems, and the in-situ pore fluid salinity. We propose to show that through the use of a novel multidisciplinary experimental approach the origin of high salinity flow back waters in shale reservoirs can be understood. Dual spontaneous imbibition (water and oil), ion expulsion experiments and sample characterization are combined to develop rock properties models. These techniques provide insight into effective characteristic time to reach equilibrium in salinity and imbibed volume, anticipated magnitude of flowback salinity, total porosity and clay mineral content for shale reservoirs. Experimental and modelling results suggest that the summation of the equivalent NaCl in the fluid due to anhydrite (salt dissolution) plus the equivalent NaCl due to the presence of clay minerals, result in the high salinity water associated with the Haynesville, Bossier and the La Luna Formations. Cation exchange capacity and salt volumes from geochemical analysis of equilibrated fluids obtained from imbibition experiments, might be used as a proxy to predict flowback salinity. Imbibition experiment provides a promising technique for estimating organic porosities in gas shale reservoirs and it could provide a basis for a possible GRI total porosity measurement correction, particularly in high carbonate content rocks.

TABLE OF CONTENTS

DEDICATION.....	ii
ACKNOWLEDGMENTS	iii
ABSTRACT	iv
LIST OF TABLES.....	viii
List of Figures.....	ix
CHAPTER 1. INTRODUCTION.....	1
1.1. Hypothesis Statement.....	4
1.2. Objectives.....	5
1.3. Recovering Hydrocarbons from Unconventional Resources.....	5
1.3.1. What is a shale gas reservoir?	9
1.3.2. Why are the Shale gas reservoirs important?.....	11
1.3.3. How can we develop these resources?.....	13
1.3.3.1 Horizontal Drilling.....	13
1.3.3.2. Hydraulic Fracturing	14
1.3.4. Shale Gas reservoir Properties.	15
1.3.4.1. Geochemistry	16
1.3.4.1.1. Organic Richness	19
1.3.4.1.2. Thermal Maturation.	20
1.3.4.2. Mineralogy and Inorganic Chemistry	21
1.3.4.3. Clay minerals	24
1.3.4.3.1. Types of Clay Minerals.....	25
1.3.4.4 Characterization of Physical Properties	28
1.3.4.4.1. Clay mineral content and Cation Exchange Capacity (CEC)	28
1.3.4.4.2. Porosity	29
1.3.4.4.3. Fluid Saturation.....	30
1.3.4.4.4. Permeability	31
1.3.5. Shale Gas Reservoirs Used in This Study.....	33

1.3.6. How the Industry Uses Flowback Water Chemistry	36
CHAPTER 2. METHODOLOGY	51
2.1. Sample homogenization.....	53
2.1.1. Handheld XRF analysis.....	55
2.1.3. Laser Particle Size Distribution Analyzer.....	57
2.1.4. Boyle’s Law porosity	59
2.1.5 Thermal Gravimetric Analysis. (TGA)	59
2.1.6 Cation Exchange Capacity (CEC) Measurements: Conductometric Titration.....	60
2.1.7. Clay Mineral Membrane Potential Test	61
2.1.8. As Received Nuclear Magnetic Resonance (NMR).....	62
2.1.9. Dual Spontaneous Imbibition Experiments	61
2.1.9.1 Water Imbibition Experiments	64
2.1.9.2. Oil Imbibition Experiments and NMR.....	66
2.1.10. Brine characterization	67
2.1.11. Post – Test Sample Characterization.....	68
2.1.12 Thin Section Analysis and SEM/EDS.....	68
CHAPTER 3. RESULTS.....	70
3.1 X- Ray Fluorescence (XRF).....	70
3.2. Thermo-Gravimetric Analysis. (TGA).....	90
3.3. CEC Results	92
3.4. Pre-imbibition Nuclear Magnetic Resonance Results	99
3.5. Spontaneous Water Imbibition and Salinity	102
3.6. Post - Water Imbibition Nuclear Magnetic Resonance Results	109
3.7 Oil imbibition Experiment Results.....	121
3.8 Inductively Coupled Plasma Results (ICP).....	124
3.9 Imaging and Image Analysis.....	128
3.9.1 Transmitted Light Microscopy and Scanning Electron Microscopy	128
CHAPTER 4. Modeling and Discussion	131
4.1 Clay mineral content and salt dissolution	132
4.2. The influence of particle size	133
4.3 Modelling Equations	136

4.4 Conductivity and Imbibition Modelling	139
4.4.1. Equilibrated Conductivity (Ce) model.	140
4.4.2 Characteristic Time for Concentration: tcc Model	142
4.4.2.1 Characteristic Time for Concentration tcc – Grain Size Effect	144
4.4.3 Imbibition Based Porosity Calculation.	146
4.4.4 Oil Imbibition.....	154
4.4.5 Characteristic Time for Imbibition: tci Model.....	155
4.4.6 tcc and tci comparison	156
4.4.7 Equilibrated Imbibed Water Imbibition: (Ve) Model	165
4.5. In situ salinity calculation	174
CHAPTER 5. CONCLUSIONS	180
REFERENCES	185
APPENDIX.....	193

LIST OF TABLES

Table 1.1	Global unproved technically recoverable shale gas and oil resources (tcf).....	12
Table 1.2	U.S. and Colombian Shale systems..	36
Table 1.3	Rock physical properties for the samples used in Yang 2015.	44
Table 1.4	XRD mineralogy analysis for the samples used in Yang 2015.....	45
Table 1.5	Mineral composition for the samples used in Yang 2015.....	47
Table 2.1	Selected sample petrophysical properties..	54
Table 3.1	XRD Data for B(60) and B(40) at the three different particle sizes	93
Table 3.2	CEC Data for all samples at the three different particle sizes	98
Table 3.2.	Summary for T2 Peaks and imbibed volumes from the post NMR experiments in the Bossier Formation.	112
Table 3.3.	Summary for T2 Peaks and imbibed volumes from the post NMR experiments in the Bossier Formation.	116
Table 3.4.	Summary for T2 Peaks and imbibed volumes from the post NMR experiments in the La Luna Formation.	119
Table 3.5.	Summary for in situ salinities with the assumptions made on each scenario.	174

LIST OF FIGURES

Figure 1.1	Horn River Flowback salinity. Why is salinity increasing with time?	2
Figure 1.2	Use of the words flowback salinity from 1985 to 2019.....	3
Figure 1.3	The American Shale Revolution Historical	6
Figure 1.4	The Lower 48 states shale plays	7
Figure 1.5	World resource pyramid	8
Figure 1.6	Compositional classification for fine-grained sediments and sedimentary rocks.	10
Figure 1.7	Schematic of solid and fluid components in source and non-source rocks	19
Figure 1.8	Milliken Mineralogy Ternary Plot.....	23
Figure 1.9	Structure of a Kaolinite Layer.	25
Figure 1.10	Structure of a Chlorite Layer.	26
Figure 1.11	Structure of Illite minerals.	27
Figure 1.12	Structure of Montmorillonite minerals	27
Figure 1.13	Permeability of general reservoir rocks.	31
Figure 1.14	Bossier and Haynesville Stratigraphic Column.	35
Figure 1.15	Imbibed Volume divided by sample volume (V_{imb}/AcL) vs SQR (t/L^2).	46
Figure 1.16	Imbibed Volume divided by surface area (V_{imb}/As) vs SQR (t).	48
Figure 1.18	Ion Diffusion Rate divided by surface area (V_{imb}/As) vs Illite Concentration. ...	50
Figure 2.1	Haynesville and Bossier Sample Selection.....	53
Figure 2.2	Compilation of permeability measurements	55
Figure 2.3	Bossier (a), Haynesville(b) and La Luna Formation (c) Sample XRF Data.....	56
Figure 2.4	Initial Sample preparation.....	57
Figure 2.5.	Particle size distribution for aliquots	58
Figure 2.6.	Thermal Gravimetric Analysis workflow.	59

Figure 2.7	Thermal Gravimetric Analysis for B(60)samples.....	60
Figure 2.8	CEC measurement by conductimetric titration.....	61
Figure 2.9	Spontaneous Water imbibition experimental set up.	65
Figure 2.10	Imbibition experiment setup.....	66
Figure 2.11	Oil Imbibition experiment setup.....	67
Figure 2.12.	Inductively Coupled Plasma (ICP) equipment.	68
Figure 3.1	Major Elements concentration in B(60).....	71
Figure 3.2	Principal elements versus aluminum crossplots for B(60).....	72
Figure 3.3	Major Elements concentration in B(40).....	73
Figure 3.4	Principal elements and Aluminum Crossplots for B(40).....	74
Figure 3.5	Major Elements concentration in B(15).....	75
Figure 3.6.	Principal elements and Aluminum Crossplots for B(15).....	76
Figure 3.7.	Principal elements and Aluminum Crossplots For Bossier Formation.....	77
Figure 3.8	Major Elements concentration in H(26).	79
Figure 3.9	Major Elements concentration in H(29).	80
Figure 3.10	Principal elements and Aluminum Crossplots for H(26).....	81
Figure 3.11	Principal elements and Aluminum Crossplots for H(29).....	82
Figure 3.12	Principal elements and Aluminum Crossplots For Haynesville Formation.....	83
Figure 3.13	Major Element concentration in LL(15).....	84
Figure 3.14	Major Element concentration in LL(8).....	85
Figure 3.15	Principal elements and Aluminum Crossplots for LL(15).....	86
Figure 3.16	Principal elements and Aluminum Crossplots for LL(8).....	87
Figure 3.17	Principal elements and Aluminum Crossplots For La luna Formation.....	88
Figure 3.18	Major Elements average concentration per sample.	89
Figure 3.19	Bossier Formation sample TGA results.....	90

Figure 3.20 Haynesville Formation samples TGA results.	91
Figure 3.21 La Luna Formation samples TGA results.	92
Figure 3.22 Bossier Formation samples CEC results.	93
Figure 3.23. Haynesville Formation samples CEC results.	94
Figure 3.24 La Luna Formation samples CEC results	95
Figure 3.25 Clay Mineral Content vs CEC for Bossier Formation Eclipse Plot	96
Figure 3.26 Eclipse Plot for the Clay Mineral Content vs CEC for Haynesville Formation... 96	
Figure 3.27 Clay Mineral Content vs CEC for La Luna Formation samples results	97
Figure 3.28 Eclipse plot compiling the results for the Clay Mineral Content vs CEC.	98
Figure 3.29 As received material (pre imbibition) NMR T2 in Bossier Formation samples. .	99
Figure 3.30 As received material (pre imbibition) NMR T2 in Haynesville Formation.....	100
Figure 3.31 Pre-Imbibition Experiment NMR T2 spectra in La Luna Formation	101
Figure 3.32 Equivalent NaCl salinity (ppm)	103
Figure 3.33. Spontaneous Water Imbibition Experiments in the Bossier Formation.	104
Figure 3.34. Volume Imbibition Experiments in the Bossier Formation.	105
Figure 3.35. Spontaneous Water Imbibition Experiments in the Haynesville Formation	106
Figure 3.36. Volume Imbibition Experiments in then Haynesville Formation.	107
Figure 3.37. Spontaneous Water Imbibition Experiments in the La Luna Formation.	108
Figure 3.38. Spontaneous Water Imbibition Experiment results in the La Luna Formation. .	109
Figure 3.39 Post - water imbibition - Nuclear Magnetic and Imbibition Results.	111
Figure 3.40 Post - water imbibition - Nuclear Magnetic Resonance Results Summary.	112
Figure 3.41. Post - water imbibition – NMR Vs Imbibed Volume Measurement.	113
Figure 3.42 Post - water imbibition - Nuclear Magnetic Resonance Results.	115
Figure 3.43 Post - water imbibition - Nuclear Magnetic Resonance Results - Haynesville. .	116
Figure 3.44 Post - water imbibition – NMR Vs Imbibed Volume - Haynesville.	117

Figure 3.45 Post - water imbibition - Nuclear Magnetic Resonance Results.	119
Figure 3.46 Post - water imbibition - Nuclear Magnetic Resonance Results Summary.....	120
Figure 3.47 Post - water imbibition – NMR Vs Spontaneous Imbibition Imbibed Volume	121
Figure 3.48 B(60) and B(15) Post - oil imbibition for the Bossier Formation samples.....	122
Figure 3.49 Post - oil imbibition Volume for samples of the Haynesville Formation.....	123
Figure 3.50 Post - oil imbibition volume results for La Luna Formation samples	124
Figure 3.51 Supernatant water ionic composition for a) B(60), b) B(40) and c) B(15).....	126
Figure 3.52 Supernatant water ionic composition for a) H(26), and b)H(29).....	127
Figure 3.53 Supernatant water ionic composition for a) LL(15), and b)LL(8).....	127
Figure 3.54 Bossier Samples B(15) thin section image analysis	128
Figure 3.55 Imaging and image analysis.....	130
Figure 4.1 Conceptual model of an unconventional reservoir:.....	131
Figure 4.2 Anhydrite Vs Clay Mineral Content.	132
Figure 4.3 Anhydrite present in supernatant fluids.....	133
Figure 4.4 Anhydrite correction to the supernatant conductivity.	134
Figure 4.5 Anhydrite.....	136
Figure 4.6 Defining the equation terms.	137
Figure 4.7 C_e is expressed in ions and imbibed water in water molecules.	138
Figure 4.8. Equilibrated C_e and Final Anhydrite Concentration	139
Figure 4.9 The α factor and CEC.....	141
Figure 4.10 Equilibrated Concentration (C_e).....	141
Figure 4.11 Equilibrated Concentration.....	142
Figure 4.12 Thin sections for Bossier Formation and the La Luna Formation.	143
Figure 4.13 Characteristic Time (T_c) vs Grain size	144

Figure 4.14 Characteristic time for conductivity t_{cc} , versus anhydrite content	145
Figure 4.15 Characteristic Time Versus Clay mineral content.	146
Figure 4.16 A comparison between the Boyle's Law , and the imbibed water volume.....	147
Figure 4.17 A comparison between the Boyle's Law and the imbibed water porosity.....	148
Figure 4.18 SEM images.....	151
Figure 4.19 Boyle's Law porosity compared with imbibed water porosity corrected for anhydrite dissolution and fracture volume created during crushing.....	152
Figure 4.20 Organic porosity from image analysis.....	153
Figure 4.21. Boyle's Law porosity and imbibed oil porosity.	155
Figure 4.22 The characteristic imbibition time.....	156
Figure 4.23 Combined plots for total conductivity C_t and total imbibed volume V_e	157
Figure 4.24 Characteristic Imbibition Time Vs Clay Mineral and anhydrite content.	158
Figure 4.25 Artificial Fracture Development	159
Figure 4.26 Characteristic Time and Artificial Fracture Porosity.	159
Figure 4.27 Porosities from images (Bossier Formation).....	162
Figure 4.28 Porosity from Images (Haynesville Formation)	163
Figure 4.29 Porosity from Images (La Luna Formation):.....	164
Figure 4.30 Clay mineral content effect on the corrected imbibed water volume (V_e)	166
Figure 4.31 Anhydrite content effect in the corrected imbibed water volume (V_e).....	167
Figure 4.32 Bossier Formation Thin Section, B(60) _{200μm} sample.	168
Figure 4.33 Bossier Formation Thin Section, B(60) _{500μm} sample	168
Figure 4.34 Bossier Formation Thin Section, B(60) _{700μm} sample	169
Figure 4.35 Haynesville Formation Thin Section, H(26) _{200μm} sample.	169
Figure 4.36 Haynesville Formation Thin Section, H(26) _{700μm} sample.	170
Figure 4.37 La Luna Formation Thin Section, LL(15) _{200μm} sample.....	170

Figure 4.38 La Luna Formation Thin Section, LL(15) _{700μm} sample.....	171
Figure 4.38 Laser particle size distribution for the particle sizes used in the study.....	172
Figure 4.39 Corrected V_e as a function of clay mineral content	173
Figure 4.40 Corrected V_e and the anhydrite content	173

CHAPTER 1. INTRODUCTION

Unconventional reservoirs are defined as having permeability/viscosity ratios that require the use of technology to alter either the rock permeability or the fluid viscosity in order to produce reservoir fluids. This definition accommodates tight gas, tight oil, shale gas, shale oil, and heavy oil reservoirs, among others. Tight oil and gas reservoirs are emerging as an important source of energy supply in the United States (U.S) and Canada (Franz and Jochen, 2005). Natural gas demand in the United States is expected to increase from 25 Tcf/year currently, to 34 tcf /year by 2025 and unconventional gas sources will play a significant role in this production.

The Energy Information Agency (EIA) estimates that known shale gas deposits worldwide add 50 percent to the global technically recoverable natural gas resources. In 2012, shale resources constituted 40 percent of U.S. natural gas production and if developed responsibly, this resource has the potential to catalyze the economy and reduce emissions from other conventional energy sources. Compared with coal, natural gas results in less carbon dioxide, particulates, and mercury per unit of energy produced. Conversion to natural gas could substantially reduce carbon emissions from electrical power generation from coal.

Understanding the controls on productivity is critical to increasing the recovery factor in shale gas reservoirs. The volume and salinity of the water produced after hydraulic fracturing may provide insights into reservoir properties and well deliverability.

Produced water from shale gas reservoirs raises several questions. The first involves the high salinity of flowback water. Although hydraulic fracturing fluid is typically essentially fresh water, produced water, or flowback, is often very saline. It is not currently known whether the

recovered salt comes from residual water in the formation, from dissolution of mineral salts, or interaction between bound water and frac fluid. Further, if salt is produced from interaction between stimulation fluids and the formation, it is not known whether it is produced mainly from the rock matrix (e.g., interaction with clay mineral surfaces), or from minerals or fluids present in micro or macro fractures.

The two questions this project investigates are 1) What is the origin of the salt in shale gas flowback water and 2) what this observation tells us about the properties of the reservoir. Figure 1.1 (Ghanbari 2013) shows the continuous change in salinity of flowback water for wells completed in the Horn River Formation in Canada. Maximum salinities between 40 and 80 kppm are observed. However, in other Horn River wells, flowback water salinity up to 200 kppm has been observed (Blauch, (2009); Pritz and Kirby, (2011)). Blauch (2009), observed this same behavior in the Marcellus Formation and proposed possible hypotheses for the salt origin. These authors infer that the salt might be present as a solid phase and dissolved from the shale, or from possible connate water mobilization.

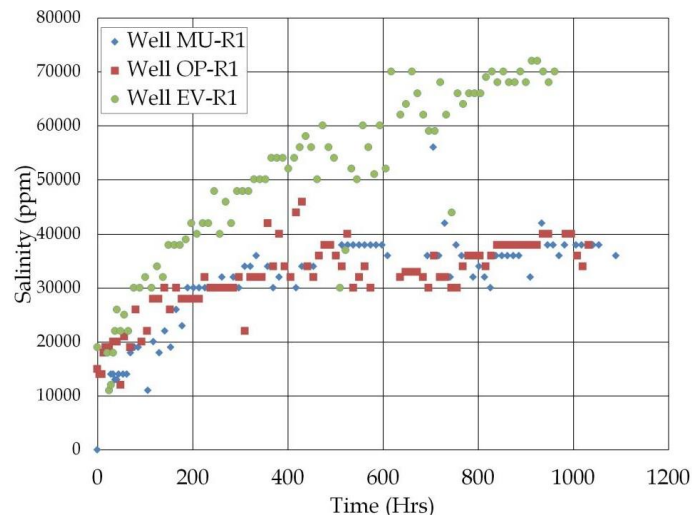


Figure 1.1 Horn River Flowback salinity. Why is salinity increasing with time? Source: Ghanbari, 2013. Used with permission.

magnetic resonance measurement (NMR), dual imbibition experiments, post-imbibition chemical analysis of supernatant fluid, X-ray diffraction (XRD) and X-ray fluorescence (XRF) analysis of bulk material, thin section analysis, and Scanning Electron Microscope (SEM) imaging and image analysis is the approach used to evaluate the controls on flowback water salinity, and will allow us to quantify important reservoir properties (total porosity, in situ salinity and clay mineral content (brittleness)).

This research is divided into five chapters. Chapter I presents a shale gas reservoir overview and literature review. Chapter II presents the methodology, as-received sample characterization, sample selection, and homogenation procedures. Chapter III illustrates the sample characterization results, including the laboratory and imaging techniques.

Chapter IV presents a discussion of the experimental results, including the modelling of the petrophysical parameters and the possible origin of the high salinity. Chapter V presents conclusions and recommendations.

1.1. Hypothesis Statement

In this work, we want to demonstrate that a new approach, combining oil and water imbibition/ ion expulsion experiments, and detailed sample and brine characterization can be used to quantify the properties of the stimulated rock volume (SRV) in shale gas reservoirs including:

- Clay mineral content
- Total Porosity.
- Present-day pore fluid salinity.
- Ion origin and location (precipitated salts, exchange cations, residual water).

Sample characterization includes:

- Thermal Gravimetric Analysis (TGA)
- Particle Volume measurement using Boyle's Law
- Bulk mineralogy using X-ray diffraction (XRD)
- Bulk chemical characterization using hand held XRF
- Laser Particle Size Analysis (LPSA)
- Cation exchange capacity (CEC).
- Nuclear Magnetic Resonance (NMR) measurements pre- and post- imbibition.
- Imaging techniques (TS, SEM).

Brine characterization will include

- Analysis of the supernatant fluid from the imbibition experiments using Inductively Coupled Plasma (ICP)

1.2. Objectives

The objective of this research is to develop a qualitative interpretation for the impact of mineralogy, and petrophysical properties such as permeability, total porosity and wetting state on the results of spontaneous imbibition experiments. The process of spontaneous imbibition is inferred to be analogous to the process of frac fluid interaction with shale gas reservoirs. The results of this experimental work will lead to an improved understanding of the rock-fluid interactions that give rise to the high salinity flowback water in the Bossier, Haynesville and La Luna Formations.

1.3. Recovering Hydrocarbons from Unconventional Resources.

Although some unconventional resources, such as heavy oil and oil sands, have been common targets in the oil and gas industry for some time now, the American oil and gas

revolution from unconventional resources, such as shale gas and shale oil, has occurred since 2005. (Figure 1.3).

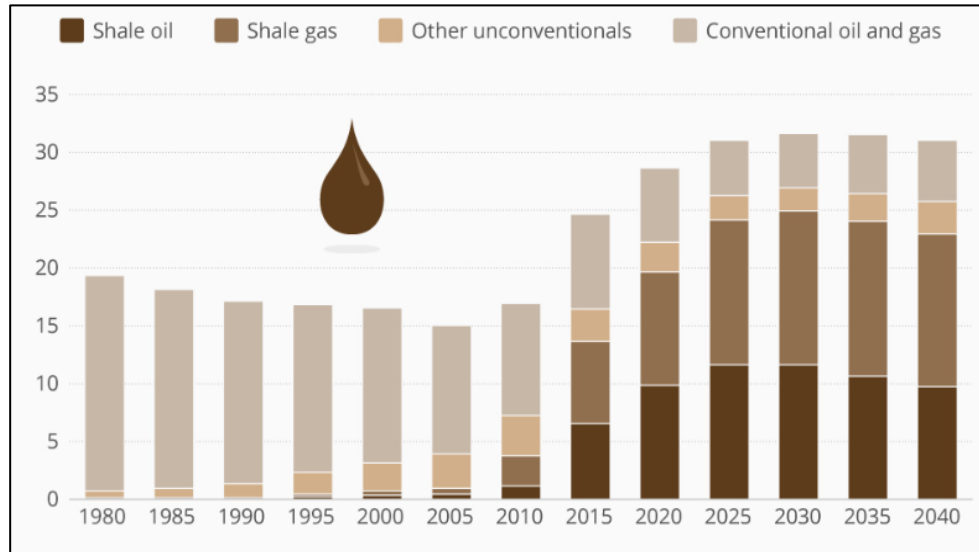


Figure 1.3 The American Shale Revolution Historical and projected US oil and gas production. (million barrels oil equivalent per day). Source: EIA World Energy Outlook 2018.

The shales now being targeted as reservoirs have been known for decades as the source rocks for many of the onshore conventional plays. Geologists have known that vast natural gas resources were locked in shales over much of North America. However, they have been categorized as hard – to - produce resources. Figure 1.4 shows the lower 48 state shale plays in the United States of America. Based on the Energy Information Agency, (EIA) 2021 technical report, the technically recoverable U.S. dry gas resources from these plays is 2359.8 Tcf/year.

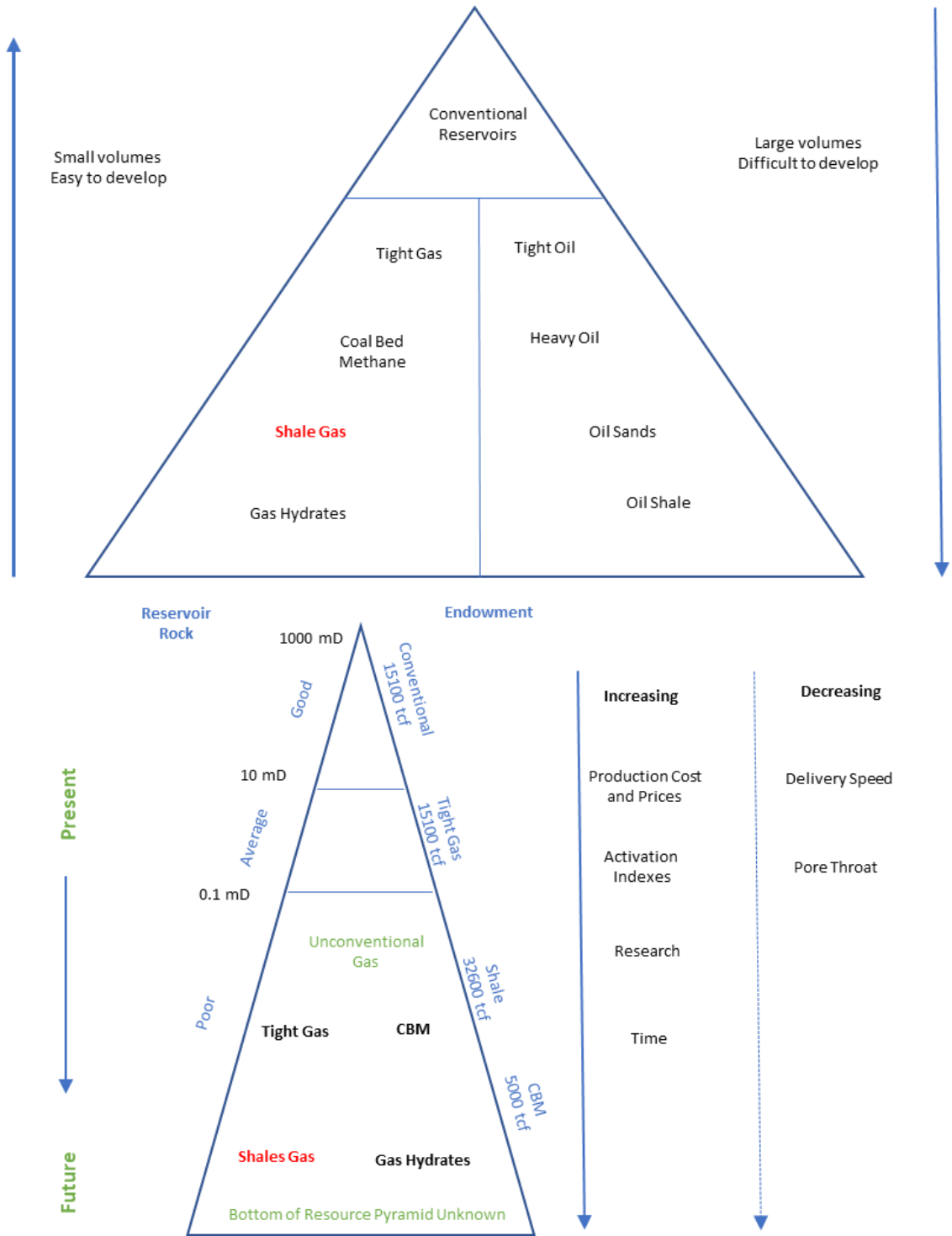


Figure 1.5 World resource pyramid of a) hydrocarbons and b) gas with estimated endowment. Source: Aguilera 2014.

Unconventional resources represent a variety of geological formations, including tight gas sands, gas shales, heavy oil sands, coaled methane, oil shales, and gas hydrates. The EIA defines them using an umbrella term for oil and natural gas that are produced by means that do not meet the criteria for conventional production. Figure 1.5 shows worldwide oil and gas resource pyramids that include general characteristics and global endowment for each resource (Aguilera, 2014). Endowment is defined as the summation of cumulative production, reserves, and undiscovered gas.

1.3.1. What is a shale gas reservoir?

The use of the term “shale” is an example of rather careless use of terminology. Authors do not even agree on an encompassing term for the whole class of formations: shale, claystone, mudstone, mudrock, lutites, pelite, are some of the most general terms that have been widely applied and widely rejected among geoscientists who study the rocks that constitute approximately two-thirds of the sedimentary record on Earth (Milliken 2014).

The term “shale” describes a sedimentary rock type which is a mixture of clay sized particles, mainly comprising clay minerals, silt sized particles, and perhaps some sand-sized particles, for example quartz, occasionally feldspar and calcite (Jorden & Campbell, 1984). Curtis (2002), defined shale gas reservoirs as fine-grained, clay and organic matter rich rocks, which act as both the gas source rock and the reservoir rock components of the petroleum system.

Milliken proposed a tripartite compositional classification for sediments and sedimentary rocks that have grain assemblages with greater than 50 percent by weight or volume of particles smaller than 62.5 μm (Figure 1.6). The rock type “Tarl” (terrigenous– argillaceous mudrock) contains a grain assemblage dominated by more than 75 percent particles of

extrabasinal derivation, including grains derived from continental weathering and volcanogenic debris. The rock type “Carl”(calcareous–argillaceous mudrock) contains less than 75 percent particles of extrabasinal derivation and among its intrabasinal grains contains a preponderance of biogenic carbonate particles including carbonate aggregates. The rock type “Sarl”(siliceous–argillaceous mudrock) contains less than 75 percent particles of extrabasinal derivation and contains a preponderance of biogenic siliceous particles over carbonate grains. These three classes of fine-grained particulate sediments and rocks effectively separate materials that have distinct depositional settings and systematic contrasts in organic-matter content, minor grain types, diagenesis, and mechanical properties.

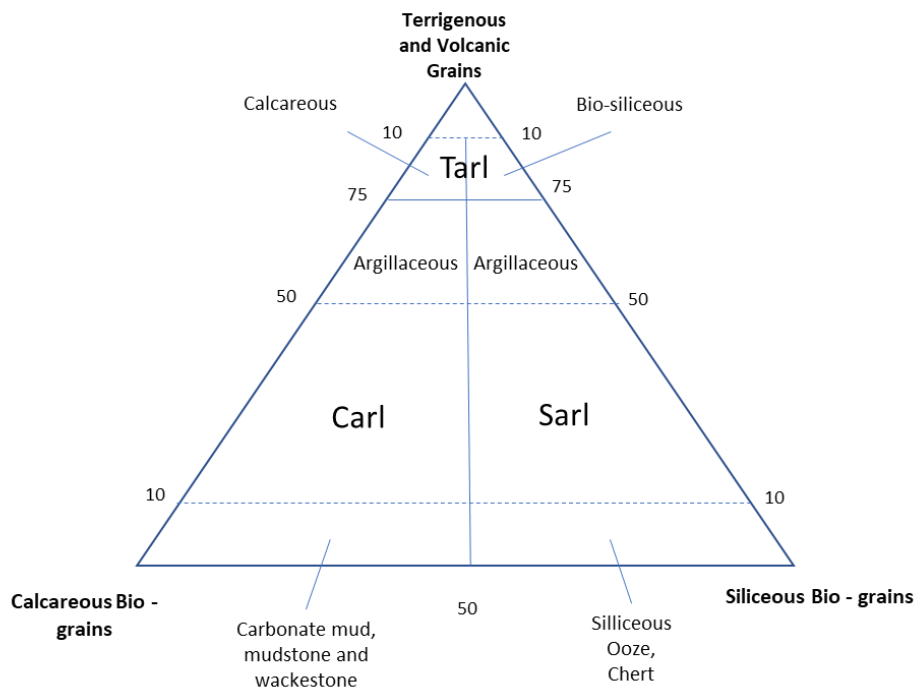


Figure 1.6 Proposed compositional classification for fine-grained sediments and sedimentary rocks. Source: Milliken, 2014.

Shale reservoirs typically have very low permeability and porosity. A typical shale reservoir has a matrix permeability on the order of 1 to 100 nD and a porosity less than 10%.

At deposition, shale reservoirs contain variable volumes of primary organic material, or kerogen. Kerogen is transformed into hydrocarbons during progressive burial and exposure to elevated stress and temperature conditions. Typically, the geological properties of a shale gas play are assessed in terms of organic geochemistry, organic richness, thickness, thermal maturity and mineralogy. For successful production, high total organic carbon (TOC) content and thermal maturity, substantial thickness, and low clay content/high brittle mineral content are needed (Rezaee, 2015). A discussion of these features will appear in a later section.

1.3.2. Why are the Shale gas reservoirs important?

According to the EIA report (2014), by 2035, natural gas will surpass coal as the largest source of United States electricity generation. The report anticipates that the share of electricity generated from natural gas will grow steadily so that natural gas plants will account for more than 70% of all new capacity. The predicted 56% increase in total natural gas production from 2012 to 2040 results from increased development of shale gas, tight gas, and offshore natural gas resources. Although the United States has led the world in unconventional gas production, gas and oil production from shales is of interest worldwide. Estimates for shale gas resources in other countries are often very uncertain because data are sparse. Several European countries are interested in domestic shale gas because of the high cost and political uncertainty inherent in importing natural gas. There are 137 prospective shale formations in 41 countries, 345 billion barrels of world shale oil resources, and 7200 trillion cubic feet of gas resources based on data reported by the EIA in 2014.

Shales in Canada, Britain, Germany, Poland, Ukraine, China, India, Australia, South Africa, Argentina, Brazil, and other countries are being investigated for hydrocarbon potential (U.S. Energy Information Agency, 2015a). The possibility of cheaper and cleaner energy has

prompted interest from governments around the world. China may be able to reduce its dependence on coal and shift to a lower carbon economy (Huang, 2014). The UK has some potential gas shales in England. Germany has also been tentatively investigating potential environmental risks of shale gas development. Argentina recently started joint-venture projects with multinational companies, and Mexico lifted the government's 75-year-old monopoly on oil and gas production, opening some of the world's largest shale formations for development. Worldwide shale gas resources are voluminous. Thus, a better understanding of shale physical properties, and stimulation fluid and reservoir interaction is needed. This understanding is key to improving stimulation techniques and petrophysical interpretation in shale gas reservoirs. A summary of global unproved, technically recoverable shale gas and oil resources is shown in Table 1.1

Table 1.1 Global unproved technically recoverable shale gas and oil resources (tcf). Source: EIA 2013.

2013 EIA Wet Shale Gas / UTRR					
Region and Selected Countries					
Europe	470	North America	1685	Middle East and North Africa	1003
Bulgaria	17	Canada	573	Algeira	707
Denmark	32	Mexico	545	Egypt	100
France	137	USA	567	Jordan	7
Germany	17			Libya	122
Netherlands	26	Asia - Pacific	1607	Morocco	12
Poland	148	Australia	437	tunisia	23
Romani	51	China	1115	Turkey	24
Spain	8	Indonesia	46	Western Sahara	8
Sweden	10	Mongolia	4		
United Kingdom	26	Thailand	5	South Africa	390
Former Soviet Union	415	South Asia	201	South America and Caribbean	1430
Russia	287	India	96	Argentina	802
Ukraine	128	Pakistan	105	Bolivia	36
				Brazil	245
				Chile	48
				Colombia	55
				Paraguay	75
				Uruguay	2
				Venezuela	167
TOTAL WORLD					7201

1.3.3. How can we develop these resources?

The first commercial American gas well was dug by hand into a Devonian-aged shale in 1821 by a gunsmith named William Hart along the bank of Canada Way Creek in Fredonia, New York (Curtis, 2002). Subsequently, hundreds of shallow shale wells were drilled in the late 1800's. However, after the Drake Well in 1859 in Cherry Tree Township, Pennsylvania, shale gas production was discouraged because of the much larger volumes produced by conventional reservoirs. Between 1860 and 1930, shale gas spread westward along the southern shore of Lake Erie and reached northeastern Ohio. By 1926, the Devonian Shale gas field of eastern Kentucky and West Virginia was the largest known natural gas resource in the world. Hydraulic Fracturing was first used was in the 1940's on a gas well operated by Pan American Petroleum Corporation in Grant county, Kansas, USA. Subsequently, larger frac designs, rigorous reservoir characterization, horizontal drilling, and lower cost hydraulic fracture operations led to the successful development of the Barnett Shale play by Mitchell Energy, changing the face of shale gas resources forever.

1.3.3.1 Horizontal Drilling

Until the 1970s, most oil and gas wells were vertical or slightly deviated from true vertical. However, drilling advances and new technologies allowed the industry to go from vertical to strongly deviated wells and to horizontals. Considering that [reservoir](#) rocks are usually horizontal or nearly horizontal, a horizontal wellbore would contact more surface area in the reservoir than a vertical well, resulting in a higher production rate. By using this technology, it was also possible to reach reservoirs several miles away from the drilling location or explore reservoirs where placing a drilling rig was difficult due to environmental sensitivity, population, or natural subsurface barriers.

Due to the low permeability associated with most unconventional reservoirs, a technique was required to improve the flow capacity of those rocks. The use of horizontal drilling coupled with hydraulic fracturing, to create high-permeability flow paths into the shale, was the stimulation technique that enhanced production rates, and made hydrocarbon production from low permeability rocks economically feasible.

1.3.3.2. Hydraulic Fracturing

Hydraulic fracturing (HF) has become a very common and widespread technique in shale reservoirs in North America. Over time, the number of fractures placed in the reservoir has increased, due to the increase in lateral length and fracture stages. The well drainage area is confined essentially to the stimulated reservoir volume (SRV), the part of the formation contacted by induced fractures. The ultimate recovery from fractured shale wells increases as the SRV increases (Fisher, 2004).

Slickwater fracturing is the most common form of well stimulation in unconventional gas. The fracturing fluid is composed primarily of water and sand (> 97%). Additional chemicals are added to reduce friction, corrosion, bacterial-growth, and provide other benefits during the stimulation process.

The process of hydraulic fracturing involves high pressure injection of the fracturing fluid into a wellbore such that the fracture gradient is exceeded, creating extensional cracks in the low permeability reservoir rocks. When the [hydraulic pressure](#) is removed, [hydraulic fracture proppants \(the sand injected with the frac fluid\)](#) hold the fractures open. The fracturing fluids (water and chemical additives) are then returned to the surface in a process called flowback.

Shale formations are highly variable, and for this reason no single technique for hydraulic fracturing has universally worked. Each shale play has unique properties that need to be addressed through fracture treatment and fluid design. Slickwater hydraulic fracturing, which is used extensively in Canadian and U.S. shale basins, is suited for complex reservoirs that are brittle and naturally fractured and are tolerant of large volumes of water. Typically, water-based fluids are the simplest and most cost-effective solution to fracture these formations.

Although the aqueous fluid employed in hydraulic fracturing is typically essentially fresh water, produced water or flowback is often very saline, suggesting that the flow-back water is leaching salt from the formation. If salt is produced from interaction of stimulation fluids and the formation, it is not known whether it is produced mainly from the rock matrix (e.g. interaction with clay mineral surfaces), or from micro or macro fractures. Finally, field observations reveal an interesting phenomenon during injected water flowback. In practice, only a small fraction of the injected fluid is recovered during the clean-up phase and the mechanisms responsible for inefficient water recovery are still poorly understood. Water flowback data such as salinity and volume, can give us insight into the petrophysical properties of the formation, if we can document the mechanisms that play a role in the rock/fluid interactions.

1.3.4. Shale Gas reservoir Properties.

Measuring important petrophysical properties of shale gas reservoirs has proved to be challenging due to the low and dual porosity (inorganic and organic), clay mineral present, ultra-low matrix permeability and complex mineralogy. High uncertainties in terms of storage assessment, hydraulic fracturing results, well gas initial rates and productivity, reflects the complexity of depositional environment settings, diagenesis, and fluid condition (adsorbed and free gas).

In this section, shale gas reservoir properties that influence reserves in place and reserves recovery will be discussed. The discussion will be divided into three principal areas :**1) Organic Geochemistry**, in which the main geological properties such as organic richness and thermal maturation will be examined, **2) Mineralogy and Inorganic Geochemistry**, and their impact on shale mechanical properties and **3) Petrophysical Properties** such as porosity, permeability, adsorbed and free gas, cation exchange capacity, and water saturation among others will be widely addressed.

1.3.4.1. Geochemistry

An important factor in assessing unconventional shale reservoir quality is the content of organic material (OM) or kerogen. Kerogen is defined as insoluble sedimentary organic matter that can generate hydrocarbons upon heating (Bissada, 1982). The term encompasses all the insoluble organic matter recovered from shales and other clastic sediments after they are treated with hydrochloric and hydrofluoric acids. The fraction extractable with organic solvents is called bitumen and the term kerogen does not include it (Tissot, 1978). It should be noted that the remaining organic material in shale gas reservoirs comprises residual terrestrial kerogen (vitrinite and inertinite) and pyrobitumen. Pyrobitumen is generated/migrated hydrocarbon (bitumen) that has been heated to produce gas, leaving behind solid organic material. This is the phase that contains most of the organic hosted pores in shale gas reservoirs (Hathon, 2017).

Examining the organic matter chemical properties and visual characteristics is critical to developing an understanding of how shale gas reservoirs store, retain and release natural gas (Lu et al., 1995, Ritter, 2003, Loucks et al., 2009, Ambrose et al., 2010).

Total organic carbon (TOC) is the concentration of organic material measured in a sample of the formation and is expressed as the weight percent of organic carbon. A formation's

TOC is a determining factor in its ability to generate hydrocarbons. A value of about 0.5% TOC by weight percent is considered a minimum or threshold for an effective source rock. For shale gas reservoirs, in general, values of about 2% are considered a minimum and may exceed 10–12% (Mayal, 2017).

The OM in typical source rocks is composed of four main groups of compounds: carbohydrates, proteins, lipids, and lignin. Carbohydrates and proteins are rapidly consumed by bacteria, leaving lipids and lignin as the primary compounds resistant enough to be buried in quantity. Lipids are generated in large quantities by marine organisms, and by parts of land plants, and are the source of most oil. Lignin, in contrast, is found only in land plants and can produce only natural gas.

In the ocean, photosynthesizing marine algae are the primary producers of organic compounds. Primary productivity is controlled by five factors. Sunlight is essential for photosynthesis, and it is limited to the top 200 m of the ocean, especially the upper 60–80 m known as the photic zone. Turbidity is important because it can greatly decrease the penetration of light into the ocean. Nutrient supply in the form of phosphate and nitrate compounds is required for primary productivity. The supply of nutrients is greatly increased in zones of upwelling, such as along the equator and along the west coasts of continents. Salinity is an important factor that controls the diversity of marine organisms, and to a lesser extent their productivity, although some taxa may flourish in very salty or very fresh water. Temperature also controls the composition of phytoplankton communities but has a lesser effect on their productivity (Bissada, 2016).

Shale gas reservoirs produce methane almost exclusively, although locally there can be lesser amounts of light hydrocarbons such as ethane, and butane, and associated non

hydrocarbon gases including carbon dioxide, oxygen, nitrogen, hydrogen sulfide, radon, and other rare gases (D. Mani, 2017). The quantity, quality, and thermal maturity of organic matter accounts for the gas generation capacity of shales. The higher the organic content of the formation is, the greater is the potential for hydrocarbon generation. The type or quality of organic matter is dependent upon the source of the organic components, and the depositional environment (preservation potential). Variations in these factors result in different kerogen types with varying capacity for oil and gas generation.

As organisms die and sink to the sea floor, accumulation of their remains increases the organic content of the sediment. Most source rocks are deposited in deltas, marine basins, and in some lacustrine settings. Once organic matter is supplied to the seafloor it must withstand respiration by bacteria that use it as a food source. Anoxic conditions on the seafloor favor the preservation of organic matter, and such conditions are controlled by the amount of organic matter and the supply of oxygen in the water column. As the amount of organic matter increases, oxygen is consumed by bacteria, and if enough organic matter is supplied, oxygen will be depleted, and bacteria will shift to anaerobic respiration, which breaks down organic matter at much slower rates than aerobic respiration (Bissada, 2016).

Initially, kerogen breaks down to release CO₂ and H₂O. At higher temperatures, organic matter undergoes catagenesis, in which kerogen breaks down to form oil at 100–150° C, followed by gas at 150–230° C. At temperatures of 150–180° C, oil is rapidly cracked to gas during metagenesis. At even higher temperatures and pressure, graphite is formed (Tissot, 1978).

Organic rich rocks are assumed to be composed of three components: 1) the rock matrix, 2) the solid organic matter and 3) the fluids filling the pore space. Non-source rocks are composed primarily of only two components: the matrix and the fluid filling the pore space. In immature source rocks, solid organic matter and rock matrix comprise the solid fraction and formation water fills the pore space. As the source rocks matures, a portion of the solid organic matter is transformed to liquid or gaseous hydrocarbons which move into the pore space, displacing the formation water. This is essentially the model described by Philippi (1968), Nixon (1973), and Meissner (1978), and is the same general model used by Meyer and Nederlof (1984), Mendelson and Toksoz (1985) and Passey (1990) (Figure 1.7).

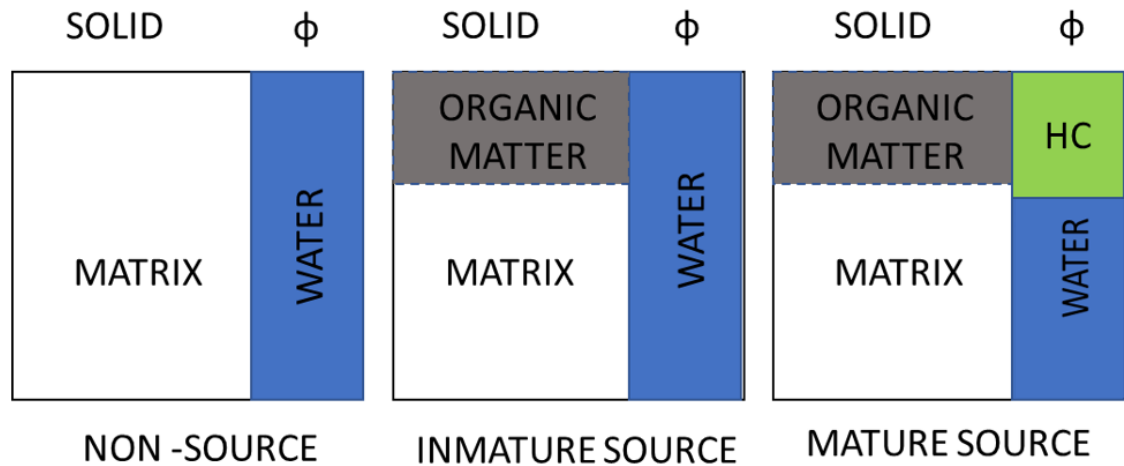


Figure 1.7 Schematic of solid and fluid components in source and non-source rocks. Source: Modified from Passey, 1990.

1.3.4.1.1. Organic Richness

The total volume of hydrocarbons that can be generated and the principal hydrocarbon type (oil versus gas) depend on the composition of the parent kerogen in a petroleum source bed. Two broad classes of dispersed kerogens can be recognized in sediments. One end member, commonly referred to as sapropelic kerogen, consists of modified amorphous algal remains with a relatively low oxygen/carbon ratio, which yield mainly oil. The other member, commonly

referred to as humic kerogen, consists of land-plant derived lignitic and cellulosic constituents enriched in aromatic structures. Humic kerogen has a low hydrogen content and a relatively high oxygen/carbon ratio. Upon thermal maturation, humic kerogen yields primarily gas. A mixture of humic and sapropelic kerogen will yield both oil and gas (Tissot, 1978).

1.3.4.1.2. Thermal Maturation.

The degree of thermal exposure experienced by a source rock in the subsurface is critical for the generation of hydrocarbons. Thermal maturity is the extent of temperature–time driven reactions, which are responsible for the conversion of sedimentary organic matter to oil and gas (Mani et al., 2015). Vitrinite reflectance ($R_o\%$) and Rock Eval pyrolysis temperature of maximum S2 peak (T_{max}) are popularly used parameters to assess the thermal maturity of kerogen. Thermally immature source rocks have not been heated sufficiently to generate significant volumes of hydrocarbons ($<0.6\%R_o$) (Mani et al., 2015a). Thermally mature organic matter generates oil ($0.6\text{--}1.35\%R_o$), whereas the post-mature organic matter is in the wet and dry gas zones (Tissot and Welte, 1984, Mani et al., 2015a).

Rock Eval pyrolysis is one of the most basic screening steps in evaluation of a source rock and is used to estimate the petroleum potential of source rocks. It involves a progressive heating of a rock sample in an inert atmosphere. Hydrocarbons already present in the rock at the time of sampling are volatilized by moderate heating, given by the first peak (S_1), increased pyrolysis temperature, and associated thermal degradation of kerogen produces another peak (S_2) which represents the potential for generating additional hydrocarbons. The total S_1 and S_2 should reflect the generation potential of the rock (Bissada, 2016). In highly mature gas window formations, Rock Eval is not particularly useful because all hydrocarbons have been generated.

1.3.4.2. Mineralogy and Inorganic Chemistry

In some unconventional formations, such as tight sandstones and carbonates, the reservoirs are not the source rock, but contain migrated hydrocarbons. In these settings, lithofacies interpretation and analysis based on cores and/or wireline logs provide the input for reservoir characterization and modeling (Ma et al., 2011). Although mineralogy plays an important role in understanding the lithofacies and rock types (Rushing et al., 2008) and the lithofacies may govern the fluid storage and flow, a detailed breakdown of mineral compositions is generally not necessary in conventional reservoirs. In contrast, for unconventional reservoirs, an accurate mineralogical model is highly important for formation evaluation. Bulk mineralogy, (e.g. XRD or FTIR), the origin (detrital vs. authigenic), and distribution of phases, impact the geomechanical behavior of these reservoir, and therefore the success of the hydraulic fracture, critical for the fluid deliverability.

High-resolution imaging reveals that fine-grained sediments contain, in addition to detrital clay minerals of clay size, a significant silt-size fraction that includes all the common grain types observed in sandstones and all the grain types common to limestones of shallow-water platforms. In addition, a variety of grain types not as commonly observed in sandstones or shallow water limestones are typically present in shale reservoirs. These include the pelagic grains typical of deep-sea sediments and a wide array of sediment aggregates produced by inorganic and biogenic processes during and soon after sedimentation (Schieber, 2007, Macquaker, 2010, Milliken, 2012, Schieber, 2013). It is also now well established that fine-grained sediments experience the full range of post-depositional effects that are observed in other sedimentary rocks, including compaction, cementation, grain replacement, and fracturing (Milliken 2004, Milliken, 2012).

Although high-resolution imaging has allowed visual characterization of shale reservoirs, it has also revealed the complexity of these fine-grained assemblages. Developing a classification for shale reservoirs using the same strategies employed for compositional classification that have worked for sandstones and limestones, is not practical because the potential sources of grains and the ranges of grain compositions are too complex (Milliken, 2014). Milliken proposed a classification based on two concepts: 1) Material Origin, Intra- or Extra-basinal, and 2) Principal grain composition (clay plus quartz), particles of biogenic carbonate, or particles of biogenic silica.

Figure 1.8 shows the tripartite classification Millikan proposed using high resolution images in three different samples 1) the Eagle Ford Formation as a Carl (calcareous–argillaceous mudstone) containing less than 75 percent extra-basinal debris, and with intrabasinal grains comprising a preponderance of biogenic carbonate particles over biosiliceous grains. 2) The Barnett Shale is classified as a Sarl (siliceous–argillaceous), containing less than 75 percent extrabasinal debris, and with intrabasinal grains comprising a preponderance of biogenic siliceous particles over carbonate grains. Finally, 3) a typical Cenozoic Succession Gulf of Mexico (GoM) sample is classified as a Tarl (terrigenous–argillaceous), which contains a grain assemblage dominated by more than 75 percent particles of extrabasinal derivation.

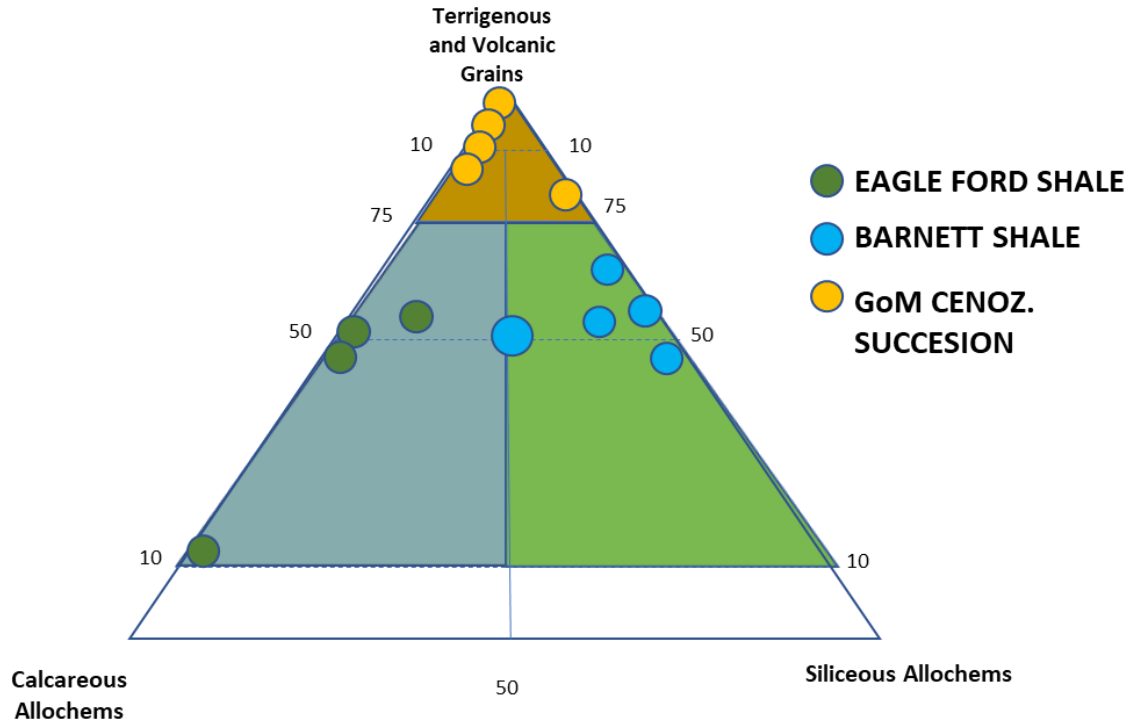


Figure 1.8 Milliken Mineralogy Ternary plot. Source: Milliken, 2014.

Using Milliken’s classification, the formations utilized in this research include two Tarl rock types the Bossier and the Haynesville Formations, and one Carl rock type, the La Luna Formation of Colombia.

In summary, understanding both the mineralogy and the origin of the grains making up shale formations is critical to understanding both reservoir quality and completion quality. As for other sedimentary rocks, texture, or particle size distribution, is also important. Despite the presence of abundant sand and silt sized particles in many samples, fine-grained extra-basinal sediments are dominated by clay sized (less than 2 microns in diameter) particles and clay minerals, certainly by grain number, if not by weight or volume. Because of their large surface area relative to volume (Dogan et al. 2006) and significant chemical reactivity (Johnston 2010), the presence of clay-sized material substantially impacts the physical and chemical properties of sediments even when the abundance of clay sized particles by weight or volume is relatively

small. Spontaneous imbibition and ion expulsion experiments are expected to be strongly correlated with the amount and type of clay minerals presents in the samples. In the next section, a description of clay minerals (typically present as clay sized material) is presented.

1.3.4.3. Clay minerals

The term clay describes both a particle size and a group of hydrous aluminosilicate minerals. Many petrophysical properties of shales/mudrocks are controlled by the presence of clay minerals. These properties include for example, gamma radiation, electrical properties, cation exchange capacity, neutron log response, and permeability among others. The presence of clay minerals in reservoir rock is an important factor in formation evaluation. Particularly in shale reservoirs, the abundance of clay minerals has substantial impact on reservoir production and development strategy.

Because clay minerals typically display extremely fine particle size, they have very high specific surface area and, therefore, they can bind a significant amount of pore water to their surfaces. Clay minerals consist of two fundamental crystal sheets or layers, the tetrahedral layer (comprising essentially SiO_2 , termed T in the following discussion), and an octahedral layer (comprising Al-oxy-hydroxide, termed O in the following discussion). The way in which these sheets are stacked together with different bonding and different metallic ions in the crystal lattice, constitute the different clay minerals (Holtz & Kovacs, 1981).

1.3.4.3.1. Types of Clay Minerals

Kaolinite

Compared with other clay minerals, kaolinite is chemically and structurally simple. It is described as a 1:1 or *TO* type clay mineral because its crystals consist of stacked *TO* layers. Each *TO* layer consists of a tetrahedral (*T*) sheet composed of silicon and oxygen ions bonded to an octahedral (*O*) sheet composed of oxygen, aluminum, and hydroxyl ions. The *T* sheet is so called because each silicon ion is surrounded by four oxygen ions forming a tetrahedron. The *O* sheet is so called because each aluminum ion is surrounded by six oxygen or hydroxyl ions arranged at the corners of an octahedron.

The two sheets in each layer are strongly bonded together via shared oxygen ions, while layers are bonded via hydrogen bonding between oxygens on the outer face of the *T* sheet of one layer and hydroxyl on the outer face of the *O* sheet of the next layer (Nesse, 2000).

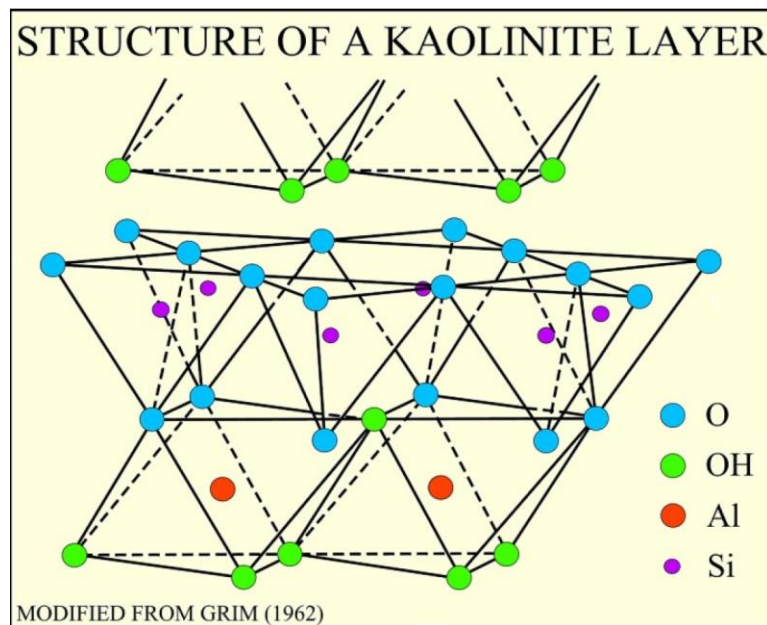


Figure 1.9 Structure of a Kaolinite Layer. Source: Modified from Grim 1962.

Chlorite

It is described as a 2:1 sandwich structure, because its crystals consist of stacked TOT layers. This layer combination creates a space between each 2:1 sandwich filled by an ion. This space is called the interlayer space and in the case of Chlorite is composed of $(\text{Mg}^{+2}, \text{Fe}^{+3})(\text{OH})_6$. This unit is more commonly reference as the brucite-like layer due to the closer resemblance to the mineral brucite ($\text{Mg}(\text{OH})_2$).

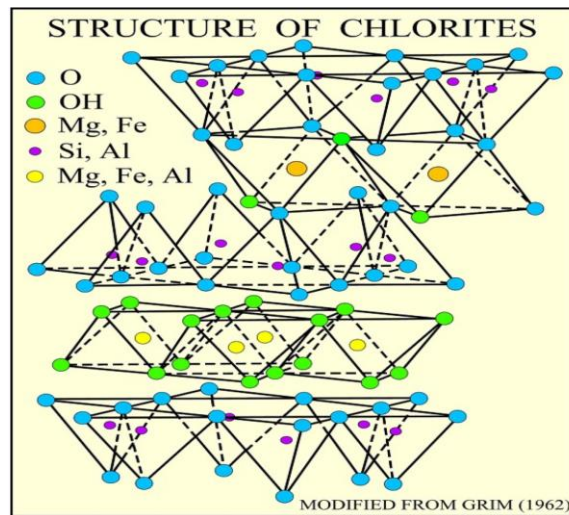


Figure 1.10 Structure of a Chlorite Layer. Source: Modified from Grim 1962

Illite

Illite forms from weathering of silicates. It was first described in the Maquoketa Shale in Calhoun County, Illinois, USA, in 1937. The name was derived from its type location, Illinois (Mitchell, 1993). It possesses a 2:1 sandwich structure (*TOT*) comprising a silica tetrahedral layer (T), an alumina octahedral layer (O) and a second silica tetrahedral (T) layers. The interlayer space is occupied by poorly hydrated potassium cations which are responsible for the absence of swelling. This is the type of clay mineral most abundant in the samples that will be used in this project's experiments.

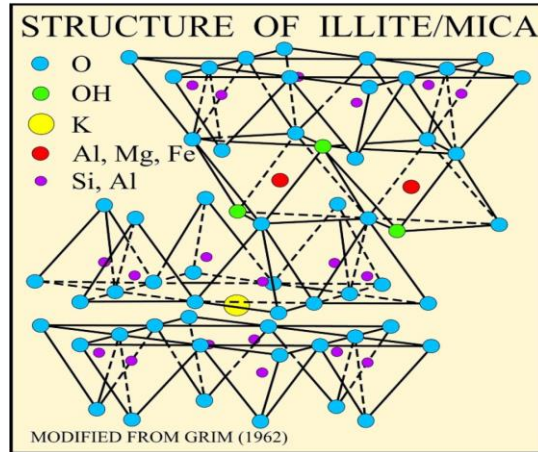


Figure 1.11 Structure of Illite minerals. Source: Modified from Grim 1962.

Smectite

The basic structural unit of smectite clays is like that of illite, two inward pointing tetrahedral (T) sheets bonded to a central alumina octahedral sheet (O), forming a TOT structure. The bonds between adjacent TOT layers are weak, resulting in excellent cleavage, allowing water to enter between the layers causing swelling (U.S Geological Survey, n.d.).

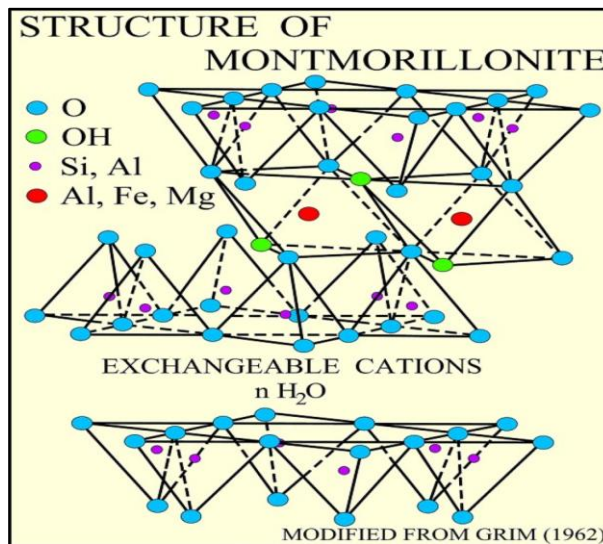


Figure 1.12 Structure of Montmorillonite minerals. Source: Modified from Grim 1962

The amount and type of clay minerals present in a formation modify the rock physical, chemical, and mechanical properties, such as porosity, pore fluid salinity, permeability and fracability among others. The next section presents an overview of the various petrophysical properties that are affected by the presence of clay minerals, as well as that the properties that may be extracted based on spontaneous imbibition and ion diffusion experiments.

1.3.4.4 Characterization of Physical Properties

The objective of this research is to extract shale gas reservoir physical properties from spontaneous dual imbibition and ion expulsion experiments. In the following subsections we discuss the physical properties that are expected to be most highly correlated with the occurrence of high salinity flowback water.

1.3.4.4.1. Clay mineral content and Cation Exchange Capacity (CEC)

Cationic substitutions in the tetrahedral and octahedral layers of clay minerals give rise to unsatisfied negative surface charges. These negative charges are satisfied by cations in solution that are electrostatically bound to the clay mineral surface and give rise to the cation exchange property of clay minerals. As stated by Johnson et al.,(1977), the cation exchange capacity is “defined as the amount of positive ion substitution that takes place per unit weight of dry rock.” Certain solids, e.g. clay minerals, have charged sites on their surface which attract ions. The Cation Exchange Capacity(CEC) may be defined as the reversible exchange of ions between a liquid phase and a solid phase which is not accompanied by any radical change in the structure of the solid. The most common exchangeable cations are Ca, Mg, OH, K, and Na (Campos and Hilchie,1980). The CEC is expressed in mili-equivalents of cations per hundred grams of dry solids. The influence of CEC on the conductivity of clay mineral bearing formations can be described by the charge concentration per unit pore volume, or Q_v . Q_v is related to the CEC by the equation

$$Q_v = \frac{CEC * (1 - \phi) \rho}{100} \quad , \quad \text{Eq. 1}$$

where Q_v is in meq/unit pore volume, $CEC = \text{meq}/100\text{g}$, ϕ = fractional porosity, and ρ = grain density, in g/cm^3 . Q_v was used by Waxman and Smits (1967) in their shaly sand interpretation model to compensate for the effect of clay minerals on the resistivity of shaly sand reservoirs. CEC measurements were obtained for all the samples in this research in order to evaluate the relationship between CEC and imbibed volume and ion diffusion during spontaneous water imbibition.

1.3.4.4.2. Porosity

Porosity is one of the most basic factors in formation evaluation for both conventional and unconventional plays, because it represents the storage capacity for hydrocarbon resources. Three types of porosity have been identified in organic-rich gas shales including matrix porosity (associated with the mineral matrix), organic porosity (pores formed within organic matter, produced primarily during hydrocarbon generation), and fracture porosity (Loucks, 2012, 2009).

An organic-rich shale is typically composed of clay and non-clay mineral matrix and contains pore space between these mineral components (Ambrose, 2012). Rocks with high total organic content (TOC) often have high porosity because the transformation from kerogen to hydrocarbons often leads to an increase in pore volume. Organic matter associated porosity tends to increase as thermal maturity increases. It is widely accepted that organic matter associated pores are hydrocarbon saturated.

The total porosity represents the pore space associated with the mineral matrix and that associated with the organic material, and includes the space occupied by hydrocarbons, mobile, and capillary-bound water, and clay-bound water.

Determining porosity in shale reservoirs is difficult and is often measured using a volume displacement or gas-filling method after crushing the rock to a specific particle size, (25-30 mesh), which is equal to 750 – 500 μm , (Luffel, 1992, Bustin, 2008, Passey, 2010, Bust, 2011). This method is called the GRI (Gas Research Institute) method. The measurement protocol is as follows. Bulk volume is measured by mercury immersion, then the sample is crushed, solvent extraction is performed, and the sample is then dried in an oven at 110C to remove pore fluids. Grain volume is measured by Boyle's Law and pore volume is calculated by the difference between bulk volume and grain volume. Due to the fine grain sizes, low permeability and organic matter presence, these measurements are not easy, and discrepancies exist when comparable samples are measured by different laboratories.

1.3.4.4.3. Fluid Saturation

Evaluating fluid saturations is an integral part of analyzing reservoir quality. In shale gas reservoirs, gas is contained within pore space and fractures or attached to active surface sites on the organic matter contain within a shale. Together, this combination of free gas and adsorbed gas make up the total gas contain in a shale. Gas storage in shales is characterized by plots of the quantity of adsorbed gas, free gas and/or total adsorbed gas at different pressures called isotherms. Adsorption isotherm measurements enable the evaluation of the maximum adsorption capacity of gas by organic matter as a function of pressure (Boyer, 2006). The most commonly applied adsorption model for shale gas reservoirs is the classic Langmuir isotherm model. The Langmuir model is one of the earliest models for adsorption, which assumes that there is a dynamic equilibrium at constant temperature and pressure between adsorbed and free gas (K.S. Lee, 2016).

In terms of water saturation, the presence of clay minerals increases the clay-bound water saturation in shale reservoirs. In addition, small pore throats associated with fine-grained clay promote high capillary bound water volumes. However, residual water saturation in shale gas reservoirs is not necessarily high. It ranges from 15- 40% in the Haynesville Formation, from 7 to 31% in the Eagle Ford Formation, and from 13-35% in the Marcellus Shale (Hammes, 2011, Jarvie, 2007, Stoneburner, 2010, Wang and Carr, 2012). The reduction of water saturation in gas reservoirs takes place by two mechanisms. First, is the immiscible displacement of the water by the flowing gas, and second, is the evaporation of subsequent irreducible water by thermodynamic equilibrium between vapor and water film (gas stripping) (J.Lin et al., 2017).

1.3.4.4. Permeability

Permeability is a measure of the capacity of the rock's pore system to transmit fluids. In general, shale gas reservoirs have much lower permeability than sandstones, limestones, or dolomites. Typically, for unconventional reservoirs, permeabilities might be several orders of magnitude less than 0.1 mD. See figure 1.13.

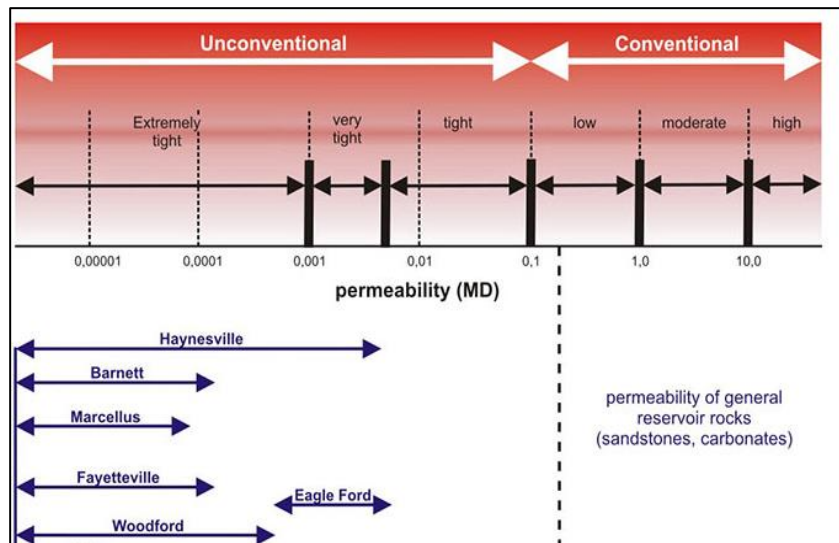


Figure 1.13 Permeability of general reservoir rocks. Source: Schlumberger.

Shale permeability is an area of active research because of the complexities involved in modelling flow through nanoscale pore throats (e.g., Sakhaee-Pour, 2012). The measured permeability of an organic rich shale sample varies significantly with confining pressure, temperature and the type of fluid used to make the measurement. The complexity is mainly caused by the stress dependence of the matrix permeability, the common presence of bedding plane parallel desiccation cracks and/or natural fractures, and because organic rich shales contain significant volumes of fluids in sorbed states (Wasaki, Asana, 2015). The measurement is also made difficult due to limitation of existing equipment, and the time required to make flow property measurements on intact samples.

Both the kerogen type and thermal maturity can also have an impact on the permeability and deliverability of the source rock. The permeability to gas in kerogen pores should be much greater than that in pores within the inorganic matrix. The presence of connected kerogen pores is the key to producing hydrocarbon from the shale. Because maturation of kerogen causes shrinkage, and continued maturation may develop a connected hydrocarbon-wet pore system, a good correlation between permeability and the amount of TOC is commonly observed (Y.Zee Ma, 2016). Understanding the evolution of porosity and permeability created through the diagenesis and catagenesis of kerogen as well as the evolution of matrix porosity and permeability are both necessary to building models for pore systems in organic-rich shales (Unconventional Oil and gas resources Handbook, Y.Zee Ma). In this project, the approach was to use the relationship between diffusion coefficients and permeability, in order to model the latter. However, imbibition experiment results suggested that diffusion is not occurring. This will be discussed in a later section.

1.3.5. Shale Gas Reservoirs Used in This Study

In this section, the petrophysical properties of the formations that were used in this study will be discussed. This includes total porosity, water saturation and clay content, as well as a briefly description of the depositional environment.

The Haynesville Formation: The Haynesville is a Jurassic aged, organic rich shale that covers Caddo, Bossier, De Soto, Red River and Bienville parishes in north Louisiana and Harrison, Panola, Shelby, and San Augustine counties in east Texas. The present-day depth ranges from approximately 10,000 ft to 14,000 ft. Its thickness varies between 80 and 350 ft. The depth and thickness of the Haynesville make it especially interesting because of generally thicker net pay and higher reservoir pressure (0.85 and 0.9 psi/ft).

The lithofacies observed in the Haynesville vary between calcite rich shale with lesser clay volumes, and silica rich shale with larger amounts of clays and lesser amounts of calcite. (Parker et al.,2009). The Haynesville is characterized as an organic and carbonate rich mudstone with total organic content ranging between 2 – 5% and carbonate content up to 40%. The total porosity is between 6 and 15%, water saturation varies between 15 – 40 %, and thermal maturity (vitrinite reflectance (Ro)) between 1.3 and 2.4% (dry gas window). Total clay content is typically less than 40% (Pope et al., 2010, Thompson et al., 2010, Hammes et al., 2011, Jayakumar et al., 2011, Johnson et al., 2013).

Mean initial production rates in the core area of Louisiana are approximately 14 mmcf/day (Wang and Hammes, 2010). Translating these high rates into estimated ultimate recoveries (EURs) is difficult because of the high initial decline rates. Estimates range from 1.5 to 7.5 bcf per well (Berman, 2009; Stoneburner, 2009).

Facies descriptions from cores from Louisiana and Texas reveal that the highly organic-matter-rich shales were deposited in a restricted basin surrounded by carbonate platforms and siliciclastic shelves. The facies, fauna, and regional tectonic features indicate deposition in a slope to basinal setting within a restricted basin. During Haynesville deposition, the Gulf of Mexico (GOM) Basin was partly open toward the south and east and was connected to the Atlantic Ocean (e.g., Salvador, 1987; Ziegler, 1989). The Haynesville carbonates and shales were deposited during a worldwide transgressive event that deposited black shales in a variety of basins associated with anoxia events (Ulmishek and Klemm, 1990). Intrabasinal highs are evidenced by missing sections and unconformities (e.g., Sabine Island) and by facies changes from shales to carbonates.

The Bossier Formation: The Bossier is often discussed in relation to the Haynesville Shale because it lies directly above it. The Bossier is approximately 1800 ft thick in the area of interest (East Texas Basin) and produces hydrocarbon and delivers large amounts of natural gas when properly treated. (Speight, 2017). In terms of depositional environment, it is similar to the Haynesville Formation, influenced by basement structures, local carbonate platforms, and salt movement associated with the opening of the Gulf of Mexico Basin with periodically restricted environments and reducing anoxic conditions. Both shales are prospective for shale-gas production, but the Haynesville mudstone is more organic matter rich, whereas the Bossier mudstone has organic matter content diluted by terrestrial input (Cicero et al., 2010). These compositional differences are related to position within the depositional sequence and geography: the transgressive Haynesville is carbonate dominated, whereas the high stand Bossier is siliciclastic dominated.

Like the Haynesville Shale, the Mid-Bossier Shale is an over-pressured, organic-rich shale characterized as an organic rich mudstone with total organic content ranging between 2 – 5% and carbonate content up to 25%. The total porosity is between 8 and 10%, water saturation

varies between 15 – 30 %, and thermal maturity (vitrinite reflectance (Ro)) between 1.3 and 2.4% (dry gas window). Total clay content is typically between 20 and 60% and TOC > 3% (Hammes et al., 2011), Recent completions in the Mid Bossier Shale range from 4-25 MMCF/day with most completions exceeding 10 MMCF/day.

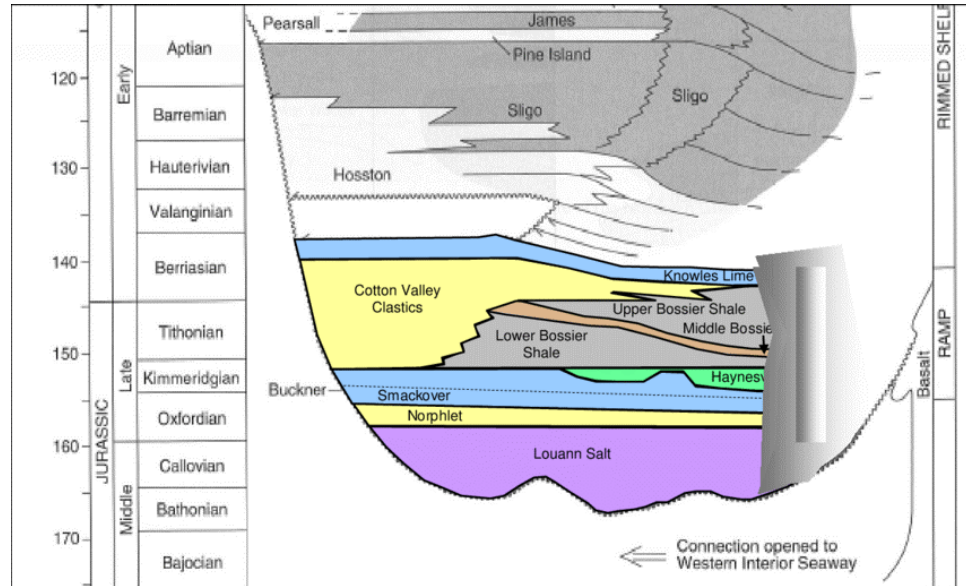


Figure 1.14 Bossier and Haynesville Stratigraphic Column. Source: Galloway, 2008.

La Luna Formation: The La Luna Formation, a Cretaceous sequence in the Middle Magdalena Valley Basin (MMVB) of Colombia, is described as calcareous shales and limestones, black in color, with high foraminifera content and with calcareous and phosphatic concretions (Torres et al., 2015). Formation members are named Galembo, Pujamana, and Salada. The Galembo member corresponds to a calcareous shale with limestone layers and nodules. It is the most calcareous interval represented largely by mixed calcareous/siliceous mudstones. The Pujamana member, comprising claystone, mudstone, gray shale, and cherts, and the Salada member comprising black shales, black mudstones, black calcareous claystone, black limestone layers, and concretions with pyrite. TOC values in the Pujamana and Salada members average approximately 3.5 wt.% and 4.5 wt.%, respectively (Zumberge, 1984), whereas TOC values in the Galembo Member reach 2.4% (Rangel, 2000b). Liquid

hydrocarbons (Ro 0.6-0.9%) are present in the northern and central parts of the Middle Magdalena Valley Basin (MMVB), and condensates and wet/dry gases are present in the formation in the southern MMVB areas. The average porosity estimated using SEM images for the Galembó member is 8.5% and is 8.11% (Torres et al., 2015) for the Salada member. The thicknesses of the members as observed in outcrop vary from 180–720 ft. for Galembó, 300–400 ft. for Salada and 500 ft. for the transitional Pujamana member. (Torres et al., 2015). Table no 1.2 summarizes the fundamental properties of the reservoirs studied in the project and data for other important shale reservoirs for comparison.

Table 1.2 U.S. and Colombian Shale systems. Source: Reservoir Engineering. The fundamentals, simulation and management of conventional and unconventional recoveries. Abdus Satter, 2017. Unconventional Assessment of La Luna Formation in the MVV, Colombia. Torres, 2017.

	Bossier	Haynesville	La Luna
Location	Gulf Coast, TX, US	Gulf Coast, TX, US	MMV - Colombia
Depth (ft)	6000-12500	12500 -13500	4000-17000
Porosity (%)	3 - 9	6-15	7-10
Permeability (nD)	658	658	920
Net Shale Pay Thickness (ft)	500-1000	60-200	200-500
TOC (wt%)	1-5	2-5	2-20
Ro (%)	1.6-3	1-2.2	0.60-3
Water Saturation (%)	20-30	20-30	20
Hydrocarbon Type	Gas	Gas	Oil-Gas

1.3.6. How the Industry Uses Flowback Water Chemistry

After hydraulic fracture generation and during production, a portion of the injected fracturing fluid returns to the surface alongside the produced hydrocarbons (Abbasi et al., 2012). This returning water is called flowback water and is different than the injected water (Rimassa et al., 2009). For instance, fresh water is injected into the reservoir to create the fractures while the flowback water is highly saline. This observation is one of the fundamental questions addressed in this research, in terms of understanding where this high salinity is coming from

and what petrophysical properties might be controlling this phenomenon.

The concept of flowback water physicochemical analysis is not a new topic. In 1989, Keller observed that the electrical conductivity of the produced water increases with time, suggesting that salt dissolved and diffused into water. In 1994, Ballard et al., developed an experimental technique that used radioactive tracers to monitor the progress of water and selected dissolved ions through a core plug. The objective was to gain a better understanding of the fundamental processes involved in maintaining wellbore integrity by chemical inhibition of water-based muds. They identified water transport rates and mechanisms for selected shales, using three outcrop samples and two preserved cores, all from North Sea. Sample porosity ranges from 8 and 60%. Samples were smectite rich with cation exchange capacities between 4 and 48 meq/100gr , which are much higher than the samples used in this project. Experiments showed that transport rates of water and ions through shales vary depending on the shale type and appear to depend on porosity when no pressure is applied in the experiment.

Woodroof (2003), monitored fracturing fluid flowback to optimize well clean up in the Bossier Formation Sand by using Chemical Frac Tracers (CFT) . Samples of the flowback fluid were collected every 10 minutes to 1 hour at the surface for a minimum of 24 hours. In some wells, fluids were sampled for up to 30 days. The collected samples were analyzed detecting the family of CFT's down to the ppt (parts per trillion) level. The mass of each CFT recovered in a given time period together with the total recovered flowback volume for that same time period were used to calculate flowback efficiencies using the mass balance technique. The resulting stage-by-stage fluid recovery profiles were then used to help characterize the effectiveness of cleanup and to make recommendations regarding potential improvements in treatment fluid cleanup that might be obtained by changes in the treatment fluid chemistry, proppant scheduling, flowback procedures, etc.

Fan et al., 2010, built a simulation model for wells stimulated with multistage hydraulic fractures in the Haynesville Shale. The models investigate factors such as 1) pore pressure, 2) matrix rock quality, 3) natural fractures, 4) hydraulic fractures and 5) complex fracture networks by history matching the observed production. Fan included in the model the recovery of flowback water and how this factor is affected by the fracture complexity around each perforation cluster. He observed that in many cases, the wells with less flowback water had better early production rates and suggested that most of this water stays in the created fractured system. He suggested that at the end of the treatment, two regions were created. Region 1, where the fractures were filled with proppant and water and Region 2, where fractures will be filled with treatment water only and may be trapped and never be returned. The more fractures created, the more fluid loss there is to the formation.

Blauch et al., (2009) proposed five different hypotheses for the origin of salt in flowback water in the Marcellus Formation: 1) Primary dissolution of Autochthonous Salt: Autochthonous means rocks that have been formed in situ. Basically, dissolution of evaporite minerals, including halite. For this hypothesis to be proved true, salts and evaporite minerals should be able to be observed in subsurface samples and the cations and anions typical of such evaporite minerals should be present in flow back water. 2) Primary Dissolution of Allochthonous Salt: Another hypothesis that Blauch suggested, was the presence of soluble salts that may be formed from hydrogeologic emplacement and subsequent crystallization in pores. Direct observation of fracture – filling and/or pore – filling salts, including halite, from subsurface cores would also be required to prove this hypothesis true. 3) Encroachment of Basinal Brine: The authors proposed a situation in which a more permeable zone that contains mobile brine is reached. 4) Mobilization of Hypersaline Residual Fluid: Blauch invokes mobilization of otherwise immobile, high saline, residual water and 5) combinations of all above.

At the end of the study, based on XRD, flowback water geochemistry, and direct observation of the core, Blauch was more inclined toward primary dissolution of salt minerals including halite as the control on flow back salinity. However, he suggested that more work was needed in many areas, including isotopic studies, ionic distribution mapping and more analysis in cores and cuttings.

In 2010, Carman and Lant published a paper about clay stabilization by analyzing clay responses to fluid exposure using a method developed in 1967 named Capillarity Suction Time (CST). CST testing defines the time to move a water front between two electrodes, which is related to the ability of the fluid to flocculate or disperse clays in a sample. When comparing multiple samples in the same fluid, the longer the time for water front movement, the greater the water sensitivity of the sample. In terms of clay stabilization, conclusion was that water concentrations of 2%, 4% and 7% KCl performed similarly in most of the cases. In terms of clay characteristics, they mentioned that clay minerals have a great affinity for water. Some clays (smectite) swell easily and may double in thickness when wet. Most have the ability to soak up ions (electrically charged atoms and molecules) from a solution and release the ions later when conditions change. These exchangeable cations can be leached out during the fracturing operations and impact the water chemistry.

Recently, flowback water high salinity has been considered as a complementary approach for evaluating reservoir properties and fracturing operation. Understanding the source of flowback salts and the mechanisms controlling the water chemistry is essential but also challenging due to the complexity of shale-water interactions (Zolfaghari, 2015). Ghanbari et al., (2013) analyzed flowback salt concentration data from hydraulically fractured horizontal wells completed in the Horn River Basin, Canada. The objective was understanding how the flowback was related to the imbibition process, presence or absence of natural fractures and the

complexity of the fracture network. Based on flowback volume and gas production analysis, Ghanbari showed that wells with low flowback efficiency have higher early time gas production and that shale samples with higher clay content and microfractures have higher water imbibition and ion diffusion rates.

Bearinger (2013), mentioned that flowback water contains information about the nature of the stimulated reservoir. He proposed an analytical model to explain the observed trends in flowback salt concentration in the Horn River Formation by hypothesizing that the water recovered from induced hydraulic fractures has a different chemical signature than the water recovered from the stimulated natural fracture network. Bearinger explained that unlike the induced fractures, natural fractures have in situ water coating the mineral surfaces of the fracture. This in situ water can mix with the injected water. Therefore, water within the natural fractures will show increased calcium and other ions relative to sodium ions as compared to the water within the induced hydraulic fracture. It was observed that the calcium to sodium ratio increased rapidly with time followed by a transition to a more gradual increase for the remainder of the sampling period. The interpretation of these observations is that the early time water is recovered from the newly formed hydraulic fractures that have less exposure to in situ water and then, from the natural fractures where the salinity is expected to increase. More study is needed to understand the contributions of mineral dissolution, ion diffusion and water mixing to produced – water chemistry (Bearinger, 2013).

Zolfaghari (2014), published a laboratory and field analysis study to improve the understanding of the origin of salts in the flowback water in two members in the Horn River Formation. The salinity and individual ion concentration field profiles were analyzed for the Otter Park (OP), and Evie (EV) and Muska (Mu) Formations. The bulk-rock mineralogy was determined using XRD and SEM-EDS was used to explore possible precipitated salt crystals on

the surfaces of the natural fractures. Zolfaghari, also analyzed freshly broken surfaces of the samples using SEM-EDS in order to compare elemental distributions in the rock matrix and natural fracture surfaces.

Water and oil imbibition experiments were performed for samples of different surface areas (A_s). Electrical conductivity and individual ion concentrations of water was monitored over time (~ 12 days). Additionally, since during the water imbibition water imbibes into the rock and ions transfer to the water; adsorption isotherms were measured to solely analyze the water adsorption process and characterize the water activity of the samples. Oil and water contact angle measurements were measured to compare shale/water and shale/oil interface properties of the samples.

The field salinity profiles of OP initially showed a gradual increase, and then reach a plateau at around 40000 ppm; the salinity profile of EV continues to increase even after reaching values of 70000 ppm. A general increase in barium and sulphate ions was observed for both formations. A similar increase in the concentration of chloride ion is also observed for the Mu and EV Formations (no data was available for the OP formation). Additionally, the concentration of iron ions shows a gradual growth over the first 200 hours during the flowback process, after which the concentration decreases with time; this trend is observed for all three formations.

The increase in electrical conductivity is faster and higher for the samples with higher surface area (A_{sp}) values, which implies that the water-rock interface area has a strong effect on ion transport during the water imbibition process (Zolfaghari (2014)). The concentration of sodium was observed to be higher than that of chloride in solution during the water imbibition

process. The origin of this high sodium to chloride ratio may be that sodium was mobilized from exchange sites associated with clay minerals in the shales (Zolfaghari (2014)).

In terms of XRD results, bulk mineralogy did not show a significant barite component, but SEM-EDS results showed remnant barite on the surfaces of the natural fractures. Zolfaghari inferred that the dissolution of the barite present in the natural fractures was responsible for the high barium content observed in the flowback water chemical analysis. Complexity of the fracture network was assumed to be proportional to the barium concentration observed.

In 2017, Zolfaghari proposed a technique to up-scale these observations in order to estimate fracture surface area and invaded reservoir volume and compare the results with those from the rate transient analysis (RTA). They measured the total ions produced during the flowback in the Horner River and two sets of imbibition experiments in the lab, in order to investigate the effect of water-rock surface area and rock volume. Both methods were then compared to investigate fracture surface area and invaded reservoir volume. Good agreement was obtained when comparing lab results and water recovery field data.

Rowan et al. 2015, investigated the concentration profiles of various dissolved ions in produced water. Their results indicate the source of the Total Dissolved Solids (TDS) is liquid brines, not solid mineral crystals of salt in the shale pores that are dissolving in the frac fluid. Because different salt crystals have different solubility in water, the ratio of chlorine to bromine, for example, should change over time as one type of salt crystal dissolves faster than the other. These ratios are essentially constant in the produced water through time, indicating that the ions were already in solution before the frac fluid ever got there (Rowan, 2015).

In 2015, Merry and Ehlig-Economides developed a material balance model that introduces the concept of a dissolved stimulated rock volume (DSRV). This is defined by the volume of shale gas rendered productive by injected water dissolving salt found in mineralized fractures sheared during hydraulic fracturing. Because the DSRV could be as much as 80% smaller than the apparent SRV from shear events identified in a micro seismic survey it is consistent with early boundary dominated flow seen in shale gas wells in the Haynesville Formation in the US and in the Fuling Formation in China (Wei, et al. 2015). The material balance also enables estimation of the volume of water that could remain trapped in the shale during flowback because of imbibition and storage in undissolved sheared fractures beyond the DSRV, thereby explaining very low load recovery of injected fracture fluid. The model presumes that produced gas will initially displace brine from propped and secondary fractures, but that continued gas production will vaporize water from the remaining salt-saturated residual brine, depositing salt that could explain observed loss of effective shale permeability previously modeled as pressure dependent permeability.

Bryndzia, 2016, develop a model using data from the Marcellus and Duvernay Shales, based on the oxygen isotopic composition of the Residual Treatment Water (RTW) and contained Total Dissolved Solids (TDS). Published oxygen isotope and TDS data from Marcellus RTW have been used to model the Water:Rock ratio (W:R) based on exchange between local meteoric water and the shale matrix. This model permits an estimate to be made of the Water/Rock ratio, being this a direct indication of the total surface area of stimulated shale that the Hydraulic Fracturing (HF) injected water has been in contact with. It was also highlighted that it is the shale matrix, dominated by illite in mature to over-mature shales, that controls the isotopic enrichment and high TDS contents observed in RTW. The routine geochemical analysis of RTW provides a rapid and inexpensive surveillance strategy for monitoring RTW associated with production from unconventional reservoirs (Bryndzia, 2016).

Finally, Liu Yang et al., (year) studied the origins of high salinity flowback in the Longmaxi, Shihezi, Huoshiling, Yincheng, Lujiaping and Niutitang Formations by using imbibition experiments, rock petrophysical property measurements and image analysis. In 2015, comparative imbibition experiments were performed on 12 core samples, (Ordos Basin, tight volcanic formation from Songliao Basin and shale formations from Sichuan Basin). The authors presented a new method to evaluate the imbibition characteristics and fracture fluid intake by studying the water imbibition capacity in diverse rock types, with varying pore size distribution and pore connectivity.

Imbibition experiments were conducted with distilled water, and orthogonally to the bedding planes. In the Table 1.3 and Table 1.4, a summary of the rock physical properties and XRD mineralogy analysis is shown.

Table 1.3 Rock physical properties for the samples used in Yang 2015. Source: SPE-17-6882-*.Modified by Palencia. Porosity was measured by Helium Porosimeter and permeability by Nitrogen pressure pulse decay porosimeter

Sample	Location	No.	Diameter(cm)	Thickness (cm)	K(mD)	Porosity (%)
Tight Sandstone	Erδος Basin	S-1	2.51	2.5	2.1	11.6
	Shihezi Formation	S-2	2.51	3.29		
		S-3	2.49	4.18		
Tight volcanic	Songliao Basin	H-1	2.50	0.8	0.0069	10.2
	Huoshiling Formation	H-2	2.51	1		
		H-3	2.50	1.69		
Tight Volcanic	Songliao Basin	Y-1	2.51	0.5	0.0012	0.71
	Yingcheng Formation	Y-2	2.52	0.8		
		Y-3	2.49	1.1		
Shale	Sichuan Basin	L-1	2.51	0.86	0.0021	1.02
	Lujiaping Formation	L-2	2.50	1.01		
		L-3	2.51	1.13		

Table 1.4 XRD mineralogy analysis for the samples used in Yang 2015. Source: SPE-17-6882-MS.* Modified by Palencia. I/S is Illite/Smectite mixed layer.

Component	Tight Sandstone - S	Tight Volcanic -H	Tight Volcanic - Y	Shale L
	Percentage %			
Smectite	0	0	0	1.8
Illite	10.3	0.6	3.8	5.6
I/S	0	0	37.3	12.6
Chlorite	0	30.6	5.3	1.9
Kaolinite	0	0	1.4	1.8
Clay	10.3	31.2	47.8	23.7
Quartz	30.2	1.3	40.6	29.4
Feldspar	26.4	61.5	11.6	7.2
Calcite	4.1	0.3	0	24.3
Dolomite	24.8	0	0	14.9
Others	4.2	5.7	0	0.4
TOC	0	0	1.2	3.1

The change in mass vs time during the imbibition experiment was measured with an analytical balance with an accuracy of 0.00001 g . Samples were encased in epoxy and only one face was exposed to the water. Samples were heated at 105 °C for 24 hours.

Yang used Handy's (1960) imbibition model, describing a horizontal piston-like imbibition process. The imbibed volume V_{imb} is given by,

$$V_{imb} = \sqrt{\frac{2A_c \phi k_w S_{wf} P_c}{\mu_w}} \sqrt{t} \quad , \quad \text{Eq. 2}$$

where P_c is the capillary pressure, μ_w is the viscosity of water, k_w is the relative permeability of the rock to water, ϕ is the porosity of rocks, t is the imbibition time, A_c is the surface area and S_{wf} is the moving water front saturation at the exposed sample face. Yang normalized the equation to the dry sample volume ($A_c L$) of the sample and plot $V_{imb}/\text{Dry Sample Volume}$ ($V_{imb}/A_c L$) vs the SQR (t/L^2).

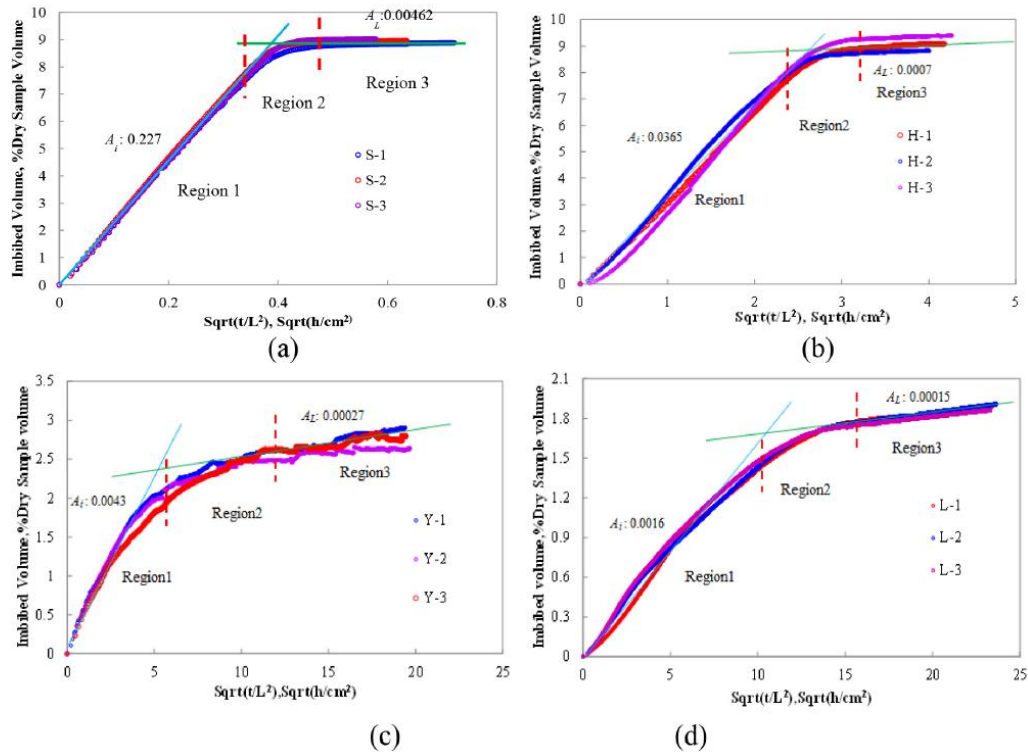


Figure 1.15 Imbibed Volume divided by sample volume (V_{imb}/AcL) vs SQR (t/L^2). (a) tight sandstone -S, (b) tight volcanic -H (c) tight volcanic Y (d) Shale – L. Source: SPE-17-6882-MS.

Yang defined three different regions: Region 1, with a high slope, A_i is the initial imbibition rate. A second line with a lower slope (Region 2), and the late stage (Region 3) which corresponds to A_L , late imbibition rate (Figure 1.15).

Subsequently, by using pore size distribution from mercury injection data and the parameters of imbibition characteristics, they found that the imbibition capacity is positively associated with clay mineral content and type. Also, that macropores display a larger time exponent in the initial imbibition region and meso and micropores have larger exponents in the late imbibition region.

In 2017, Yang included conductivity measurements in his study. The shale samples were different and selected from a typical shale formations in China, from the Marine Sichuan Basin, and a conventional sandstone reservoir, from the Ordos Basin, was included for comparison.

Table 1.5 Mineral composition for the samples used in Yang 2015. Source: SPE-17-6882-MS. I/S is Illite/Smectite mixed layer. *Modified by Palencia.

Label	Formation	Lithology	Mineral Composition, wt.%				
			Quartz	Feldspar	Calcite	Dolomite	Clay
LJP	Lujiaping	Shale	29.4	7.2	24.7	14.9	23.7
LMX	Longmaxi	Shale	40.3	8.8	7.5	6.5	36.9
NTT	Niutitang	Shale	31.2	15.8	11.5	18.2	23.3
XJH	Xujiahe	Shale	45.2	10.5	6.2	0	38.3
GCG	Ganchaigou	Shale	30.5	6.1	4.3	4.8	55
SHZ	Shihezi	Sandstone	32.2	26.4	5.1	25.8	10.3
Label	Formation	Lithology	Relative abundance, wt.%				
			Smectite	Illite	I/S	Chlorite	Kaolinite
LJP	Lujiaping	Shale	7.6	23.6	53.2	8	7.6
LMX	Longmaxi	Shale	4.3	15.9	62.3	8.7	8.7
NTT	Niutitang	Shale	3.4	5.2	78.9	12.4	0
XJH	Xujiahe	Shale	7.5	10.8	80.2	0	1.5
GCG	Ganchaigou	Shale	0	12	38	4	46
SHZ	Shihezi	Sandstone	0	100	0	0	0

Samples were dried at 105 °C, then they were covered with epoxy to only allow imbibition through one face. Samples were placed in a beaker and then removed from flask to measure the mass and the water electrical conductivity. This same procedure was repeated at different times for ~ 8 days . Imbibed volume and conductivity were normalized to the surface area and plotted vs the square root of time (Figure 1.16). Blue curves represent how much water the samples imbibed, and red curves are the conductivity measurements. Two different samples were analyzed for each formation.

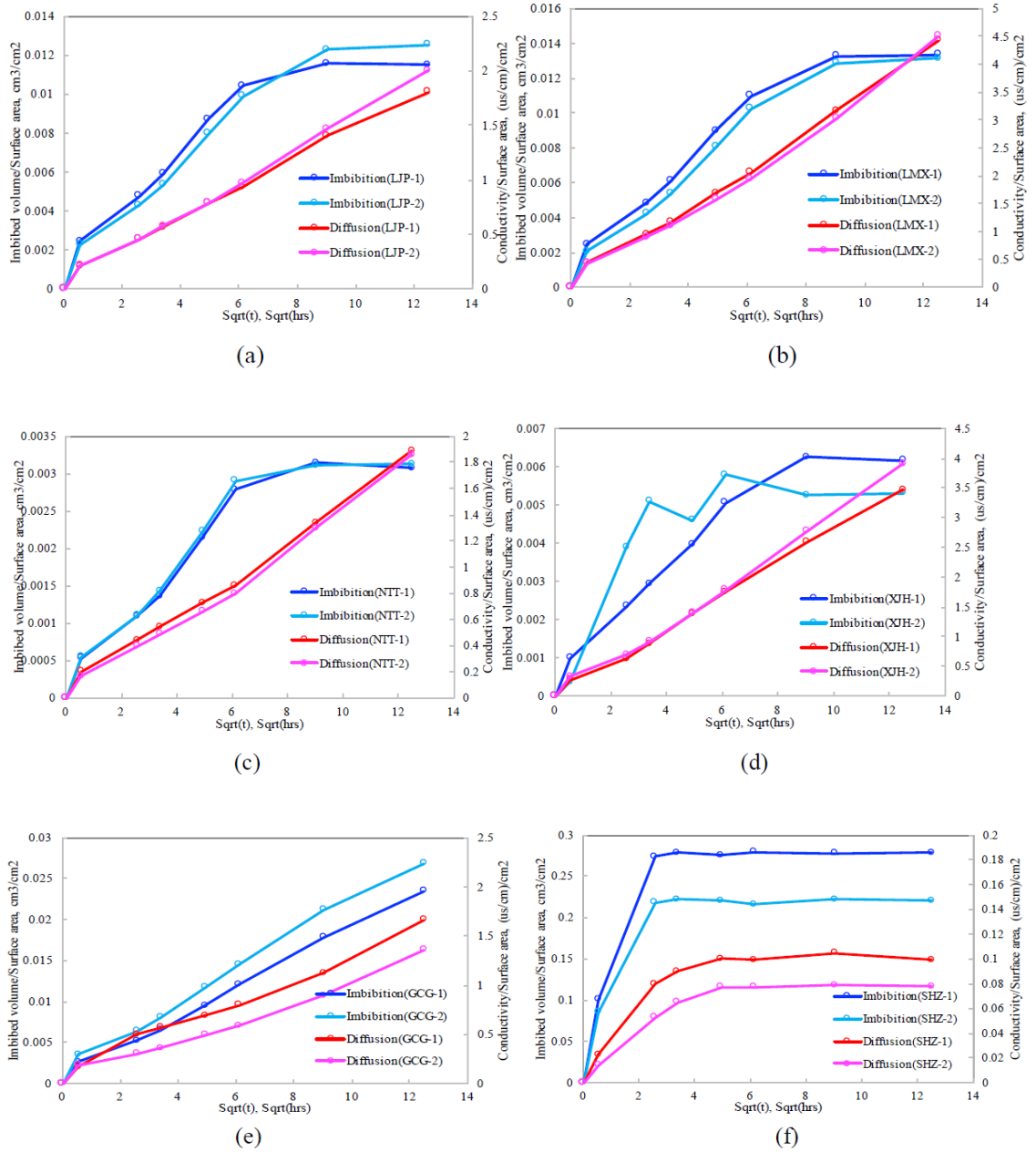


Figure 1.16 Imbibed Volume divided by surface area (V_{imb}/A_s) vs $\text{SQRT}(t)$. (a) LMX formation sample, (b) LJP formation sample (c) NTT formation sample, (d) XJH formation sample (e) GCC formation sample, (f) SHZ formation sample. Source: SPE-17-6882-MS

On these plots, Yang shows that both imbibed water and water conductivity increase with time, and the slopes decrease with time, and tend to be zero in the plateau. In sample f,

which corresponds to the sandstone sample, the electrical conductivity and the imbibition curves reached this plateau stage more quickly than in the shale samples (a,b,c,d,e).

Comparing the results with those from the mineral analysis, Yang found that the imbibition/diffusion properties depend largely on the clay mineral content and type. Yang's samples were smectite rich compare with the samples used in this research. Cation exchange capacity data was not acquired by Yang. In previous work, he suggested that the imbibition rate was proportional to the clay mineral content (Yang, 2015). In Figure 1.17, Yang suggests that the diffusion rate is weakly positively related to the concentration of clay minerals, however with a the R^2 of 0.22 for the total clay concentration and a R^2 of 0.81 for Illite/Smectite. Figure 1.18 shows that there is not a relationship observed between Illite concentration and the inferred ionic diffusion rate, indicating that illite minerals do not significantly contribute to the ion diffusion rate in these clay – rich shales (Yang et al., 2017).

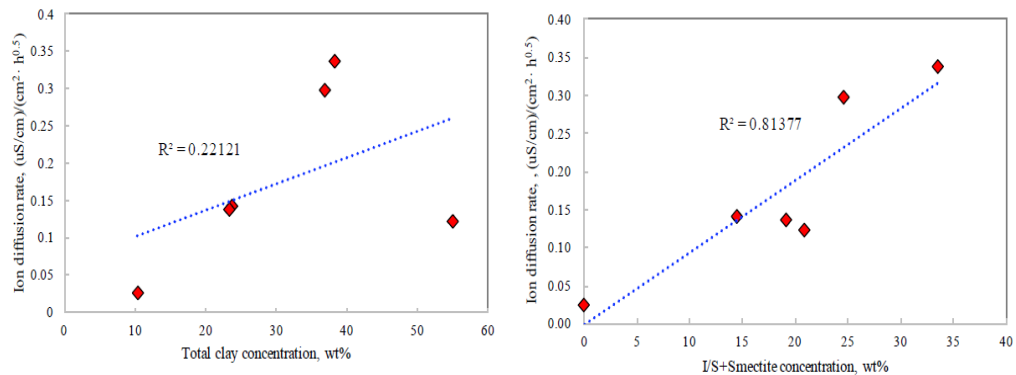


Figure 1.17 Ion Diffusion Rate divided by surface area (V_{imb}/A_s) vs Clay content. Source: SPE-17-6882-MS

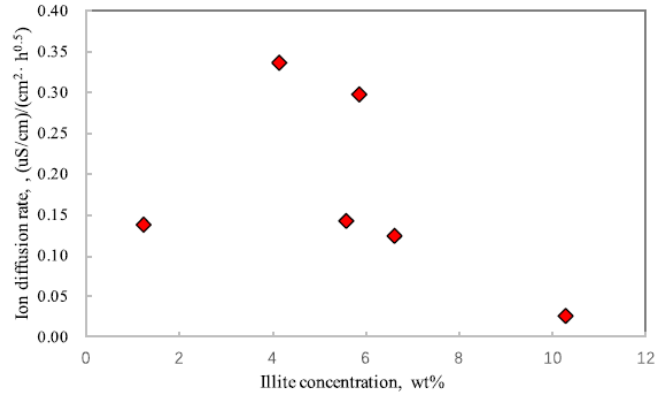


Figure 1.18 Ion Diffusion Rate divided by surface area (Vimb/As) vs Illite Concentration. Source: SPE-17-6882-MS

Yang established the countercurrent imbibition model, based on Handy’s model, to explore the correlation between imbibition and diffusion with parameters such as porosity, permeability, initial water saturation, contact angle and surface area. However, at the end of the study Yang mentioned : “The Handy imbibition model depending on piston-like horizontal displacement was developed for conventional rocks. In addition, the mathematical model of imbibition/diffusion was established based on the assumption of parallel straight capillary bundles, which is suitable for imbibition in conventional reservoir pores or shale reservoir macro-pores. Therefore, the validity of the imbibition-diffusion model for gas shale is doubtful in this manuscript. At present, there is no perfect model to describe the imbibition process of gas shale due to its complex pore structure and mineral composition. The development of an imbibition model for gas shale is not the main emphasis in this study. In future work, a tree branch model based on the fractal theory will be developed to depict the complex pore structures in gas shales and describe the imbibition/diffusion process.” In this project, the approach is to evaluate whether or not diffusion is applicable by evaluating the presence or absence of a particle size dependency in the experimental results, and, whether a square root of time model adequately describes the data.

CHAPTER 2. METHODOLOGY

In this research a novel combination of laboratory techniques was used to evaluate the origin of high salinity flow back water in the Bossier, Haynesville and La Luna Formations. The methodologies were designed to minimize problems with sample homogenization and damage, as well as the potential development of concentration gradients or the occurrence of evaporation during the water imbibition experiments. Dual imbibition experiments (water and oil) were performed by using different aliquots but within the same lithology. Additionally, multiple techniques were used to characterize the samples pre and post imbibition. The methodology can be outlined as follows:

1. Core material from the Bossier, Haynesville and La Luna Formations was used in this study. Seventy-eight feet of core from the Matthews 16 # 1 well, from the Red River Bull Bayou Field in Red River Parish Louisiana was donated to the University. In addition to the core, standard crushed rock measurements made by a vendor were also provided. Material from both the Bossier and Haynesville Formations, was available for measurements and testing. Two feet of La Luna Formation core from the La Luna 1 well in the Middle Magdalena Valley (MMV) in Colombia, were also available for the project. Information about mineralogy, petrophysical and geochemical properties were also available for Bossier and Haynesville formation; however, for La Luna Formation minimal information was provided.
2. Sample selection incorporated direct observation of the core and existing core analysis data including clay mineral content, porosity, permeability, water saturation and total organic content, among others. Permeability was also used as a qualitative indicator of sample variability.

3. Sample volumes for homogenization were selected based on geochemical analysis using an Olympus L Series Vanta handheld XRF analyzer. On average, six measurements per foot were acquired.
4. Crushed homogenized material was sieved into size fractions and representative aliquots of each were selected. Thermal Gravimetric analysis (TGA), Cation Exchange capacity (CEC) measurements, Boyle's Law grain density and Laser particle size distribution analysis data (LPSA) were acquired for the different particle size aliquots.
5. Imbibed volume and ion releasing/expulsion measurements were performed on each of the aliquots of crushed material. Pre and post imbibition sample characterization using transmitted and reflected light and SEM imaging, XRD, and XRF analyses accompanied the imbibition experiments.
6. Nuclear Magnetic resonance data were acquired to evaluate bound and free water, as well as total imbibed water volume. A 23 MHz Oxford NMR was used to acquire the data.
7. Mass spectrometry detection techniques were used to evaluate the post imbibition water in terms of the amount and types of ions present.
8. Thin sections and Scanning Electron Microscope image analysis were critical to evaluate the causes of the physical observations before and after the experiments.

2.1. Sample homogenization.

For dual imbibition and ion expulsion experiments, selecting and homogenizing representative samples from the available core was critical. Both petrophysical and geochemical data from existing core analysis were available from a core laboratory. Based on the initially available data, different depths were selected for analysis in the Bossier and Haynesville Formations, three in the Bossier and two in the Haynesville. The selected sample intervals represent the range of observed properties, including permeability, porosity, and total organic carbon content (TOC). The selection criteria are shown in Figure 2.1.

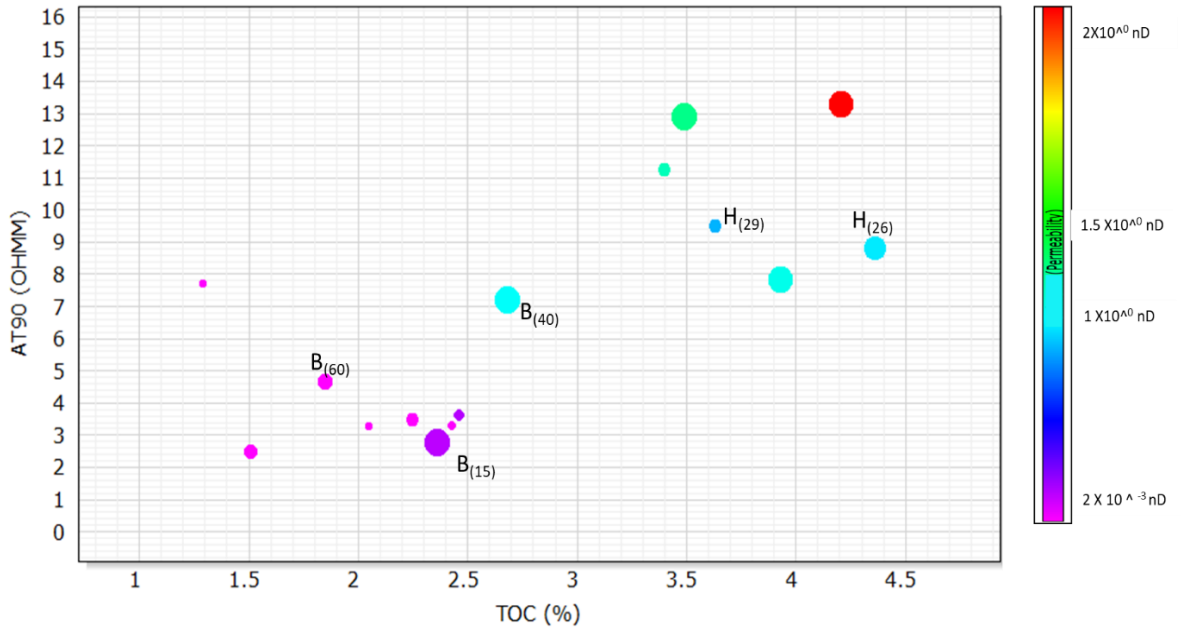


Figure 2.1 Haynesville and Bossier Sample Selection.

Color scale on the right represents permeability. Values are in nD, from 2×10^{-3} nD to 2 nD. Porosity is proportional to the size of the data point. Axes are TOC (wt. %) and deep resistivity induction log (Ohm - meters). Selected samples are designated by B (Bossier), and H (Haynesville), and subscripts indicate clay mineral content from XRD analysis (wt. %). The samples were selected to be representative of the range of observations. Twenty-one samples (three particle sizes) for seven different rock types were distributed among the three formations.

A summary is presented in table 2.1.

Table 2.1 Selected sample petrophysical properties. Physical property measurements were made on crushed material in a core laboratory by using GRI protocols.

Sample	GR	AT90	TOC	Sw	Poro	Perm *	Clay content
	API	Ohm -m	%	%	%	nD	%weight
B₍₆₀₎	191	3.8	2.4	51	9	2.E-03	59
B₍₁₅₎	140	9.0	1.5	50	10	6.E-03	15
B₍₄₀₎	157	7.3	2.7	34	12	1.E+00	40
H₍₂₆₎	124	10.2	4.4	32	12	1.E+00	26
H₍₂₉₎	155	8.2	3.6	29	10	9.E-01	29
LL(15)					14.5		15
LL(8)							8

Although, the laboratory used the Gas Research Institute (GRI) protocols for Sw, porosity and permeability (*) measurement, we were concerned about the several factors that can compromise these measurements, especially the very low permeability values. Sondergeld 2010, shows that even when measured on identical samples sets, and due to modifications to GRI protocols, various core analysis protocols are used for different laboratories, leading to petrophysical properties that are inconsistent (See Figure 2.2). Hence, the petrophysical and geochemical properties provided by a vendor were used only to select a range of samples.

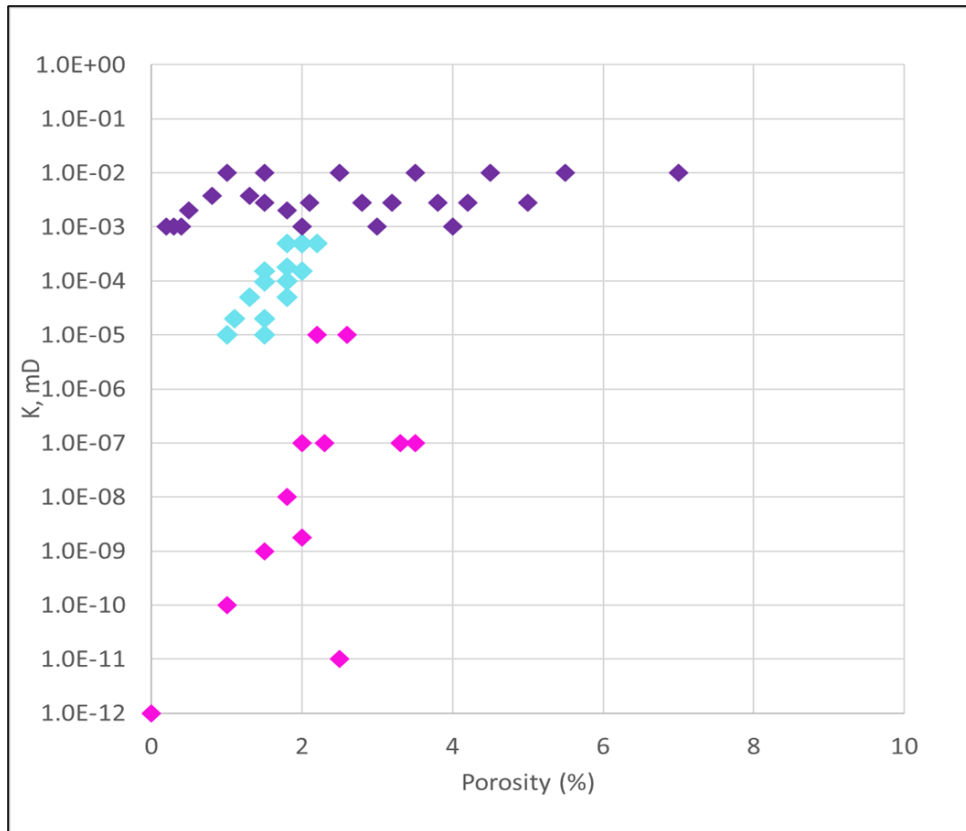
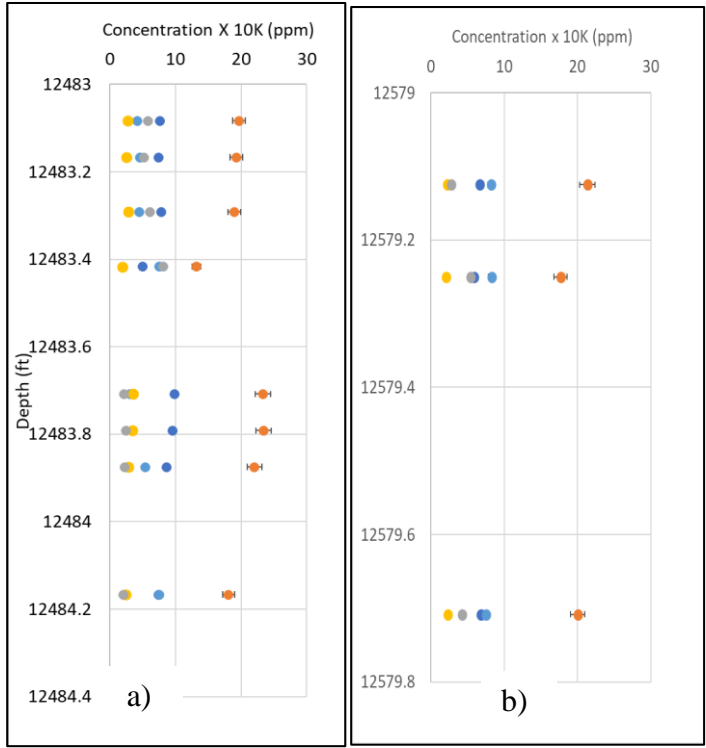


Figure 2.2 Compilation of permeability measurements on the same shale gas sample from three different labs by using the GRI protocol with individual modifications. Permeabilities range eleven (11) orders of magnitude. Magenta values (the lowest values) belong to same laboratory that measure Bossier and Haynesville permeabilities.

2.1.1. Handheld XRF analysis

After selecting the samples at different depths (1 foot per depth), X-ray Fluorescence Elemental Analysis (XRF) data were acquired to ensure the mineralogy was consistent along each one-foot interval. This was performed to minimize mixing distinctly different rock types within each aliquot for analysis. An Olympus L Series Vanta handheld XRF analyzer was used. On average, six measurements per foot were acquired. Figure 2.3 shows an example of the data. The more abundant elements are relatively constant along each one-foot interval.



c)

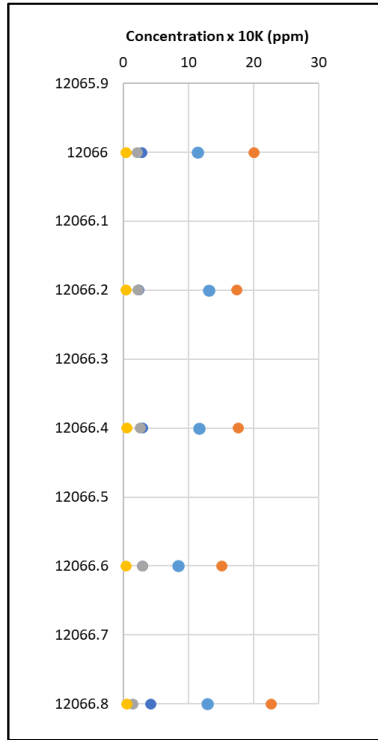


Figure 2.3 Bossier (a), Haynesville(b) and La Luna Formation (c) Sample Hand Held XRF Data. Samples are representative based on bulk XRF and they are relatively constant along each one-foot interval. Yellow: Potassium, Dark Blue :Aluminum, Sulfur, Light Blue: Calcium, Orange: Silicon.

2.1.2. Sieving the material

After reasonable homogeneity was observed in each of the samples, selected material (half a foot) was crushed and sieved to four different particle sizes. Each one-foot-long core sample was weighed, crushed, and sieved. Figure 2.4 shows the crushing and sieving workflow, and the mesh combination used in the process. Laser particle size data were acquired to confirm the mean particle size of each sieve sample.

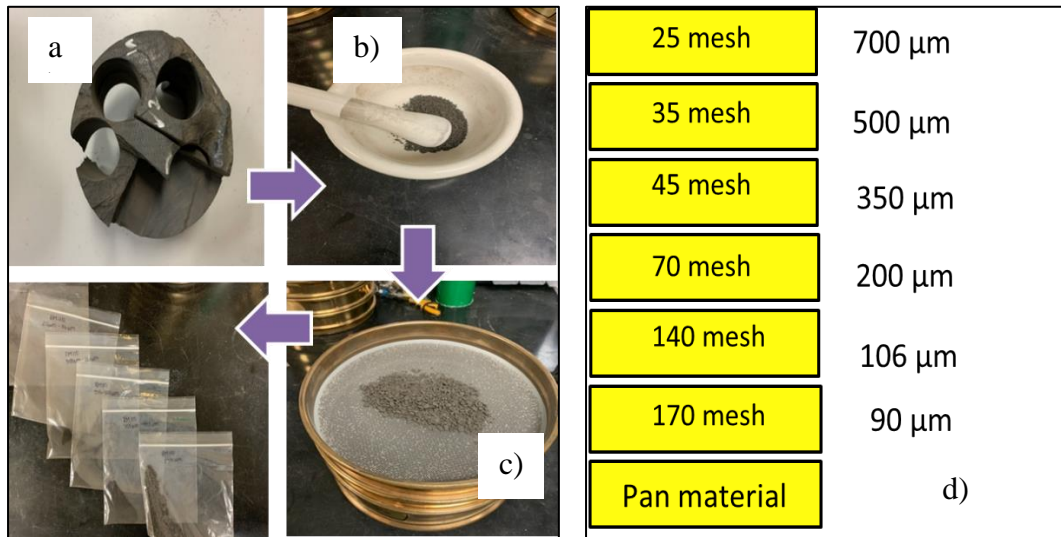


Figure 2.4 Initial Sample preparation. a) As received core material b) Crushing with the mortar c) Sieves used to sort crushed material by size. d) Sieve combination setup.

2.1.3. Laser Particle Size Distribution Analyzer.

After crushing the material and to assess the homogeneity of each aliquot, particle size distributions were acquired using a Horiba LA-350 Laser particle size analyzer. Selected sieve sizes were 750-500 μm , 500-350 μm , 212-106 μm and 106-90 μm . Mean size values for those samples were 700 μm , 500 μm , 200 μm and 50 μm respectively. Sieving the smallest material (106-90 μm) was challenging because finer material began to adhere to the sieve mesh and did not pass through. Unimodal distributions (Figure 2.5, a,b,c) for the three coarsest samples were observed and the mean particle size values were consistent with the mesh size range. However,

issues with the sieving for the finest sample resulted in a bimodal size distribution, with a median size substantially smaller than the mesh size range (Figure 2.5d). Based on this observation and to avoid inconsistencies in the data, this size sample was not utilized in subsequent experiments.

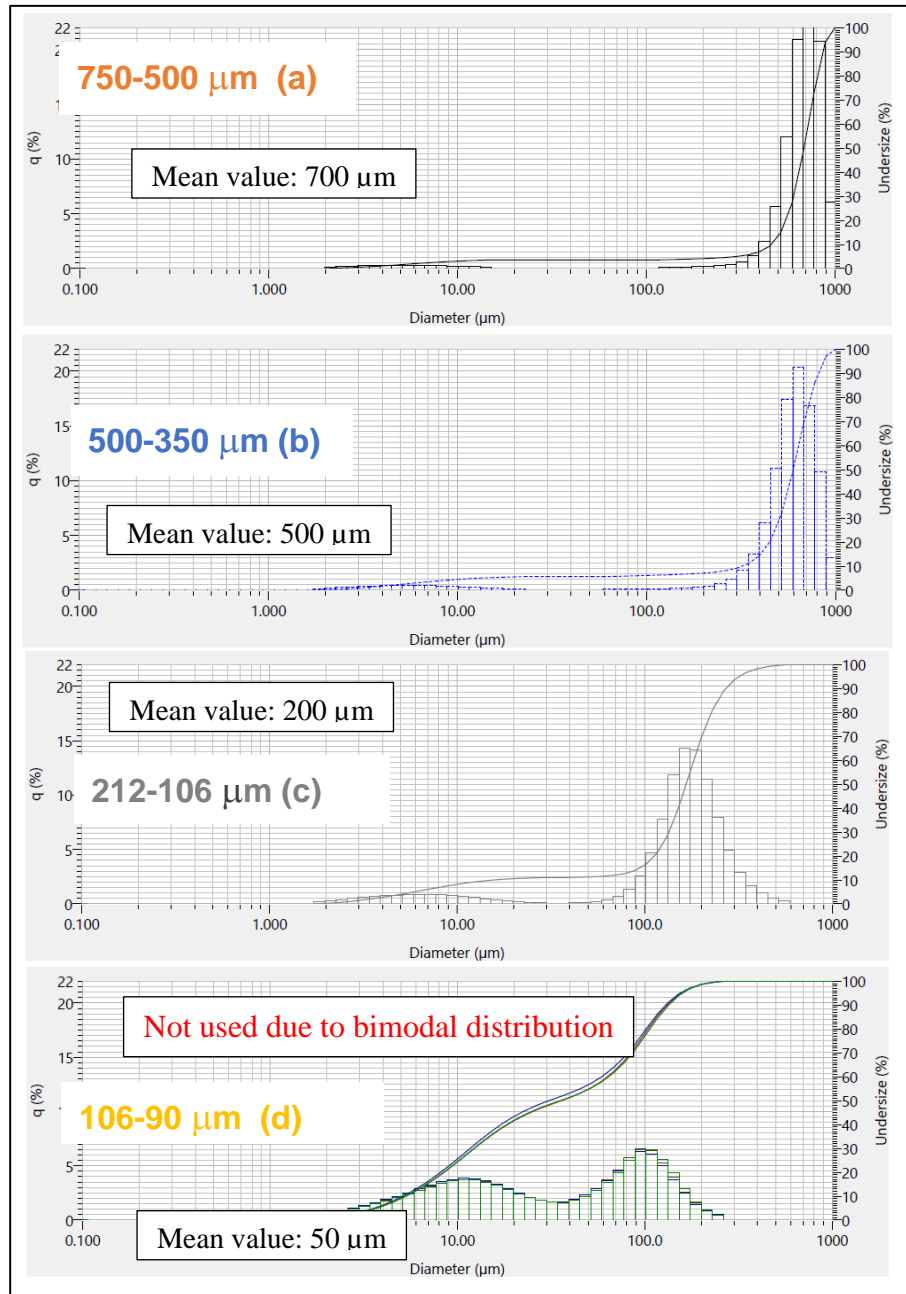


Figure 2.5. Particle size distribution analysis for aliquots ground and sieved to various particle sizes.

2.1.4. Boyle's Law porosity

Particle volume and density were measured for all the samples at each particle size. Material was placed in the oven for one hour at 60° Celsius to remove possible surface water. Samples were not exposed to higher temperatures to avoid water evaporation and associated induced fracture development. These data were acquired to assess the quality of similar data provided by a vendor for the Haynesville and Bossier Formations. Results show very similar values which increases the confidence in terms of third vendor porosity measurements.

2.1.5 Thermal Gravimetric Analysis. (TGA)

TGA data were acquired with the objective of relating the amount of water loss due to temperature changes with the imbibed volume and the equilibrated salinity observed in each sample. There should be a proportionality in terms of surface effects in both experiments. The experimental workflow is described in figures 2.6 and 2.7.

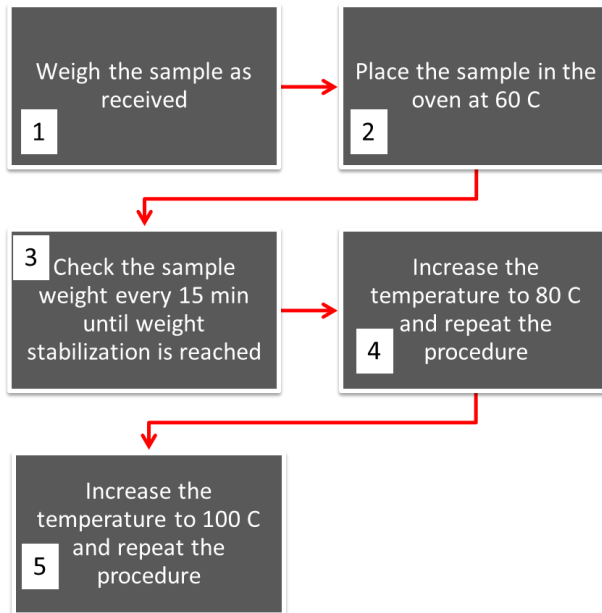


Figure 2.6. Thermal Gravimetric Analysis workflow.

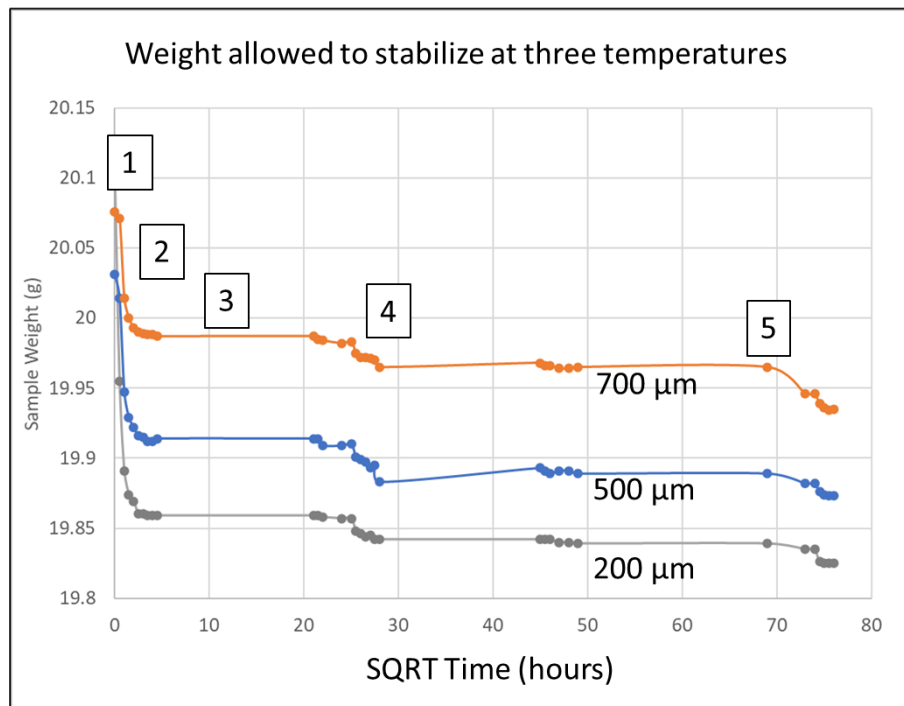


Figure 2.7 Thermal Gravimetric Analysis for B(60)samples. 1. Weigh the samples as received. 2. Samples are placed on the oven at 60 °C . 3.The sample weights are measure every 15 min until stabilization is reached. 4. Increase the temperature to 80 C and 5. Increase to 100C and repeat the procedure.

2.1.6 Cation Exchange Capacity (CEC) Measurements: Conductometric Titration

Cation exchange capacity measurements were acquired to evaluate a possible relationship between CEC and spontaneous imbibition and ion diffusion behaviors in each sample. Additionally, any particle size relationship with CEC measurements might provide insights into the controls on ionic expulsion and imbibed volume that might be observed. Fifteen (15) grams of as received material were acquired for this measurement. The process includes several washes to prepare the sample. In order of occurrence, the samples are washed with:

- Deionized (DI) water (two to three washing stages)
- $\text{Na}_2\text{S}_2\text{O}_3$ to remove Anhydrite (three to four washing stages)

- BaCl₂ to prepare the clay surface with Ba⁺² ions (Two to three washing stages)

After Ba⁺² surface preparation, the conductance was measured using a probe submerged into the solution while titrating with 0.1N MgSO₄. Enough time must be allowed for the system to approach equilibrium. As Mg⁺² ions replace the Ba⁺² on the exchange sites of the clay minerals, no appreciable change in conductance is noted until all Ba⁺² ions are replaced. After that point, because BaSO₄ is insoluble, the additional linear conductivity increment is due to continuously adding Mg⁺² ions. This minimum point is proportional to the sample CEC (Figure 2.8).

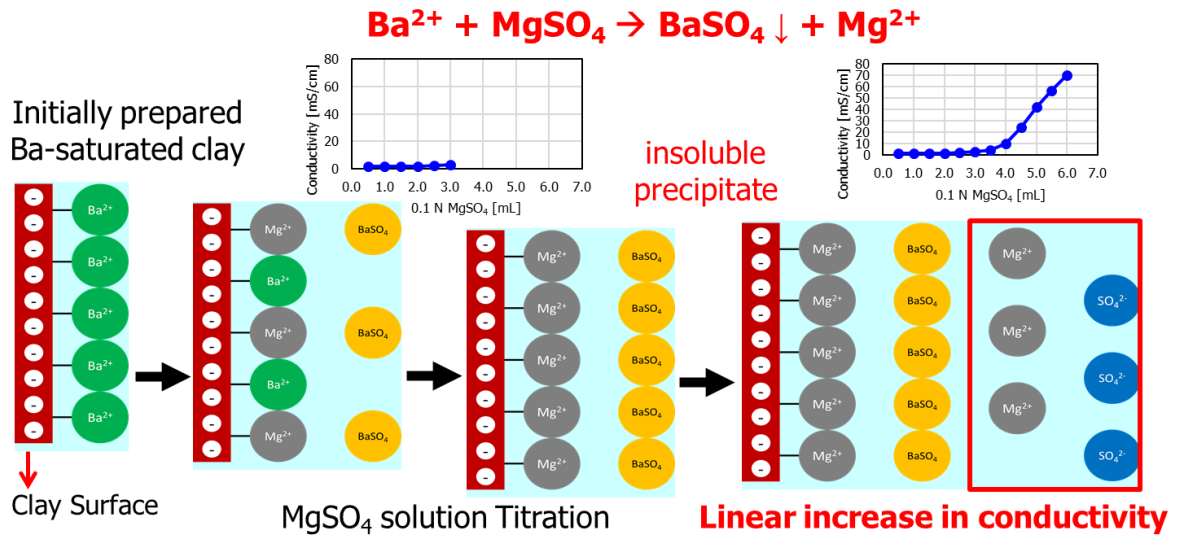


Figure 2.8 CEC measurement by conductimetric titration. As received samples are prepared by washing them with Deionized water and Barium chloride. Titration with Magnesium Sulfate while measuring the conductivity.

2.1.7. Clay Mineral Membrane Potential Test

Clay minerals have the ability to restrict ion flow, they allow cations to pass while restricting the flow of anions. Therefore, clay minerals are considered to be ion – selective membranes. When two aqueous solutions with different ionic concentrations are separated by this type of membrane, an electrical potential develops . The membrane potential test measures

the voltage drop across a clay mineral rich sample that is in contact with fluids of different salinities. This voltage drop is used to calculate the clay's ion selectivity which is correlated with the ion type, ion concentration, sample permeability and Cation Exchange Capacity (CEC). It has been observed that the ion selectivity of clay minerals increases when the permeability decreases. As permeability decreases because of burial and compaction, the clay's ability to restrict solute transport increases and ion selectivity increases. Additionally, ion selectivity increases as the CEC increases, the higher exchange capacity translates into higher negative surface charge. The negative surface charge, indicated by the CEC, restricts the flow of anions through the pore system, only allowing cations to move more freely. In doing so, an electrical potential, indicated by the voltage drop, is created that directly indicates the ability to screen out anions. The higher the electrical potential, the better the clay's ability to screen out anions (Al-Bazali, 2007). This capacity of the clay mineral is potentially relevant in the understanding of high salinity in flowback water; however, it was not an approach taken in this research. Due to the extremely low permeability reported for the samples, the clay mineral type, and the expected low CECs, the voltage drop measurement in the membrane potential test would be difficult to measure, suggesting that a different experimental set up would be necessary. This will be the subject of future work.

2.1.8. As Received Nuclear Magnetic Resonance (NMR)

A 23 MHz Oxford MQC NMR was used to acquire NMR data on as received material. This is the ideal tool for characterizing unconventional mudstone reservoirs because it is capable of detecting hydrogen signals not only from water and oil but also from solid organic matter (Harry Xie, 2018). The traditional 2 MHz NMR instruments are the industry standard for conventional reservoir analysis and characterization. In NMR analysis, the instrumental sensitivity and inter-echo spacing time (TE) play critical roles,

especially in quantifying porosity and clay bound water. However, the traditional low frequency NMR suffers from low sensitivity which leads to a low signal to noise ratio when making measurements, requiring a long data acquisition time. The low sensitivity makes it difficult to detect and measure small amounts of water or oil in the sample. Clearly the traditional surface relaxation based low frequency NMR does not meet the requirements for unconventional mudstone reservoir core analysis which must address issues such as low signal sensitivity due to low porosities, short T₂s due to small pore sizes, and identifying water, hydrocarbons, and solid organics which co-exist in fresh core samples. The limitations of low frequency NMR can be overcome by using high frequency (HF) NMR at 23 MHz which has many advantages including much enhanced sensitivity, much shorter inter-echo spacing time, and more comprehensive NMR data acquisition methods (Harry Xie, 2018).

Free induction decay (See Appendix I) and CPMG sequences were performed to get the T₁ and T₂ distributions for the samples pre and post spontaneous imbibition experiments. T₁ is defined as the longitudinal relaxation time for the nuclei of hydrogen to align with the presence of a magnetic field. T₂ is the transverse relaxation time of those nuclei after being disturbed by a radio frequency pulse. T₂ measurement provides a useful snapshot of pore body size and the area under the T₂ distribution equals the NMR porosity independent of the mineralogy. Also, the numbers of peaks observed in the T₂ distribution plots correspond to the number of porosity systems that might be present in the rock. The number of signals averaged was 16 for both T₁ and T₂, and 3676 echoes were used for T₂ with a T₁ Max and T₂ Max of 100 ms. These parameters were identical for the entire set of NMR experiments. The objective of the NMR

measurements is to acquire information about as received material porosity systems, imbibed water and oil volumes, and porosity systems after the spontaneous dual imbibition experiments.

2.1.9. Dual Spontaneous Imbibition Experiments

These sets of experiments are the fundamental core of the project and it is from these that petrophysical properties might be extracted. Combining imbibition experiments with all the other measurements and image analysis was critical to understanding the physics behind the experiments and modeling the results. The combination of imbibition and ion expulsion experiments and sample/brine characterization was the approach this project took to gain insight into the petrophysical properties of the stimulated rock volume.

2.1.9.1 Water Imbibition Experiments

The samples (10 g of dry material) were placed in 600 cc of Deionized Water (DI) at room temperature and a Hanna 4382 conductimeter was used to measure the solution conductivity to explore ionic transport characteristics and influencing factors (Ghanbari et al., 2013). The objective was to evaluate ionic transport and to use the stabilization of conductivity (salinity) to indicate that equilibrium had been achieved.



Figure 2.9 Spontaneous Water imbibition experimental set up.

All data are reported at 25 °C. Because a closed apparatus with continuous stirring was used for the experiments, evaporation was avoided, and concentration gradients did not develop. These two phenomena would introduce important errors in the acquired data, so, we built a laboratory setup that avoided those two problems (Figure 2.10).

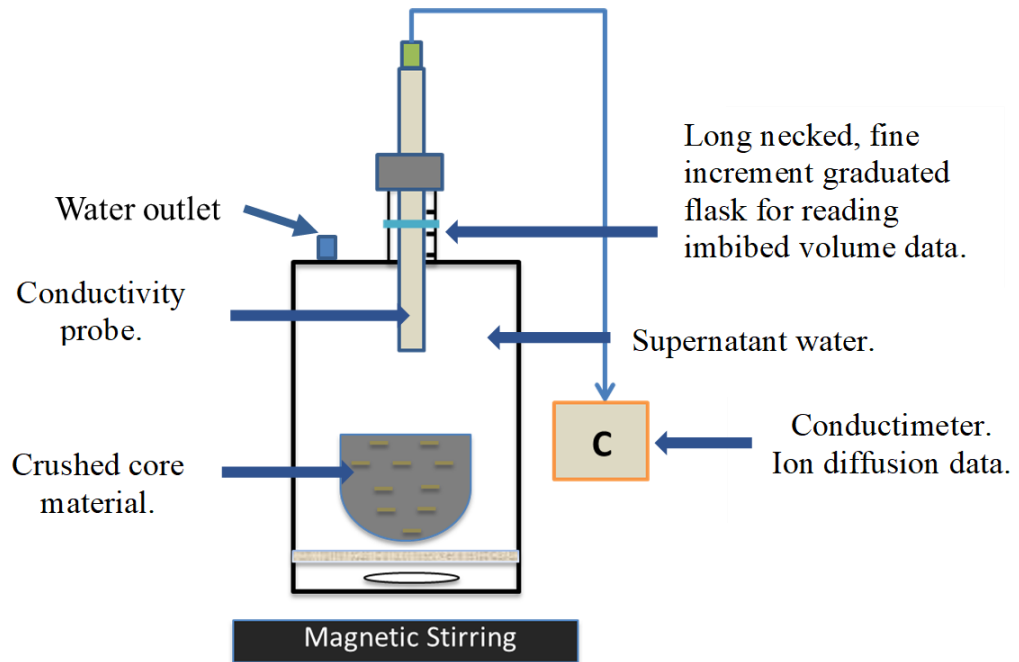


Figure 2.10 Imbibition experiment setup. Conductivity and imbibed volume were measured simultaneously. No evaporation, no concentration gradients

Three experiment setups were used allowing simultaneous measurement of the three particle sizes. Conductivity was measured every 30 mins for the two first two hours and then once daily until equilibrium was reached (~ one month).

2.1.9.2. Oil Imbibition Experiments and NMR.

Using a separate aliquot of the same sample, 20 g of dry sample were placed in dodecane ($C_{12}H_{26}$) at room temperature and the imbibed volume was measured as a function of time until equilibrium was reached. The objective was to evaluate the organic porosity present in the sample. Fluid levels were measured every 30 minutes for the two first hours and then once daily until equilibrium was reached (~ 20 days). Subsequently, post imbibition nuclear magnetic resonance measurements were acquired.

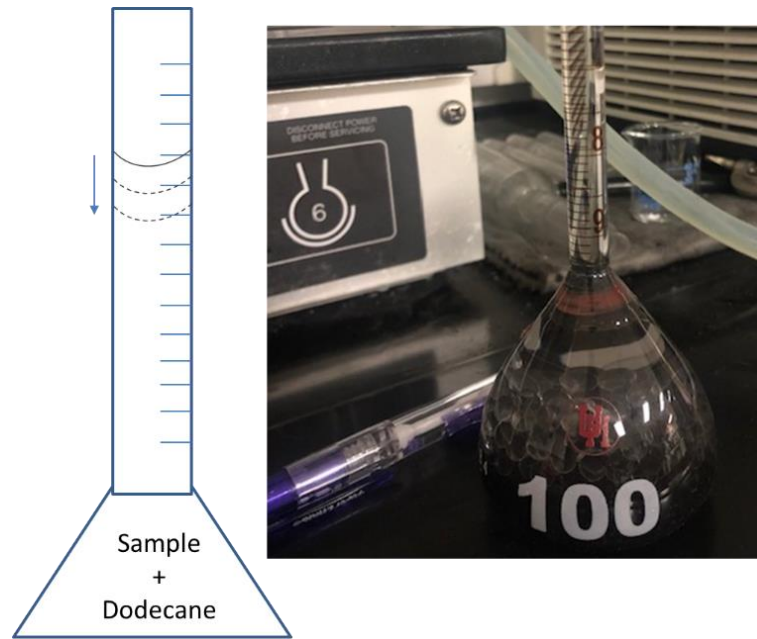


Figure 2.11 Oil Imbibition experiment setup. Imbibed volume was measured during the experiment.

2.1.10. Brine characterization

Inductively Coupled Plasma (ICP) analysis was performed to evaluate the chemical composition of the cations released from the samples during the imbibition experiments. ICP mass spectroscopy uses an ionization source that fully decomposes a sample into its constituent elements and transforms those elements into ions. The objective was to evaluate the ions present in the supernatant fluid in order to evaluate possible sources of the ions in solution (e.g. interactions with clay minerals, residual water saturation, salt dissolution, etc.).

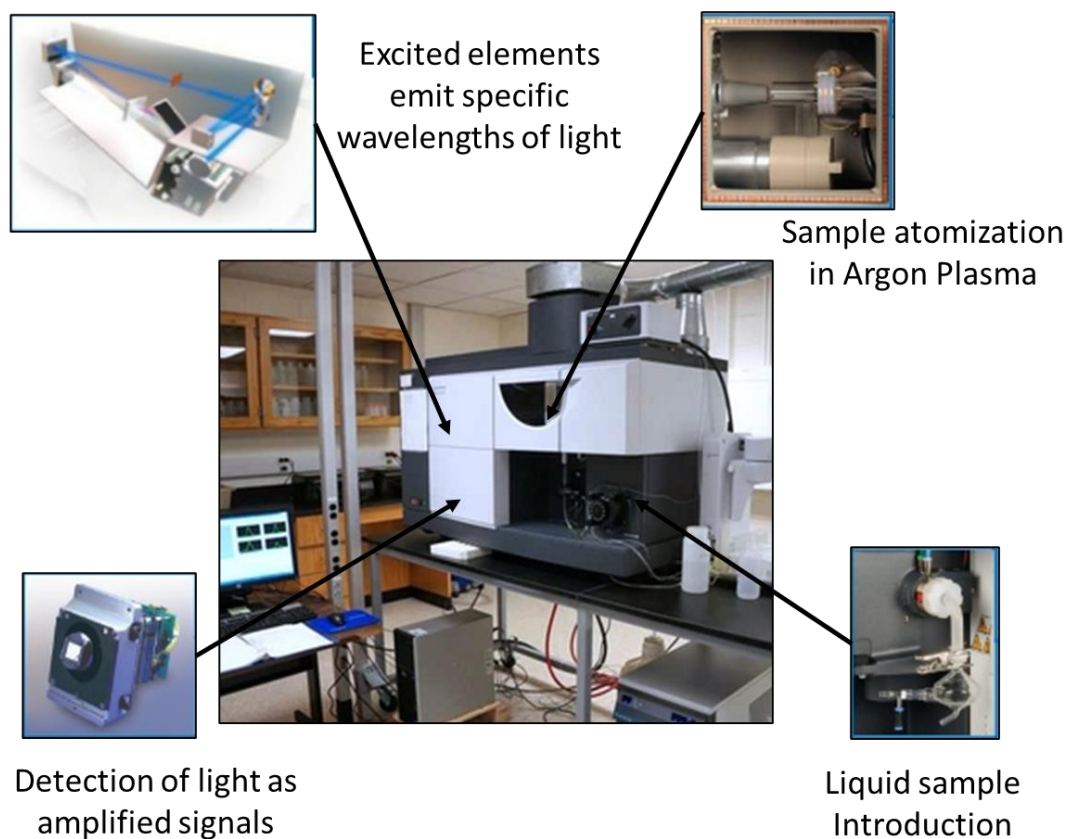


Figure 2.12. Inductively Coupled Plasma (ICP) equipment.

2.1.11. Post – Test Sample Characterization

Nuclear Magnetic Resonance (NMR) data were collected after both water and oil spontaneous imbibition experiments in order to evaluate the pore systems (oil versus water wetting) in the samples and to quantify the imbibed volumes. The same protocols used for the pre-test samples were followed for post-test sample analysis.

2.1.12 Thin Section Analysis and SEM/EDS.

Finally, image studies, that included transmitted light and high-resolution SEM (pre and post imbibition experiments), were performed. The objective was to document mineralogy, texture, and pore systems (mineral hosted versus organic matter hosted pores). This allows us to characterize the samples and relate mineralogy (clay content and distribution, authigenic

versus detrital phases) and porosity distributions with the results of the other experimental techniques. This proved critical to understanding the physical observations. Pre and post imbibition images were analyzed to a) evaluate mineral phases contacting the perimeter of the ground sample, b) evaluate the distribution of the minerals in the samples, c) analyze possible damage present in the sample due to sample preparation, and d) compare image analysis results with those based on the other experiments. This information aided in the interpretation of the imbibed volume results and the dual imbibition experiments.

CHAPTER 3. RESULTS

In this section, the results of the experiments are presented. They will be discussed in the same order they were performed in the laboratory and by formation.

3.1 X- Ray Fluorescence (XRF)

X- Ray Fluorescence measurements were acquired on each of the one foot full diameter core samples to document homogeneity in terms of mineralogy along the sample length. Figure 3.1 shows the major elements present in sample B(60). In this sample, magnesium (Mg) is the element with the lowest concentration with an average of 12 Kppm and it is constant along the interval. Ca, Fe and S show similar concentrations and they also remain relatively constant. Ca, S, Fe and Mg have concentrations under 100 Kppm. In contrast, Al and Si are both present in concentrations greater than 100 Kppm which, is interpreted to be related to the sample's clay mineral content. This high concentration of Si, and Al, is consistent with the 60 wt% clay mineral content reported for this sample.

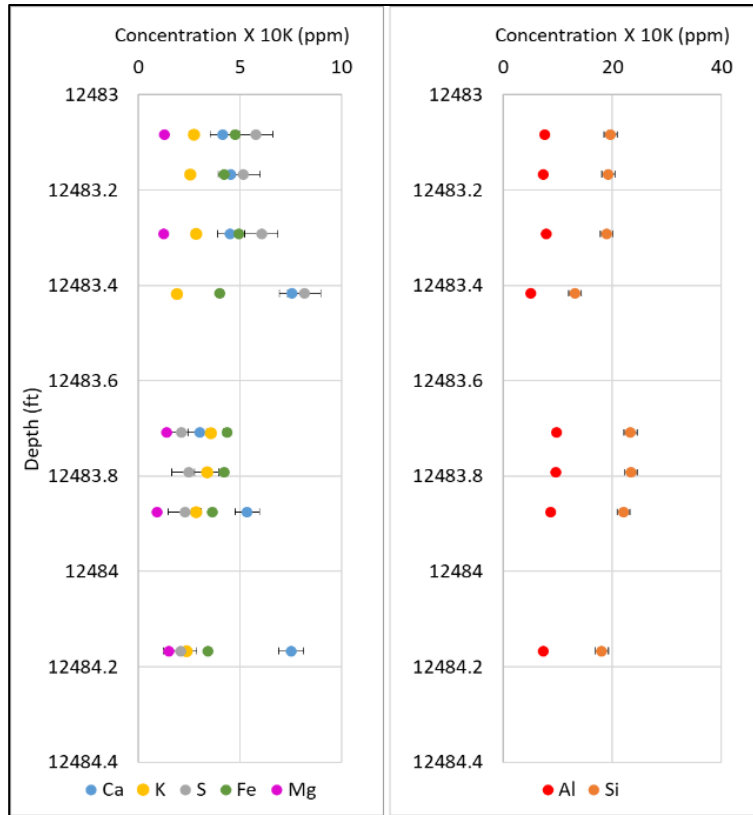


Figure 3.1 Major Element concentration in sample B(60). A homogeneous condition with some variation in terms of Al and Si, and Ca can be observed.

Crossplots between the major elements and Aluminum for B(60) are shown in Figure 3.2, as well as the crossplot between Ca and S, and Fe and S. A positive correlation with Si and K is observed, which reflects the illitic mineralogy of the sample. Ca decreases with increasing Al, which suggests that the calcium present in the sample is authigenic, meaning it was formed in their present position, most likely as carbonate cement. Very poor correlations are observed between Al and Fe or Mg suggesting that iron and magnesium are not present in clay mineral phases but as pyrite and carbonate (dolomite) respectively. A positive correlation is observed as well between Ca and S, which suggested the presence of anhydrite. (CaSO₄). Two samples fall off of the Ca-S trend. These samples may have higher carbonate cement content. Fe is not positively correlated with S, suggesting that although there is pyrite in the sample, the occurrence of sulfur is more strongly associated with anhydrite,

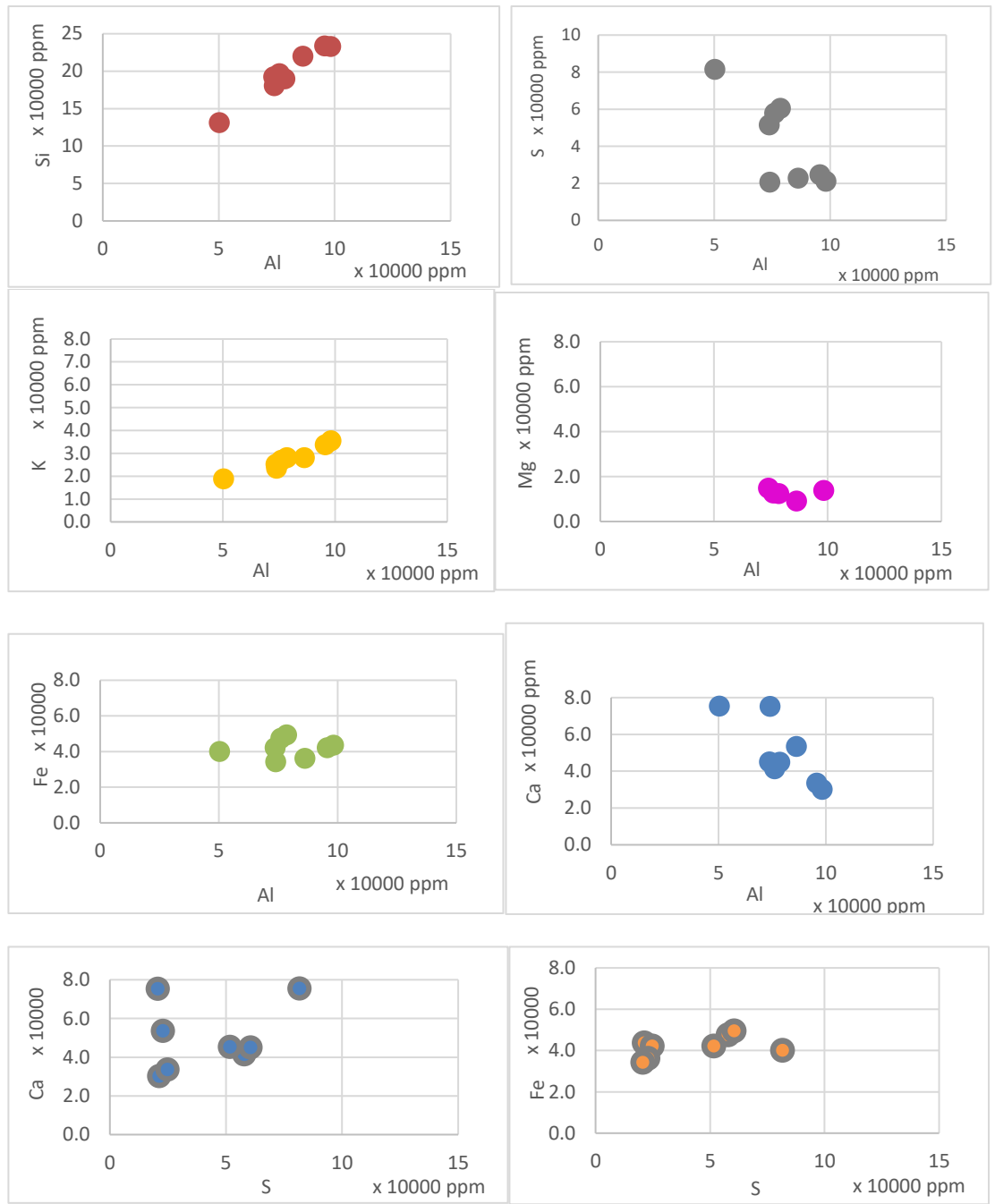


Figure 3.2 Principal elements versus aluminum crossplots for B(60). The weight% of Si increases with Al, as well as K, which suggests they are present primarily as illite clay minerals. Due to the negative relationship between Ca and Al, one scenario is the presence of Calcium as intrabasinal grains and as carbonate cement, as well as the presence of anhydrite due to the positive correlation between Ca and S.

For sample B(40), shown in Figure 3.3, Ca, K, S and Fe are consistent along the interval, showing concentration values under 100 Kppm. Magnesium was not detected in this sample, possibly because it is present in low concentrations and Mg is near the lower detection limit for light elements in the hand held XRF instrument. Similar to sample B(60) Al and Si show higher concentrations. Few measurements were acquired in the sample due to the presence of very thin bedding plane fractures in the full core for this interval, resulting in disks of material that were thinner than the measurement window of the instrument.

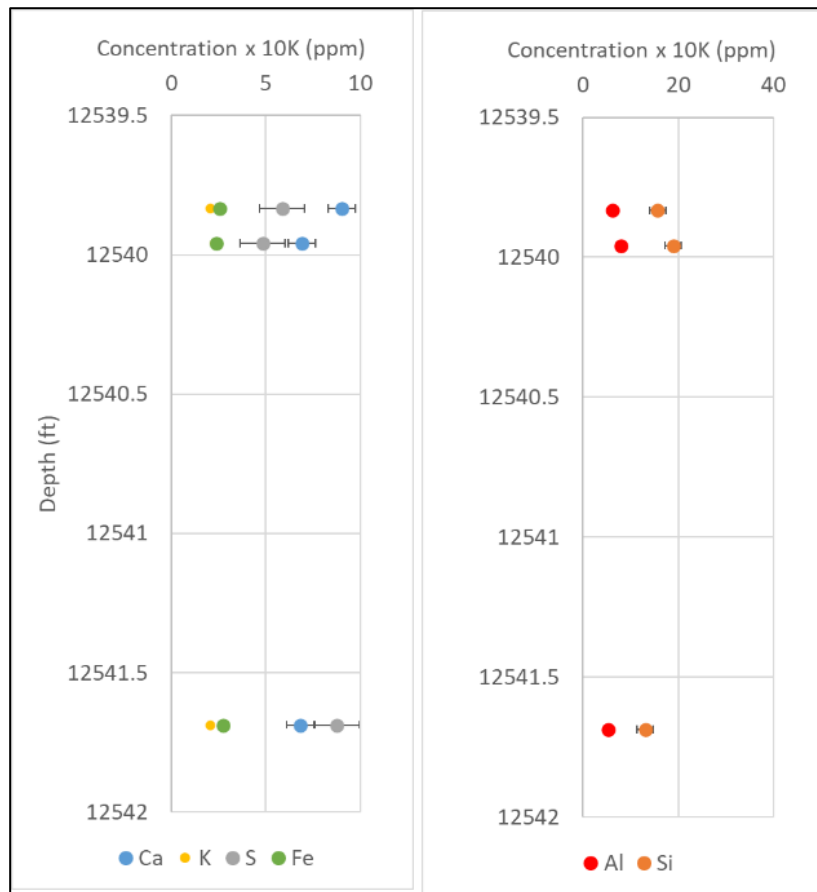


Figure 3.3 Major Elements concentration in B(40). A homogeneous condition with some variation. Fewer measurements due to the inability to place the instrument due to core condition.

Crossplots between the major elements with Aluminum for B(40) are shown in Figure 3.4, as well as the crossplot between Ca and S, and Fe and S. Due to core condition (highly fractured)

only a small numbers of points could be measured and therefore the correlations are difficult to identify in this sample. However, a positive correlation between Si and Al is observed again, similar to the B(60) sample. Fe is correlated with S, suggesting the presence of pyrite.

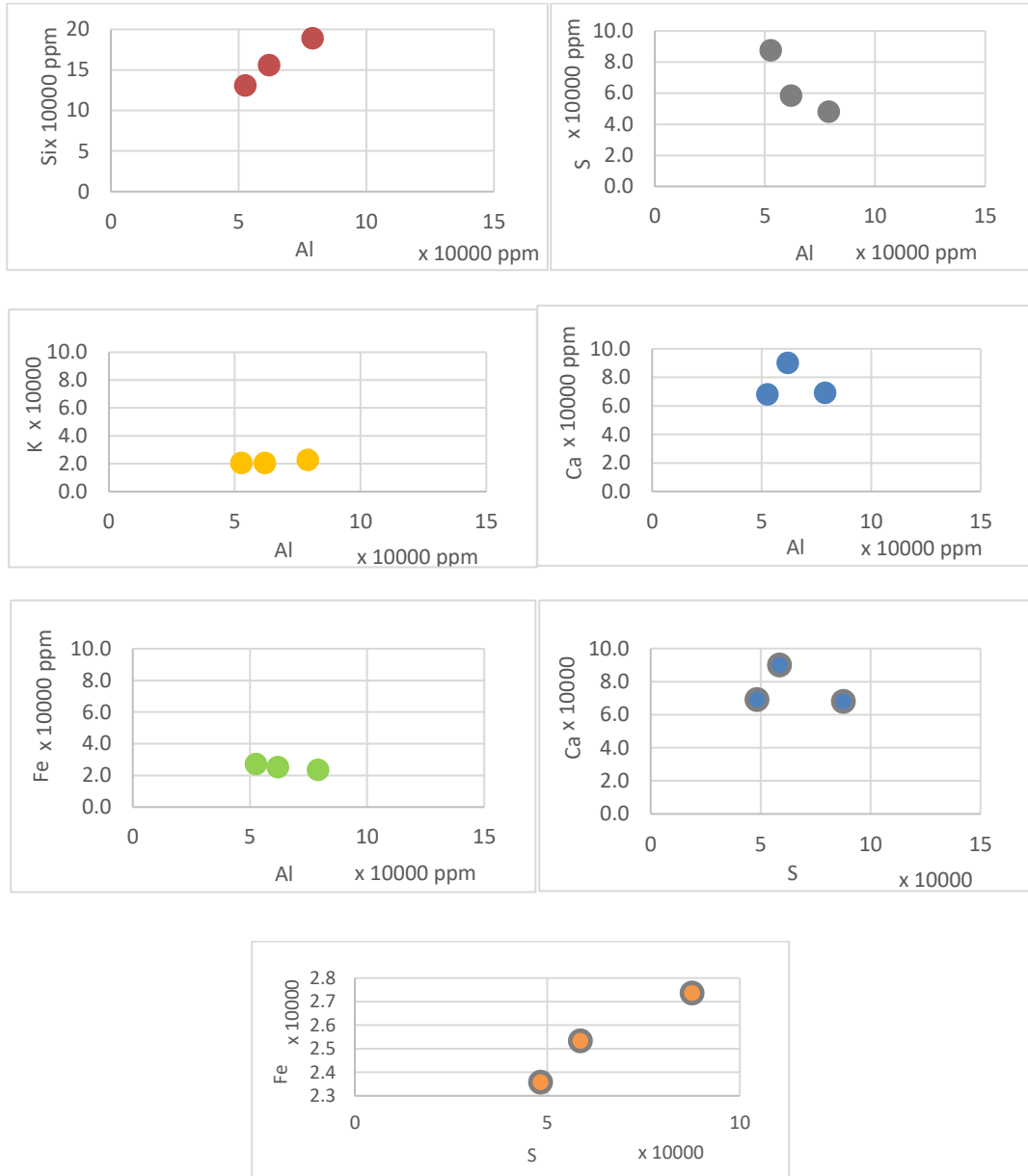


Figure 3.4 Principal elements and Aluminum Crossplots for B(40). The weight% of Si increases with Al, as well as K, which suggests the presence of clay minerals. The presence of Calcium as carbonate cement, as well as the presence of anhydrite is suggested.

For Sample B(15), magnesium is present, with an average concentration of 17Kpppm. This sample displays the lowest aluminium and silicon concentrations observed in the Bossier Formation, which is consistent with this sample having the lowest clay mineral content, only 15 wt%. In this sample there appears to be two distinct lithologies, one more clay mineral rich (top portion of core) and one more carbonate rich (bottom half of the the sample). Only the bottom half of the core section was homogenized. For the other two samples a homogeneous condition with some variation in terms of Al and Si, and Ca are observed.

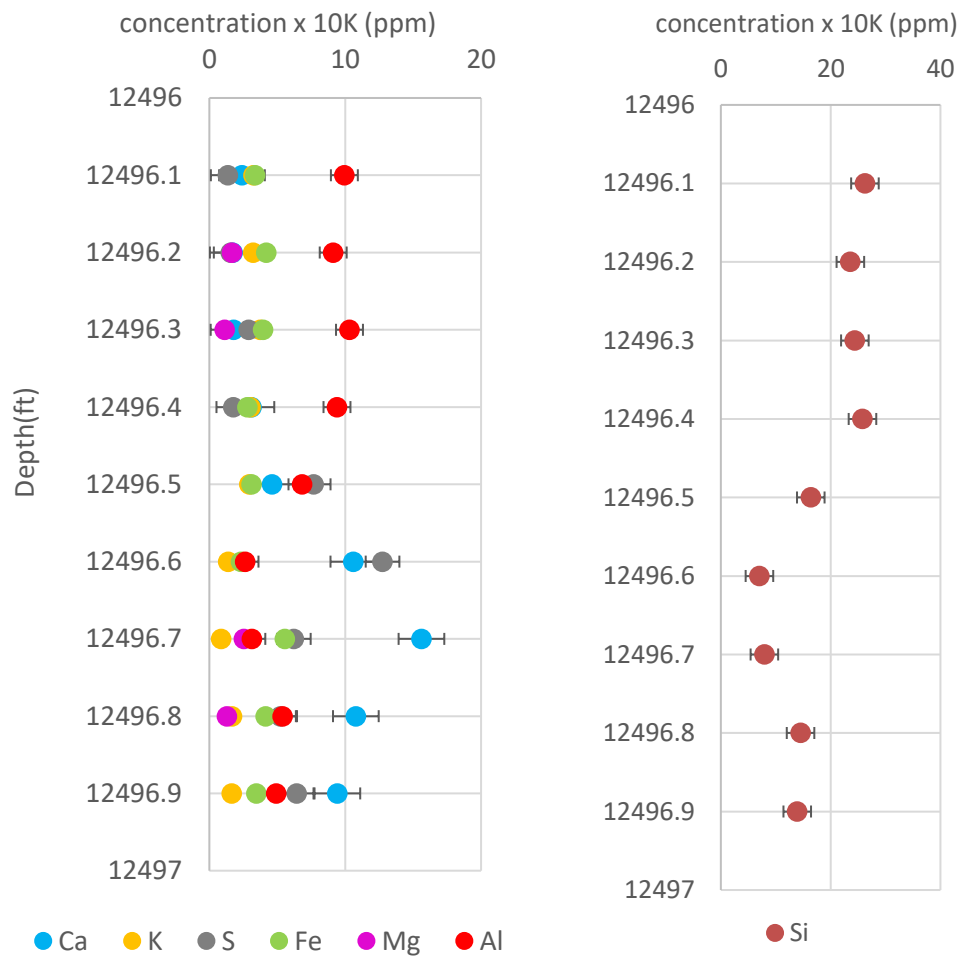


Figure 3.5 Major Elements concentration in B(15). Two distinct lithologies, one more clay mineral rich (top portion of core) and one more carbonate rich (bottom half of the sample). Only the bottom half of the samples was homogenized.

Figure 3.6 shows the cross plots between the major elements and Aluminum for B(15). Additionally, the cross plots between Ca and S , and Fe and S. A positive correlation with Si and K is observed. Ca is decreasing with the increment of Al , which suggested that calcium is present in the sample most likely as carbonate cement. A positive correlation is observed as well between Ca and S, which suggested the presence of calcium as anhydrite (CaSO_4).

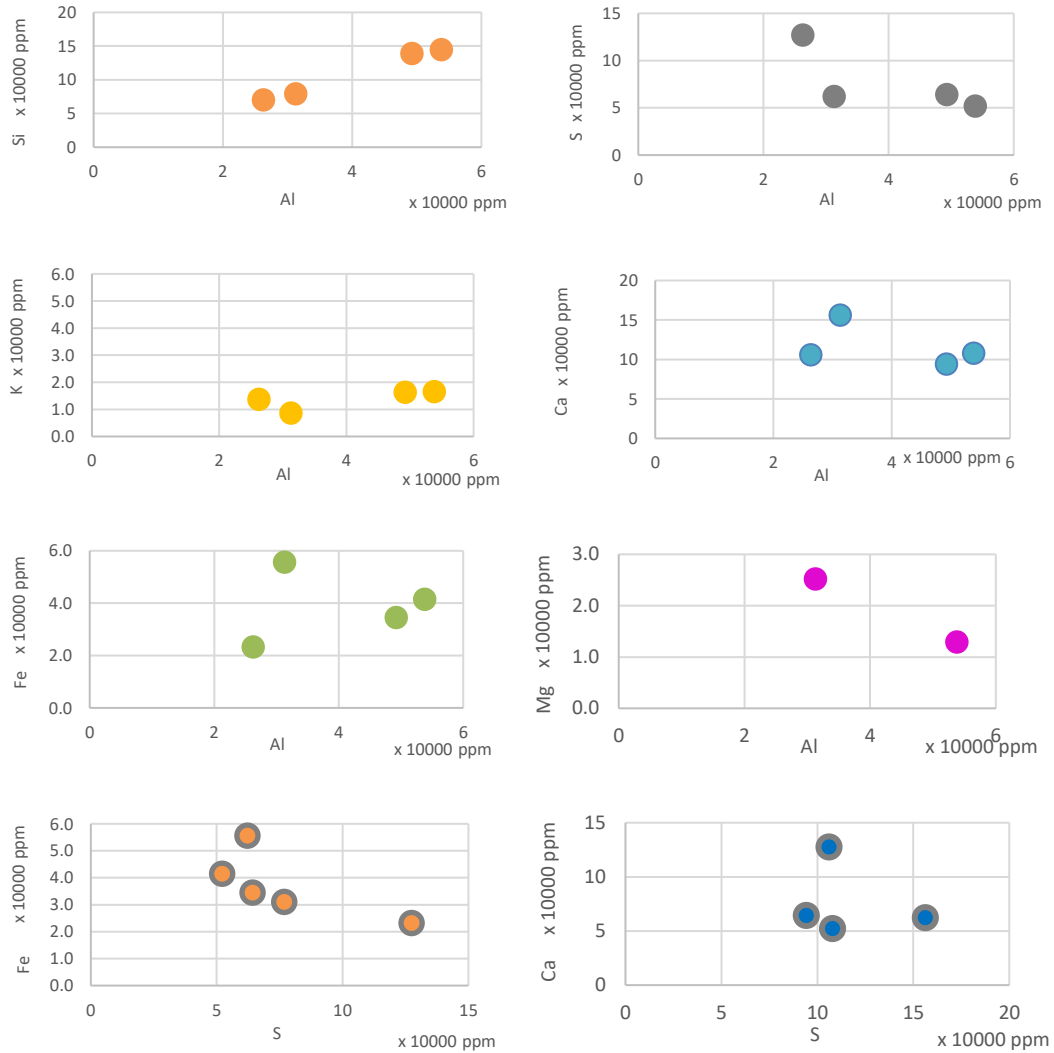


Figure 3.6. Principal elements and Aluminum Crossplots for B(15). Data is suggested the present of clay minerals, due to the positive correlation between Si , K, and Al. CaSO_4 presence is also suggested based on the Ca , S crossplots.

Figure 3.7 is a summary of the crossplots between the major elements and Al and Ca with S. The size of the point represents the clay mineral content of each sample. In general for the Bossier Formation, clay mineral presence is suggested by the positive correlation between Si, K and Al. Carbonate may be comprised of either intrabasinal grains or authigenic cements, because it has a negative correlation with Al. Anhydrite presence is suggested based on Ca and S positive correlation.

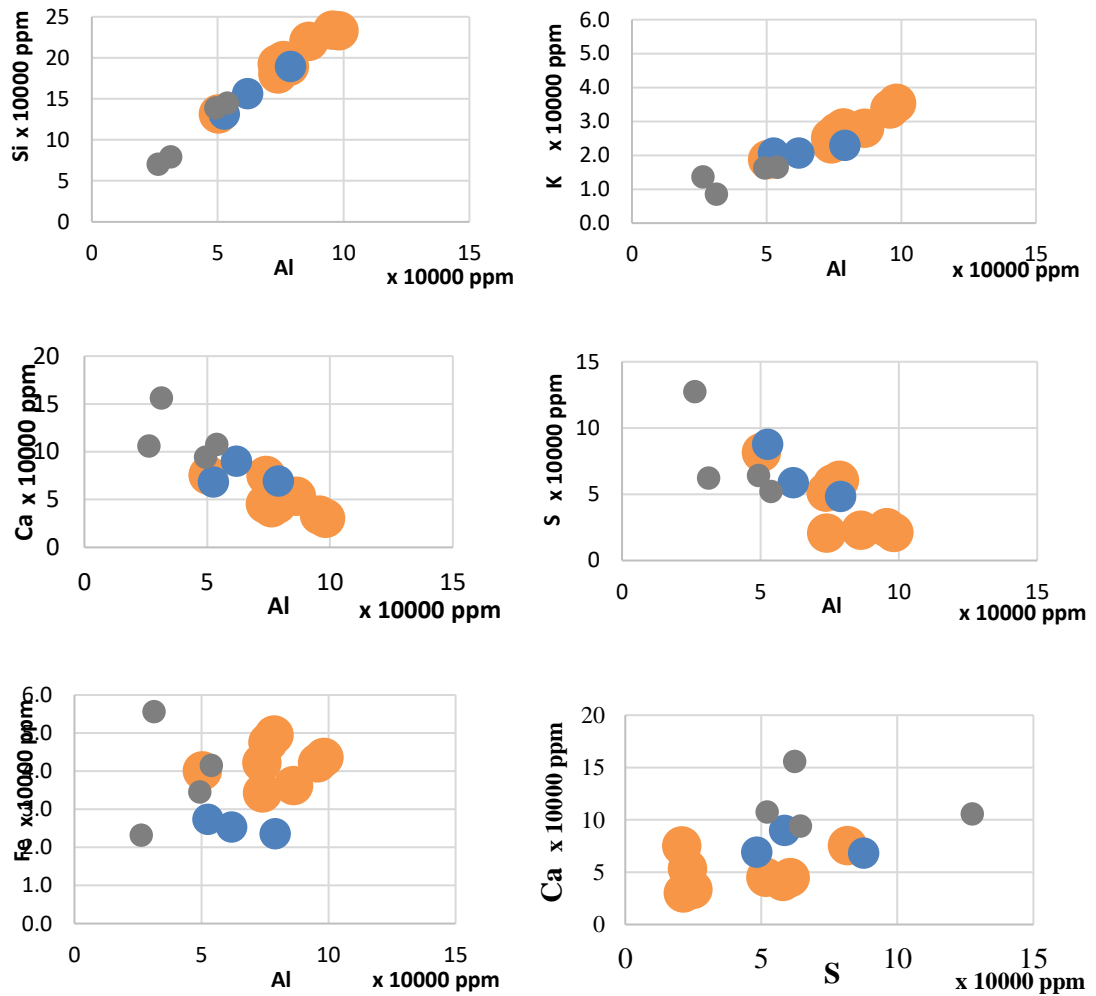


Figure 3.7. Principal element Cross plots For the Bossier Formation. B(60) is represented by the orange points, B(40) is the blue and B(15) is the gray color. Good agreement between XRF and clay mineral content of the samples. Presence of clay mineral, mostly illite, authigenic carbonate and anhydrite are suggested.

For the two samples from the Haynesville Formation, minimal differences are observed in terms of the abundance of Si. We selected these two samples due to their different TOC values, not on the basis of mineralogy.

In Sample H(26) , silica concentration is on average 178 Kppm and in H(29) it is 213Kppm. The high concentration of silica relative to aluminum, suggests that much of the silica in the Haynesville is associated with quartz, rather than clay minerals. Aluminum concentrations display a similar trend. This is consistent with the clay mineral content reported for each of the samples. Magnesium was not detected most likely due to low overall concentration and being near the instrument's detection limits. In general, the other major elements are similar along the lengths of the cores. Result are shown in Figures 3.8 and 3.9.

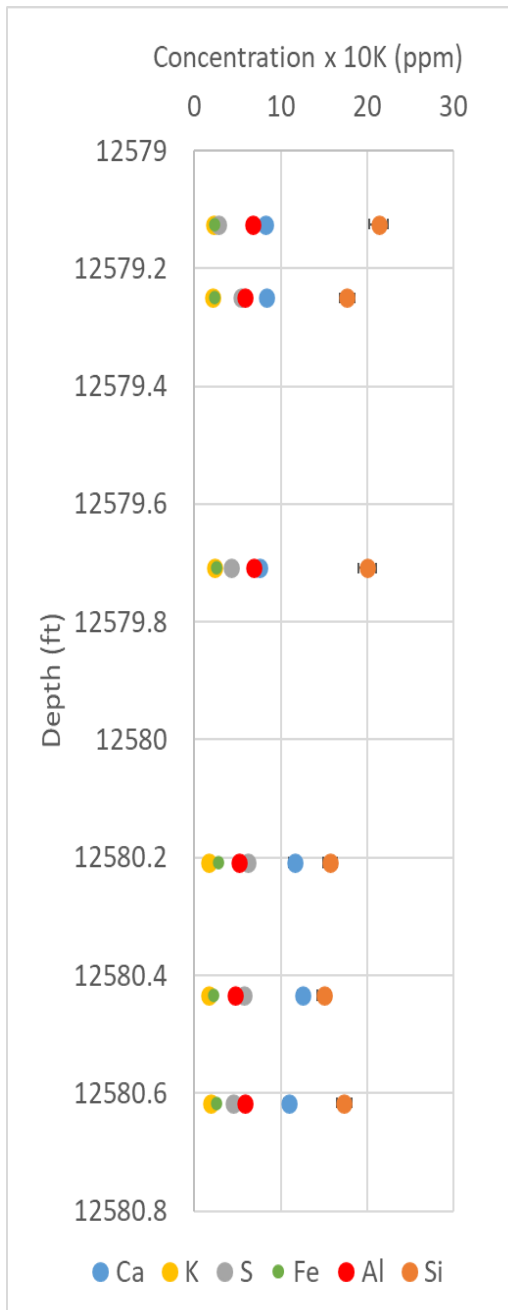


Figure 3.8 Major Elements concentration in H(26). Major elements are similar along the lengths of the core.

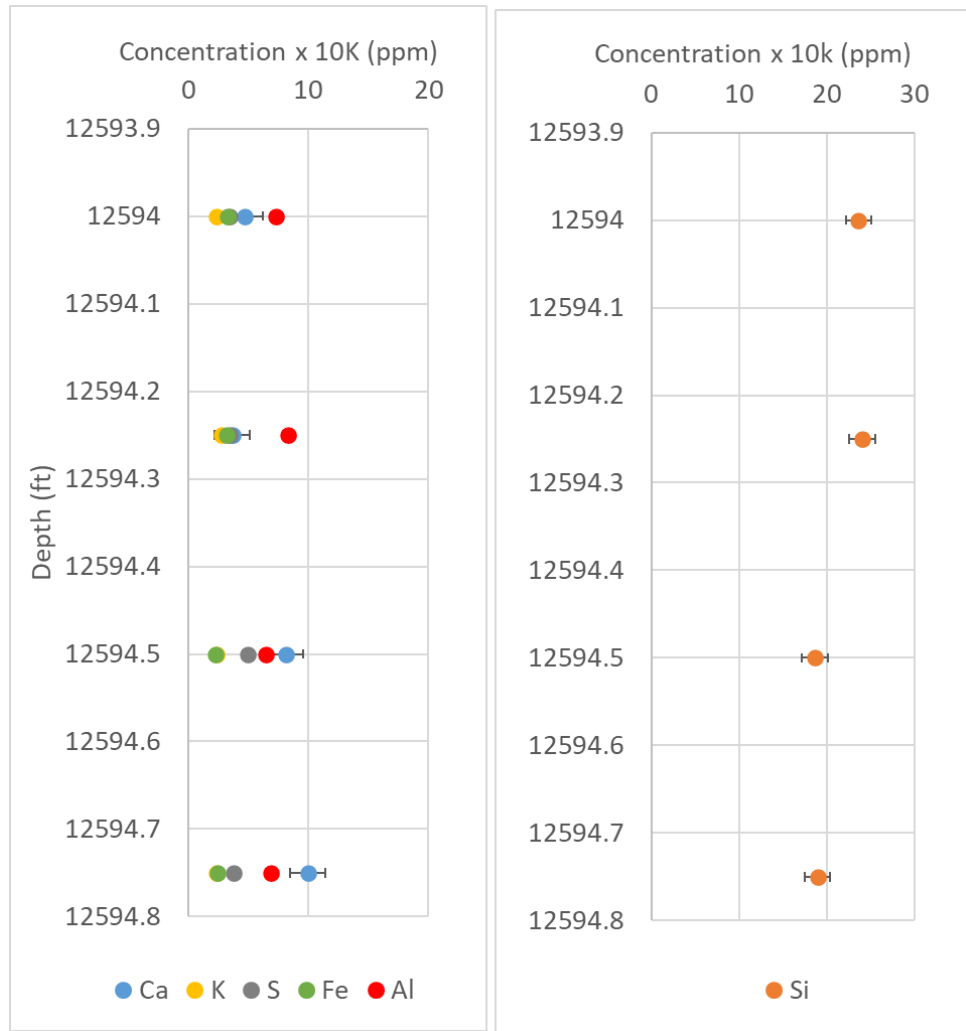


Figure 3.9 Major Elements concentrations in H(29). A homogenous condition was observed. Similar to sample B(40), fewer points were taken here due to full core condition.

Figure 3.10 and Figure 3.11 shows the cross plots between the major elements and Aluminum for H(26) and H(29). Additionally, the cross plots between Ca and S, and Fe and S. Similar relationships are observed for both samples, however, correlations are better defined for sample H(26) because of the larger number of points. For both samples, positive correlations between Si, K and Al are observed. Ca and S decrease with increasing Al. A positive correlation is observed as well between Ca and S.

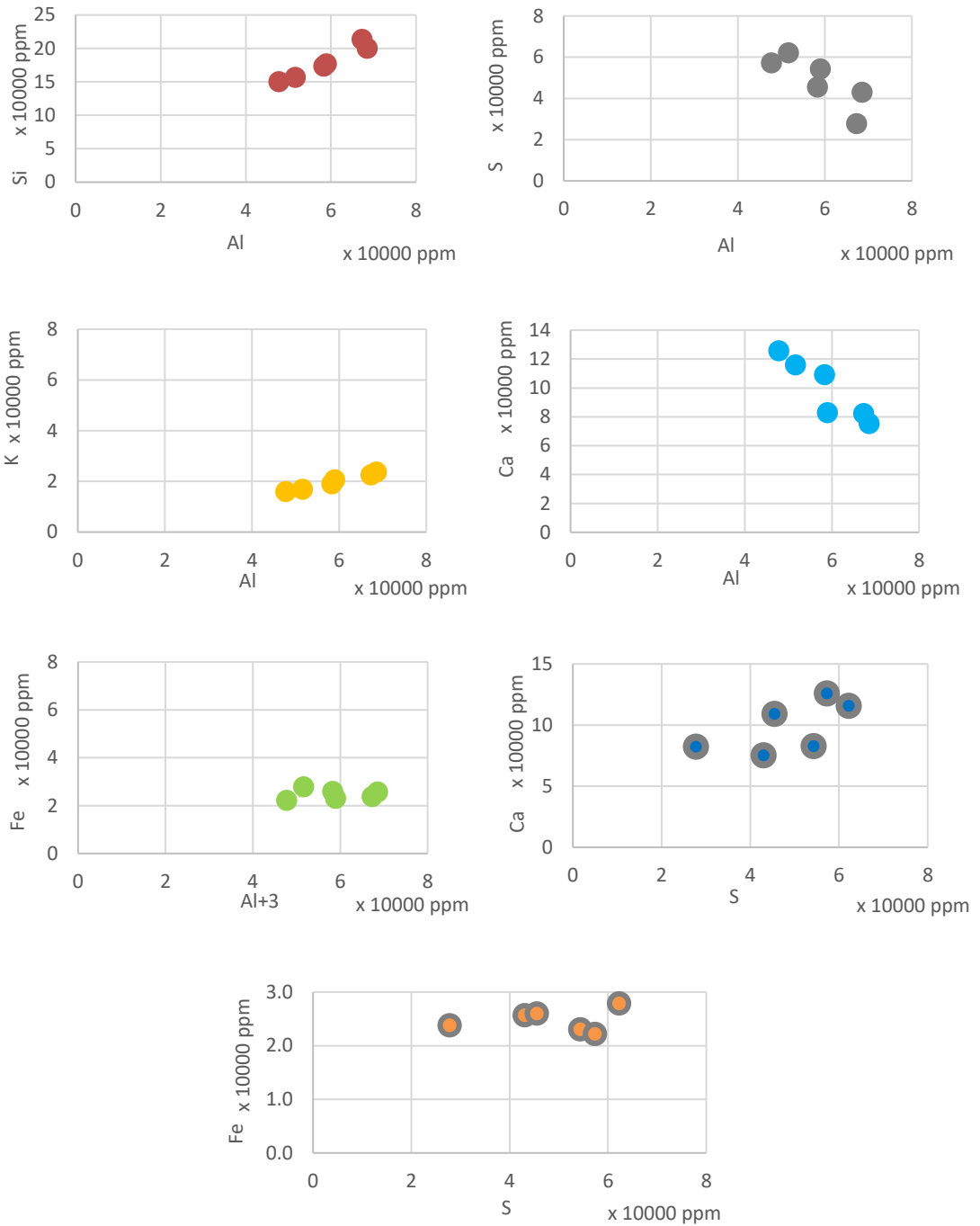


Figure 3.10 Principal elements and aluminum Cross plots for H(26). Good positive correlation between silica and aluminum, calcium and sulfur can be observed.

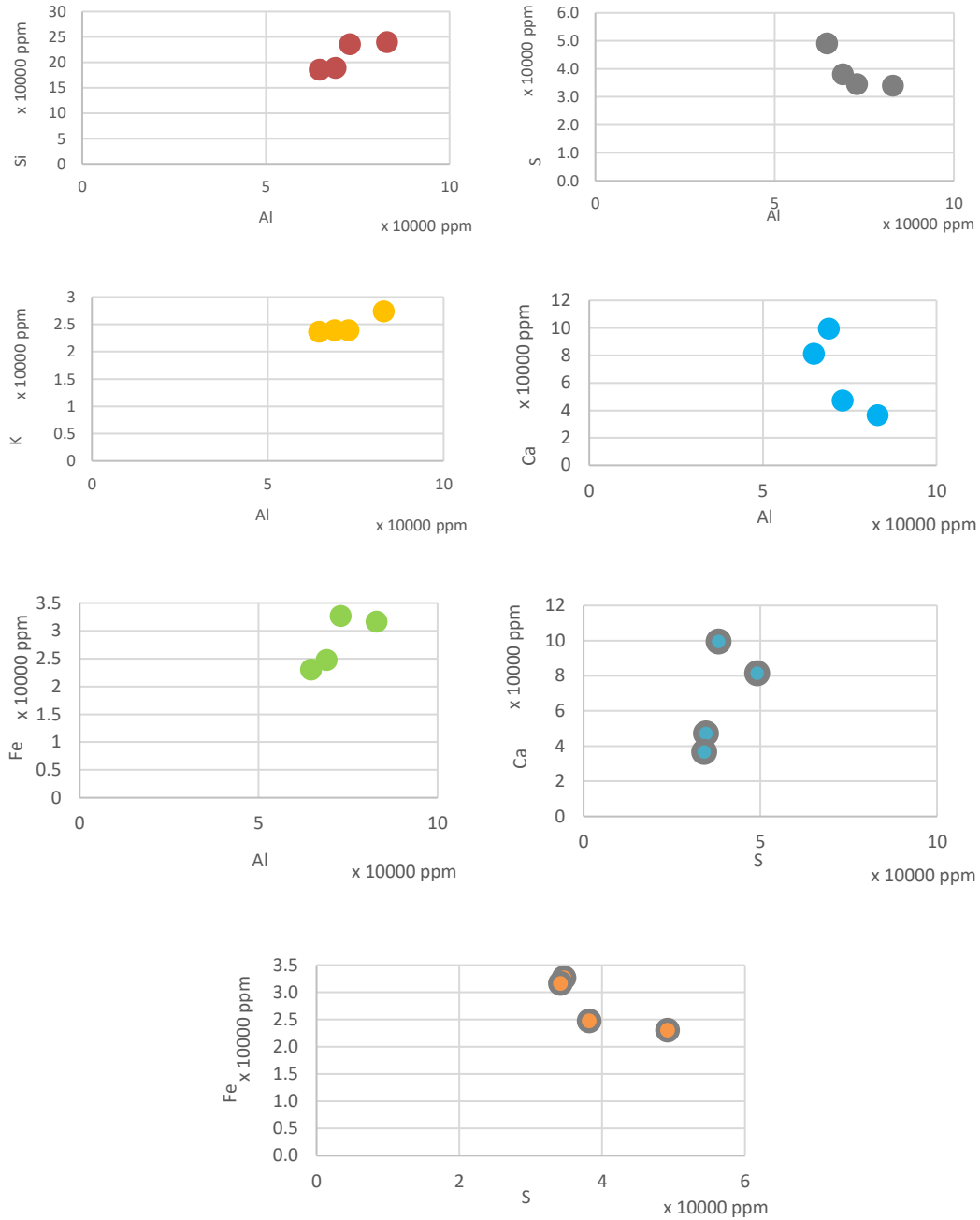


Figure 3.11 Principal elements and Aluminum Cross plots for H(29). Positive correlation between Si and Al are observed.

A summary of the crossplots between the major elements is presented in Figure 3.12. The size of the point is proportional to the clay mineral content. In general for the Haynesville Formation, clay mineral content is suggested by the positive correlation between Si, K and Al.

Carbonate is inferred to be of intrabasinal or authigenic origin, due to the negative correlation with Al and anhydrite presence is suggested based on Ca and S positive correlation.

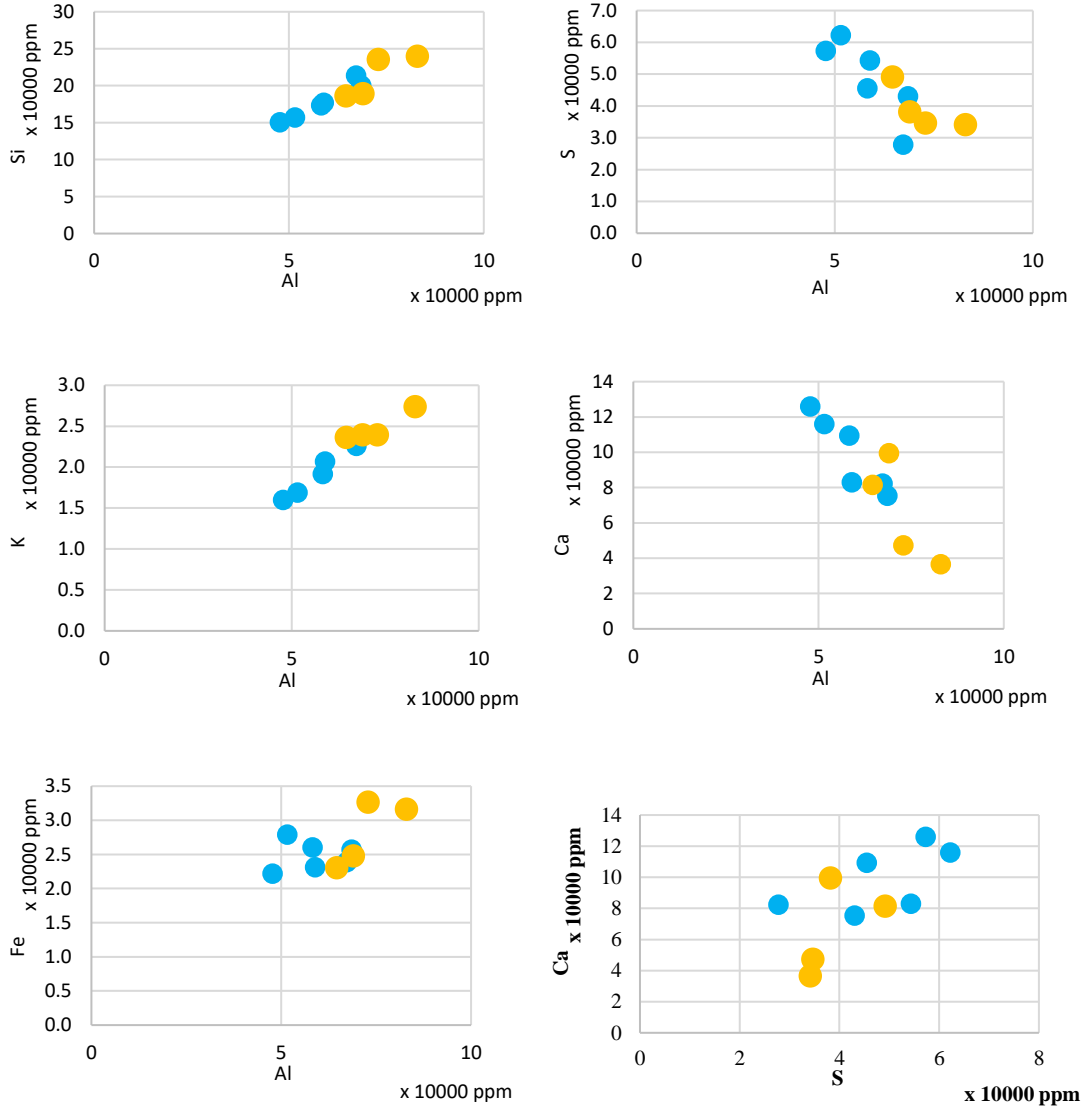


Figure 3.12 Principal elements for the Haynesville Formation. Clay mineral content is consistent with the XRF data. H(26) is represented by the blue points, H(29) by the yellow color. Presence of clay minerals, authigenic carbonate and anhydrite are suggested.

For samples LL(15) and LL(8), K, S, Fe and Al were detected, and their concentrations were under 50Kppm along the interval. For sample LL(15), calcium displays an average concentration of 116 Kppm. Silica is the element with the highest concentration in sample

LL(15), with an average of 200 Kppm. Values for all of the principal elements are similar along the length of the full core. The results are presented in Figures 3.13 and 3.14.

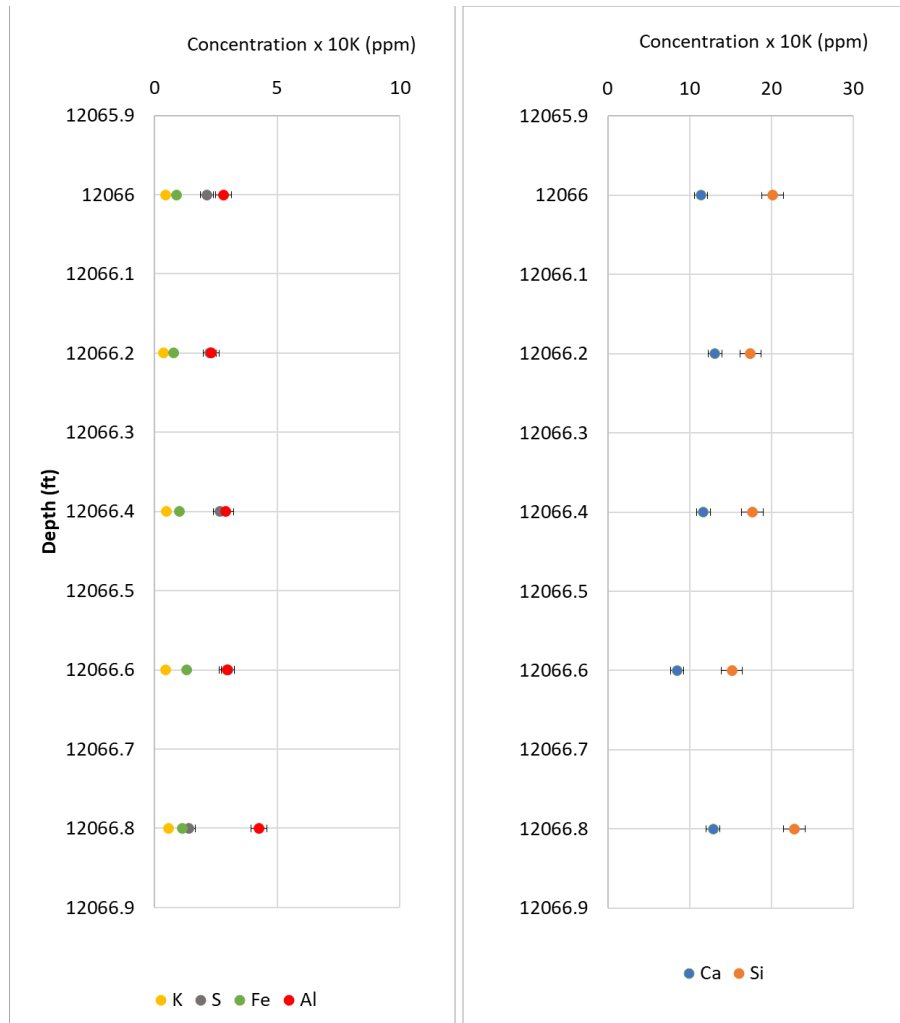


Figure 3.13 Major Element concentrations in LL(15). Values for all of the principal elements are similar along the length of the full core for this sample.

For LL(8), the data suggested that the two samples are not similar. Si, S and Ca are more abundant in LL(8), and there are two different trends in the full core. One in the half top which is more carbonate rich, and its concentration is decreasing towards to bottom half of the core. Same condition is observed in the S. Si shows a decreasing in the middle of the core and then increases again at the bottom.

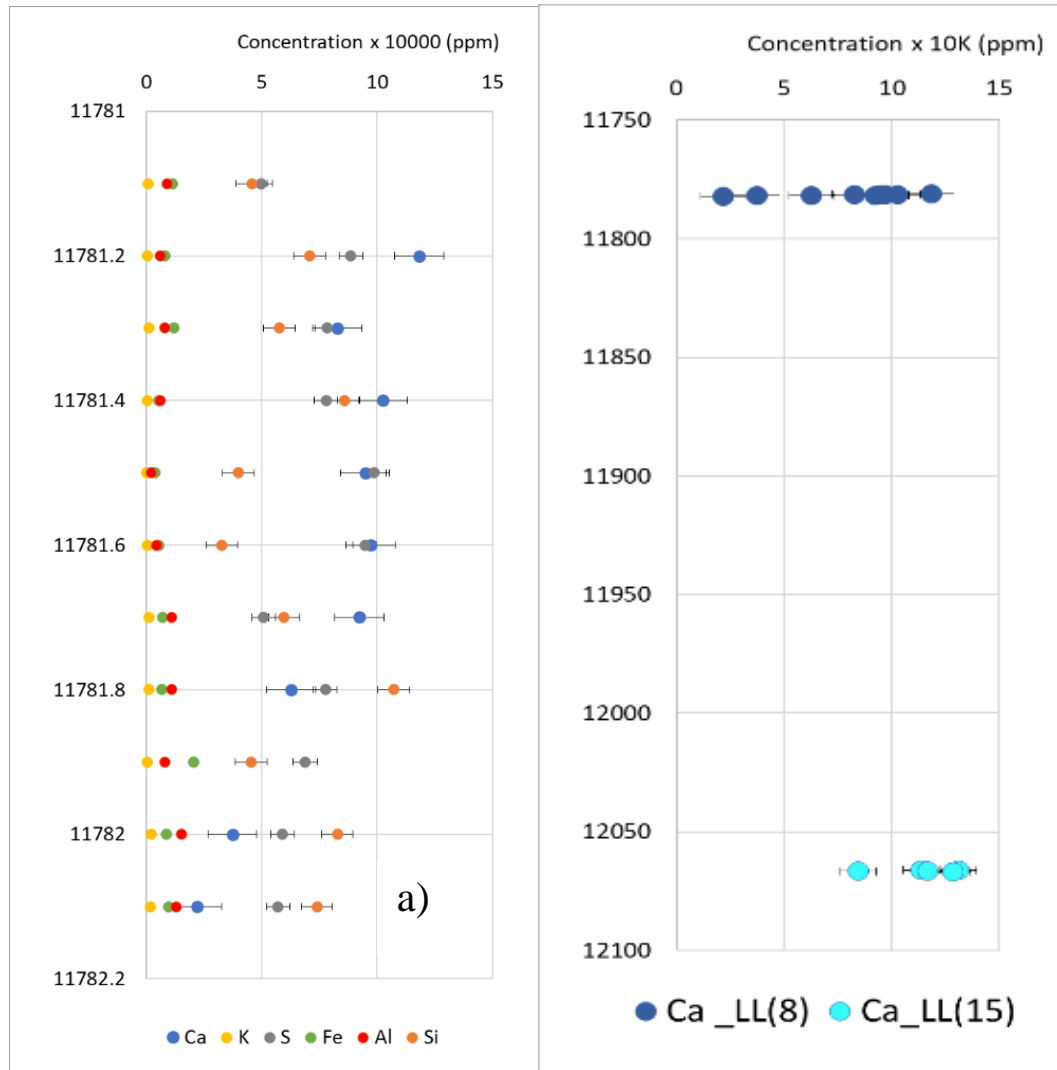


Figure 3.14 Major Elements concentration in LL(8). a) K, Fe, and Al are similar along the core. However, Ca, S, and Si show variation. Ca is more abundant at the top of the foot of core and decreases towards the base as Si increases b) Ca content of both cores shown in one plot to demonstrate that carbonate content is different between the two samples.

The crossplots for the La Luna Formation samples are shown are Figure 3.15, LL(15), and Figure 3.16, LL(8). For LL(8), although there are few points, a correlation between Si and Al can be observed. This sample does not show a correlation between Ca and Al, nor Ca and S, which suggest that Ca is more detrital than authigenic. Presence of anhydrite is not conclusive.

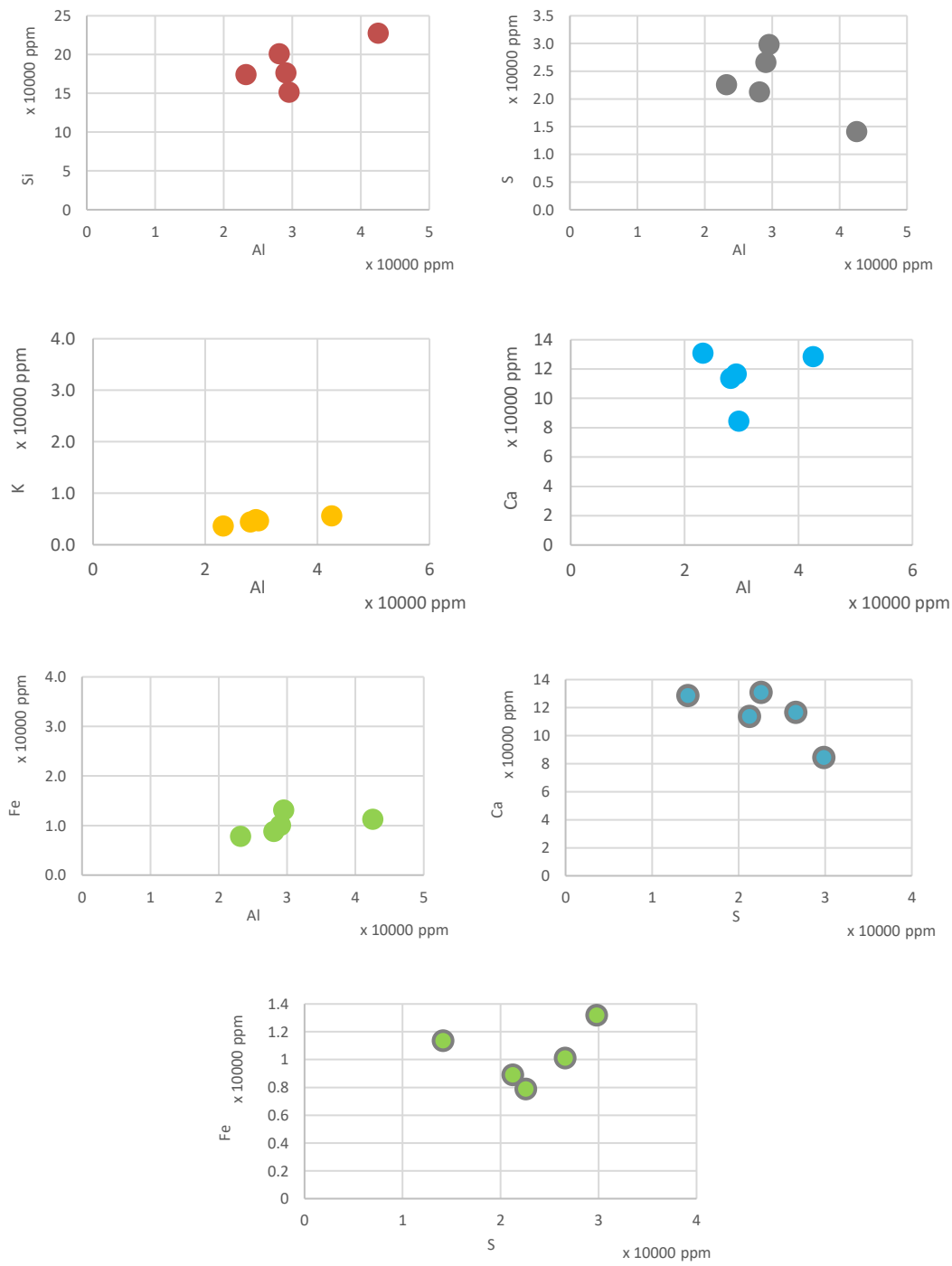


Figure 3.15 Principal element cross plots for LL(15).

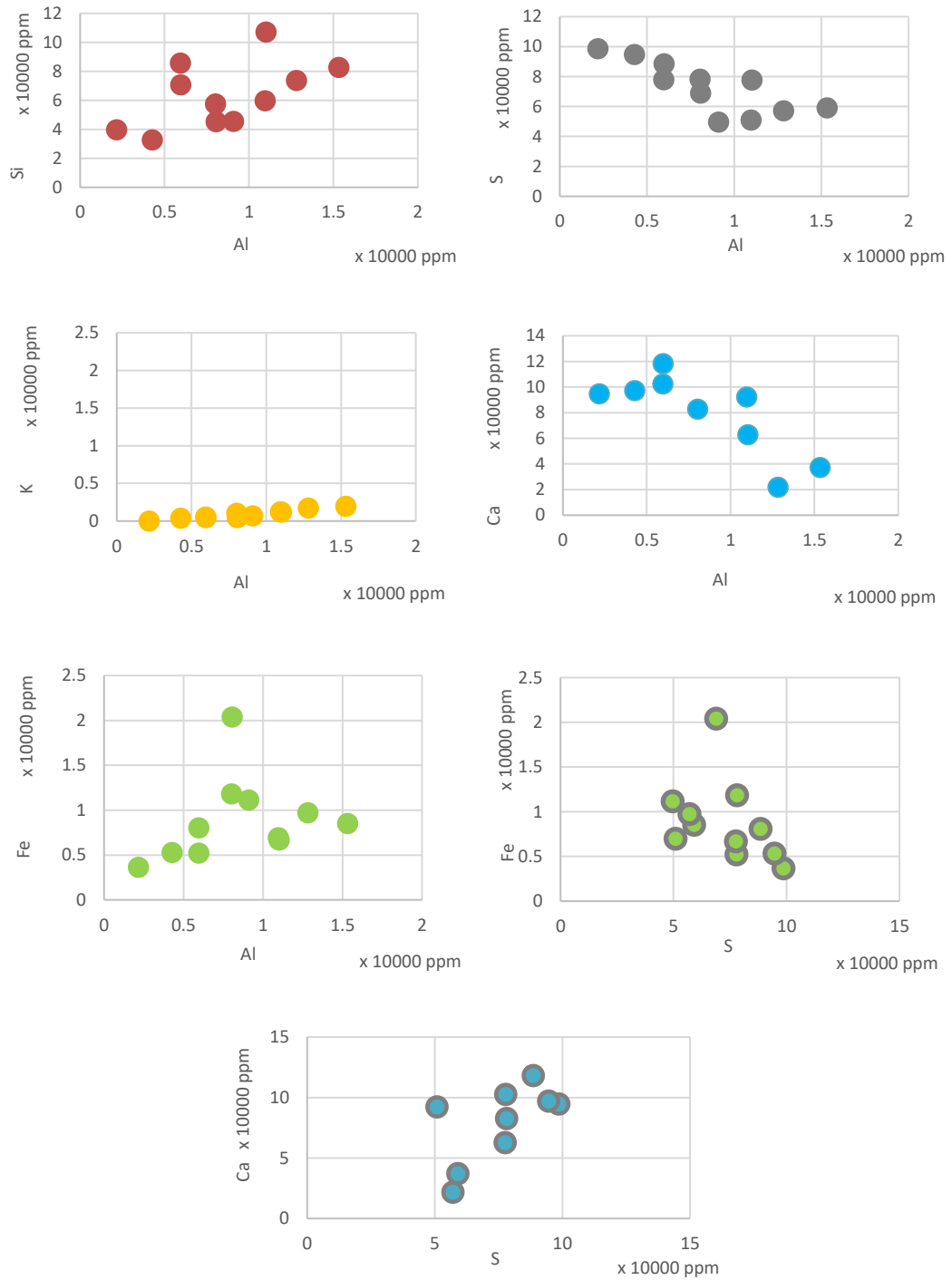


Figure 3.16 Principal element cross plots for sample LL(8). Data suggest that the sample is more carbonate rich than LL(15). These two samples are substantially different based on XRF data.

The two the La Luna samples display distinctly different compositions with respect to S, Ca and Si content. S varies dramatically between the two and is substantially higher in LL(8). Si also changes dramatically between these two samples, differing by 50%. Similar observations are made with respect to K, Ca and Fe.

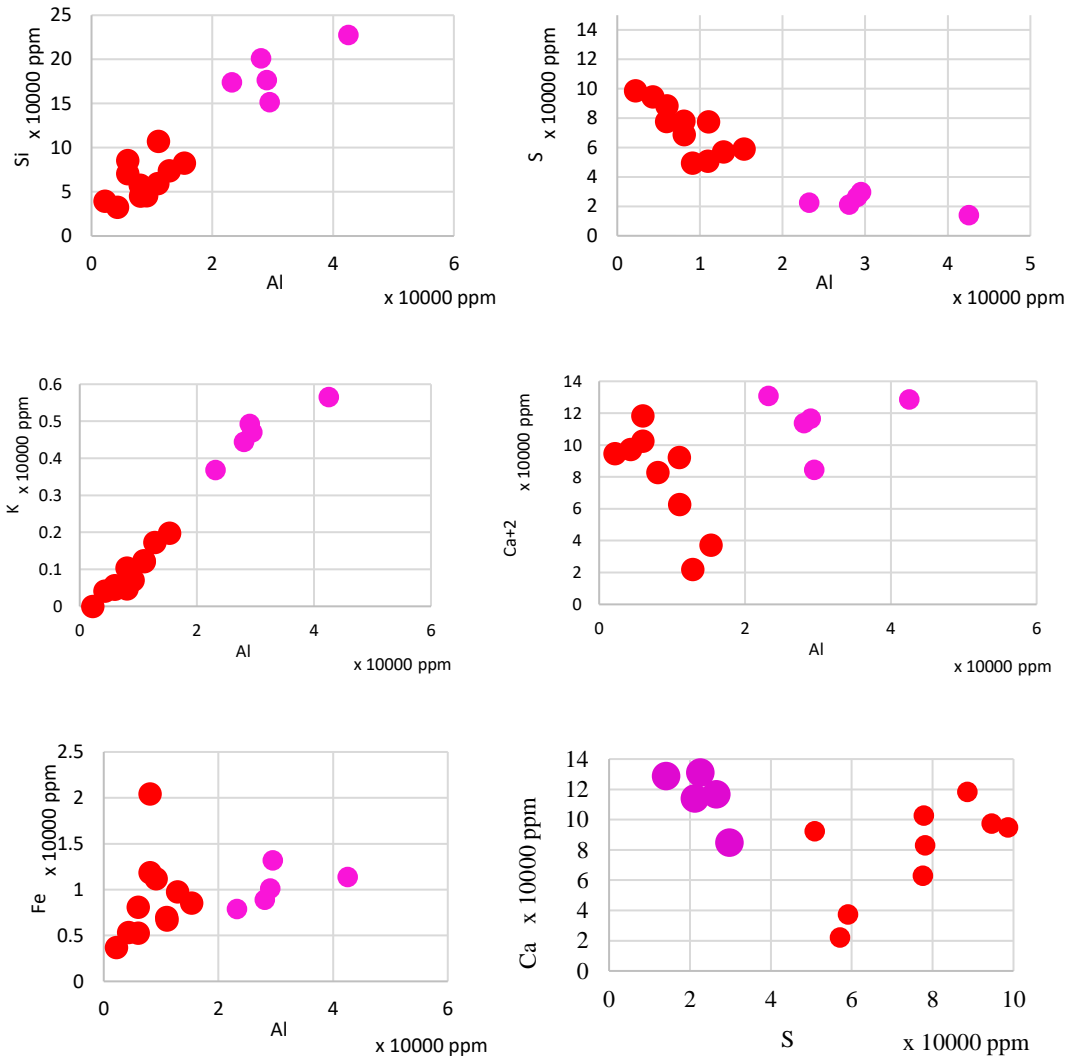


Figure 3.17 Principal element cross-plots for the La Luna Formation. Results show the significant differences between the two samples. LL(15) is more clay mineral rich, and LL(8) is more carbonate rich.

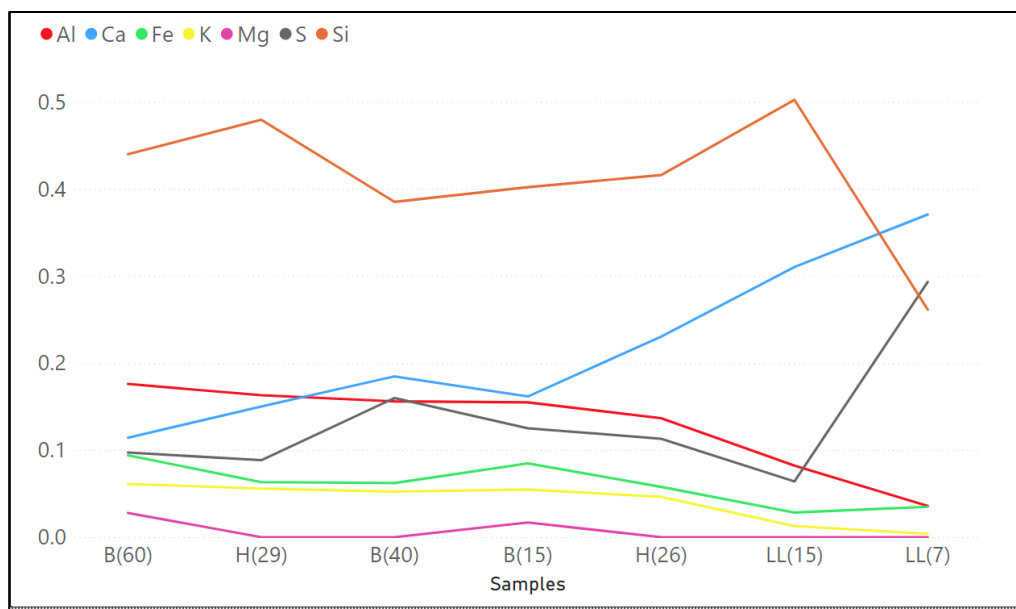


Figure 3.18 Major Elements average concentration per sample. Results separated the samples between in terms of more clay mineral or carbonate richness.

The samples with the highest concentrations of magnesium are B(60), and B(15), both of which have on the order of 5wt% Mg. Mg is most likely present as chlorite in sample B(60) and as dolomite in sample B(15). For the remaining samples, magnesium was not detected. Weight percent Potassium is similar in all of the samples although it is less abundant in the two samples of the La Luna Formation. This may suggest that clays other than illite are common in the La Luna as opposed to the Haynesville and Bossier. Iron has a higher concentration in samples B(60) and B(15) and is inferred to be present in those samples primarily in chlorite and ankerite (ferroan dolomite), respectively. Iron is present in fairly low concentrations in the La Luna samples. This might be associated with the presence of pyrite or chlorite. B(40) exhibits the highest concentration of Ca and S in the Bossier Formation. This may be due to the presence of anhydrite. Al concentration is similar in the Bossier, and Haynesville, with an average of 16%. and decreases to 8% and 4% for LL(15) and LL(8) respectively. Si is similar for both Haynesville samples, with 48 and 42% for H(29) and H(26) respectively. For the Bossier samples, Si varies between 48% for sample B(60) and 39% for sample B(40). Ca varies

substantially between the two Haynesville samples , with concentrations of 23% and 15% respectively for samples H(26) and H(29).

3.2. Thermo-Gravimetric Analysis. (TGA).

After demonstrating suitable homogeneity for the analysis, the samples were crushed and sieved into various size fractions. Following that, Thermo-Gravimetric experiments were performed. The objective was to observe the amount of water present in the samples, by measuring the weight loss during equilibration at increasing temperatures of 60, 80 and 100 °C. Temperatures were increased after the sample weight stabilized for 24 hours. These observations might be useful in interpreting the early time mechanisms in the imbibition experiments.

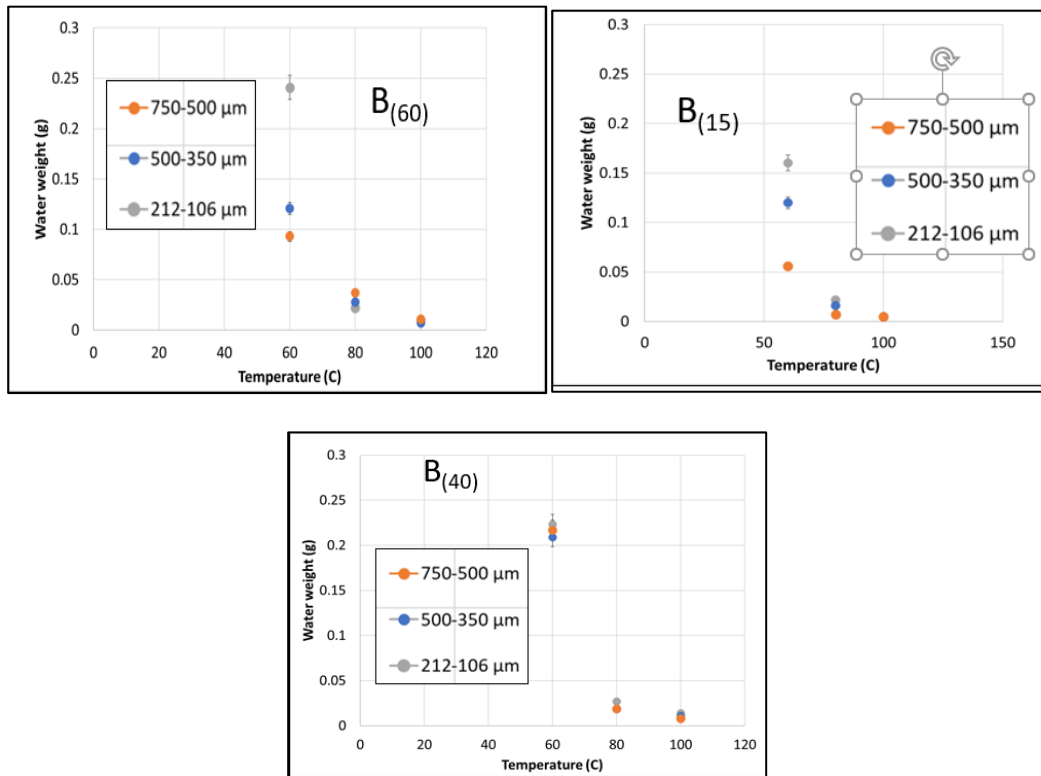


Figure 3.19 Bossier Formation sample TGA results. 20g of material was used for each experiment. In general, the higher the clay mineral content, the higher the volume of water lost.

In the Bossier Formation, the higher the clay mineral content, the larger the water weight removed from the sample. B(60), with a particle size 200 μm , is the sample that shows the higher water loss among all the three samples from a room temperature condition to 60 $^{\circ}\text{C}$. Particle size dependency is observed in samples B(60) and B(15) at 60 $^{\circ}\text{C}$, especially between the 200 μm and 500 μm size fractions. The 500 μm and 700 μm values are similar. This is not observed in sample B(40), where all the values are within the error margin, at all temperatures. There is not a simple correlation between particle size and measured weight loss during drying.

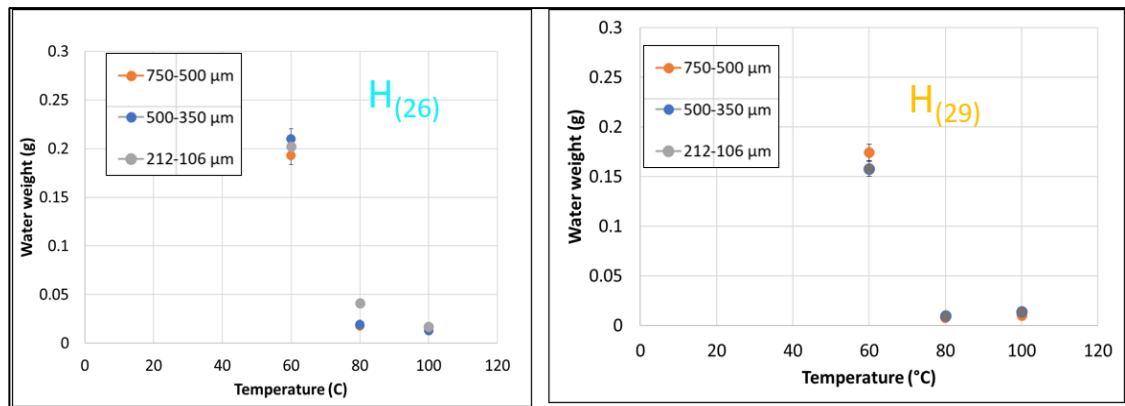


Figure 3.20 Haynesville Formation samples TGA results. These two samples are similar in terms of water loss, consistent with their similar clay mineral content.

For both Haynesville Formation samples, water losses are similar. This is not unexpected given their similar clay mineral content and suggests that similar results in imbibition and ion diffusion experiments might be observed. Measurements for the three different particle sizes are within error bars for each point.

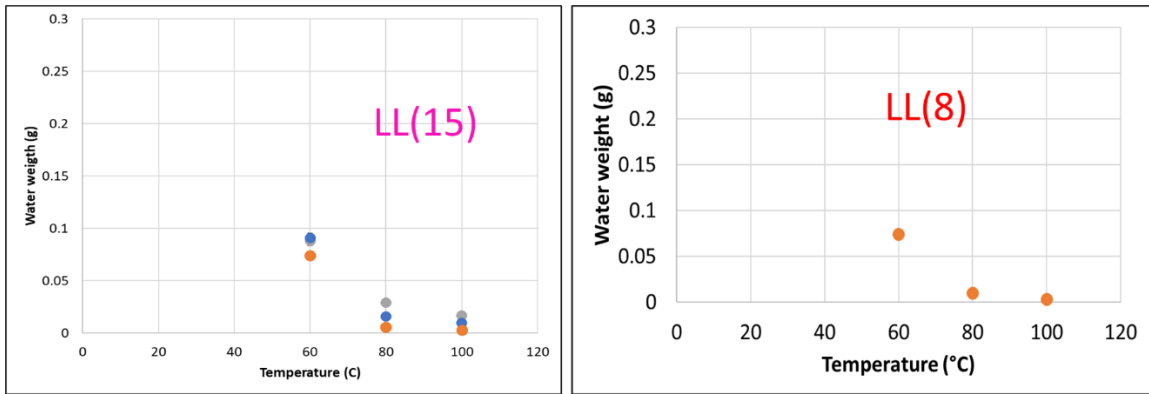


Figure 3.21 La Luna Formation samples TGA results. In general, results for the LL(15) were similar when compared with the B(15). Including all the samples in the study, LL(8) is the sample with the smallest water losses. For the sample with 8 % clay mineral content, all of the size fractions show the same results, and they overlaid on top of each other.

For samples of the La Luna Formation, a particle size dependency is observed in the sample with 15% clay mineral content. For the sample with 8 % clay mineral content, all of the size fractions show the same results. The La Luna samples, are lowest in clay mineral content, and undergo the lowest weight loss upon heating. In general, in all the samples, the largest water loss due to heating occurred at the first increment in temperature, changing from room temperature to 60 C.

3.3. CEC Results

Cation exchange capacity (CEC) measurements are expected to be related to the imbibition and ion expulsion experiments, due to the correlation with clay mineral content and type. For the Bossier Formation, nine measurements were acquired, one for each particle size, in the three different samples. In figure 3.22, the results are shown in a 3D plot that includes particle size, cation exchange capacity, and clay mineral content. CEC decreases with decreasing clay mineral content and does not show any variability as a function of particle size. The slope of the line between samples of different particle size is on the order of 10^{-6} meq/(gr/ μ m). Bossier sample B(60)_{200 μ m} has the highest CEC among the set of samples analyzed.

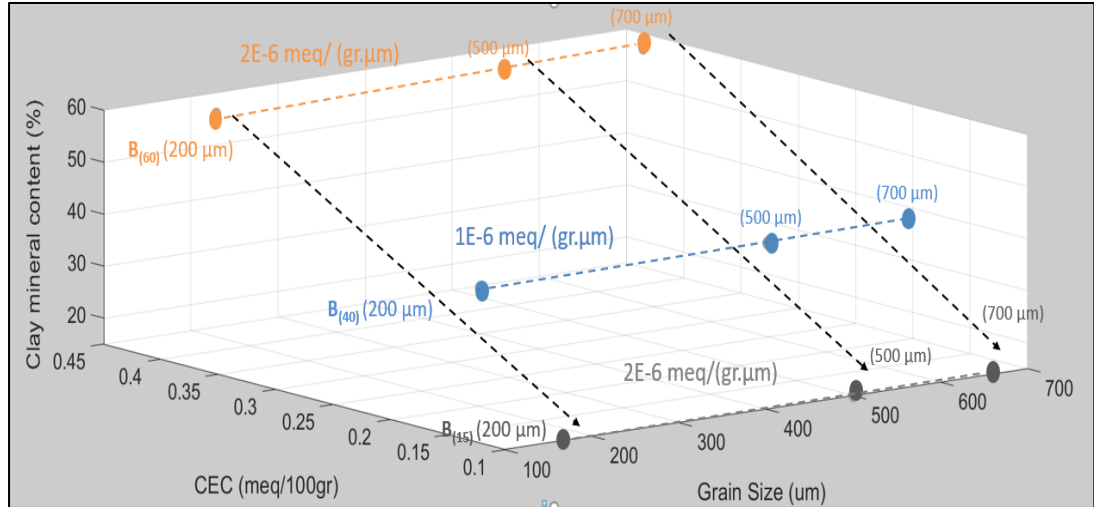


Figure 3.22 Bossier Formation CEC results. CEC decreases with decreasing clay mineral content in the Bossier Formation, and it does not show a particle size dependency.

To help in understanding the CEC and TGA results, X Ray Diffraction data were acquired for samples B(60) and B(15) at different particle sizes, in order to evaluate how the clay mineral content changed in each particle size aliquot. The results are shown in Table 3.1 indicating only small changes in the clay mineral content as a function particle size, well within what is considered the standard error for XRD analysis (typically ~ 5 wt%). In B(60)_{200µm}, 61.3% clay is observed compared with 59.2 and 59.9 % for B(60)_{700µm} and B(60)_{500µm} samples respectively. For B(15), the values are identical.

Table 3.1 XRD Data for B(60) and B(40) at the three different particle sizes

XRD DATA		
Sample Identity	Grain Size um	PHYLLOSILICATES (CLAY GROUP MINERALS)
B ₍₆₀₎	750-500	59.2
	500-350	59.9
	212-106	61.3
B ₍₁₅₎	750-500	13.9
	500-350	13.9
	212-106	13.7

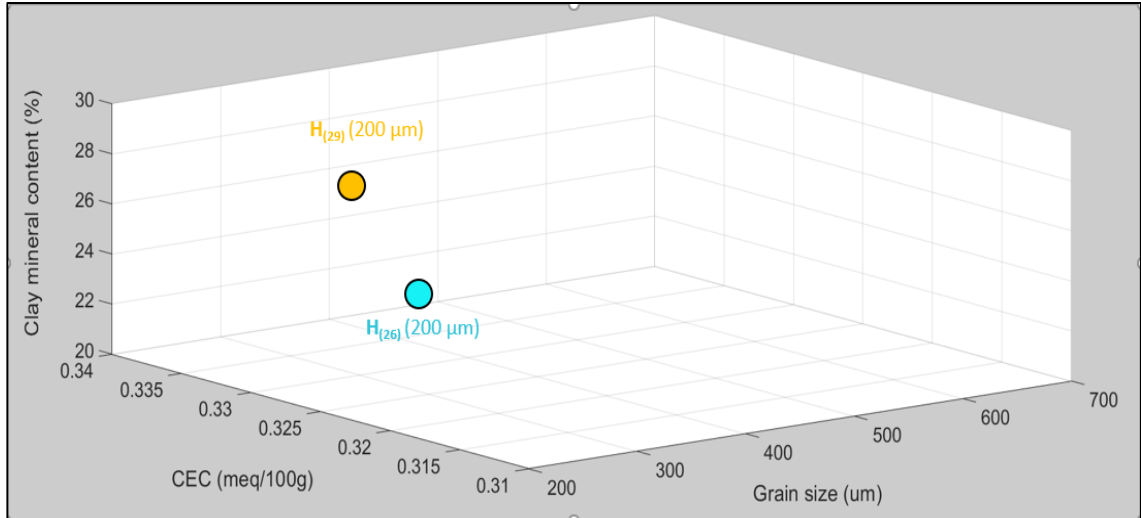


Figure 3.23. Haynesville Formation samples CEC results. X axis is particle size, Y axis is CEC and Z is clay mineral content. Only two CECs were measured for these samples due to material limitations. CEC was similar for both samples. Values are 0.318 meq/100 g in H(26) and 0.323 meq/100g in H(29).

For the Haynesville Formation, two measurements were acquired, one for each sample, H(26) and H(29), in the smallest particle size aliquot (200 μm) (Figure 3.23). Values are 0.318 meq/100 g in H(26) and 0.323 meq/100g in H(29). Although the results suggest that CEC decreases with clay mineral content, the values are quite low and possibly within error bars of each other. We interpret that the two samples have the same CEC, which is consistent with the clay mineral content reported (26 and 29 %).

For the La Luna Formation, three measurements were acquired, one for each sample at the same particle size (200 μm) and one at 700 μm , for sample LL(8). LL(8) 500 μm was not included due to sample amount limitation. The 3D plot is shown in figure 3.24. Values are 0.161 meq/100 g in LL(15)200 μm , 0.175 meq/100g in LL(15) 700 μm , and 0.171 meq/100g in LL(15) 200 μm . Note that a particle size effect is not observed, based on the comparison between the two samples at different particle sizes in LL(8), similar to the condition observed

in the Bossier Formation. Measurements of CEC suggest a change as a function of clay mineral content. However, because the values are quite low (possibly within the error margin), we again conclude that the two samples have the same CEC.

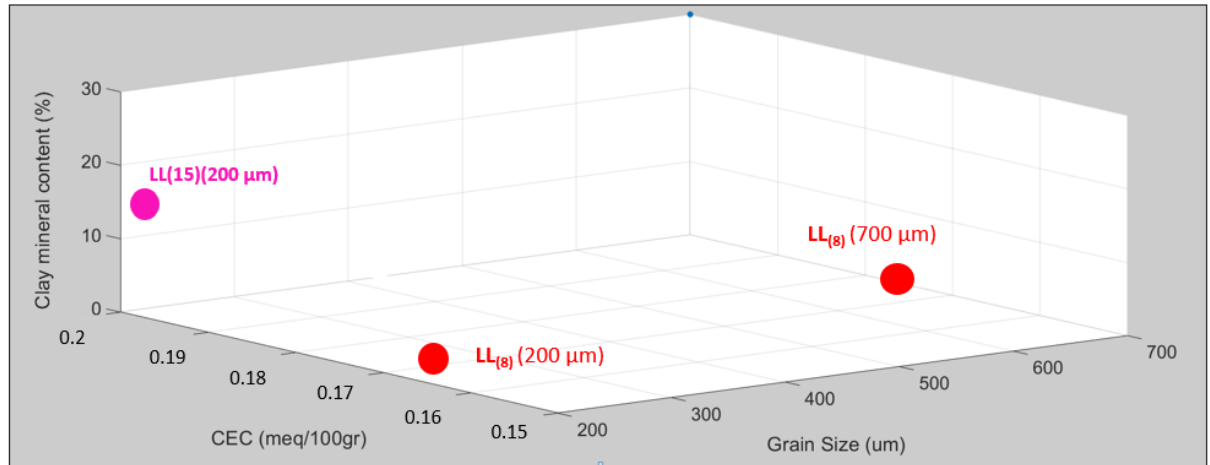


Figure 3.24 La Luna Formation samples CEC results. X axes is particle size, Y axes is CEC and Z is clay mineral content. For LL(8), measurements were acquired in two different particle size. CEC did not change with particle size. Although a difference is observed in terms of CEC and clay mineral content, these CEC values are within the error range.

The next three figures (Figures 3.25-3.27) show the results per formation in terms of clay mineral content and cation exchange capacity, using 2D plots. The size of the point is proportional to the sample particle size. Figure 3.28 is a summary plot, showing results for all three formations. When presenting the results per formation, the color code will be explained in each figure, and is consistent with the colors that have been used in previous figures. In the summary figure 3.28 a color code per formation will be implemented. Orange color will represent the Bossier Formation, blue colors will represent the Haynesville, and red colors will be used for the La Luna Formation results.

Figures 3.25 to 3.27 are called eclipse plots and they show the results for the Bossier, Haynesville and La Luna Formation in 2D plots, in which all the particle sizes are plotted

proportional to the point size. For the Bossier Formation, clay mineral content is proportional to the CEC, and a direct proportionality is suggested. For the Haynesville samples (Figure 3.26), due to the similar value of clay mineral content, the CEC is essentially the same value. More discussion will be presented in chapter 4.

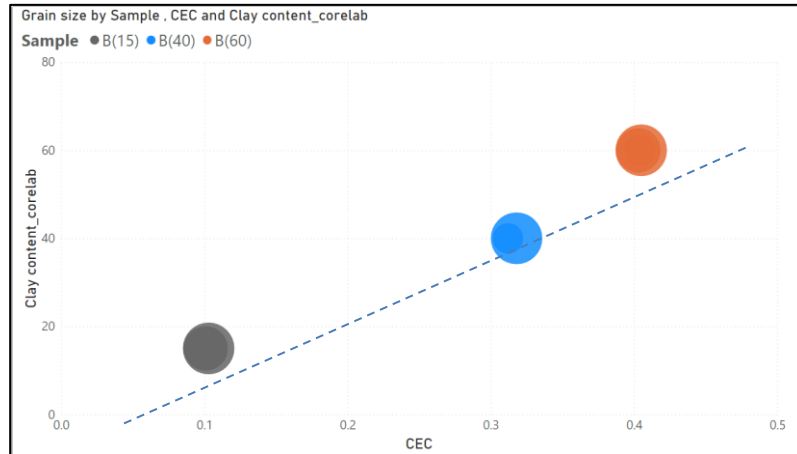


Figure 3.25 Clay Mineral Content vs CEC for Bossier Formation Eclipse Plot. CEC is independent of particle size; it is directly proportional to the clay mineral content.

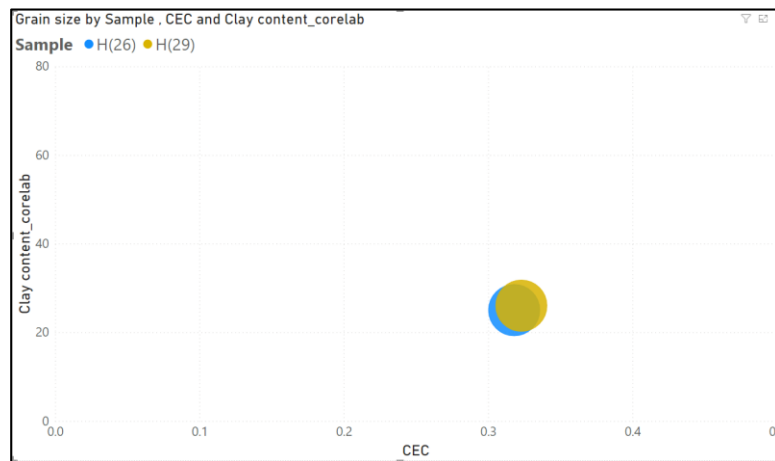


Figure 3.26 Eclipse Plot for the Clay Mineral Content vs CEC for Haynesville Formation. Same CEC value for the two samples in Haynesville Formation, which was expected due to the similar clay mineral content.

For the La Luna Formation samples, along with sample B(15) from the Bossier Formation, the CEC values are the lowest among all of the samples. Similar to the observations in the

Haynesville samples, the measurements suggest that the CECs for the two samples are within the error margin, even though the clay volumes are different. This is probably due the low clay mineral content. In addition, based on XRF results, the clay mineral type in the La Luna Formation is probably chlorite, which has a very low CEC value.

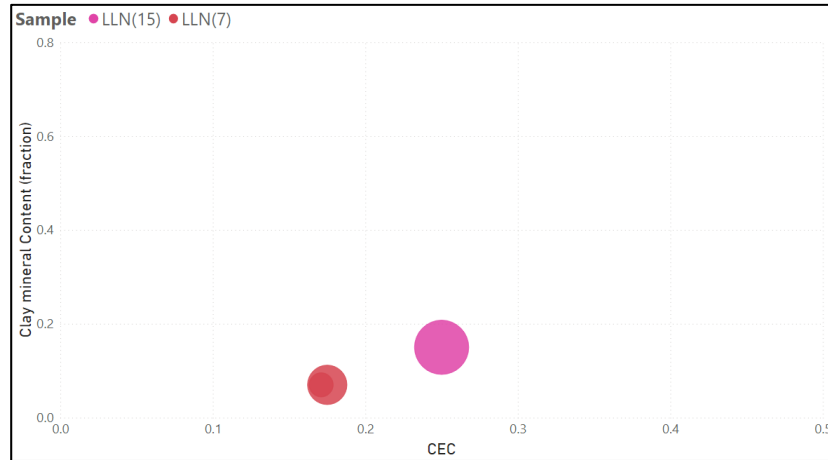


Figure 3.27 Clay Mineral Content vs CEC for La Luna Formation samples results . Values are within the error margin. Same CEC value for these two samples is assumed.

An eclipse summary plot illustrating all of the data is presented in Figure 3.28. Orange colors represent the Bossier Formation, blue colors are Haynesville Formation and the La Luna Formation samples are represented by the red colors. All samples and particle sizes are plotted at the same time. When plotted together, a relationship is observed between the clay mineral content and the CEC. Further evaluation of this observation will be discussed in Chapter 4.

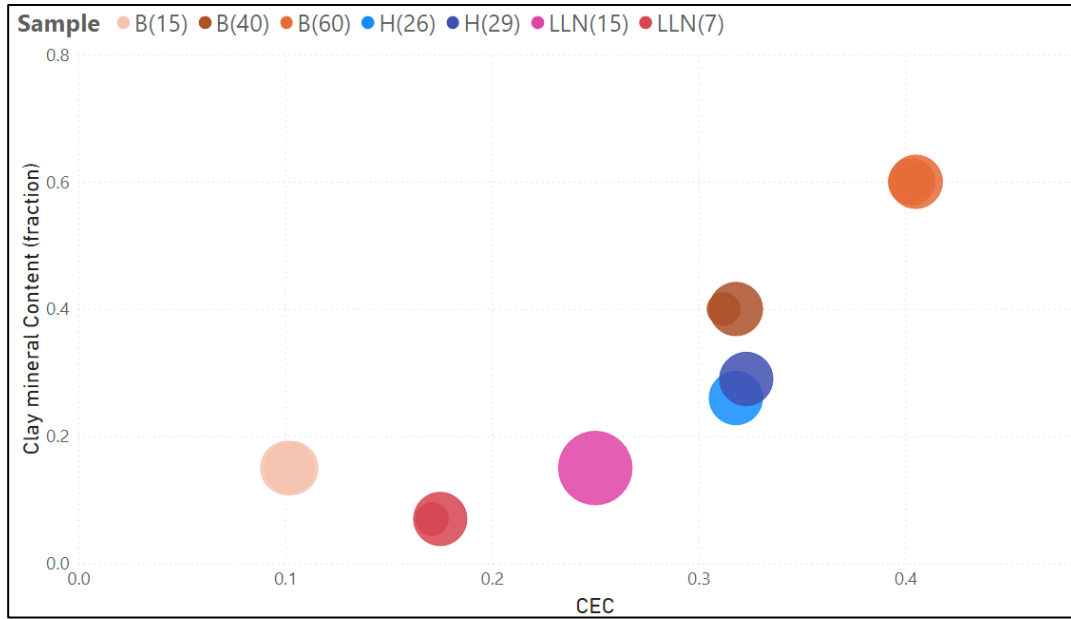


Figure 3.28 Eclipse plot compiling the results for Clay Mineral Content (fraction from XRD) vs CEC (meq/100gm). A possible direct proportionality is observed when all the samples are plotted with the various particle sizes.

Table 3.2 CEC Data for all samples at the three different particle sizes

Sample	Particle size um	CEC meq/100 g
B(60)	700	0.41
B(60)	500	0.40
B(60)	200	0.40
B(15)	700	0.10
B(15)	500	0.10
B(15)	200	0.10
B(40)	700	0.32
B(40)	500	
B(40)	200	0.31
H(26)	700	0.32
H(26)	500	
H(26)	200	
H(29)	700	0.32
H(29)	500	
H(29)	200	
LLN(15)	700	0.25
LLN(15)	500	0.25
LLN(15)	200	0.25
LLN(8)	700	0.18
LLN(8)	500	
LLN(8)	200	0.17

3.4. Pre-imbibition Nuclear Magnetic Resonance Results

Figure 3.29 shows the NMR T₂ spectra for as received material (pre imbibition) ground to various particle sizes for the Bossier Formation (B(60), B(40) and B(15)). The dominant peak for all samples has a T₂ on the order of 0.3 msec and is interpreted to be associated with bound water. Above 3 msec, a series of two or three peaks with longer T₂s but representing very small volumes of free fluid are also present in each sample. We infer that this may, in part, be related to oil-based mud contamination (Ravinath, (2016)). Particle size dependency is observed in the cumulative pore volume, which corresponds to the total area under the curve. As grain size increases, total porosity tends to decrease.

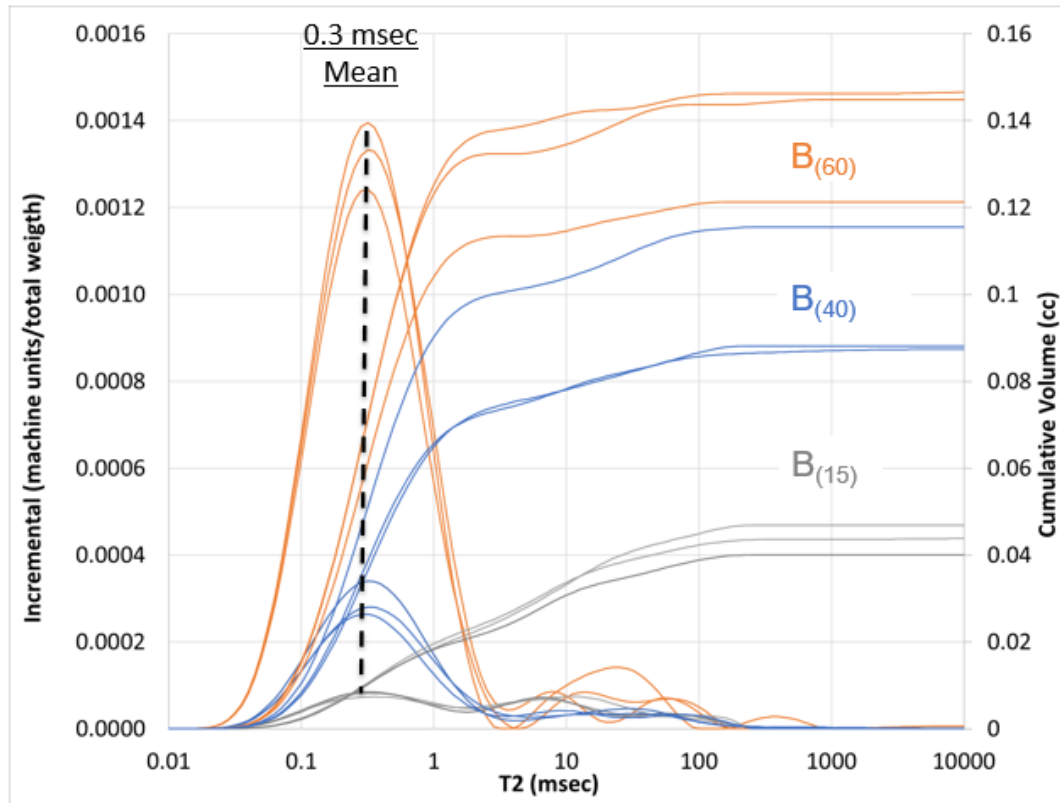


Figure 3.29 As received material (pre imbibition) NMR T₂ spectra in Bossier Formation samples. The cumulative volume response from the NMR is proportional with the clay mineral content reported for the samples.

Figure 3.30 shows NMR T_2 spectra for as received material (pre imbibition) ground to various particle sizes for the Haynesville Formation samples (H(26), and H(29)). Similar to the Bossier Formation, a dominant peak for all samples is observed at 0.3 msec T_2 associated with bound water. Similarly, two or three peaks with longer T_2 s are also observed (10-100 ms). A 3 msec cutoff to divide bound water from free fluids can be used in both formations. Particle size dependency is observed in the cumulative pore volume.

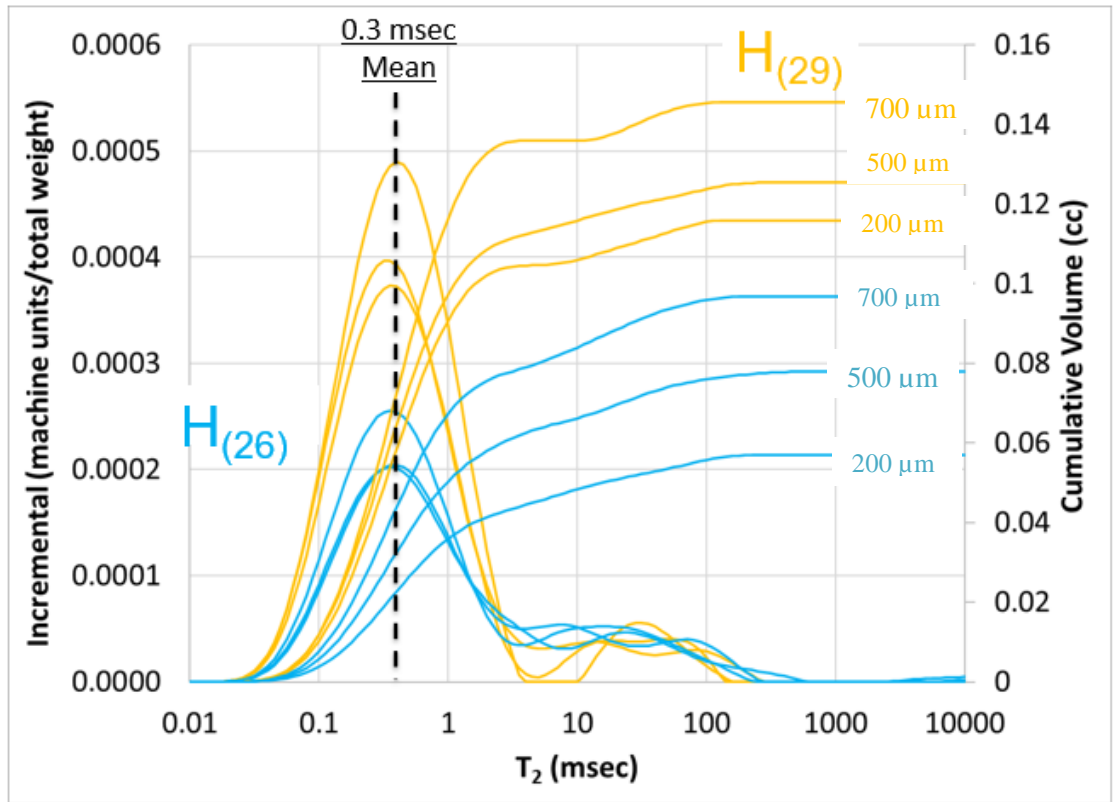


Figure 3.30 As received material (pre imbibition) NMR T_2 spectra in Haynesville Formation Samples. Cumulative volume from the NMR are proportional with the clay mineral content reported for the samples.

Figure 3.31 shows the NMR T_2 distributions for as received La Luna Formation samples. The two La Luna samples show distinctly different responses. For LL(15), the dominant peak for all the particle size samples has a T_2 on the order of 0.3 msec, similar to the results from the Bossier and Haynesville Formations. For LL(8), the dominant peak is no longer at 0.3 msec,

but is shifted to 3 msec. There is a lower T₂ shoulder on the peak, suggesting the presence of a smaller bound water response. This is consistent with the fact that this is the sample with the lowest clay mineral content in the sample set. Similar to previous results, a particle size dependency is observed in the cumulative pore volume.

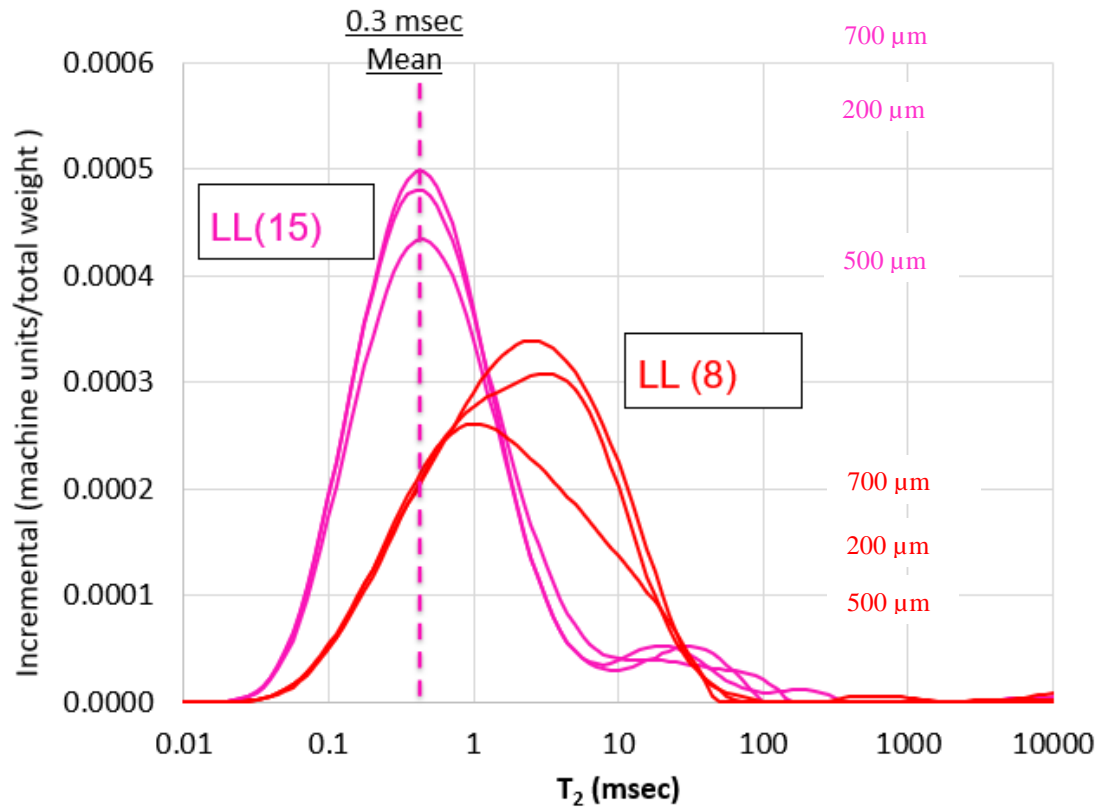


Figure 3.31 Pre-Imbibition Experiment NMR T₂ spectra in La Luna Formation to the various particle sizes. These two samples in la Luna Formation shows a significant difference in terms of T₂ distributions.

3.5. Spontaneous Water Imbibition and Salinity

The following experimental results represent the fundamental data that will be used to gain insight into the petrophysical properties of the various formations. Correlation with other measurements will be evaluated and from those relationships estimates of fundamental rock properties will be extracted. In these experiments, the equivalent NaCl conductivity was reported by the conductivity meter, and then, the supernatant salinity was estimated from the fluid conductivity using the method of Bateman and Konne (1997), which corresponds to the following equations,

$$ppm(NaCl) = 10^x \quad \text{Eq. 3}$$

$$\text{and } x = 3.562 - \log(Rw_{75} - 0.0123), \quad \text{Eq. 4}$$

where Rw_{75} is the water resistivity at 75 degrees Fahrenheit and x is the water salinity. Bateman and Konne's (1997) estimation of salinity from conductivity assumes that the bulk of the ions are Na^+ and Cl^- . Based on the results of the ICP experiments, Ca^{+2} and S^{+6} are the most abundant ions detected in solution. Therefore, the influence of ionic composition on the conductivity was investigated.

To validate the conductivity data, equivalent NaCl calculations were performed. Schlumberger chart GEN-4 (Schlumberger, 2009) was used to calculate equivalent sodium chloride total dissolved solids from a known water chemistry sample from ICP. In figure 3.32, a crossplot of the estimated NaCl equivalent salinities from the conductivity meter and our calculation is shown. The values fall very close to the 1:1 line which provides confidence in the salinity estimates from the conductivity values.

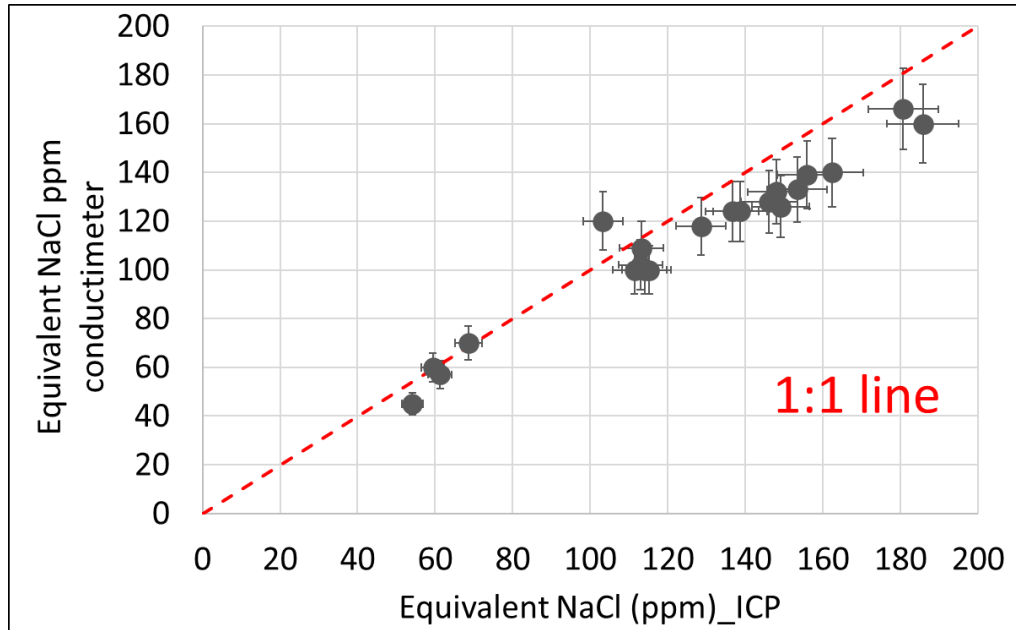


Figure 3.32 Calculated equivalent NaCl salinity (ppm) is in good agreement with the equivalent NaCl salinity from the ions detected by the ICP experiments, which provides confidence in the conductivity data.

The results of the spontaneous imbibition experiments are shown in Figures 3.33 through 3.39. Supernatant concentration (C_t) expressed in total number of ions and imbibed water volume (V_t), expressed in total number of water molecules, are plotted as a function of time. All of the spontaneous imbibition data show two distinct phases in terms of sample response.

The initial phase, is characterized by a linear increase in salinity as a function of time, the slope of which increases as particle size decreases. As salinity increases the samples continue to imbibe fluid. This phase can take between 20 days and one month. Finally, a second phase is characterized by stabilization of both salinity and imbibed volume. Stabilization of these values is used to indicate that the experiment is complete. Imbibition occurs at a much slower rate than ionic expulsion in the Bossier and Haynesville Formations. In the La Luna Formation, both, ionic expulsion and imbibition, occur more slowly than in the Bossier, and at similar rates

to those observed in the Haynesville. The data also suggest that as the particle size decreases for each sample, the equilibrated salinity of the supernatant fluid increases. Further evaluation of this observation will be discussed in a later section. Figures 3.33 and 3.34 illustrate the results for samples of the Bossier Formation. The point size is proportional to the particle size for each aliquot. All samples reached equilibrium. Orange curves correspond to B(60), blue curves correspond to B(40) and B(15) is represented by the gray curves. B(60)_(200 μm) and B(40)_(200 μm) are the samples for which the highest conductivity was measured.

These samples also imbibed the largest volume of water among the Bossier Formation samples. The opposite was observed in B(15) when conductivity is the lowest for all particles sizes, and also for the volume, with the exception of B(15)_(200 μm). The conductivity response appears to be linear with the clay mineral content, but the relation is not perfect.

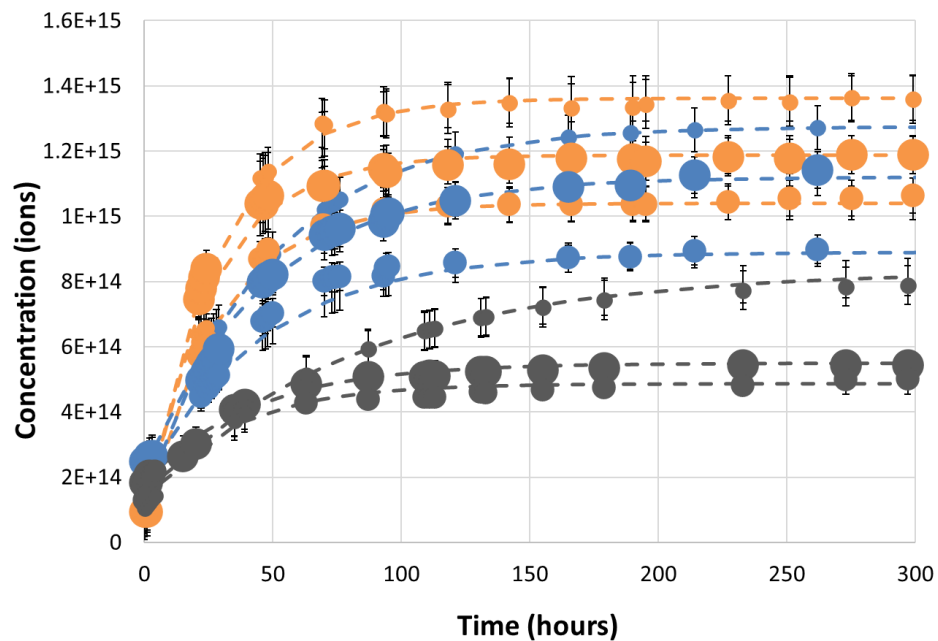


Figure 3.33. Spontaneous Water Imbibition Experiments in the Bossier Formation. Concentration estimates, converted from conductivity and expressed as number of ions, for the various particle sizes are plotted against time. In general, the 200 μm particle size experiments display the highest salinity, followed by very

similar response from 700 μm and 500 μm size fractions. 700 μm provides more conductivity than 500 μm . In general, a proportionally with clay mineral content is observed, however is not perfect.

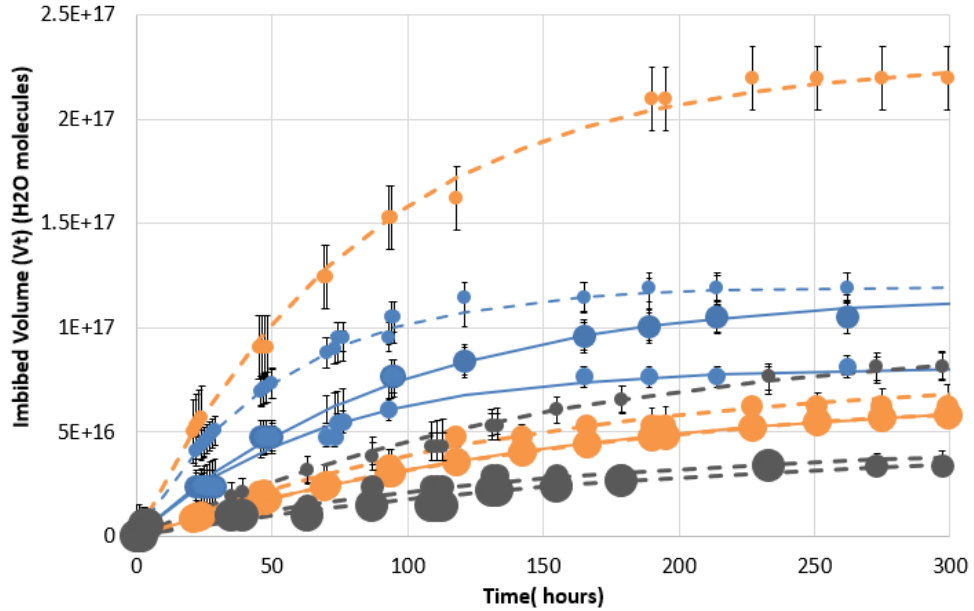


Figure 3.34. Volume Imbibition Experiments in the Bossier Formation. In general, the imbibed volume increases as clay mineral content increases. Sample B(40) represented by the blue color does not follow the same trend of particle size and imbibed volume, which is observed in B(15) in gray and B(60) in orange.

Figures 3.35 and 3.36 show the results for the experiments in the Haynesville Formation. Salinity estimates calculated from the measured conductivity and the imbibed volume are plotted as a function of time. Similar to results in the Bossier, two distinct phases are also present in these samples. H(26) and H(29) show similar results in terms of conductivity, a result that was expected due to the similar clay mineral content, TGA and CEC results. Both samples stabilize in the same amount of time, approximately 20 days.

We observe that although the conductivity has reached stabilization, imbibed volume continues to increase. Additionally, similar to the B(40) sample in the Bossier Formation, in the Haynesville samples, the proportionality between salinity and particle size is not as clear, although the finest particle size, H(26)_{200 μm} and H(29)_{200 μm} still produces higher conductivity

and therefore the higher salinity. However, the supernatant fluid for the 700 μm samples displays a higher conductivity than that for the 500 μm aliquots. A second observed difference between the Haynesville and Bossier Formation results is the volume of imbibed water, which is larger in the Haynesville than in the Bossier. Differences in mineralogy and porosity might explain these results. This will be evaluated by using imaging and image analysis, and post imbibition NMR evaluation.

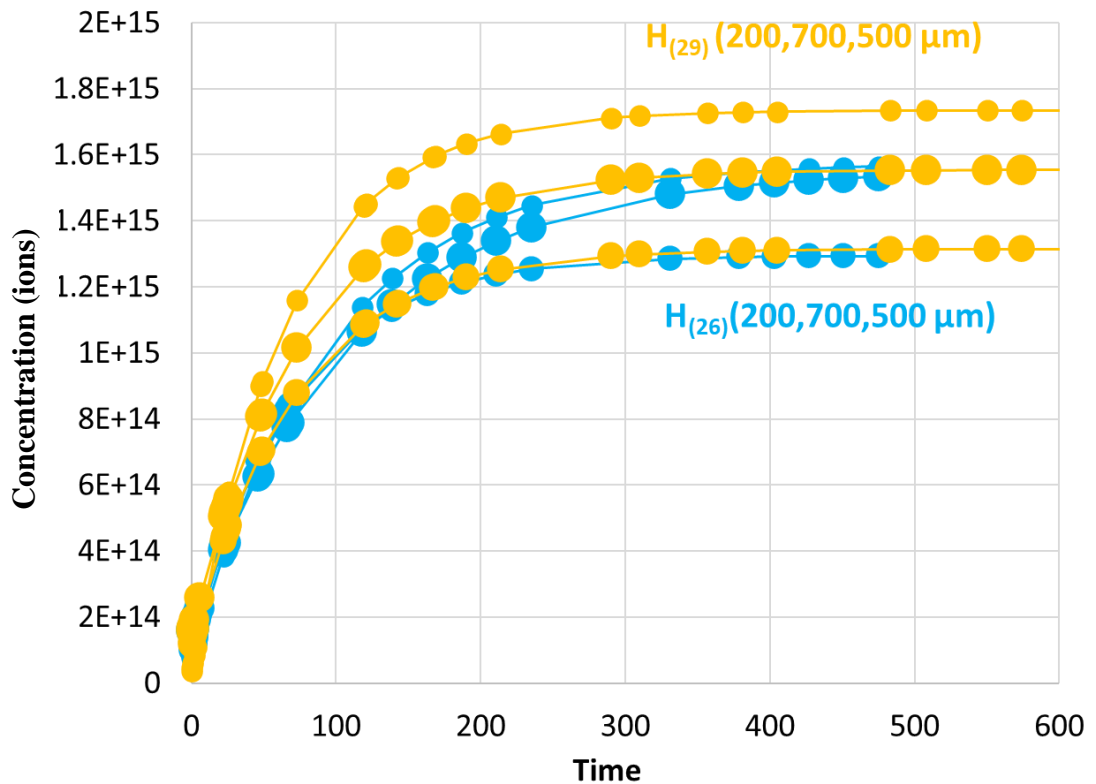


Figure 3.35. Spontaneous Water Imbibition Experiments in the Haynesville Formation. Salinity measurements for the various particle sizes are plotted against time. Each sample has three curves, corresponding to the three particle sizes. The 200 μm samples display the highest salinity, followed by the 700 μm and 500 μm size samples.

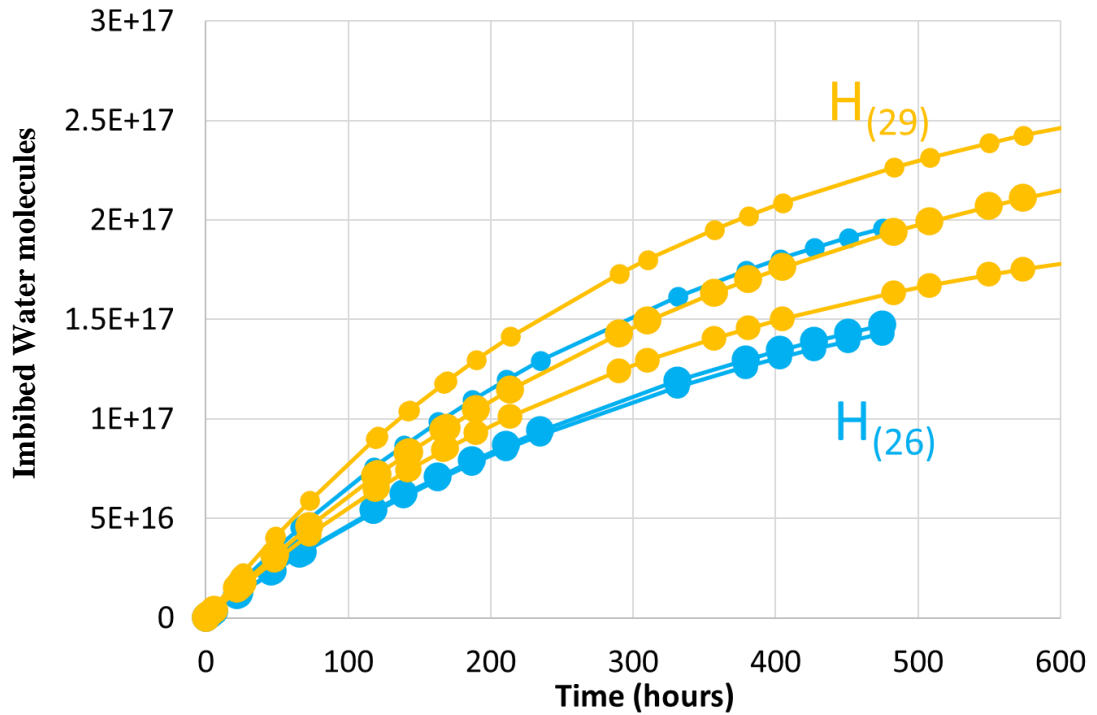


Figure 3.36. Volume Imbibition Experiments in the Haynesville Formation. Imbibed water volume measurement for various particle sizes are shown. These samples did not equilibrate in terms of imbibed volume. We estimate equilibrated imbibed volumes by curve fitting to the data.

Salinity results for the La Luna Formation are shown in Figure 3.37. Imbibed water volumes are shown in Figure 3.38. The larger particle sizes in these sample (LL(8)_{700 μ m} and LL(8)_{500 μ m}) produced equal equilibrated salinities.

Sample LL(15) produced higher salinity and, similar to the B(40) in the Bossier and all aliquots in the Haynesville Formation, there is not a simple correlation between equilibrated salinity and particle size, although equilibrated salinity increases as clay mineral content increases. Results suggest that LL(8) reaches equilibrium faster than LL(15). Evaluation of equilibration time data appears in a later section.

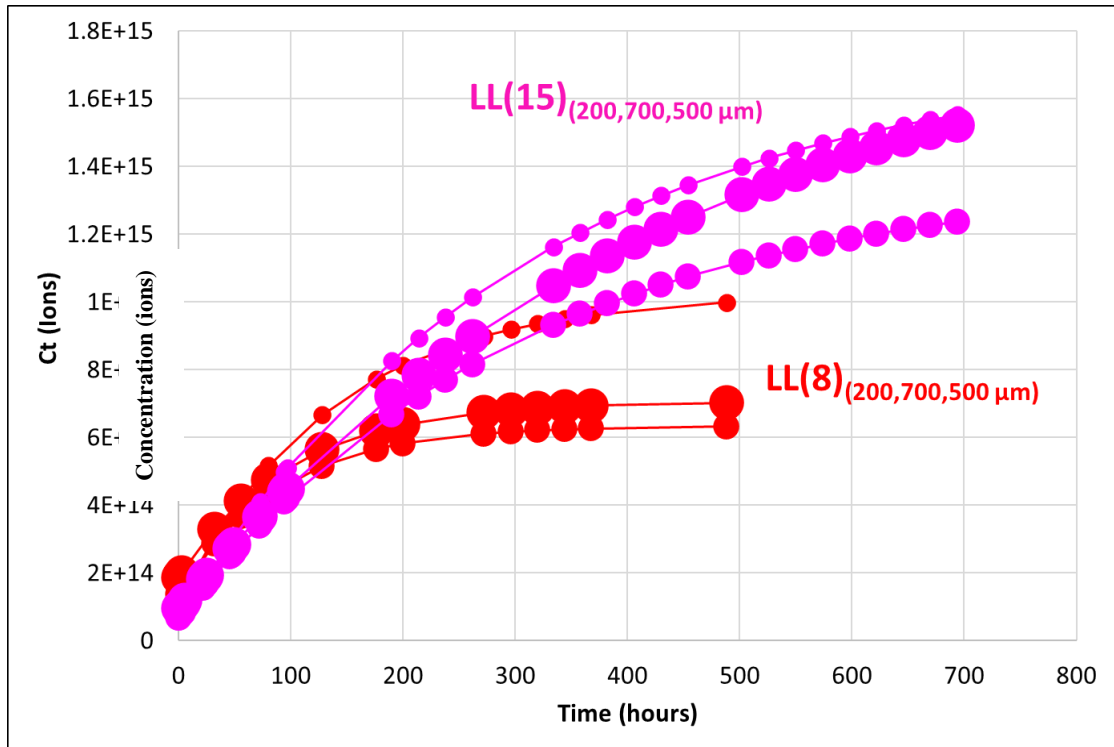


Figure 3.37. Spontaneous Water Imbibition Experiments in the La Luna Formation. Salinity measurement for the various particle sizes plotted against as a function of time. Each sample has three curves, corresponding to the three particle sizes. The 200 μm particle size produces the highest salinity. The 700 μm and 500 μm salinities are nearly equal.

The La Luna Formation samples imbibed the largest volumes of water in the tested formations. For LL(8) the imbibed water volumes are 7, 5.7 and 4 ccs for 200 μm , 500 μm , and 700 μm samples, respectively, and stabilization was not reached. For sample LL(15) the imbibed water volumes are 7, 6.6 and 5.5 ccs for the same particle sizes and it seems that equilibrium is nearly achieved. The 200 μm particle size in both samples imbibed the same volume of water although clay content varies. Sample LL(8) reaches equilibrium faster than sample LL(15), in contrast to observations in the Bossier Formation. LL(15) shows that imbibition equilibrated faster than conductivity. These observations are evaluated in a later section.

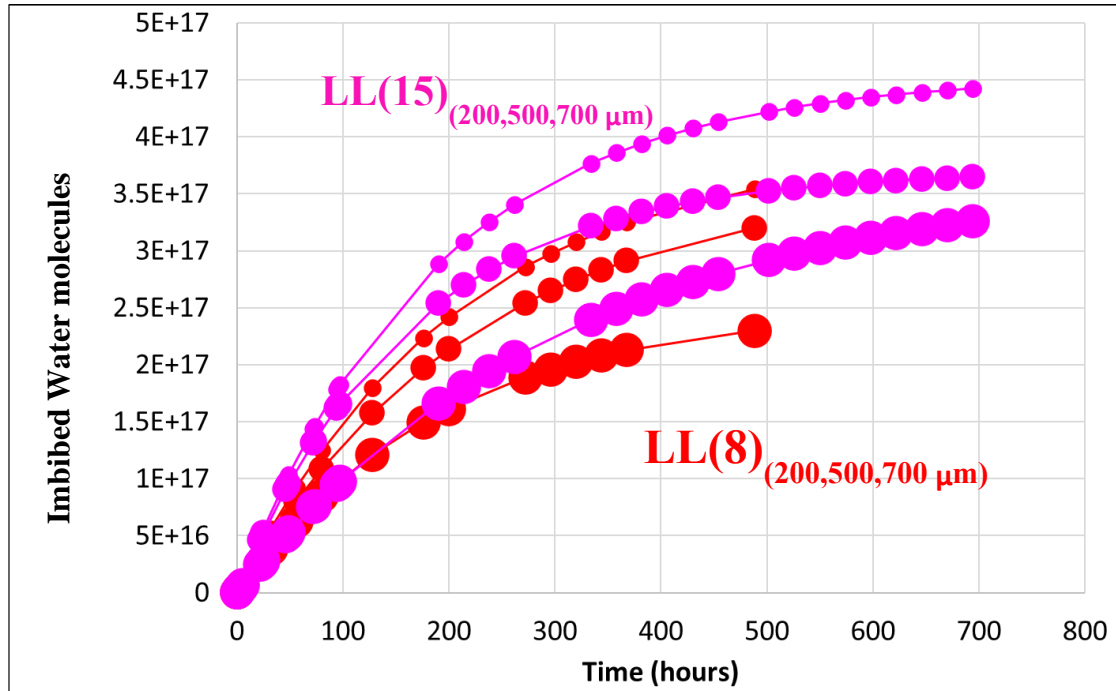


Figure 3.38. Spontaneous Water Imbibition Experiment results in the La Luna Formation. Imbibed water volume varies as a function of particle size. In sample LL15 the imbibed volume equilibrated before the conductivity.

3.6. Post - Water Imbibition Nuclear Magnetic Resonance Results

After the water imbibition experiments, and to evaluate the pore systems and imbibed water volumes, NMR data were again acquired for the samples.

In Figure 3.39, results for the Bossier Formation are presented. B(60), B(40), and B(15) post imbibition NMR measurements display two different pore systems. These peaks in the T₂ distribution suggest a slight increase in the volume of bound fluid, and a slight shift in the peak position with a T₂ at 0.6 msec on average. After imbibition there is a significant increase in the free water saturation. Sample B(60), (Figure 3.38a), shows a particle size difference in the T₂ position for the peak related to free water. B(60)_{200μm}, has this peak at 10 msec, whereas samples B(60)_{500μm}, and B(60)_{700μm} display the free water peak at 20 msec. A third peak is observed only

in the B(60)_{700μm} sample, with a mean T₂ at 200 msec. In terms of imbibed water volume, B(60)_{200μm}, B(60)_{500μm} and B(60)_{700μm} imbibed 3.93 cc, 3.80 and 3.51 ccs respectively.

Figure 3.38b, shows the results from sample B(40). B(40)_{200μm} displays two peaks. The peak associated with free water occurs at 70 msec. Samples B(40)_{500μm} and B(40)_{700μm} display very similar results, both comprising three peaks. One is associated with bound water at approximately 1 ms, a second peak at 20 msec, and a prominent third peak at 280 msec. In terms of imbibed water volume, B(40)_{200μm}, B(40)_{500μm} and B(40)_{700μm} imbibed 3.36 cc, 2.73 cc and 2.52 cc respectively. Imbibed volume decreases as particle size increases.

Figure 3.38c, shows the results from sample B(15). B(15)_{200μm} shows a T₂ distribution with a peak at 22 msec and a shoulder effect at lower relaxation time, suggesting that two peaks are probably present. This particle size imbibed the most water, 2.64 cc.

B(15)_{500μm} shows three peaks, one related to bound water at approximately 1 msec, a second peak at 14 msec, probably associated with free water, and a larger peak at 281 msec. This sample imbibed a similar volume of water to the B(15)_{200μm} sample. B(15)_{700μm} shows only two peaks. One associated with bound water and a second peak at 1 msec. A second peak, possibly associated with free water is observed at 141 msec. The presence of a shoulder effect is observed on the lower T₂ side of the free water peak, suggesting that two peaks are present. This sample imbibed the lowest volume of water, 2.03 cc.

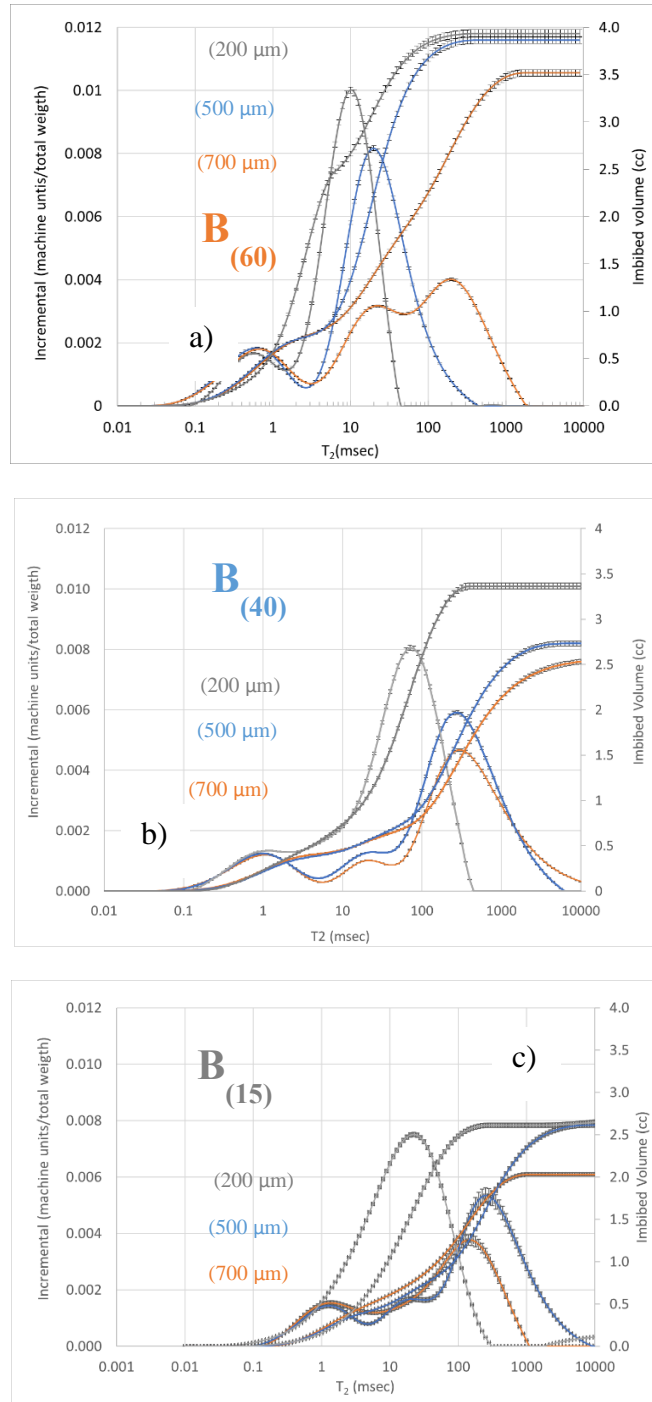


Figure 3.39 Post - water imbibition - Nuclear Magnetic Resonance and Imbibition Results. a) B(60), b) B(40) and c) B(15). Two pore systems, including bound water, can be observed in the smallest particle sizes. A third por systems, that is inferred to be associated with fractures generated in the sample preparation is also observed.

Table 3.2. Summary for T2 Peaks and imbibed volumes from the post NMR experiments in the Bossier Formation.

Sample	Size um	T2 Peaks			Volume cc
		usec	usec	usec	
B ₍₆₀₎	200	0.6	10		3.9
B ₍₆₀₎	500	0.6	20		3.8
B ₍₆₀₎	700	0.7	20	200	3.5
B ₍₄₀₎	200	1.0	71		3.4
B ₍₄₀₎	500	1.0	20	280	2.7
B ₍₄₀₎	700	1.0	20	280	2.5
B ₍₁₅₎	200	1.0	20		2.6
B ₍₁₅₎	500	1.0	14	280	2.6
B ₍₁₅₎	700	1.0	14	141	2.0

Figure 3.40, shows a 3D plot summarizing the clay content and imbibed volume as a function of particle size. In general, as clay mineral content decreases, the imbibed water volume decreases. As the particle size to which the sample was ground increases, so does the T₂ for the principal peak that is inferred to represent imbibed free fluid, although the total imbibed volume decreases. The size of the points on the plot is proportional to the imbibed volume, so, as particle size increases, the symbol size decreases.

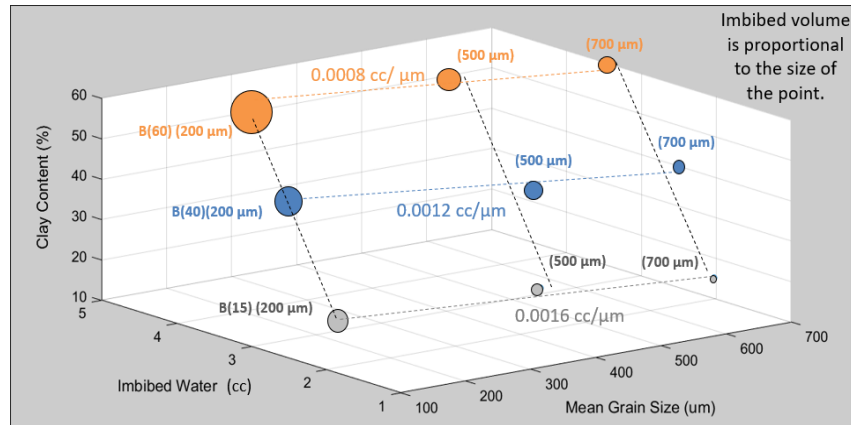


Figure 3.40 Post - water imbibition - Nuclear Magnetic Resonance Results Summary. Imbibed volumes from the NMR are consistent with the imbibed volume from the imbibition experiments. The point size is proportional to the imbibed volume, which increases with clay mineral content and with decreasing particle size.

The imbibed volumes from the spontaneous imbibition experiments are consistent with the NMR volumes. A cross plot of the values falls close to a 1:1 relationship for the Bossier Formation. Most of the values fall just above the 1:1 line indicating a slightly higher imbibed volume from NMR than from the imbibition experiment measurements (Figure 3.41). This may be due to errors in reading the imbibed volume from the calibrated glassware. One sample, B(60)_{200 μm}, imbibed more water during the imbibition experiment than suggested by the NMR data. These results will be the subject of further evaluation (See Figure No 3.41).

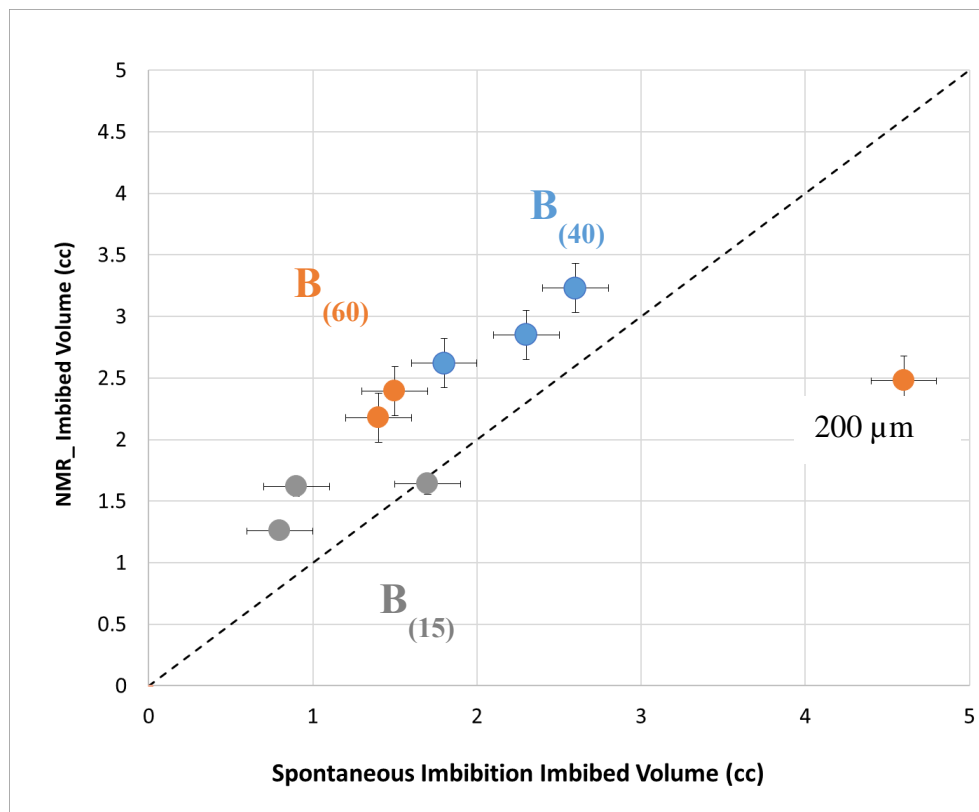


Figure 3.41. Post - water imbibition – NMR Vs Spontaneous Imbibition Imbibed Volume Measurement. Results lie close to the 1:1 line. One point showed unexpected imbibed volumes. B(60)_{200 μm} imbibed more water during the imbibition experiment than suggested by the NMR data. This will be evaluated in a later section.

Figure 3.42 shows the post imbibition NMR results for the two samples in the Haynesville Formation. Figure 3.42a shows the results for sample H(26). The T_2 spectrum for sample H(26)_{200 μm} shows two peaks, one related to bound water at approximately 1 msec, and a second one related to free fluids at 70 msec.

A shoulder on the left side of this peak suggests the presence of an additional peak. Sample H(26)_{200 μm} imbibed 5.22 cc of water, slightly more than the second Haynesville Formation sample. Samples H(26)_{500 μm} and H(26)_{700 μm} show similar results to one another in terms of T_2 distribution. Both display three peaks, one associated with bound water at approximately 1 msec, a second peak at 20 msec, and a third large peak at 280 msec. H(26)_{500 μm} imbibed 4.60 cc of water and H(26)_{700 μm} imbibed 3.89 cc.

Figure 3.42b shows the results for the three particle size aliquots for sample H(29). As expected, given their similar mineralogy, post imbibition T_2 spectra for H(29) are similar to those observed for H(26). H(29)_{200 μm} shows two peaks, one associated with bound water at approximately 1.4 msec and a second peak associated with free fluids at 35 msec. This sample imbibed 4.80 cc. Samples H(29)_{500 μm} and H(29)_{700 μm} show similar results in terms of T_2 distribution. Both display three peaks, one associated with bound water at 1.4 msec, a second peak at 20-25 msec, and a dominant peak at 200-250 msec. Sample H(29)_{500 μm} imbibed 4.42 cc and sample H(29)_{700 μm} imbibed 4.10 cc of water.

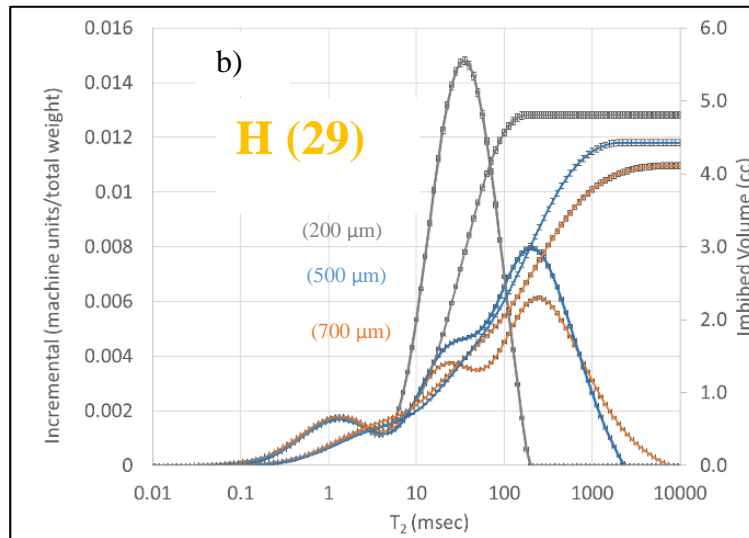
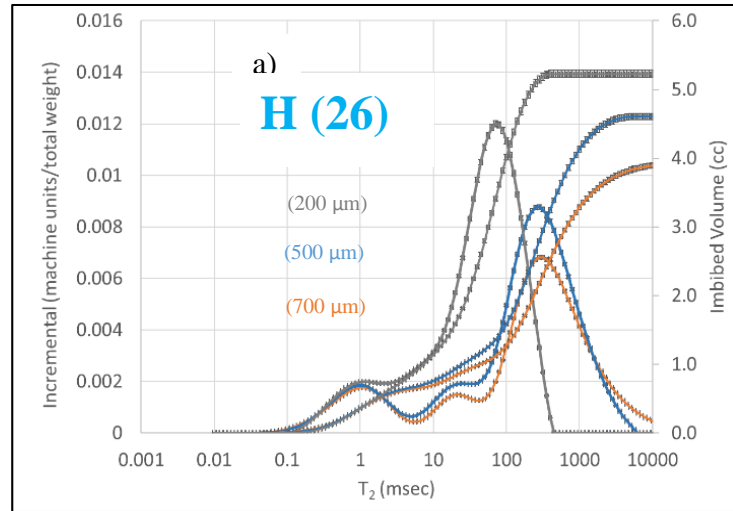


Figure 3.42 Post - water imbibition - Nuclear Magnetic Resonance Results. Haynesville Formation results from post-imbibition NMR are similar. The smallest particle size exhibits two pore systems and the largest exhibits three. Cumulative imbibed volumes are similar. This behavior was expected due to the similarity in clay mineral content for the two samples.

Table 3.3. Summary for T2 Peaks and imbibed volumes from the post NMR experiments in the Haynesville Formation.

Sample	Size um	T2 Peaks			Volume cc
		usec	usec	usec	
H ₍₂₆₎	200	1.0	71		5.2
H ₍₂₆₎	500	1.0	20	280	4.6
H ₍₂₆₎	700	1.0	20	280	3.9
H ₍₂₉₎	200	1.4	35		4.8
H ₍₂₉₎	500	1.4	25	200	4.4
H ₍₂₉₎	700	1.4	20	250	4.1

Figure 3.43 shows a summary diagram for the Haynesville Samples. Imbibed volume is proportional to the size of each point. The volume of water imbibed increases as particle size decreases. Results for H(26) and H(29) are similar. This was expected due to their similar clay mineral content.

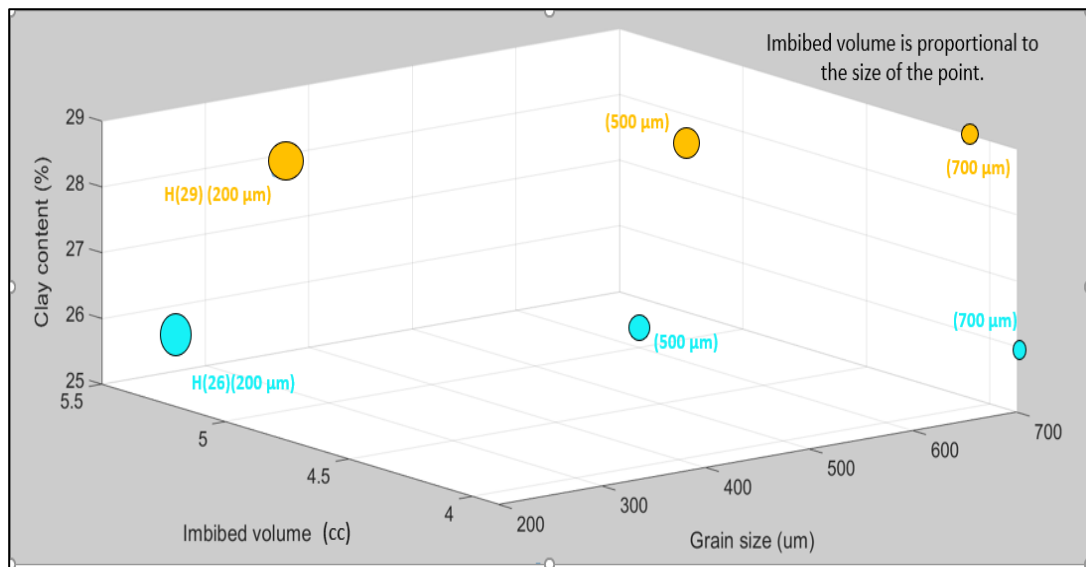


Figure 3.43 Post - water imbibition - Nuclear Magnetic Resonance Results Summary-Haynesville. Imbibed water volumes are similar between the two samples. Imbibed volume is proportional to the size of each point. The volume of water imbibed increases as particle size decreases. Results for H(26) and H(29) are within the error margin.

Figure 3.44 shows a comparison between the imbibed volume from the spontaneous imbibition experiments and the NMR volumes. NMR imbibed water volumes are consistent with the imbibed volume measured during the imbibition experiments; they are very close to the 1:1 line. The agreement between the two techniques is better than for the Bossier samples.

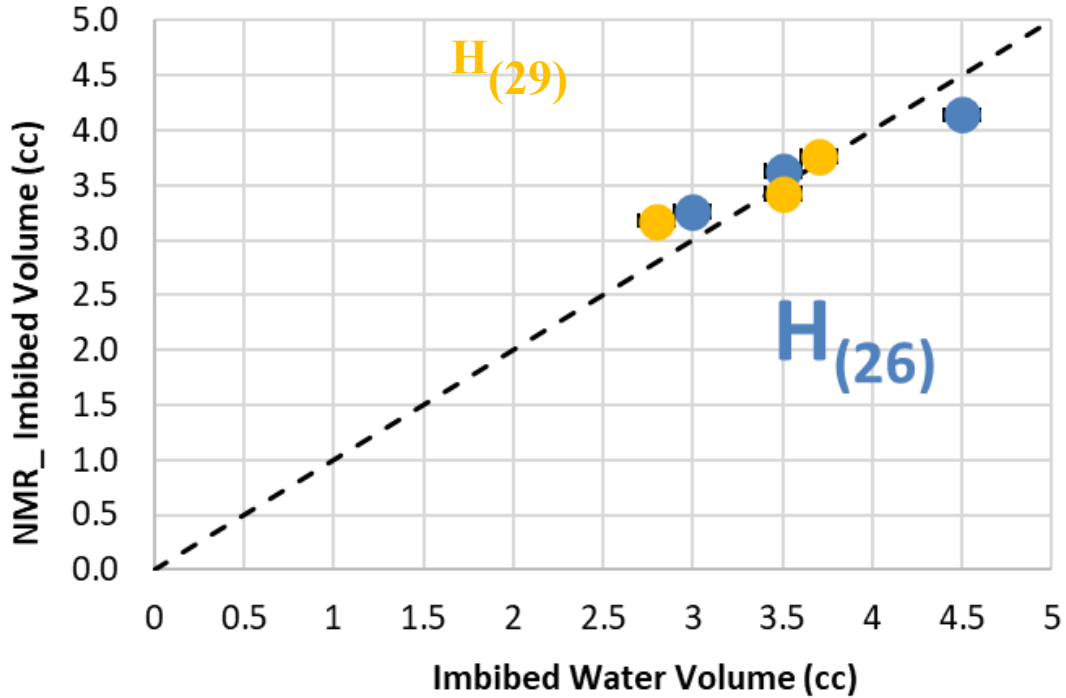
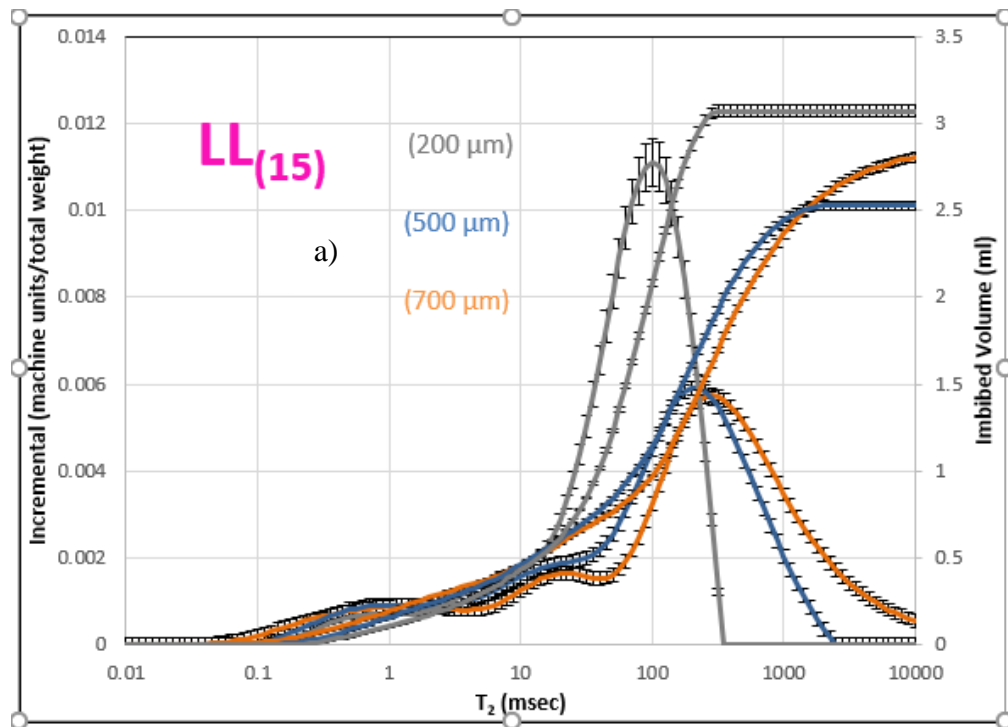


Figure 3.44 Post - water imbibition – NMR Vs Spontaneous Imbibition Imbibed Volume - Haynesville. Comparison between the measurements in terms of imbibed volume are consistent. Proximity to the 1:1 line illustrates the agreement between the two techniques.

La Luna Formation results are shown in Figure 3.45. For LL(15)_{200mm}, (Figure 3.45a), two peaks are observed, one associated with bound water at shorter T₂ (slightly less than 1 msec), and a second one at larger T₂ associated with free water, at 100 msec. This peak is significant in terms of cumulative volume. Sample LL(15)_{200μm} imbibed 3.1 cc of water. Samples LL(15)_{500μm} and LL(15)_{700μm} both display three peaks, one associated with bound water at 1 msec, a small second peak at approximately 20 msec (free water), a third peak with a T₂ time of 220 - 280 msec. This might be associated with fractures created during sample preparation.

For sample LL(8)_{200μm} (Figure 3.45b) two peaks are observed that correspond to bound water at approximately 1.5 msec and free water with a T₂ on the order of 20 msec. Samples LL(8)_{500μm} and LL(8)_{700μm} both display three peaks, one associated with bound water at 1 msec, a small second peak at approximately 20 msec (free water), and a third peak with a T₂ time of 250 and 310 msec respectively. This third peak may be associated with fractures created during sample preparation. The La Luna Formation is the only sample set for which the largest particle size is observed to imbibe the highest volume of water.



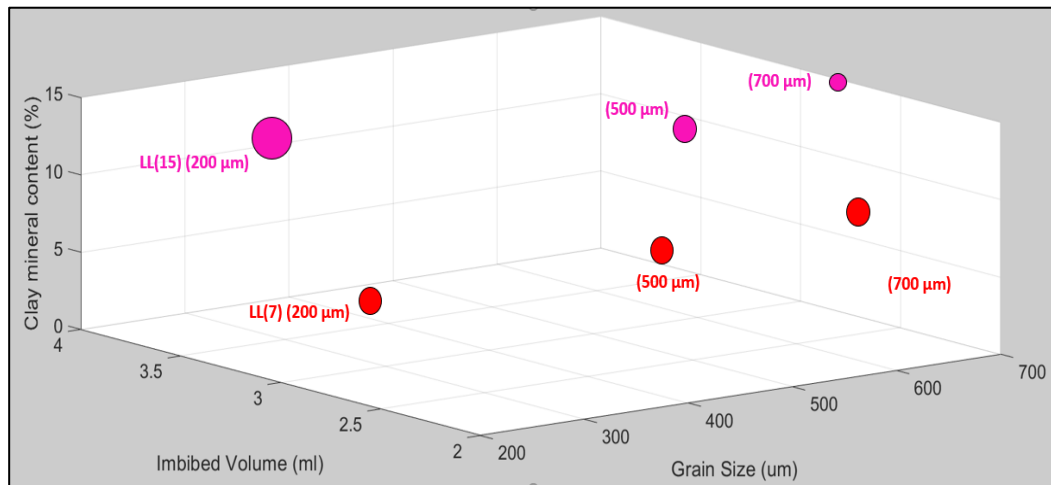


Figure 3.46 Post - water imbibition - Nuclear Magnetic Resonance Results Summary – La Luna Formation. Imbibed volume increases with clay mineral content in the La Luna Formation. Particle size trends in imbibed volume are not consistent.

Comparing the two techniques, NMR and imbibition experiments, the La Luna Formation samples are unique. The NMR imbibed water is less than the spontaneous imbibition experiment imbibed water volume. For sample LL(8), all the particle sizes imbibe the same amount of water based on the NMR results; in contrast, the volumes are different based on the imbibition results; by 2 cc for samples LL(8)_{700µm} and LL(8)_{500µm}, and by 1.5 cc of water for samples LL(8)_{500µm} and LL(8)_{200µm} in the spontaneous imbibition experiments (See figure 3.47).

Based on the NMR data, La Luna Formation corresponds to the lowest imbibed water samples. However, they were the samples that imbibed the most in the spontaneous imbibition experiment. Because the samples remained in the lab for an extended period of time between the end of the imbibition experiment and the NMR measurement due to Covid related shutdowns, some evaporation may have occurred prior to collecting the NMR data.

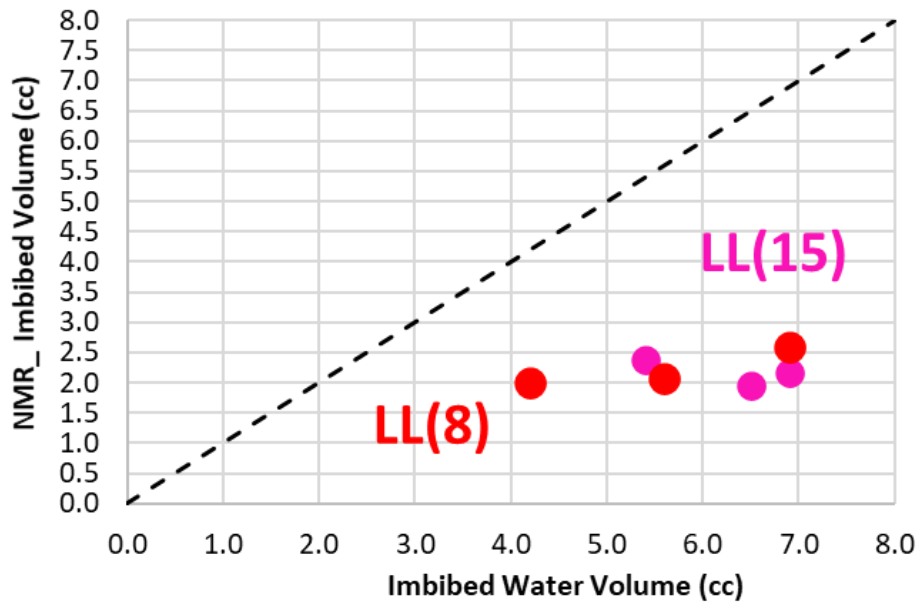


Figure 3.47 Post - water imbibition – NMR Vs Spontaneous Imbibition Imbibed Volume – La Luna Formation. The Y axis represents the imbibed water volume measured by the NMR and the X axis is the imbibed volume from the imbibition experiments. Only in the La Luna Formation do NMR results show less water than the imbibition experiment results. Because of the very low clay content and Covid related lab shutdowns that delayed NMR measurement relative to the imbibition studies the samples may have partially dried prior to the NMR measurement.

3.7 Oil imbibition Experiment Results

A second set of sample aliquots was used for the oil imbibition experiments. The oil imbibition volumes are presented in Figure 3.48. Each point represents the equilibrated volume at the end of the experiment for various particle sizes and clay mineral content samples. B(60)_{200μm}, B(60)_{500μm} and B(60)_{700μm} imbibed 0.9 cc, 0.7 cc, 0.5 cc respectively. B(15)_{200μm}, B(15)_{500μm} and B(15)_{700μm} imbibed 0.4 cc, 0.3 cc, and 0.3 cc respectively. Error bars are associated with the volume readings using the graduated flask and are equal to 0.05 cc. A particle size effect can be observed in sample B(60) but is not observed in sample B(15). This may be related to differences in total organic carbon content (TOC). Sample B(60) has a

reported TOC of 2.43 wt % whereas sample B(15) has a reported TOC of 1.51 wt %. Because we do not know how representative the sampling was for the reported TOC values was (data were provided by a third party), we will make independent estimates of TOC using image analysis on each sample aliquot.

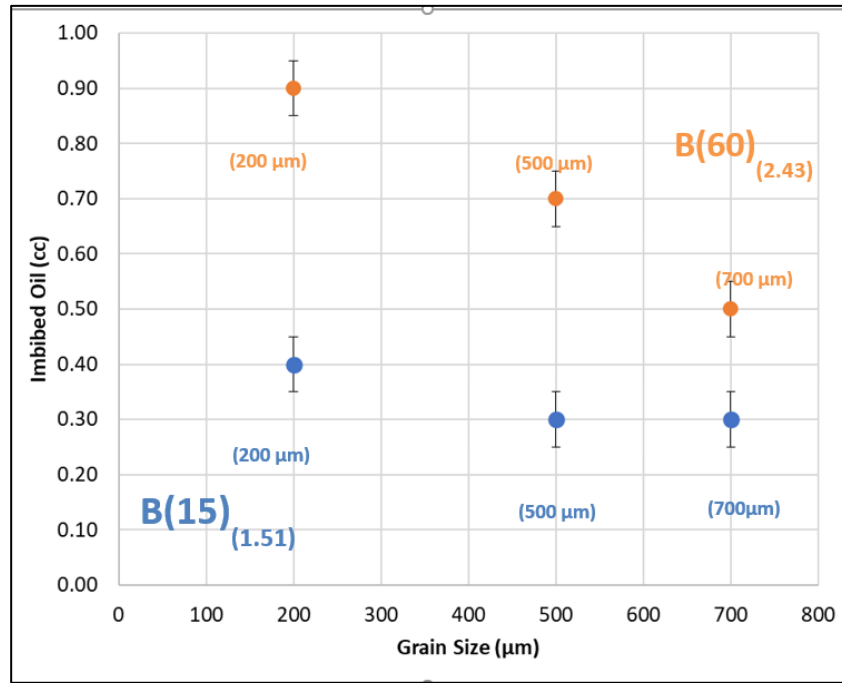


Figure 3.48 B(60) and B(15) Post - oil imbibition volume results for the Bossier Formation samples. B(60) imbibed more oil than B(15) and a particle size effect is present in both samples, being more strongly developed in B(60). As organic matter increases, so does the imbibed oil volume. B(40) was not acquired because sample amount limitation.

Imbibed oil volumes for the Haynesville Formation samples are shown in Figure 3.49. Samples H(29)_{200µm}, and H(29)_{700µm} imbibed 1.1 cc, 0.9 cc, respectively. In contrast, samples H(26)_{200µm}, H(26)_{500µm}, and H(26)_{700µm} all imbibed equal amounts of oil, 0.3 cc. The criteria used for the error bars are as described for Figure 3.48. A particle size effect is observed in sample H(29) but is not present in sample H(26). Both samples have relatively high TOC content. Sample H(26) has a reported TOC of 4.44 wt % and sample H(29) has a reported TOC of 3.8 wt %). These values will be validated using the results of image analysis for the individual

aliquots. Sample H(29)_{200μm} imbibed the largest volume of oil among all the tested samples.

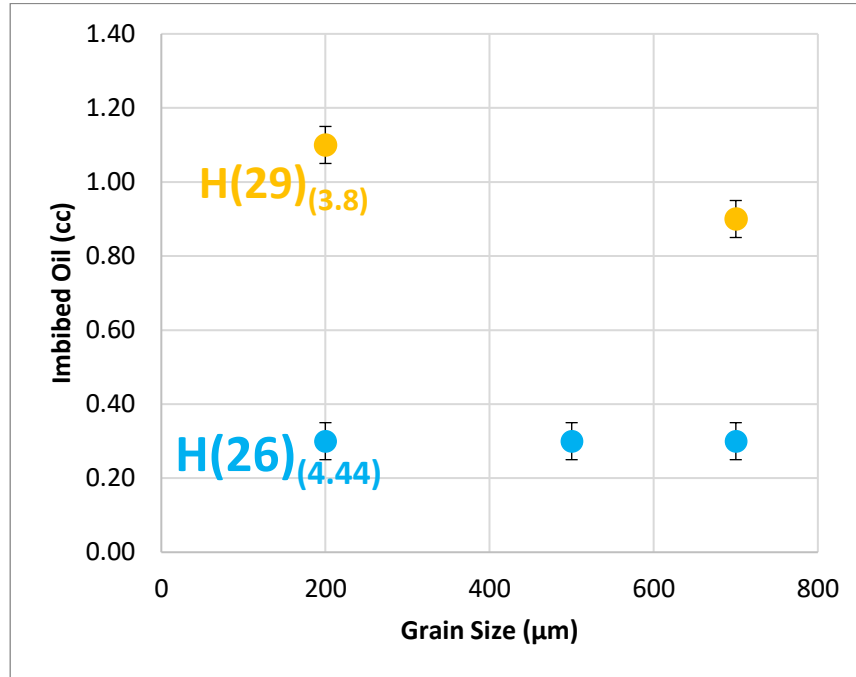


Figure 3.49 Post - oil imbibition Volume Results for samples of the Haynesville Formation. A particle size effect can be observed in H(29) but is not present in sample H(26). There is no correlation between imbibed volume and reported TOC. These values will be validated using image analysis results on the individual sample aliquots.

Oil imbibition volumes for the La Luna Formation samples are shown in Figure 3.50.

A particle size effect is observed for both samples. Samples LL(15)_{200μm}, LL(15)_{500μm} and LL(15)_{700μm} imbibed 0.4 cc, 0.3 cc, 0.15 cc respectively. Error bars are equal to 0.05 cc. Samples LL(8)_{200μm}, and LL(8)_{700μm} imbibed 0.3 and 0.1 cc respectively.

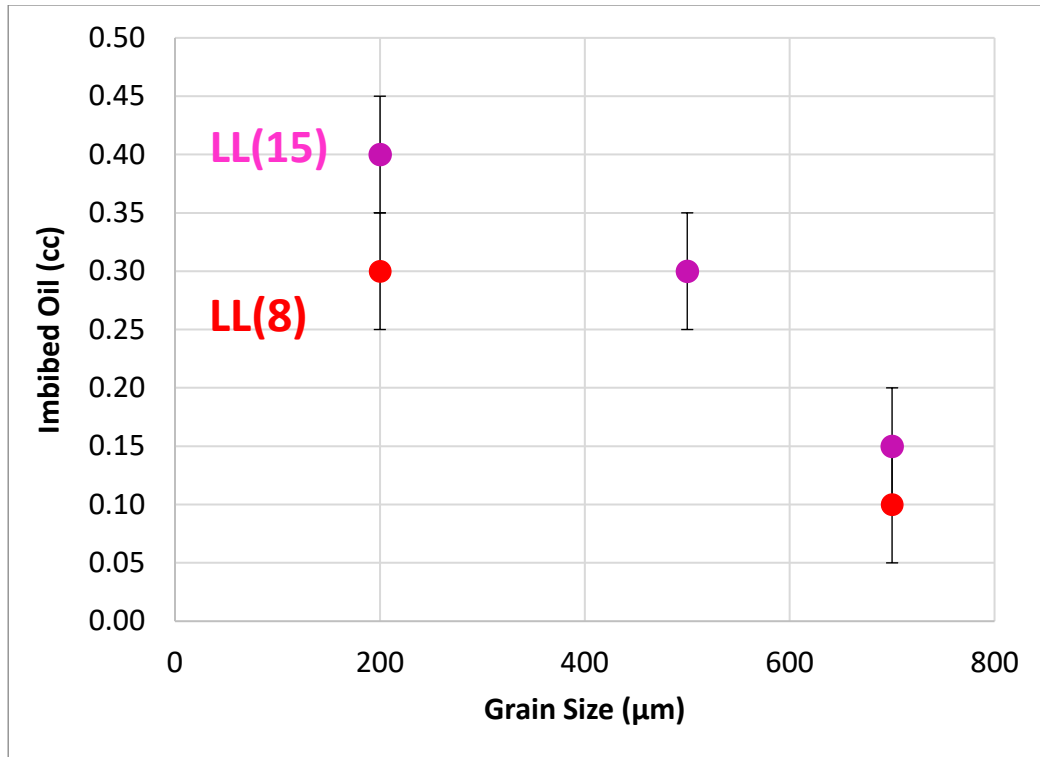
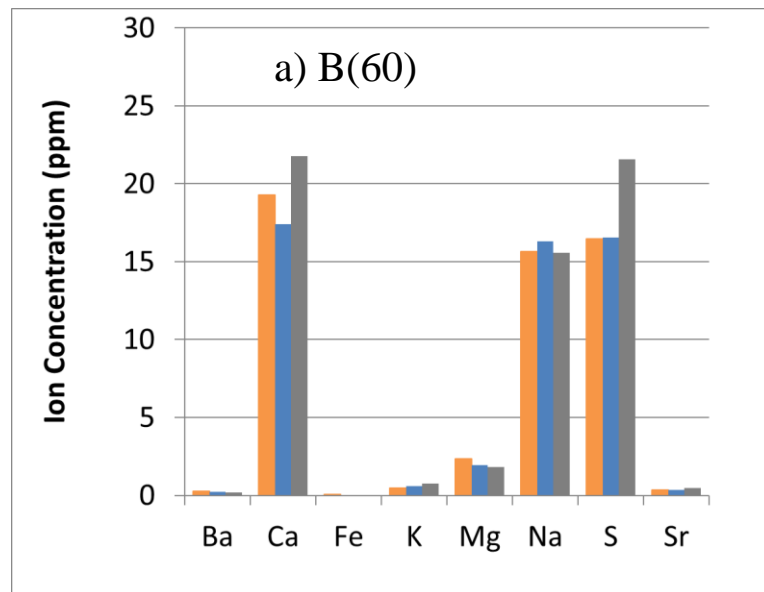


Figure 3.50 Post - oil imbibition volume results for La Luna Formation samples. A particle size dependency is observed in both samples. These sample oil imbibition volumes are lower than expected. Further analysis of these results will be discussed in a later section.

3.8 Inductively Coupled Plasma Results (ICP)

ICP data were acquired on a diluted aliquot of the supernatant fluid from the end of each water imbibition experiment. The ions evaluated were Ba^{+2} , Ca^{+2} , Fe^{3+} , Fe^{2+} , K^{+1} , Mg^{+2} , Na^{+1} , S^{+6} and Sr^{+2} . Summation of total ionic concentrations, assuming charge balance by chloride ions, and inversion for equivalent NaCl salinity shows that these results are in good agreement with the estimate of NaCl equivalent salinity from the conductivity measurements made during the imbibition experiments. This also validates the method used to convert conductivity to an equivalent salinity with the Bateman and Konne (1997) equation. High concentrations of calcium and sulfur ions are inferred to result from dissolution of anhydrite. This is in good agreement with the correlation observed in the XRF data for these elements,

particularly for samples B(60), B(15), H(26) and LL(8). The samples that show the lowest salinities in the imbibition experiments, B(15) and LL(8), are the samples with the lowest supernatant concentration of Ca^{+2} . In Figure 3.51 a-c, the results for the Bossier Formation samples are shown, with B(60), B(40) and B(15) indicated by orange, blue and gray bars respectively. The concentrations presented in the plots are measured on diluted samples and do not indicate in situ salinity values. In Figures 3.52 and 3.53, results for Haynesville and the La Luna Formations are presented. Colors represent each particle size, decreasing from left to right. Calcium and Sulfur ions are more abundant in the supernatant fluids associated with the smallest particle size. This observation applied to all the samples in the three different formations. We believe this is an artificial effect, created by crushing the samples and that a correction must be applied.



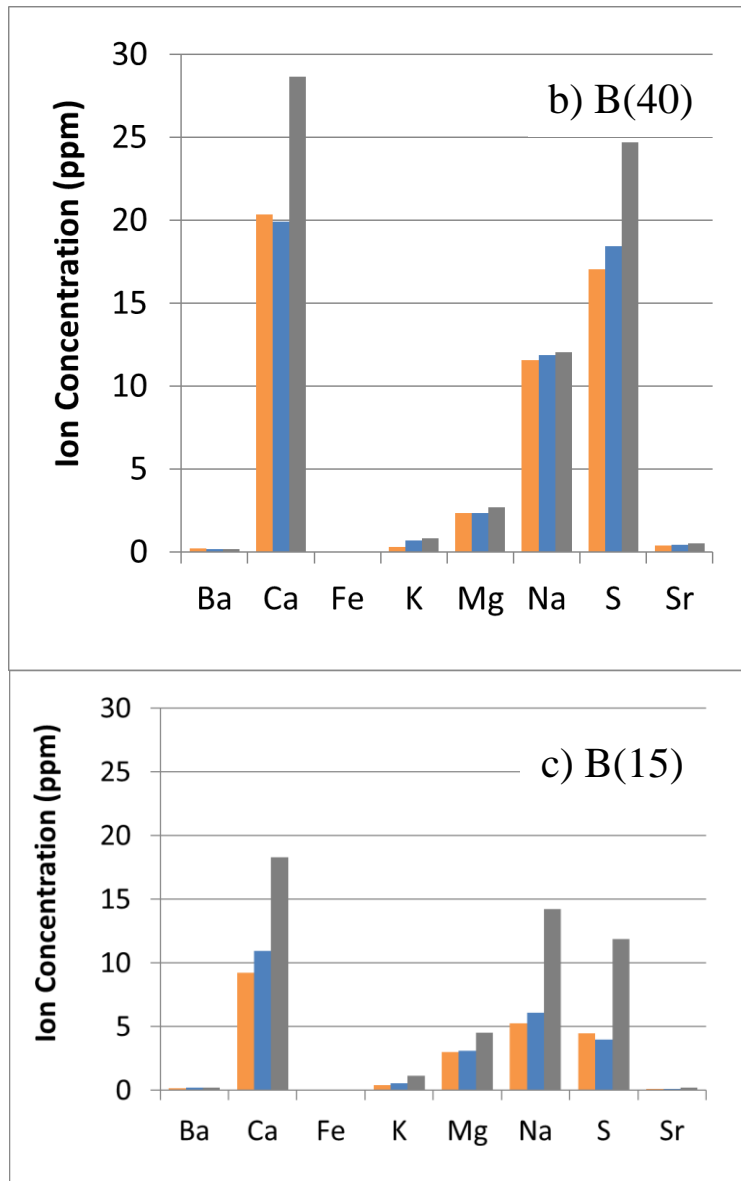


Figure 3.51 Supernatant fluid ionic composition for samples a) B(60), b) B(40) and c) B(15). Based on the data, the number of ions in solution is proportional to the clay mineral content. Ca^{+2} , Na^{+1} , and S^{+6} , are the most abundant ions in the supernatant fluid. Orange colors represent the 700 μm , blue 500 μm and gray 200 μm particle sizes respectively.

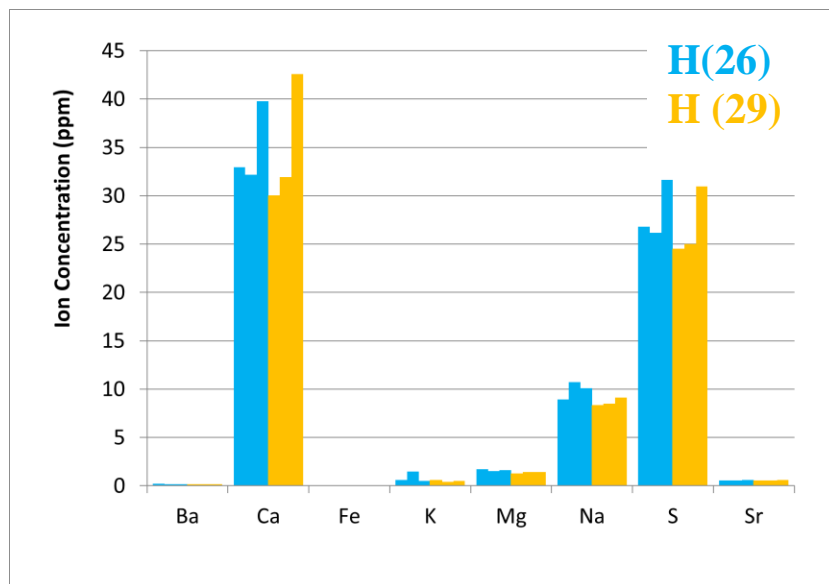


Figure 3.52 Supernatant fluid ionic composition for a) H(26), and b) H(29). As expected, the number of ions released from these samples is similar. Ca^{+2} , Na^{+1} , and S^{+6} , are the most abundant cations in the supernatant fluid. Particle size increases from left to right for all the samples.

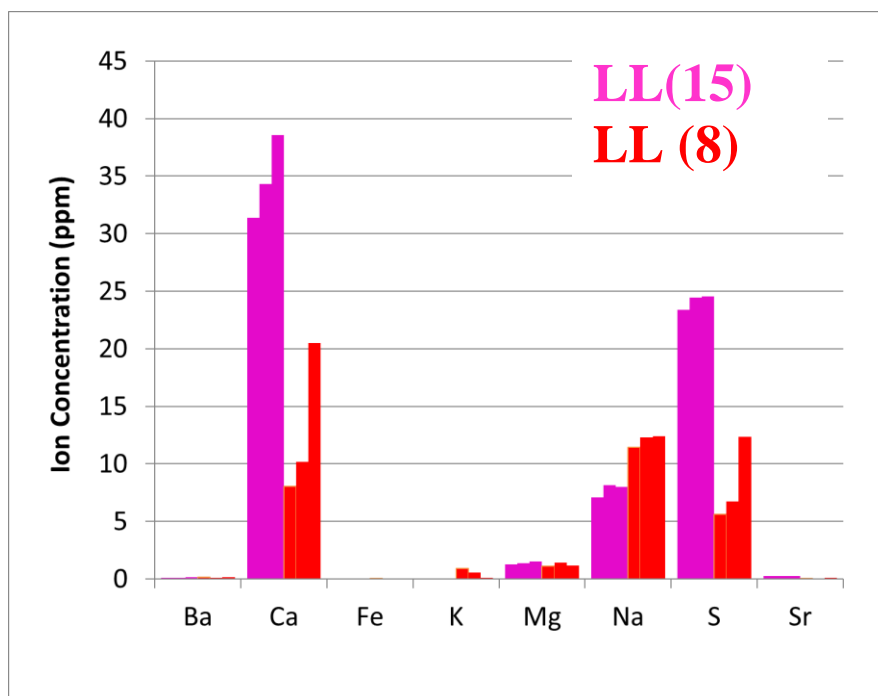


Figure 3.53 Supernatant fluid ionic compositions for a) LL(15), and b) LL(8). The number of detected ions is proportional to the clay mineral content and is in good agreement with the salinity results estimated from conductivity. Ca^{+2} , Na^{+1} , and S^{+6} , are the most abundant ions in the supernatant fluid. Particle size increases from left to right for each of the samples.

3.9 Imaging and Image Analysis

3.9.1 Transmitted Light Microscopy and Scanning Electron Microscopy

Thin sections were made using subsamples of the material of each particle size in order to characterize the samples used in the imbibition experiments. Figure 3.54, illustrates a single field of view from thin section scans of the coarsest and finest material, from sample B(15). The images were segmented for the clay plus organic matter phase (dark in plane light) to estimate the volume of clay material present in each sample size. Samples corresponds to the 750 – 500 μm and 212 -106 μm particle sizes. The area of clay plus organic matter (shown in light blue; proportional to volume), for porosity (darker blue), and for dolomite content. The area percent of phases corrected for the area of interparticle space in each image was calculated.

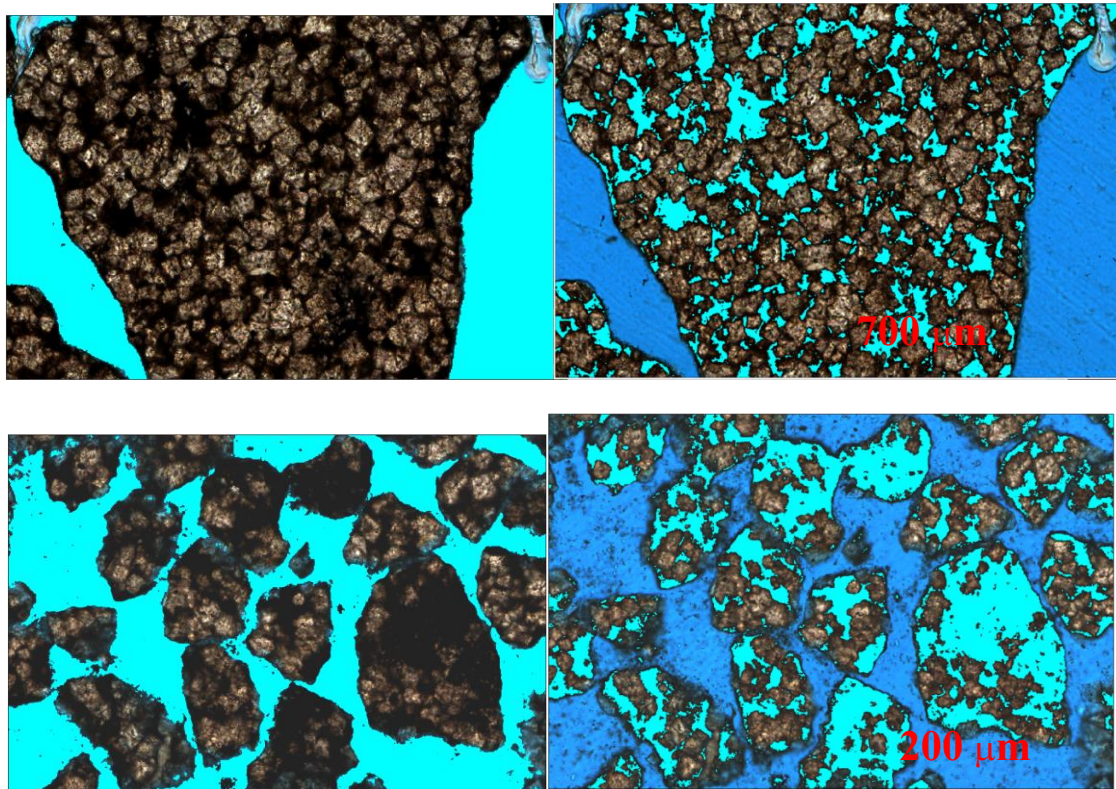


Figure 3.54 Bossier Sample B(15) thin section image analysis for the coarsest and the finest material. For both samples, the original (left) and the segmented images (right) are shown. Both fields of view are 677 microns wide by 448 microns high.

Light blue regions in the segmented images (right side) indicate the area in each image that is interpreted to comprise clay minerals (including clay sized quartz, feldspar, and pyrite) and organic material.

SEM images were acquired and analyzed using an in house interpretation software (QPI – Quantitative Petrographic Interpretation). Figure 3.55 shows an original image (a) for sample H(26) and the interpretation (b) by segmenting the components using different colors. Quartz, calcite/dolomite, pyrite, clay minerals, and porosity plus organic material were identified. For the same image a separate segmentation was performed for porosity only and organic matter associated pores and mineral associated pores identified. All images were analyzed and two groups of principal components were identified. The first group of components will have only a minor impact on conductivity and imbibition (quartz, calcite/dolomite). The second group of mineral components (clay minerals and anhydrite) will significantly influence both processes. Figure 3.55 (b) shows in gray the clay minerals and in light blue the total organic material plus porosity, respectively. Figure 3.55 (c) is an image from sample B(60) illustrating anhydrite present between the clay platelets.

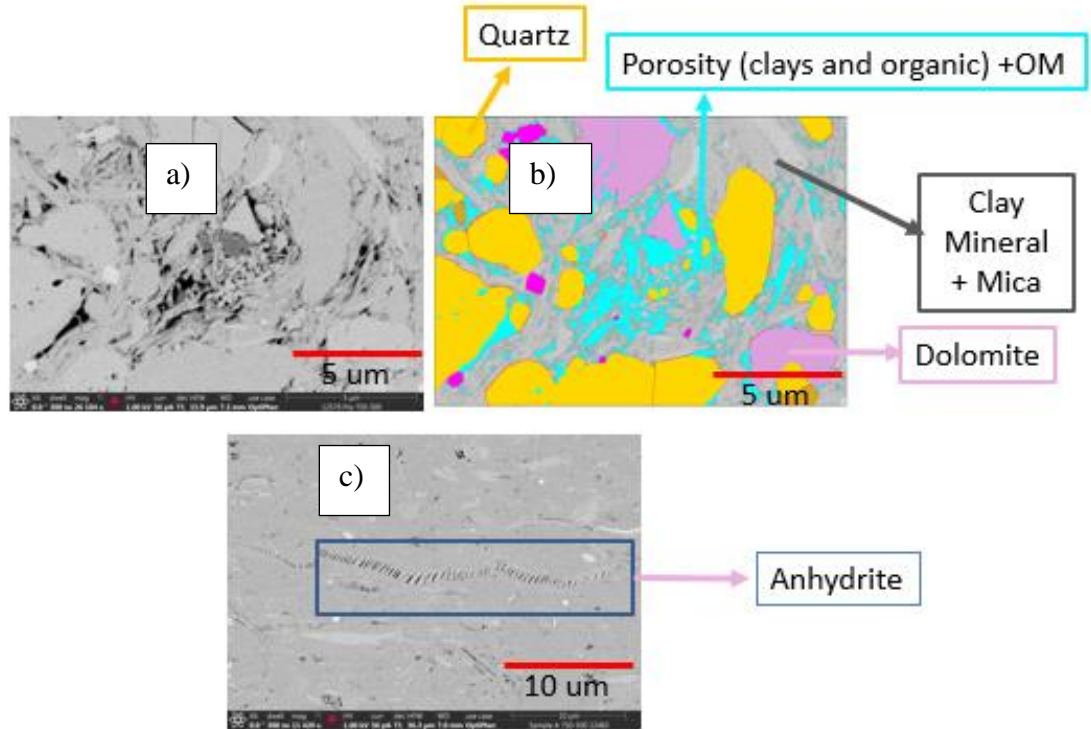


Figure 3.55 Imaging and image analysis were performed to help to develop the conceptual model. The original image is shown in a) and b) shows the different components of that original image, segmented by relative gray levels . Yellow represents quartz, purple represents dolomite, pink is pyrite, light blue is organic material plus porosity and the remaining area in gray comprises clay minerals and micas. In c) an example of the typical distribution of anhydrite is shown.

CHAPTER 4. MODELING AND DISCUSSION

On the basis of imagining, image analysis and experimental observations, a conceptual model was defined. Our observations establish that each particle can be described as being composed of two groups of components : 1) those components that do not significantly impact either the conductivity or imbibition processes, such as calcite (CC) /dolomite/quartz and 2) components that contribute to both processes.

Both ion expulsion and imbibition are controlled by this second group of components which includes:

- Clay minerals, where most of the surface area is present
- Mineral salts, in this case anhydrite (A) and,
- Total Porosity (inorganic, or mineral hosted, and organic matter hosted)

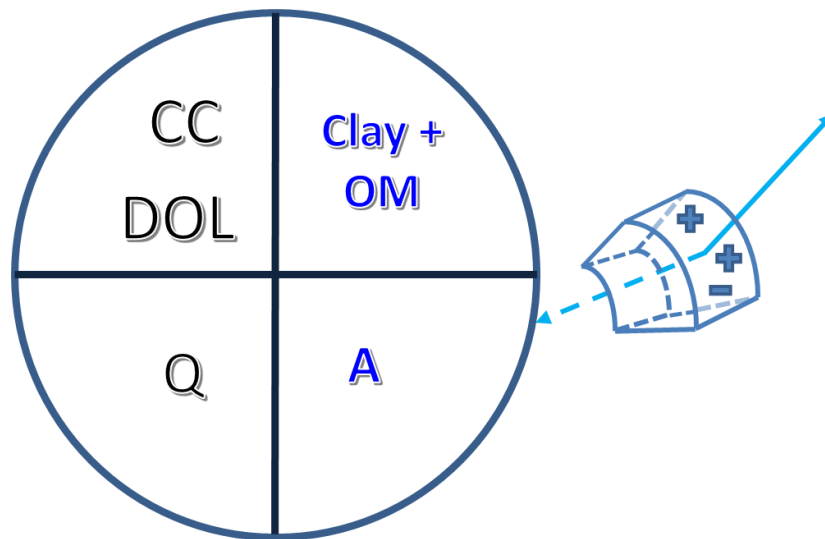


Figure 4.1 Conceptual model of an unconventional reservoir: One group of components comprising CC- Calcite , DOL-Dolomite and Q - Quartz, and a second group comprising clay minerals, anhydrite, and organic components. The second group directly contributes ions to the supernatant fluid and is responsible for the increasing conductivity with time, and provides the pathways for fluid imbibition.

4.1 Clay mineral content and salt dissolution

Experimental results suggest that clay mineral content and salt dissolution strongly influence the results of the spontaneous imbibition/conductivity experiments. Therefore, it is important to evaluate whether there is any relationship between the two mechanisms. Figure 4.2 illustrates the total Ca^{+2} and SO_4^{-2} ions in the supernatant fluid based on ICP results plotted against clay mineral content from XRD data for the three different formations. There is no observed correlation between clay content and the volume of dissolved anhydrite. This suggests that the occurrence of these phases are independent of each other (ie. Anhydrite is not preferentially associated with clay mineral associated porosity). Thus, the model developed using the experimental results treats these two components separately.

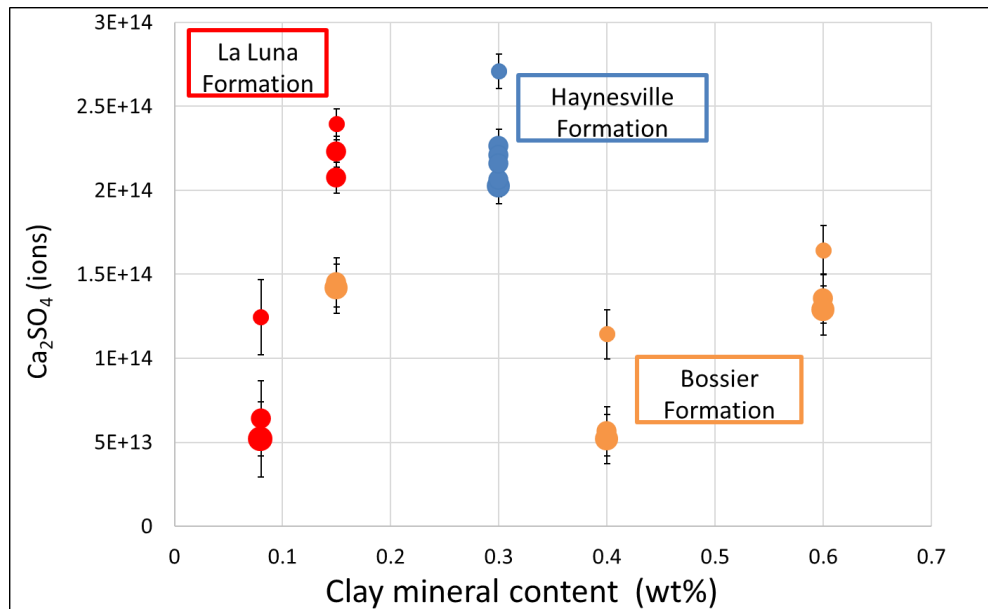


Figure 4.2 Anhydrite Vs Clay Mineral Content. For all of the formations studied, there is not a strong correlation between clay mineral content and anhydrite content.

4.2. The influence of particle size

The initial examination of the experimental data showed a relationship between the particle size to which the samples were ground and the supernatant conductivity and imbibed volume as a function of time. However, CEC and XRD measurements did not vary as a function of particle size. The cause of this apparent disagreement among the techniques became apparent when the supernatant fluid chemistry was analyzed. The contribution of Ca^{+2} and SO_4^{-2} ions present in the supernatant fluid was observed to increase as particle size decreased. Figure 4.3, shows those results, which are consistent for all of the samples. Because anhydrite cleaves and has a hardness of only 3.5 on the Mohs hardness scale, it is inferred to break more easily during sample preparation (crushing) and become concentrated in finer sieve fractions. For this reason, a correction for anhydrite was applied to the conductivity data. Figure 4.4 shows the results of anhydrite corrected supernatant conductivity, and the particle size dependence is no longer observed. This agrees with the CEC and XRD results.

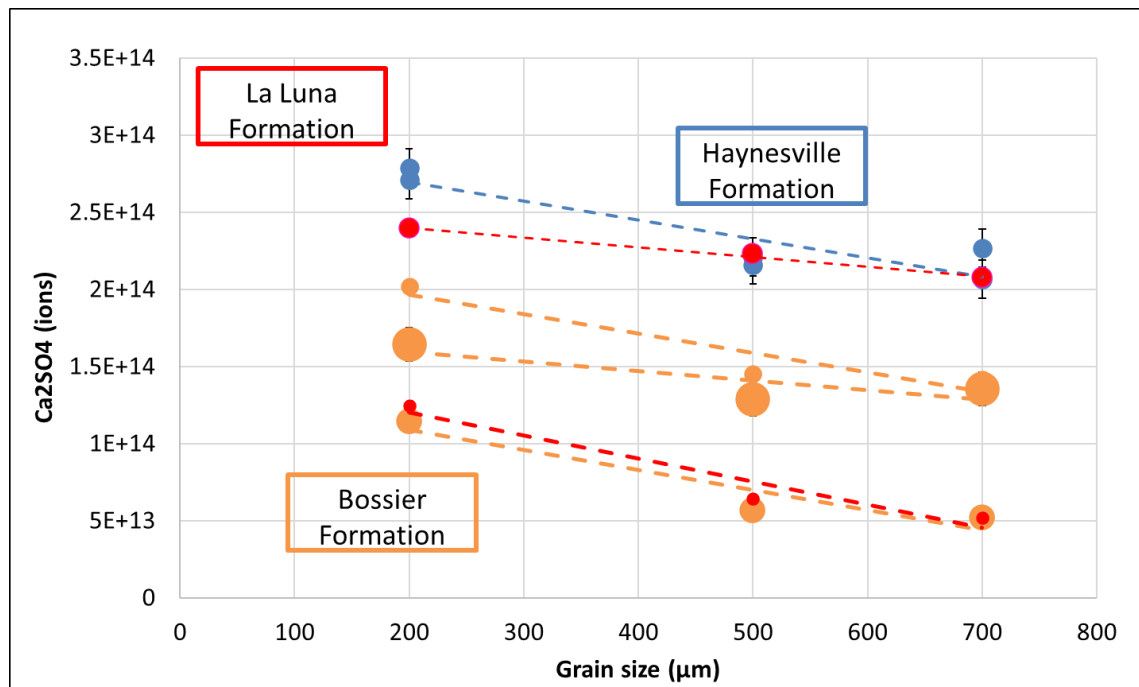


Figure 4.3 Anhydrite present in supernatant fluids is observed to be a function of particle size in all the tested formations. See text for discussion.

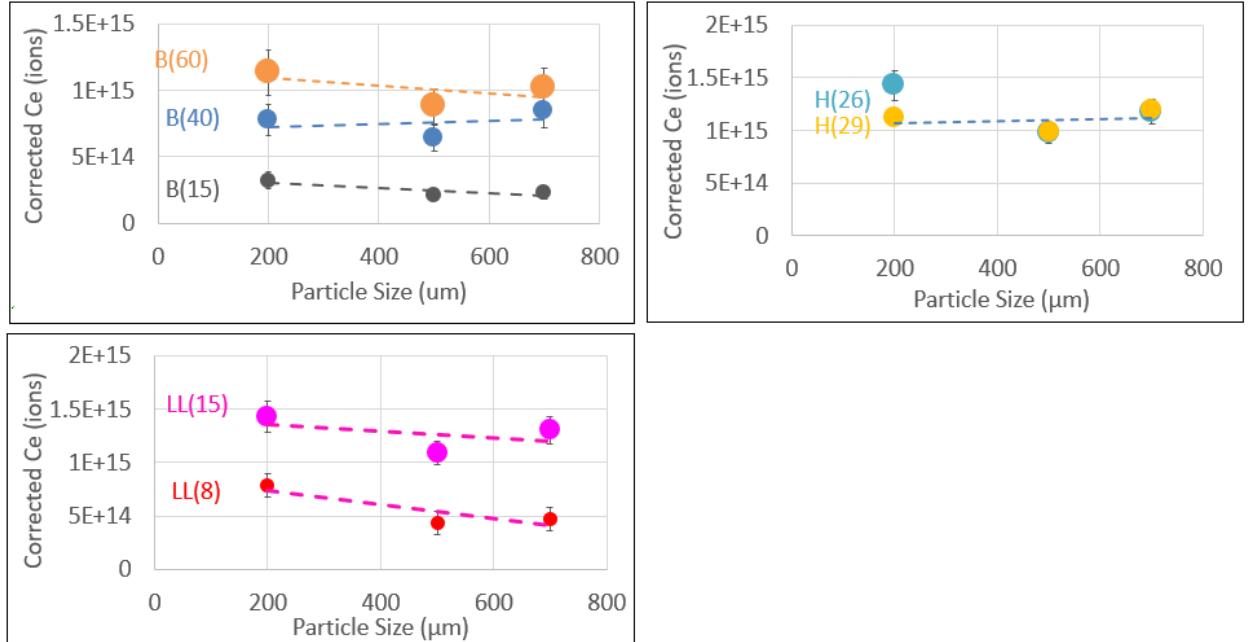


Figure 4.4 Anhydrite correction to the supernatant conductivity. After applying the anhydrite correction to the supernatant conductivity, only a weak relationship or no relationship between particle size and equilibrated conductivity is observed. B is for Bossier and the number in parentheses is the clay mineral content (wt%).

The distribution of the anhydrite remaining within the samples will also impact the conductivity and imbibition processes as a function of the relative exposure of the anhydrite to the DI water (supernatant fluid). Figure 4.5 shows the two typical distribution types for the anhydrite (indicated by blue boxes in the images) that were observed in the samples. Anhydrite is observed precipitated in between clay platelets, figure 4.5 (a), particularly in the Bossier Formation. It is also observed filling larger fractures, figure 4.5 (b), which is more common in the La Luna Formation. The Haynesville Formation exhibits both of these distributions in similar proportions.

When exposed to the DI water used for our experiments, we expect that any precipitated salts present in the samples will be subject to dissolution. Numerous researchers have carried

out experimental and numerical investigations into the factors affecting the dissolution process, including: the effects of temperature, pressure, mineral solubility, salinity of solvent, the area exposed to fluid flow, flow velocity, and purity of the sample. Gypsum, anhydrite and halite are common soluble minerals widely found at varying depths within global reservoirs. When anhydrite is in contact with pore water, it begins to dissolve, releasing calcium and sulphate ions. Once the equilibrium concentration of gypsum is reached, the latter starts to precipitate (Serafeimidis, 2018). The kinetics of gypsum dissolution are found to be transport-controlled, whereas the rate of dissolution of anhydrite is controlled by both chemical and transport processes (Barton and Wilde, 1971). The dissolution rate for anhydrite is much slower than that for gypsum (Klimchouk, 2000). This is consistent with the long times required for imbibition experiments in samples containing anhydrite. This observation, along with the Ca/S ratio of the calcium sulfate phase obtained from electron microprobe analysis, both suggest that the precipitated phase in the samples is anhydrite (precipitated in the subsurface) and not gypsum (precipitated at the surface after core acquisition). Anhydrite dissolution not only expels ions to the supernatant fluid, it also creates new pore space that must be accounted for in the imbibed fluid volumes.

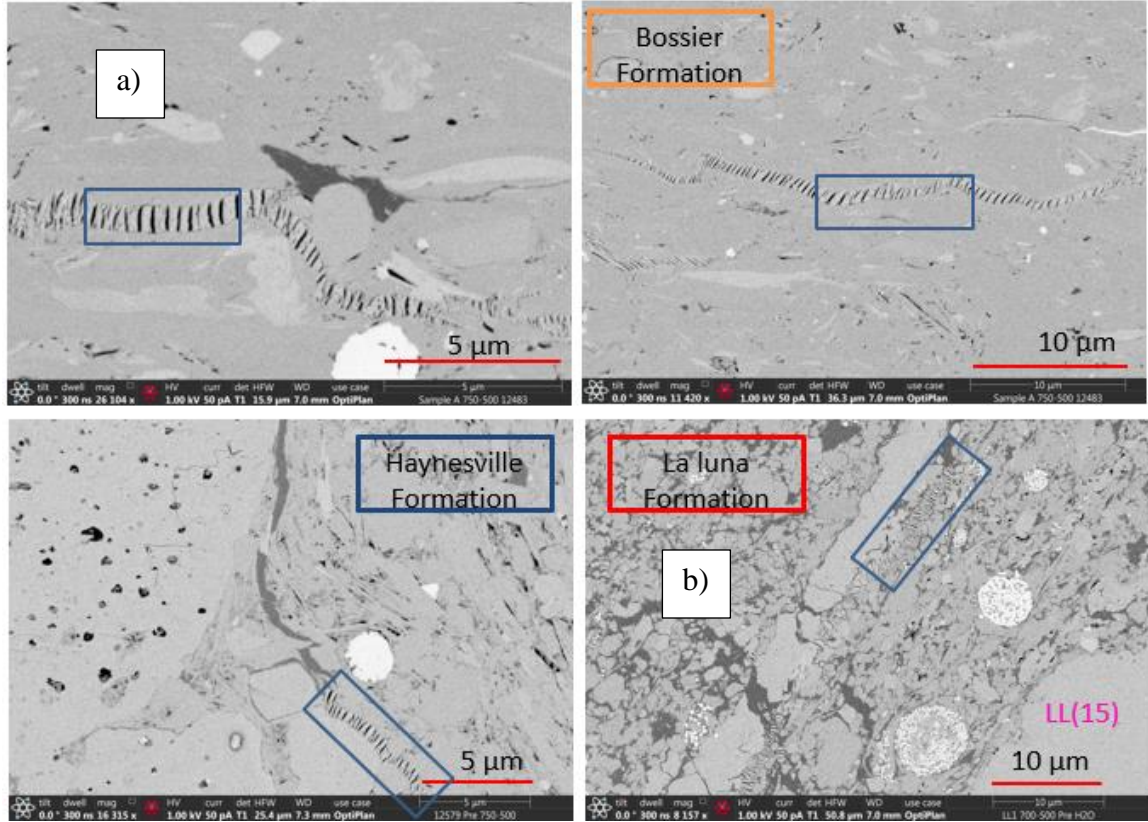


Figure 4.5 Anhydrite is observed precipitated between clay platelets, (a), more common in the Bossier Formation or filling larger fractures, (b), more observed in the La Luna Formation. Haynesville Formation shows both distribution types.

4.3 Modelling Equations

After the conceptual model was defined, spontaneous imbibition experiment data were fitted using regression techniques. The resulting equations are shown in equations 5 and 6,

$$Ct = Ce * (1 - \exp^{(-\frac{t}{t_c^c})}) \quad \text{Eq. 5}$$

and
$$Vt = Ve * (1 - \exp^{(-\frac{t}{t_c^i})}) \quad \text{Eq. 6}$$

where, Ct is the fluid equivalent ionic concentrations calculated from conductivity, Vt is the imbibed fluid volume, t is the experiment duration time required to reach Ct , t_c^c is the

characteristic time that is needed for the concentration to reach equilibrium, C_e is the equilibrated fluid concentration, V_e is the equilibrated imbibed fluid volume at the end of the experiment and t_c^i is characteristic time for the imbibition process to reach equilibrium.

In Figure 4.6, an example of the data for one of the samples is presented, where both, total concentration (C_t) and total volume are plotted as a function of time. The points represent the experimental data and the lines represent the best fit line to the data. Concentration is represented by points and error bars in gray. Blue points and error bars correspond to the imbibition data. The V_e scale was selected such that both equilibrated values merge together, being in equilibrium from that point forward.

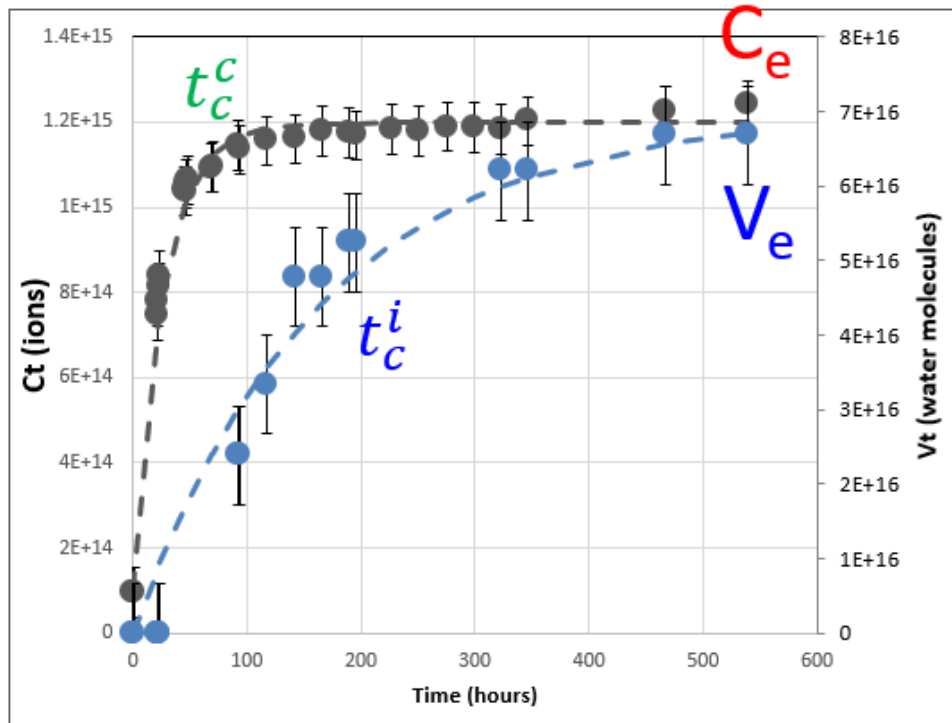


Figure 4.6 Defining the equation terms. concentration increases with time, at a rate that is a function of mineralogy and the connectivity of the phases. The final equilibrated concentration (C_e) is, controlled by clay mineral content and the presence of anhydrite.

Results of the combined imbibition/conductivity measurements suggest a direct proportionality between the conductivity at equilibrium and the imbibed volume at equilibrium and that the relationship is unique to each formation (Figure 4.7). Equilibrated concentration is consistent with a direct proportionality to the equilibrated imbibed water volume.

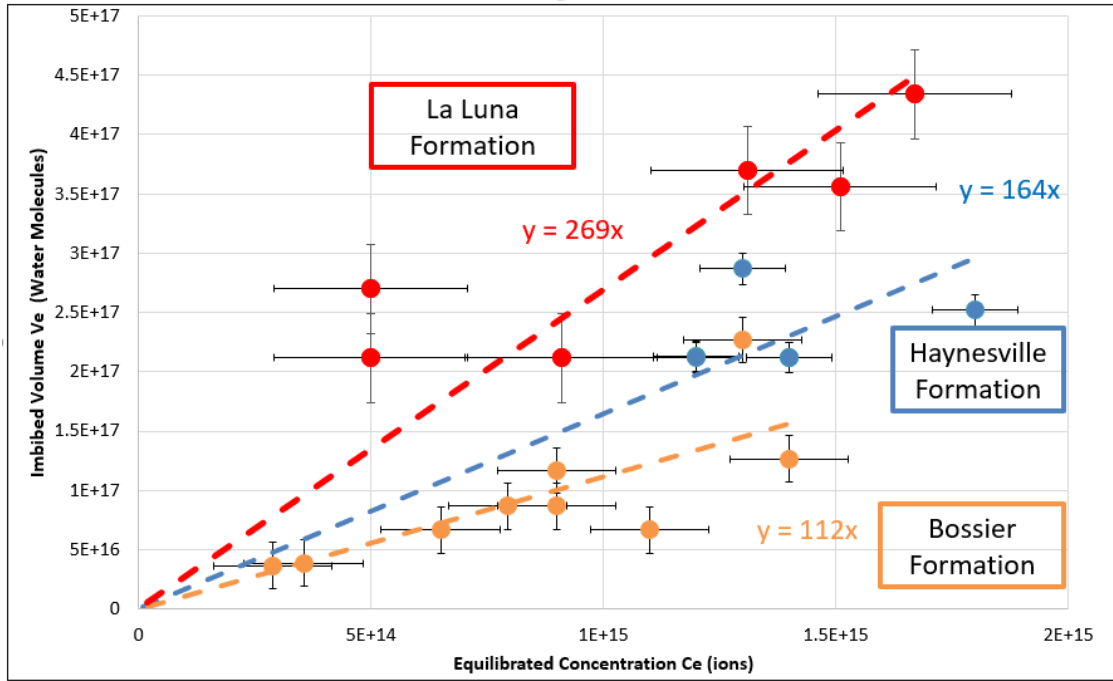


Figure 4.7 Ce is expressed in ions and imbibed water in total water molecules. A direct proportionality between Ce and Ve is observed and the relationships varies by formation. Color represent the different formations.

Based on the positive correlation between the Ca and S observed in the XRF, the presence of these ions in the supernatant water from the ICP, and the anhydrite observed in the images, the impact of anhydrite on the equilibrated conductivity (Ce) of each formation was evaluated. Figure 4.8 shows the equilibrated concentration expressed in number of ions (Ce) against the final concentration from the ICP. Although there is a strong positive correlation between CaSO4 and Ce for the La Luna Formation, suggesting that anhydrite dissolution is the primary

mechanism, this is not the case for the Haynesville and Bossier Formations. For those formations, other mechanisms are controlling the Ce at equilibrium.

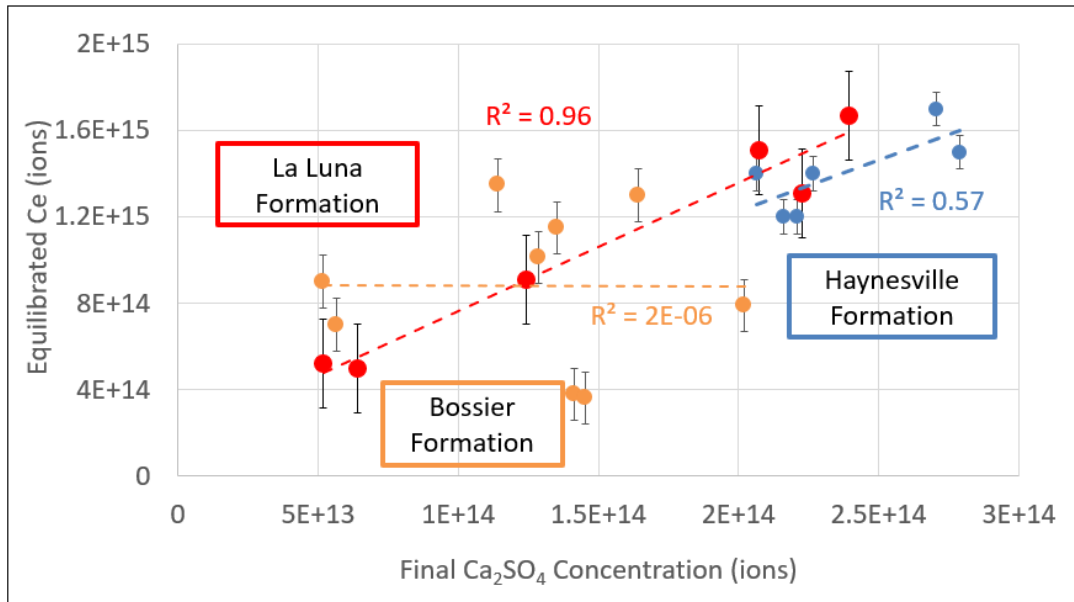


Figure 4.8. Equilibrated Ce and Final Anhydrite Concentration: In the La Luna Formation the correlation is significantly important based on the R², but for Haynesville and Bossier, there is more to be evaluated.

4.4 Conductivity and Imbibition Modelling

The change in conductivity with time is divided into three phases. At early time, water reacts with the surface of the particles and dissolves precipitated salts producing the initial conductivity (C_i) in the experiment. Subsequently, imbibition starts, and the water interacts with the internal surface area of the particles. During this phase, the increased conductivity is principally related to the clay mineral content. Additionally, the dissolution of anhydrite precipitated in clay mineral associated pores contributes to increasing salinity during this phase. Ions are expelled into the supernatant fluid, until salinity equilibrium (C_e) is reached. The higher the volume of clay minerals present in the sample, the shorter the time required to reach equilibrium.

4.4.1. Equilibrated Conductivity (Ce) model.

For the origin of the increasing conductivity, two mechanisms are observed: dissolution of anhydrite, and neutral NaCl ion pairs associated with the clay mineral surfaces (Equation 7). The weight of NaCl referred to in equation 7 is the total NaCl equivalent conductivity that was validated using the ICP data and the conductivity calculation, the total NaCl weight in the fluid ($W_f NaCl$) is the sum of the equivalent weight of NaCl in the fluid due to anhydrite dissolution ($W_f^a NaCl$) plus the equivalent weight of NaCl in the fluid due to interaction with clay mineral surfaces ($W_f^c NaCl$),

$$W_f NaCl = W_f^a NaCl + W_f^c NaCl \quad \text{Eq. 7}$$

$$\text{and} \quad W_f NaCl = W_f^a NaCl + \alpha W^c NaCl. \quad \text{Eq. 8}$$

In Equation 8 we assume that $W_f^c NaCl$ in the supernatant fluid is proportional to the weight of clay present in the sample ($W^c NaCl$), and that they are related by a constant α

$$\alpha = \frac{W_f NaCl - W_f^a NaCl}{C_c * W_t Sample}, \quad \text{Eq. 9}$$

where C_c is clay mineral content. This α factor, or the fraction of conductivity that is present in the supernatant fluid due to the clay mineral content of the sample, is related to the CEC (Figure 4.9).

Figure 4.9 illustrates the relationship between the α factor and the cation exchange capacity measured for each formation (A,B,C) and for all the samples together (D). In the Bossier Formation, the data suggest a good correlation ($R^2 = 0.97$). However, not enough

variability in clay content was measured in the Haynesville or in the La Luna Formations to define a relationship with confidence. Therefore, we use the relationship observed when the three formations are evaluated together ($R^2 = 0.54$) to describe how clay mineral content (CEC) influences the equivalent weight of NaCl in the supernatant fluid.

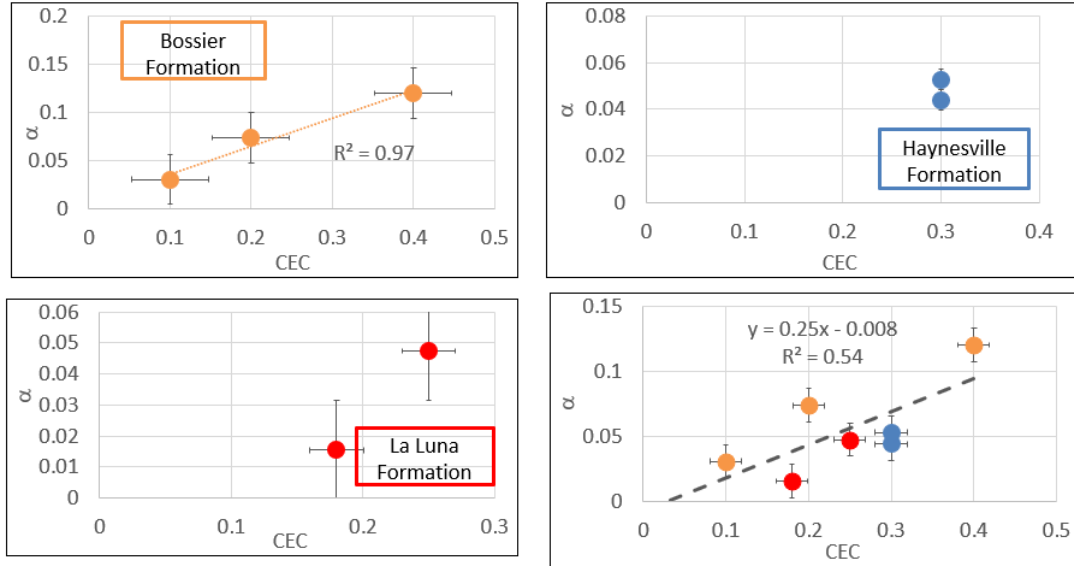


Figure 4.9 The α factor and CEC. This figure illustrates the relationship between the α factor and the cation exchange capacity measured for each formation (A,B,C) and for all the samples together (D). Clay mineral content (CEC) influences the equivalent weight of NaCl in the supernatant fluid.

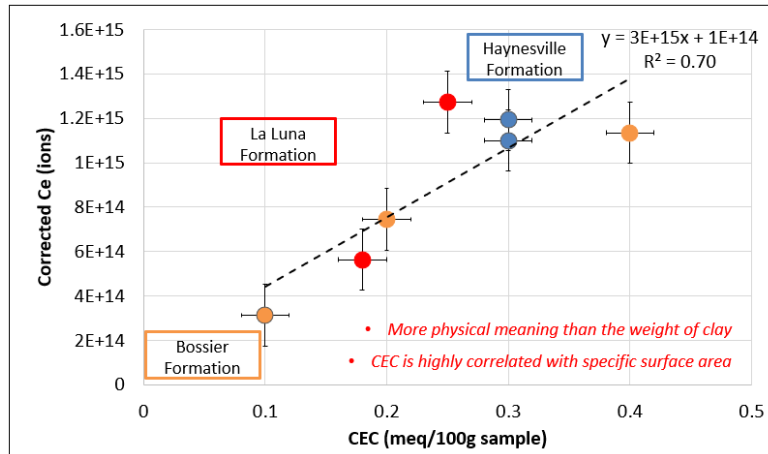


Figure 4.10 Equilibrated Concentration (C_e) expressed as a number of ions, and corrected for the presence of anhydrite, as a function of the cation exchange capacity, expressed in meq/100g of sample. The larger the cation exchange capacity, the more salinity is produced by the sample.

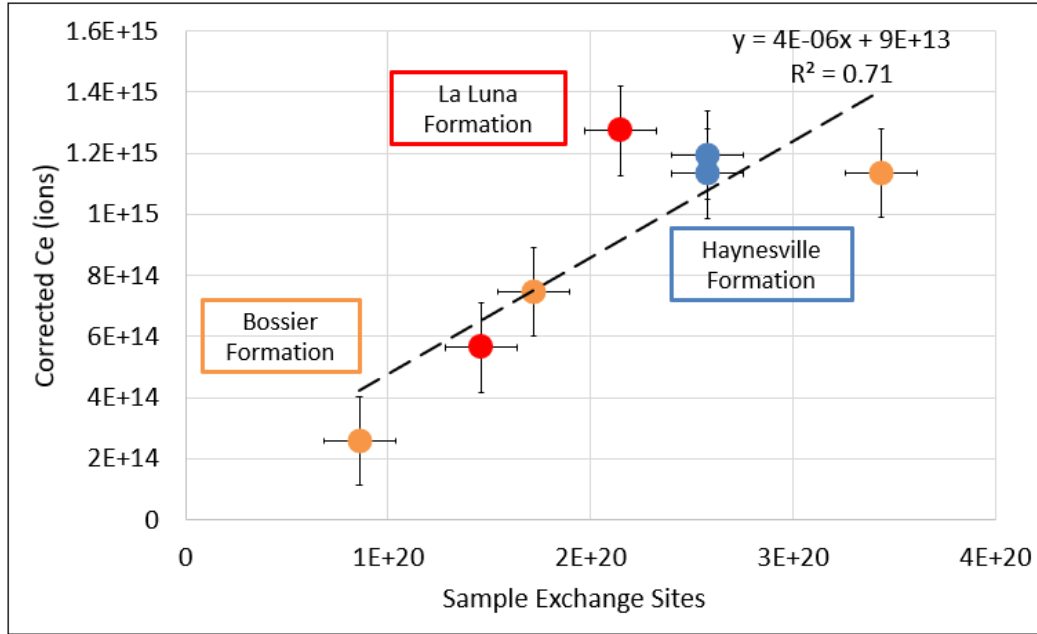


Figure 4.11 Equilibrated Concentration expressed as a number of ions as a function of the numbers of exchange sites present in the sample.

4.4.2 Characteristic Time for Concentration: t_c^c Model

The characteristic time for concentration t_c^c is defined as the time required for the concentration to reach equilibrium. Observations and results suggest that t_c^c is a function of the exposure of clay minerals to the supernatant fluid and the clay mineral connectivity through the particles (percolation), both a function of overall clay mineral content, and the presence and distribution of anhydrite.

In Figure 4.12, thin sections and SEM images from the Bossier Formation, which is similar to the Haynesville, and the La Luna Formation are presented as an example. In Bossier Formation thin sections, the clay minerals, which corresponds to the darker color in the image, are more exposed to the water (orange contour line) and anhydrite is not observed at this resolution. Anhydrite can be observed in the SEM image (figure 4.11b) and occurs between the clay mineral platelets. These observations suggest that clay minerals control the ion expulsion

process in the Bossier and Haynesville Formations, in which they form the connected phase, and they provide the conduits for fluid flow.

In the La Luna Formation thin sections, shown in Figure 4.11c, the clay minerals are also exposed to the water, but, in this case, anhydrite can be observed in almost all the particles filling fractures along the total particle length. In the SEM image for this formation (figure 4.11d) anhydrite exposure at the surface of particles is very clear. Extension of anhydrite through the particles provides the pathway for the fluid imbibition and ion expulsion.

These observations, together with the fact that the La Luna samples have lower clay mineral content, suggest that anhydrite controls the imbibition and ion expulsion processes in the La Luna Formation being the connected phase.

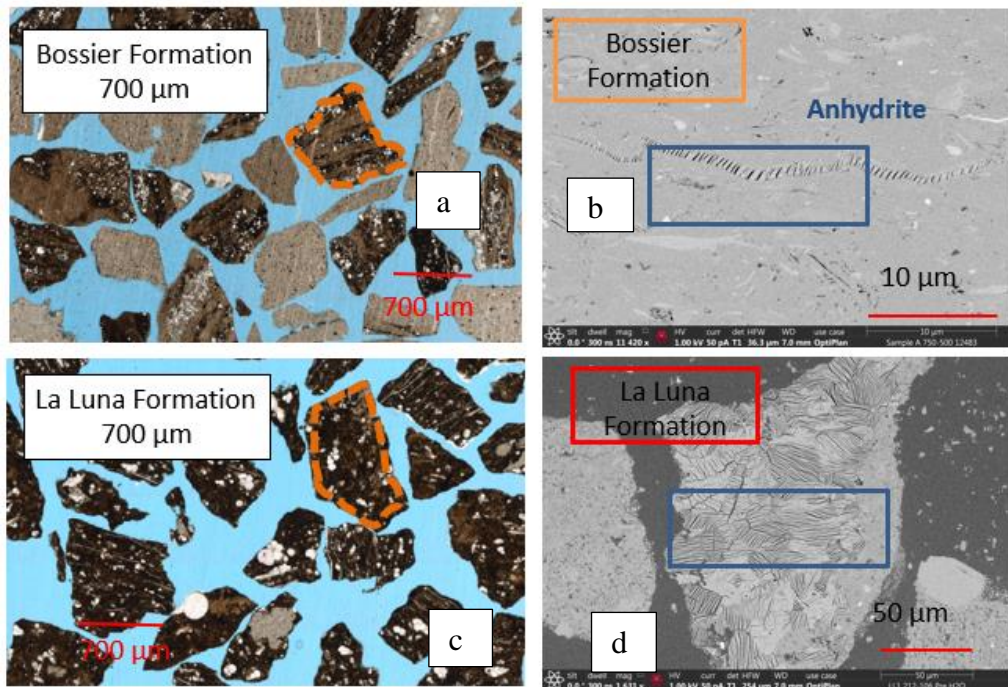


Figure 4.12 Thin sections for Bossier Formation and the La Luna Formation. (a), particles for Bossier do not show anhydrite at this resolution (b) SEM for Bossier Formation where anhydrite is between the clay mineral platelets. In the La Luna Formation (c) anhydrite is visible in the thin sections and often present as fracture fill in the La Luna Formation and it is commonly exposed to the particle surface (d).

4.4.2.1 Characteristic Time for Concentration t_c^c – Grain Size Dependence

The characteristic time for concentration is plotted against the particle size in Figure 4.13. The point size in the figure is proportional to the clay mineral content. A particle size control on t_c^c is not observed. Additionally, in the Bossier Formation, as the weight percent of clay minerals increases, the characteristic time required to reach equilibrium decreases. These two results suggest that diffusion is not the dominant sample response mechanism, and that convection is the principle physical mechanism in the imbibition experiments. In the La Luna Formation, clay mineral content is very low, clay minerals do not percolate through the formation, and the content of anhydrite is higher, suggesting that in these samples, a correction for anhydrite dissolution is required.

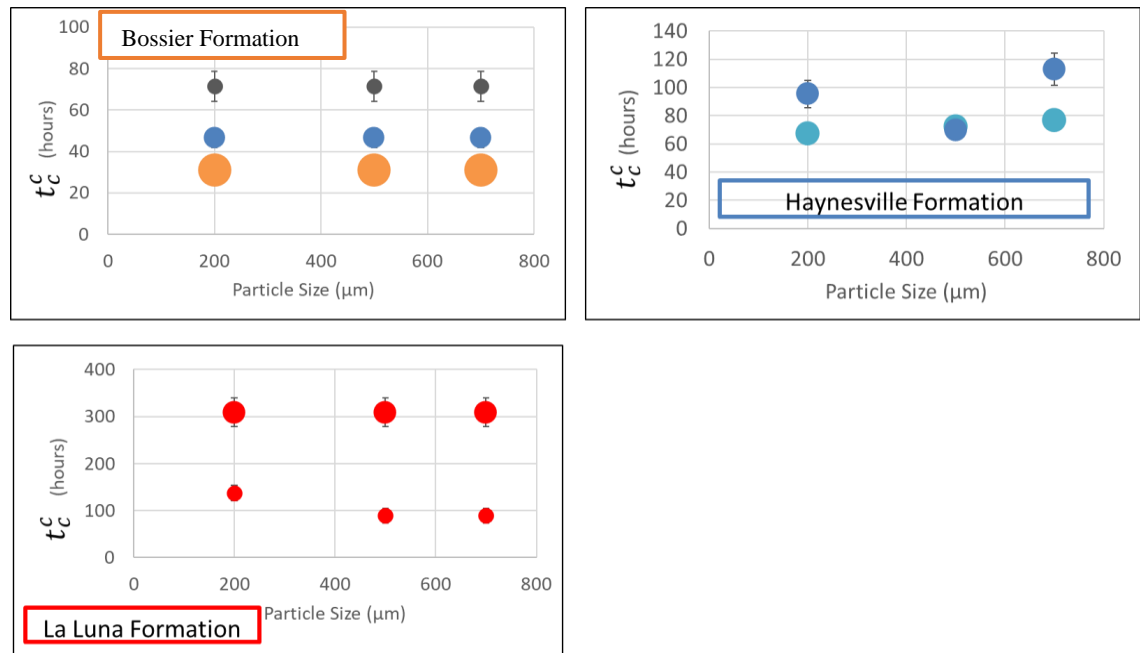


Figure 4.13 Characteristic Time (t_c^c) vs Grain size. No particle size dependence is observed. For the Bossier Formation, as clay mineral content increases, the characteristic time decreases. For the La Luna Formation, anhydrite dissolution is controlling the process and a correction might be needed for the t_c^c .

Figure 4.14 illustrates how anhydrite content (salt dissolution) impacts the characteristic time for conductivity, t_c^c . Results suggest that as the volume of CaSO_4 increases the time required to reach equilibrium increases. Figure 4.13 suggests that a relationship between t_c^c and anhydrite content is present in the La Luna Formation, but not in the Bossier and Haynesville Formations. These observations suggest that anhydrite is controlling ion release and imbibition processes in the La Luna Formation and that clay minerals are controlling the process in the Bossier and Haynesville Formations.

Figures 4.14 and 4.15, illustrate the relationship between anhydrite content and clay mineral content, and t_c^c respectively. As anhydrite content increases in the samples, the time required to reach equilibrium (t_c^c) increases.

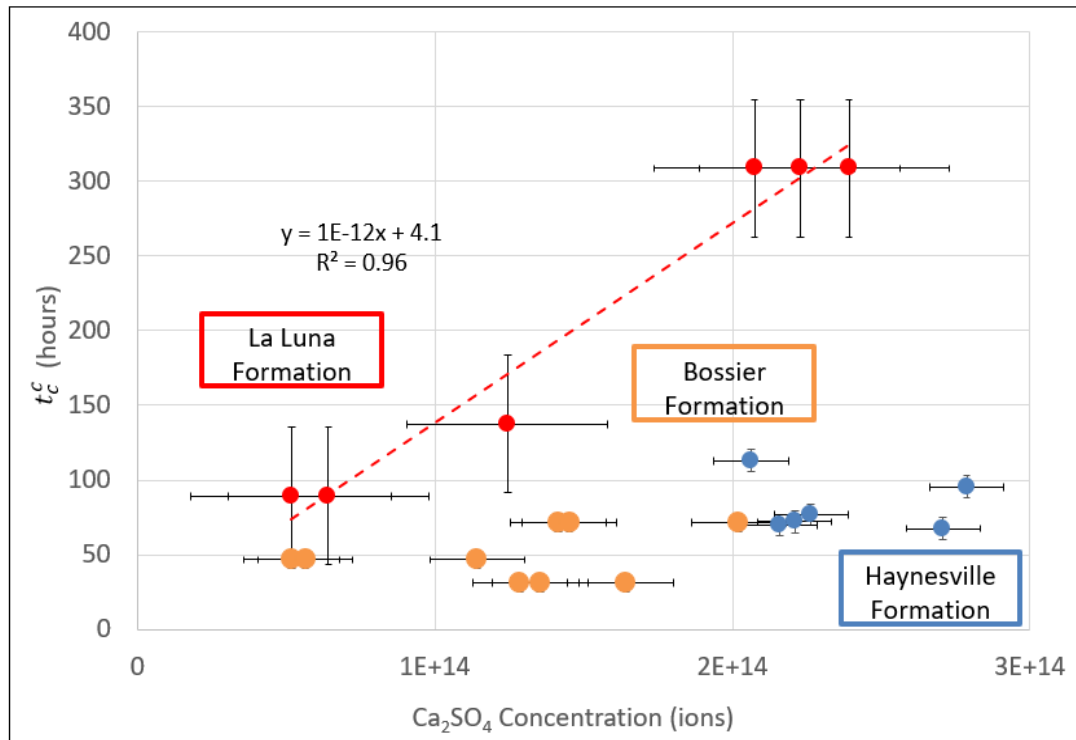


Figure 4.14 Characteristic time for conductivity t_c^c , versus anhydrite content (from ICP). A relationship is observed in the La Luna Formation, in which t_c^c is a function of increasing anhydrite content. No relationship is observed in the Bossier or Haynesville Formations.

Figure 4.15 illustrate the relationship between clay mineral content and t_c^c . As clay mineral content increases in the samples, the time required to reach equilibrium (C_e) decreases. Again, this is an indication that diffusion is not the rate controlling mechanism in the experiments. The relative rate of anhydrite and clay minerals effect on the conductivity characteristic time can not be deconvolved because supernatant fluid time series aliquots were not collected for geochemical analysis. For this reason, one the sample with the high anhydrite content in the La Luna formation is not in the plot.

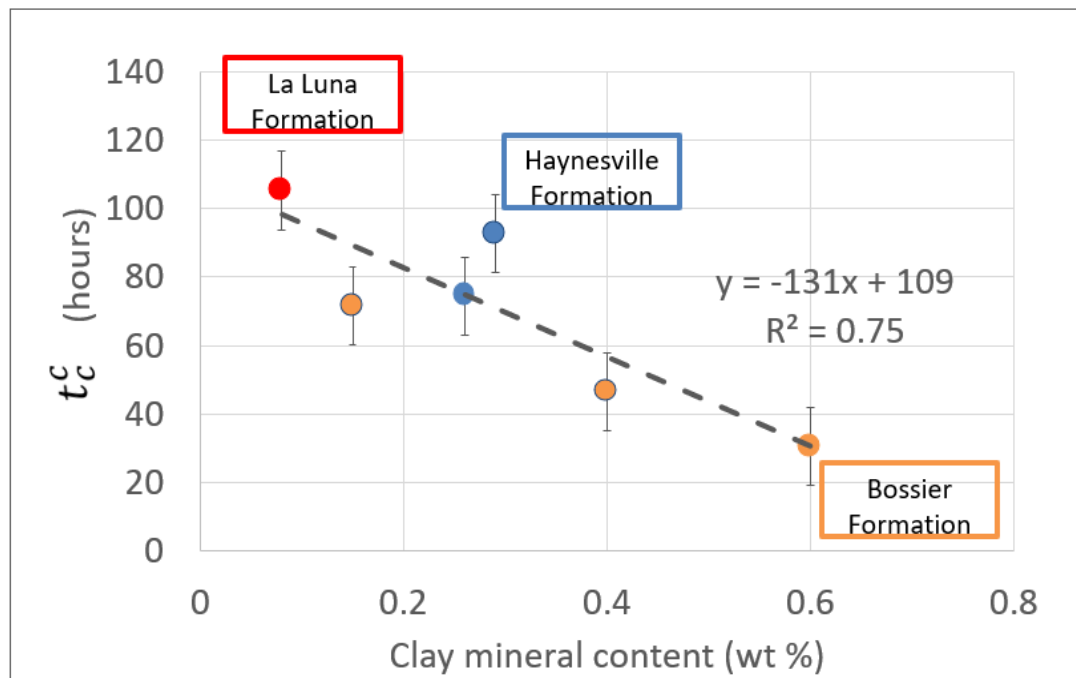


Figure 4.15 Characteristic Time Versus Clay mineral content. In general, the larger the weight % of clay minerals present, the shorter the time necessary to reach equilibrium.

4.4.3 Imbibition Based Porosity Calculation.

Comparison between the Boyle's Law porosity, and imbibed water porosity, will provide insight with respect to wettability and the porosity system that is imbibing water. Figure 4.16 illustrates the relationship between total porosity (Boyle's law) and imbibed water volume. The

1:1 line is shown for comparison. The plot indicates that the samples are imbibing considerably more water than the measured total porosity, requiring corrections to the imbibed fluid volumes.

Corrections to the imbibed fluid volume include: 1) the effect of dissolution pores (new pores are created by anhydrite (salt) dissolution) which are not present in the pre-test porosity measurement and 2) artificial fractures created during sample preparation (crushing), a condition that was observed in the pre- and post-imbibition NMR results, and also, in SEM image analysis.

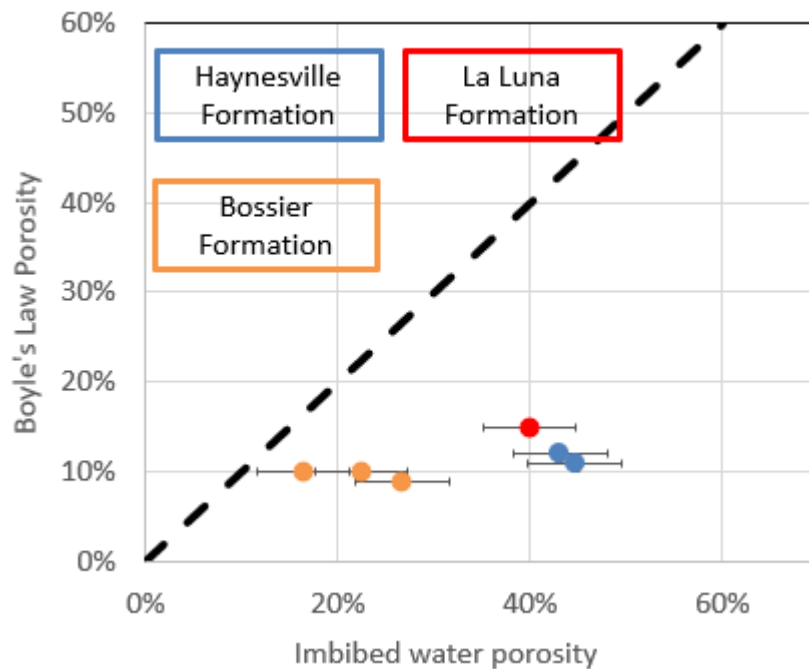


Figure 4.16 A comparison between the Boyle's Law porosity, and the imbibed water volume. Imbibed water volume is much larger than the total measured, pre-test porosity. The large difference may be explained by anhydrite dissolution and damage in the samples due to sample preparation (crushing).

In Figure 4.17, the anhydrite dissolution effect has been removed from the imbibed water porosities. This correction is based on the anhydrite volume from the supernatant ionic composition. Figure 4.17 shows that 1) the correction in the Bossier samples is relatively small,

which is an indication that anhydrite dissolution is not a significant process, and 2) the Haynesville and La Luna samples show a considerable correction for the presence of anhydrite.

After applying this correction, the water imbibed porosity is still larger than Boyle’s Law porosity, therefore a second correction needs to be applied. This correction is related to sample damage (artificial fractures created by sample preparation (crushing)).

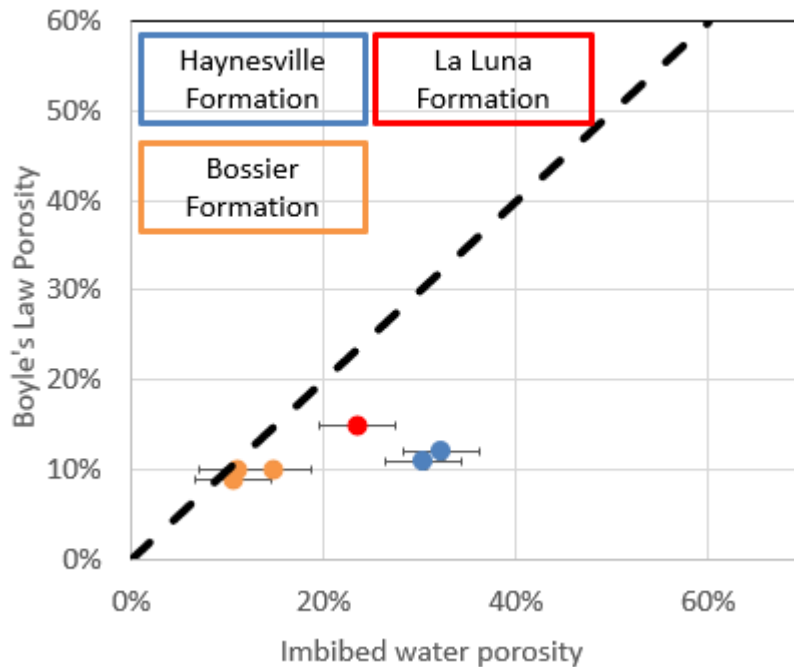
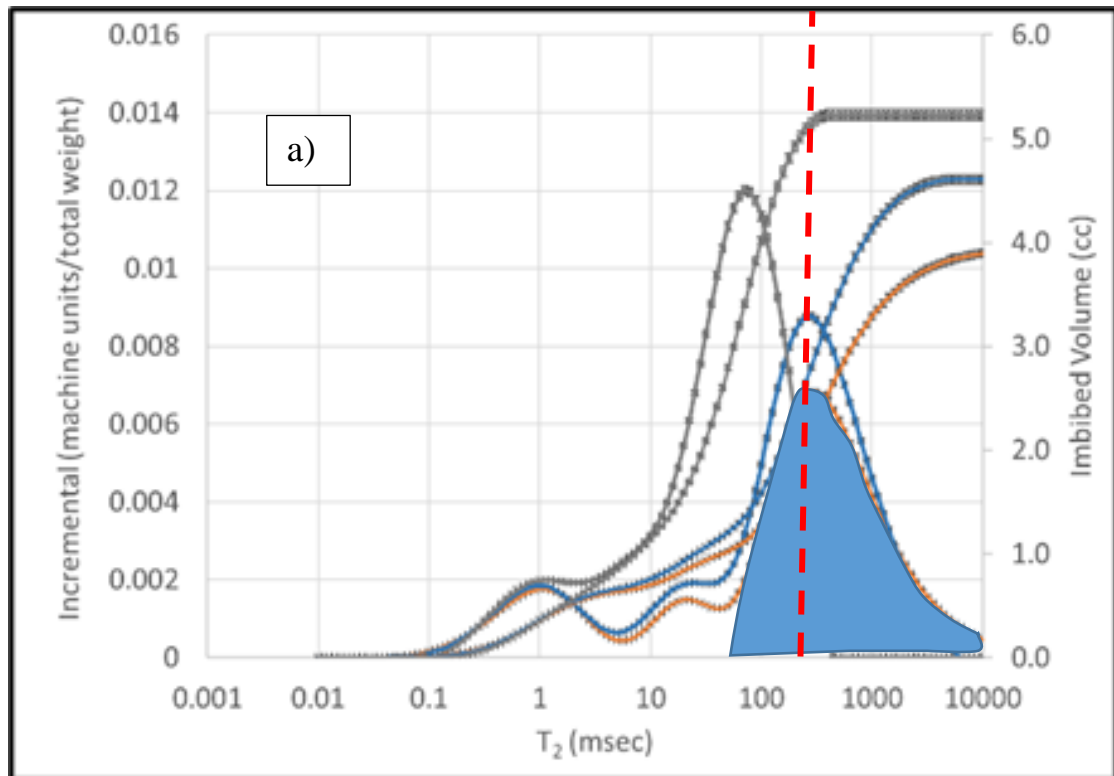


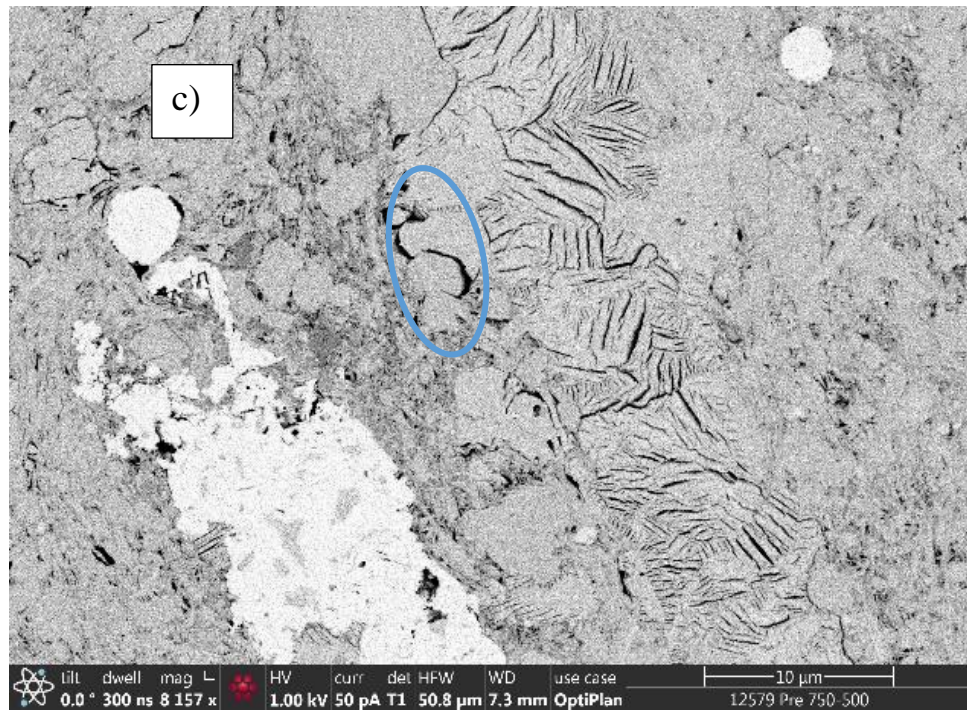
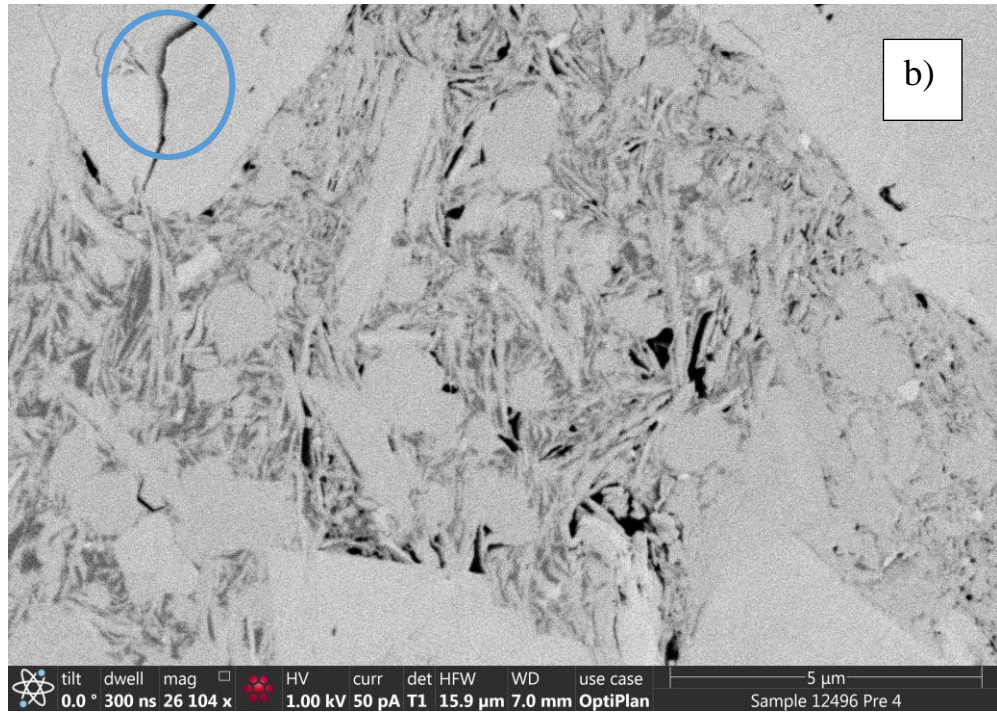
Figure 4.17 A comparison between the Boyle’s Law porosity and the imbibed water porosity, corrected for the volume of dissolved anhydrite. Imbibed water porosity is still larger than total porosity.

Figure 4.18a shows an NMR measurement from a Bossier B(60) sample as an example. In this sample a third peak at longer T2 is observed in both the 500 and 700 μm samples (blue area under the curve). Observations in SEM (blue circles in b, c, and d) suggest that this pore system may be the result of fracture generation during sample preparation (crushing). This new

induced volume needs to be removed from the imbibed water volume in order to compare with as received Boyle's law porosities.

To remove this induced volume, a cutoff was defined per sample, at the inflection point on the cumulative imbibed volume curve (secondary y axis), to define the NMR response associated with induced fractures (see Figure 4.18a). The volume of the induced fracture peak was removed from the total imbibed volume. This correction was applied for all particle sizes, even in the 200 μm samples in which the peak was only weakly developed.





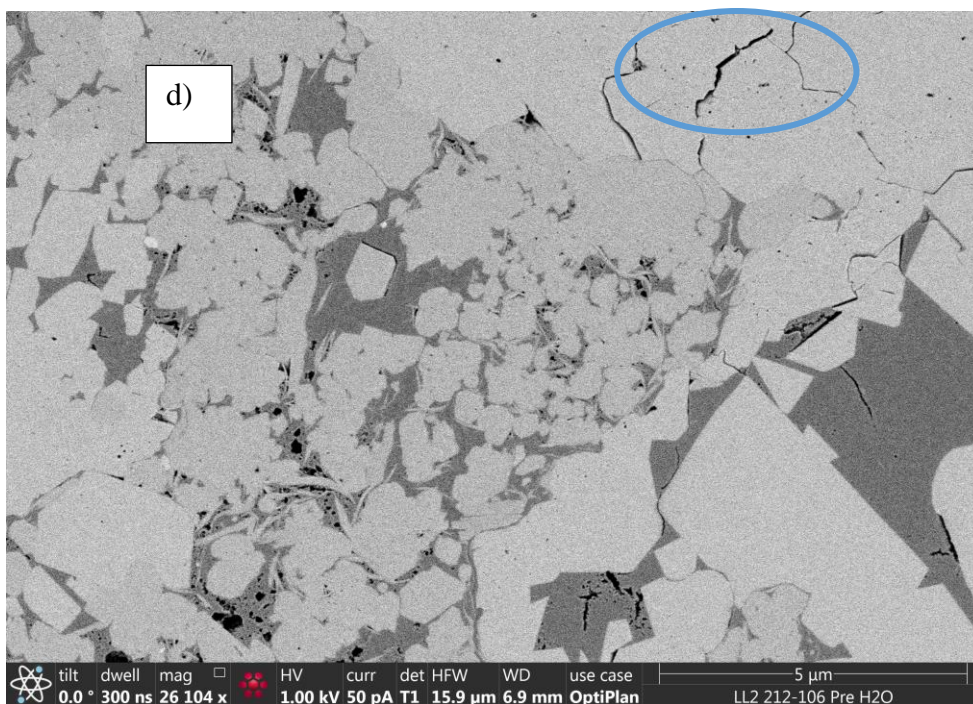


Figure 4.18 SEM images for Bossier B(15) (b), Haynesville H(26) (c) and the La Luna Formation LL(8) (d) in which artificial fractures can be identified (blue circles) which were created during sample preparation. These fractures are observed as a third peak in the NMR results (a), partially develop in the 200 μm and completely in the 500 and 700 μm s . This created volume must be removed from the imbibed water volume porosity calculation.

The data in figure 4.19 corresponds to the imbibed water volume porosity calculation, corrected for both salt dissolution, based on the volume of anhydrite identified by the ICP measurements, and induced fracture porosity, the extra volume of water observed in the third porosity system identified based on the NMR data. When these two corrections are applied, the imbibed water porosity is less than the as received total porosity from Boyle's Law. This corrected imbibed water porosity is interpreted to represent the inorganic, mineral hosted porosity. The difference between the imbibed water porosity and the 1:1 line is interpreted to correspond to the organic matter hosted porosity, which should be oil wetting.

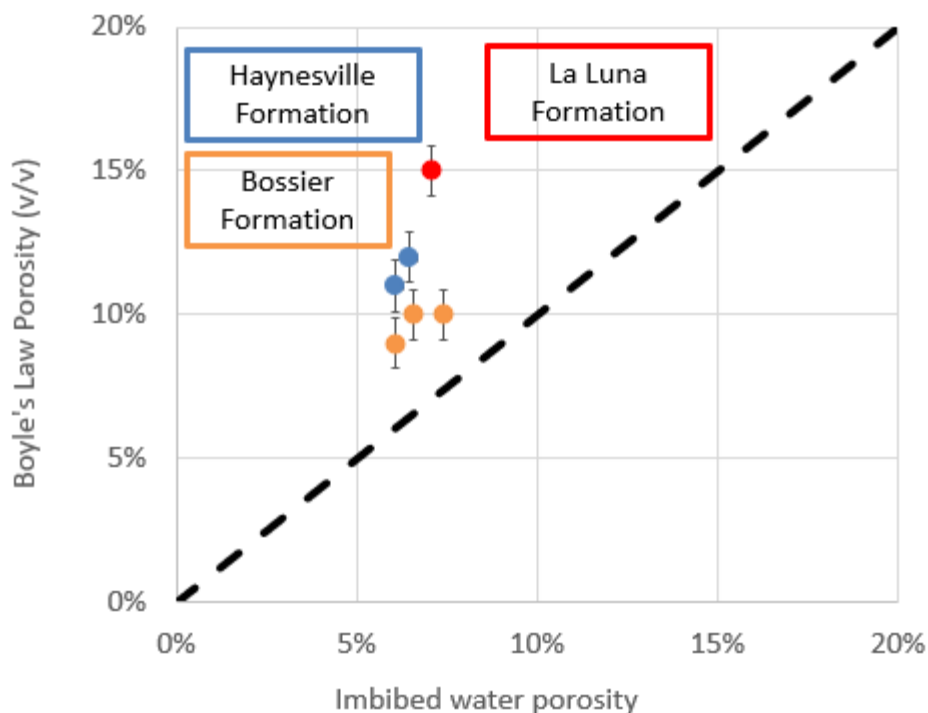


Figure 4.19 Boyle's Law porosity compared with imbibed water porosity corrected for anhydrite dissolution and fracture volume created during crushing.

Figure 4.20 illustrates a comparison of the estimated organic matter hosted porosity and organic pores estimated by image segmentation, with a 1:1 line comparing the methods. In the Bossier Formation, the ability to resolve the organic versus mineral porosity is limited. This is due to the overall small pore size and intermediate gray levels associated with clay mineral hosted pores in back-scattered electron imaging. For this reason, some mineral associated porosity is misidentified as organic porosity, causing the value to fall above the 1:1 line. In contrast, for the Haynesville and the La Luna Formations there is better agreement. Overall, the comparison shows relatively good agreement between the two measurements. This is then a promising technique for estimating organic porosity from imbibition experiments and also could provide a basis for a possible correction for the GRI (Gas Research Institute) method, in which the sample is also crushed but no correction for artificial fractures is applied. This result

also provides a good indication that water is not entering the organic pores, which suggests that at these maturation levels (1.4-2.5% Ro), the organic material remains oil wet.

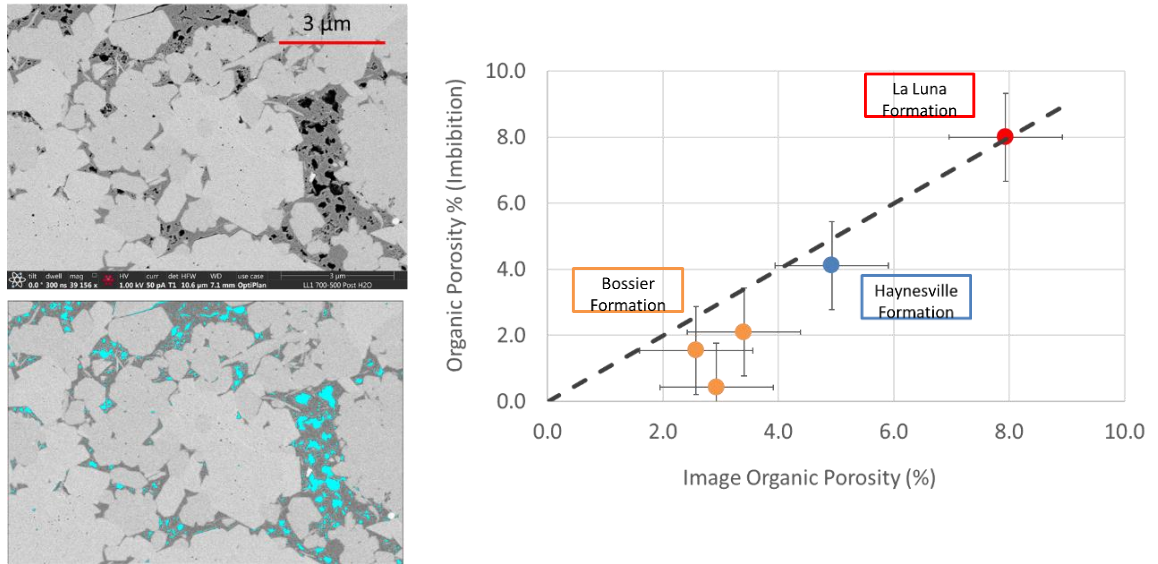
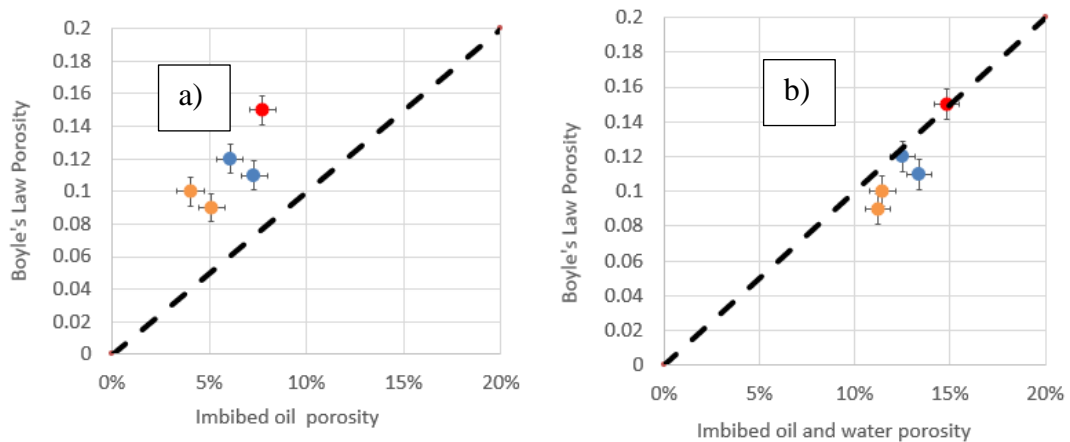


Figure 4.20 Organic porosity from image analysis, and from corrected imbibed water calculations are in good agreement, although slightly overestimated in the Bossier Formation. See text for discussion.

4.4.4 Oil Imbibition

A similar approach to that applied above was applied to the volume of oil imbibed by the samples. Figure 4.21a shows the comparison with a 1:1 line between the Boyle's Law porosity and imbibed oil porosity. The difference between the two measurements will correspond to the inorganic porosity, which was calculated in the previous section. When we add the two porosities together, a good agreement between the methods is observed. (Figure 4.21b).

Figure 4.21c shows the comparison between the imbibed oil porosity and the image based organic porosity. The ability to resolve organic matter hosted pores in the Bossier is limited because the size of the pores, and some of them have not been identified.



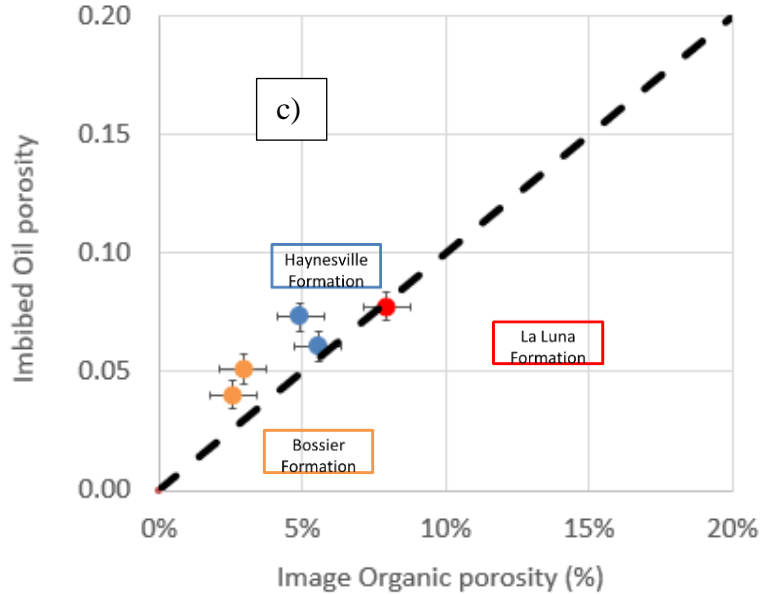


Figure 4.21. Boyle’s Law porosity and imbibed oil porosity. a) comparison with a 1:1 line between the Boyle’s Law porosity and imbibed oil porosity. When we add the two porosities (organic matter hosted pores and mineral hosted pores), a good agreement between the methods is observed. (Figure 4.21b). Figure 4.21 c shows the comparison between the imbibed oil porosity and the image based organic porosity. The ability to resolve organic matter hosted pores in the Bossier and Haynesville is limited due to the small size of the pores, and the use of BSE images (lower resolution), and prominent salt and pepper noise in the images.

4.4.5 Characteristic Time for Imbibition: t_c^i Model

Characteristic imbibition time, t_c^i , is defined as the time required for water to saturate the particles and reach equilibrium. In figure 4.22, the different characteristic times by formations are plotted against Boyle’s law total porosity. t_c^i seems to increase with total porosity, however, previous analysis shows that water is not filling the organic pores. The water is saturating clay mineral associated pores and anhydrite dissolution pores. As clay mineral connectivity increases (clay minerals percolate through the sample) t_c^i decreases. Therefore, where the inorganic porosity is better connected and the anhydrite content is low, as in the Bossier, t_c^i will be shorter. In contrast, more time will be required for those samples in which clay mineral content is low and anhydrite dissolution is prominent, as in the La Luna and

Haynesville Formations. A power law relationship is observed, which is a function of the different length scales and porosity systems that are present in the samples.

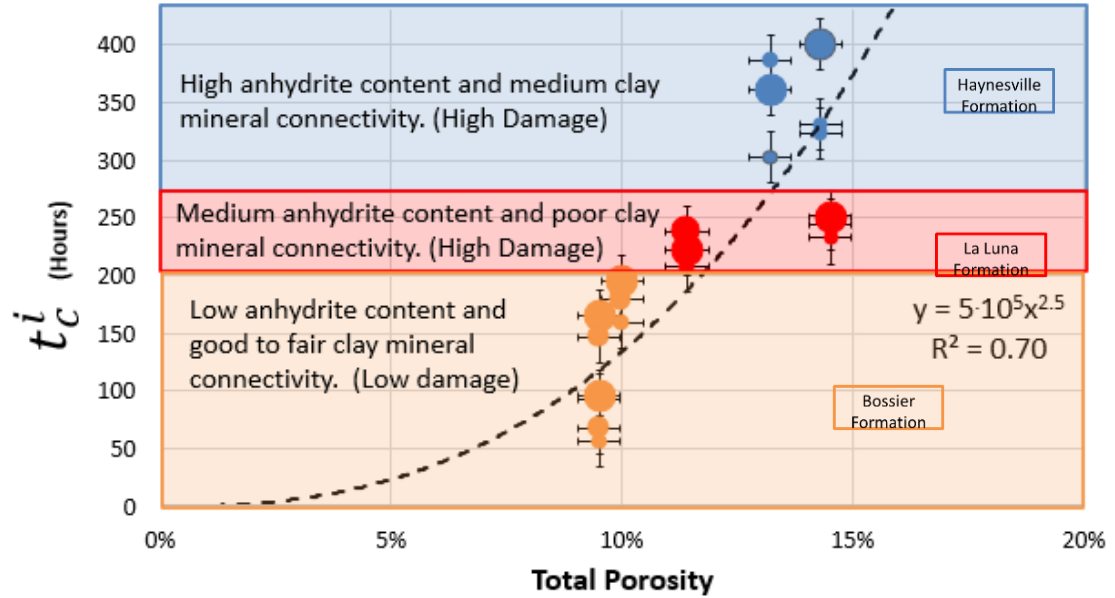


Figure 4.22 The characteristic imbibition time is affected by the clay mineral connectivity and the amount of anhydrite present in the samples. Characteristic time is also affected by the presence of artificial fractures that were created during sample preparation. These three effects influence the time required for water to saturate the water wet porosity system.

4.4.6 t_c^e and t_c^i comparison

Figure 4.23 presents the combined plots for total conductivity C_t (left axes) and total imbibed volume V_e (right axes) versus time, for the complete set of samples. Only one sample of Haynesville is plotted because the results are similar. Points represent the data, and the dashed lines represent the fits to the data. A lag time is observed between t_c^e and t_c^i in the three formations ($d t_c^e t_c^i$). Imbibition (t_c^i) happens at a much slower rate than ion expulsion (t_c^e) in the Bossier and Haynesville. In the La luna Formation, both, ionic expulsion, and imbibition, happen more slowly than in the other formations and t_c^i and t_c^e are larger.

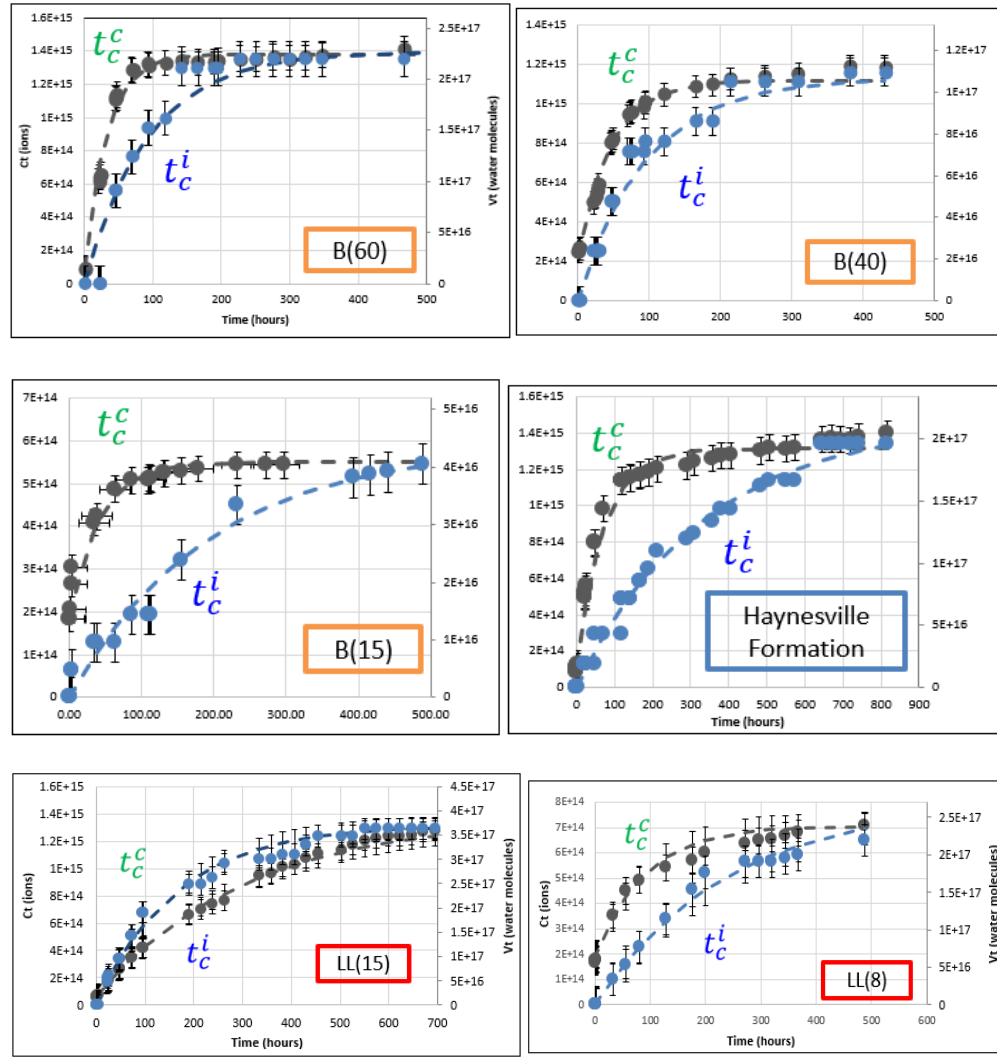


Figure 4.23 Combined plots for total conductivity C_t and total imbibed volume V_e for all the samples. A lag time is observed between t_c^c and t_c^i in the three formations ($d t_c^c t_c^i$).

The difference in equilibration times suggests that, although the two processes are highly related, imbibition is a more complex process than ion expulsion, resulting in more time required for equilibration. Multiple porosity systems, both artificial and natural, are imbibing water. We propose that this lag time is related to the number of porosity systems that impact each process. t_c^c includes the porosity systems that impact the conductivity of the supernatant, which are 1) clay mineral associated pores and 2) new pores created by anhydrite dissolution. The

higher the clay mineral content, the faster the conductivity equilibrates. In contrast the greater the volume of anhydrite that is present, the slower the equilibration process. For the imbibition time t_c^i , more porosity systems must be considered: 1) clay mineral associated pores, new pores created by anhydrite dissolution, and artificial fractures created by the sample preparation (crushing) (Figure 4.24).

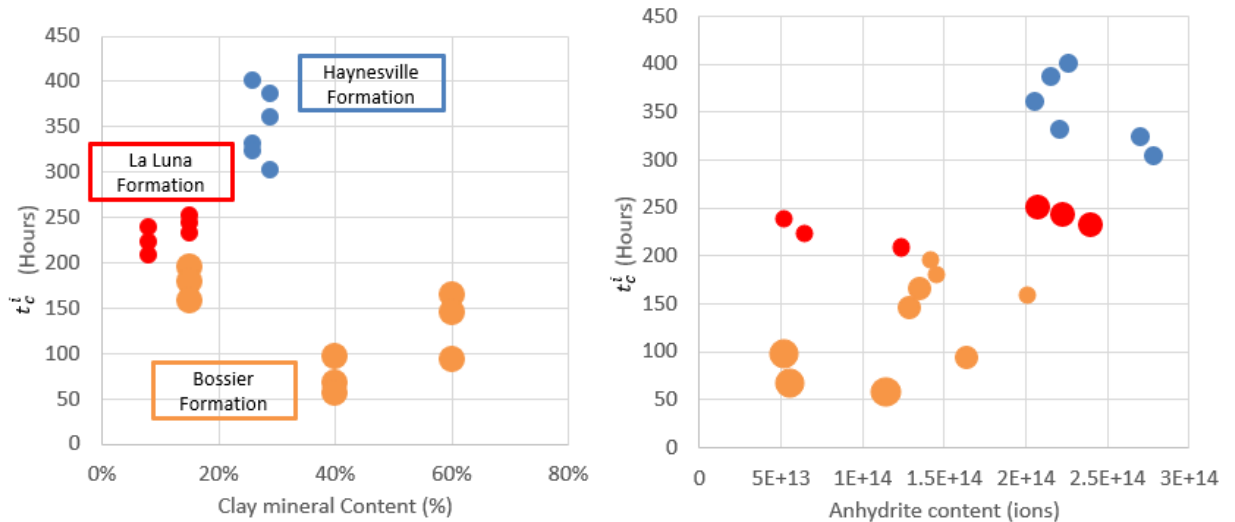


Figure 4.24 Characteristic Imbibition Time Vs Clay Mineral and anhydrite content. The Bossier Formation has the shortest characteristic time for imbibition due to the higher clay mineral content and lower anhydrite content. Haynesville shows the largest time due to higher anhydrite content, and intermediate clay mineral content. The La Luna Formation has a high anhydrite content and very low clay mineral content resulting in a longer equilibration time. The artificial fracture effect also increases imbibition time as many of the observed fractures are intragranular and not transgranular

Artificial fractures are most frequently observed in the carbonate/dolomite grains in the samples. These generated fractures impact imbibition but not conductivity, explaining the observed lag time. (t_c^i) is difficult to correct for the amount of artificial porosity. However, figure 4.26 shows a good relationship between (t_c^i) and the carbonate content in the sample. Because carbonates cleave and are not as hard as quartz it is reasonable to expect that carbonate grains should be more prone to brittle failure than associated quartz. Because of its higher

carbonate content, the La Luna Formation is likely to develop more intragranular fractures, increasing the time to reach imbibition equilibrium. In the Haynesville samples, the carbonate content is also high, and more anhydrite is present, making the time required for imbibition the longest among all the tested samples. In the Bossier samples, due to the low carbonate and high clay mineral content, the samples do not develop as many fractures, imbibing and reaching equilibrium faster.

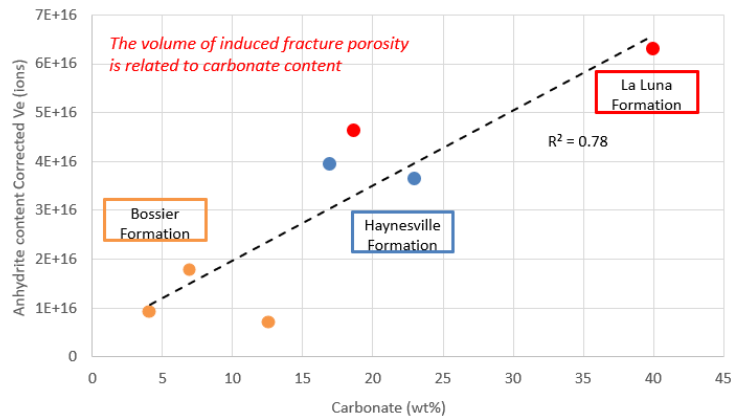


Figure 4.25 Artificial Fracture Development. As carbonate content increases in the samples, the likelihood of artificial fracture development increases, resulting in increased imbibed volumes. In this plot V_e has been corrected for the amount of anhydrite.

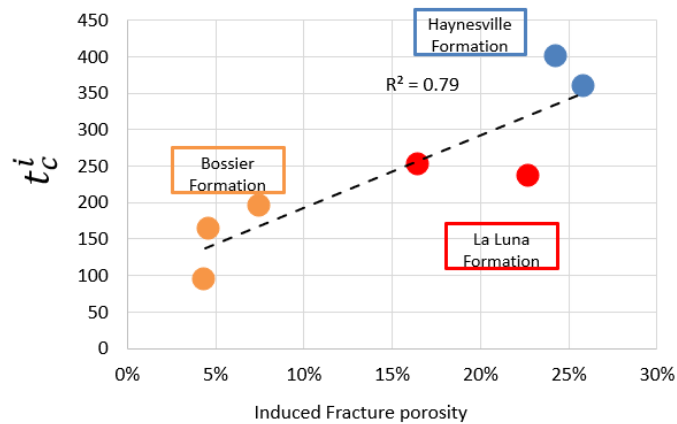


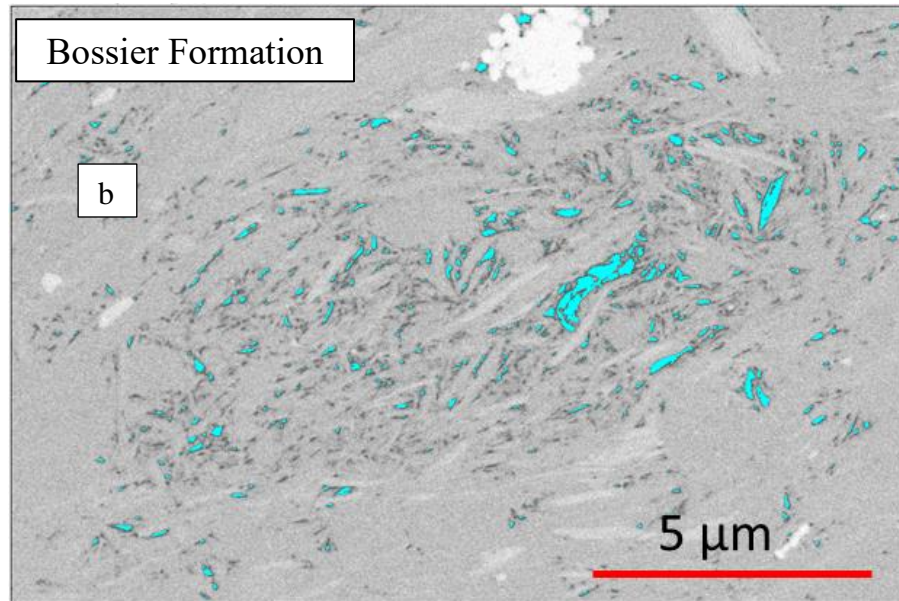
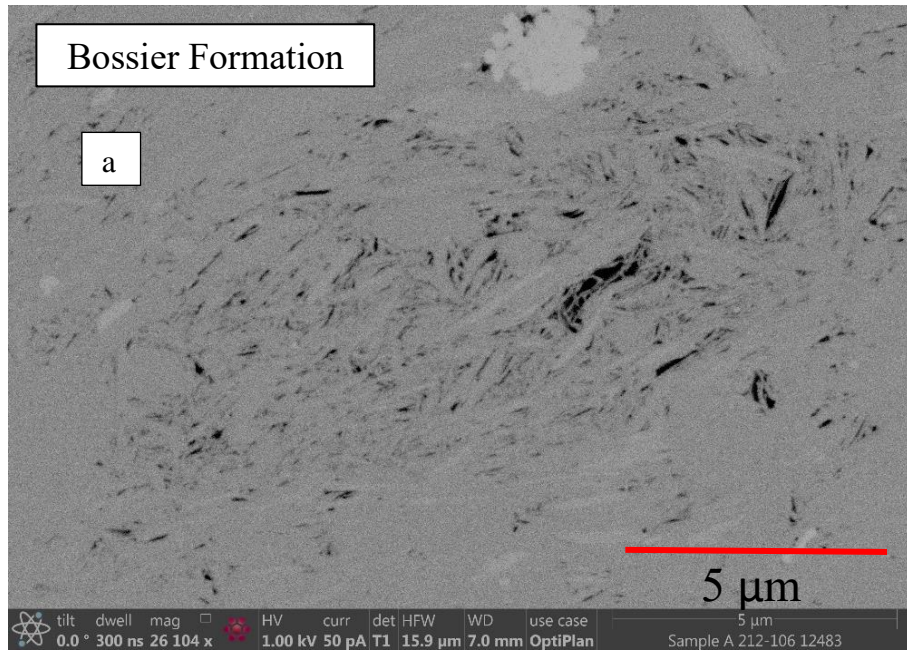
Figure 4.26 Characteristic Time for Imbibition and Artificial Fracture Porosity. As artificial fracture porosity increases, the characteristic imbibition time increases. The relative rate of anhydrite and clay minerals effect on the imbibition characteristic time cannot be deconvolve because supernatant fluid time series aliquots were not collected for geochemical analysis.

Results of image analysis support the observations described above. Figure 4.27 shows in a) and c) two original images for sample B(60) in the Bossier Formation, and b) and d) show the segmentation for total porosity. In a) light gray areas correspond predominately to clay minerals (with minor quartz) and the black color to clay mineral associated porosity (light blue in b).

In figure 4.27 c) the light gray color corresponds to clay minerals and quartz, dark gray corresponds to organic matter, black to porosity and bright regions to pyrite. In these two images, most of the porosity is inorganic with some organic pores. When present organic matter is highly interconnected with the clay minerals.

In the Bossier, because clay minerals are the connected phase, and they are providing the conduits for fluid flow, the water will saturate those conduits, at a rate that depends on the clay mineral content. In addition, where anhydrite is present, anhydrite dissolution will occur. Imaging suggests that the anhydrite is distributed between clay mineral platelets, also impacting the conductivity.

Finally, imbibing water will access the less well-connected pore systems (e.g. intra-granular fractures generated during crushing). Imbibition into sample preparation related fractures will impact the imbibition results but not the conductivity results. Organic porosity analysis, presented earlier, suggests that water does not enter organic pores.



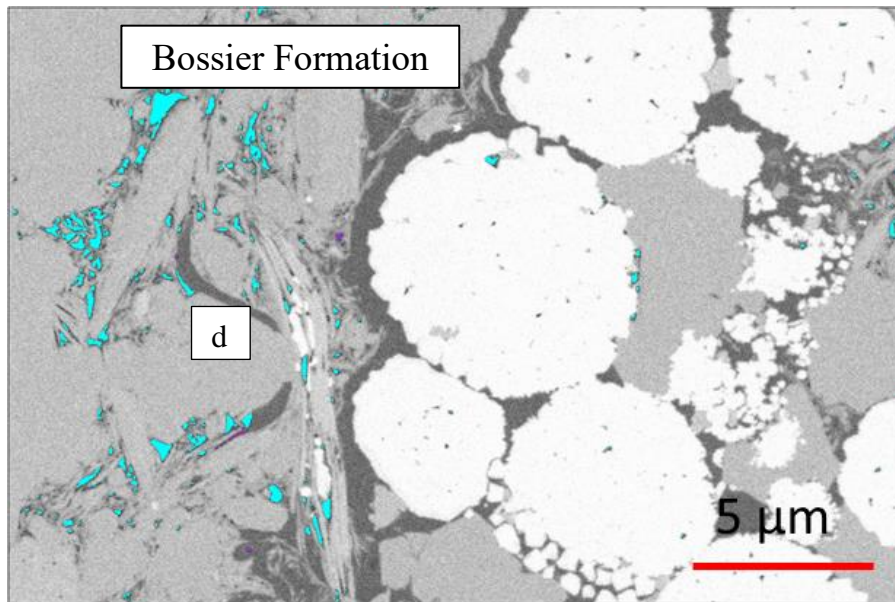
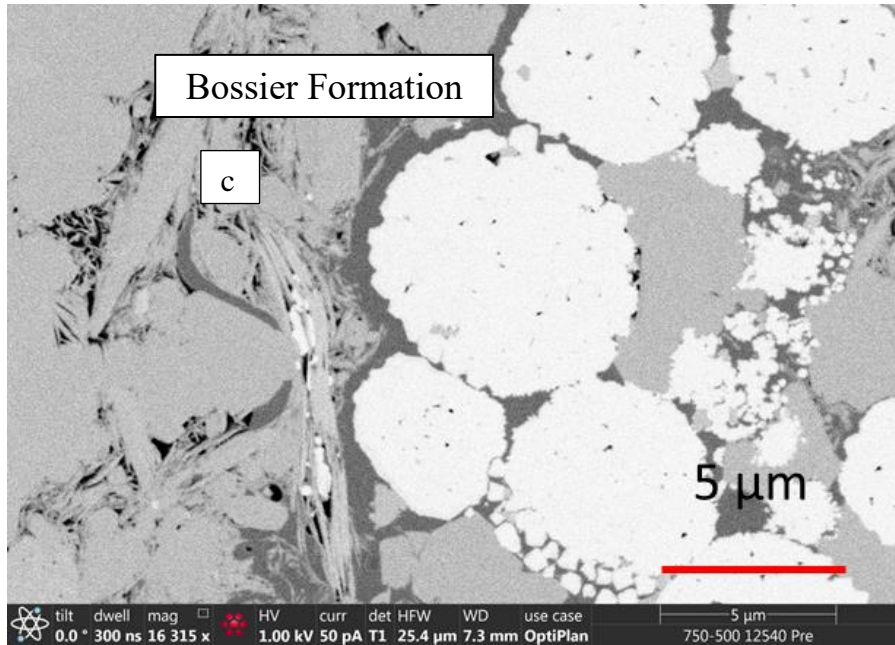


Figure 4.27 Porosities from images of the Bossier Formation: a) is the original image for sample B(60) and b) is the segmentation for total porosity. and c) is the original images for sample B(40) and d) show the segmentation for total porosity. In b) and d) light gray areas correspond to clay minerals and clay sized quartz grains, black regions are porosity (segmented to light blue). Dark gray corresponds to organic matter. In these two images, most of the porosity is mineral hosted. Porosities from images Bossier Formation are normalized to the total image area.

In the Haynesville formation (Figure 4.28), the scenario is similar to the Bossier with the exception that the anhydrite content is the highest among the samples. Water first saturates the clay mineral associated pores, and dissolve the anhydrite, at a rate that will depend on its content. For samples with higher carbonate content, isolated artificial fractures will also be saturated making the imbibition process slower.

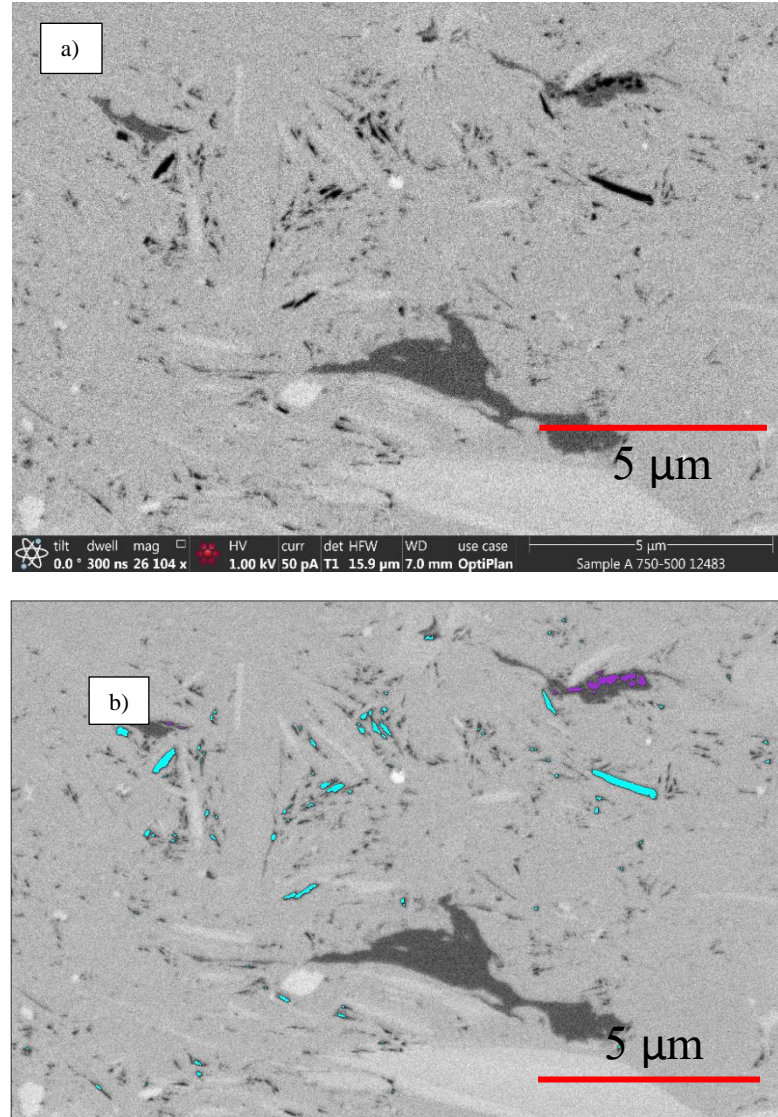


Figure 4.28 Porosity from Images of the Haynesville Formation: a) is one of the original images for sample H(26) and b) shows the segmentation for total porosity. Light gray areas correspond to clay minerals and clay sized quartz and feldspar, inorganic porosity is segmented in light blue. In these two images, most of the porosity is inorganic with some organic pores in purple (b).

In the La Luna Formation, clay mineral content is low, making the ion expulsion process slower. Anhydrite content is moderately high, which increases the imbibition time. Additionally, carbonate content is the highest, when compared to the Bossier and Haynesville Formations, making the rocks more prone to being damaged during sample preparation. This creates relatively isolated, intragranular fracture pores which also increase the time required to complete the imbibition process.

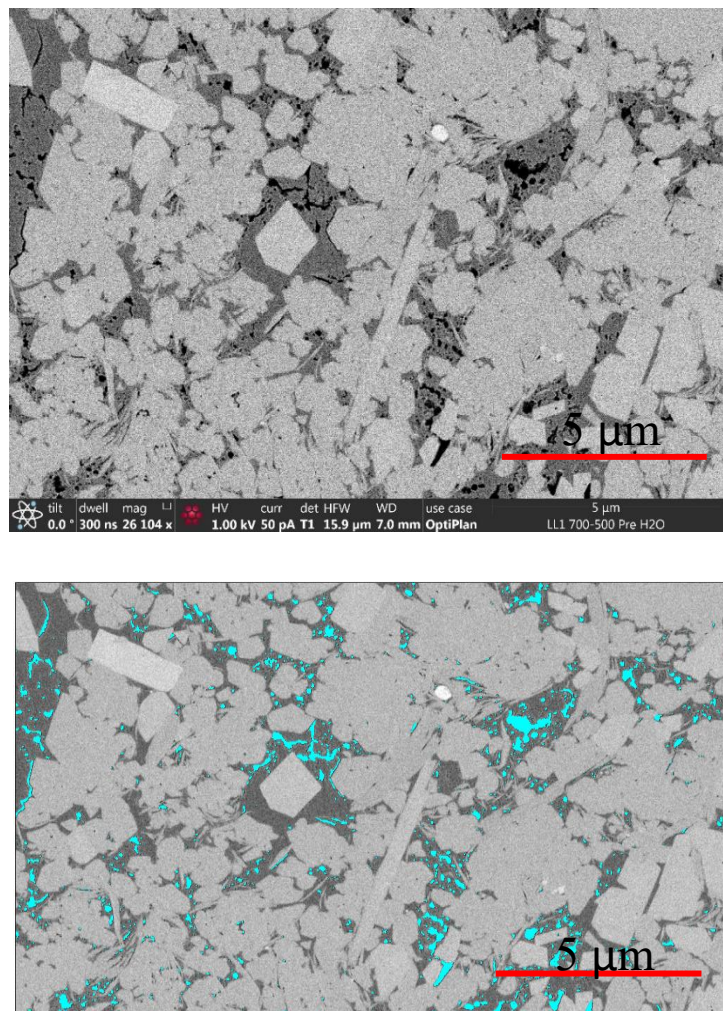


Figure 4.29 Porosity from Images of the La Luna Formation: a) an original image from sample LL(15) b) shows the segmentation for total porosity. Light gray areas correspond to carbonate and quartz with a small volume of clay minerals, organic porosity is in light blue. In this image, the porosity is nearly entirely developed in organic material

4.4.7 Equilibrated Imbibed Water Imbibition: (Ve) Model

Discussion in the previous section suggested three pore systems to be considered in the V_e analysis. First, the dissolution of anhydrite is creating new pores. Second, an induced fracture system was identified. Finally, water is imbibing into mineral hosted pores and not into the organic matter hosted pores. Therefore, equilibrated imbibed water volume (V_e) is controlled by three components: 1) clay mineral associated porosity, new pores created by anhydrite dissolution, and induced fractures created during the sample preparation.

To isolate the effect of each component, corrections need to be applied to V_e . Figure 4.30 shows the relationship between the corrected V_e and clay mineral content. This corrected V_e , includes a correction for the volume associated with the presence of anhydrite components in the supernatant and for the additional induced fractures volume (estimated using NMR). In figure 4.30, the point size is proportional to the particle size. The smallest particle size falls outside the margin of error in all of the samples. The same condition is observed when anhydrite is plotted against the V_e (Figure 4.31)

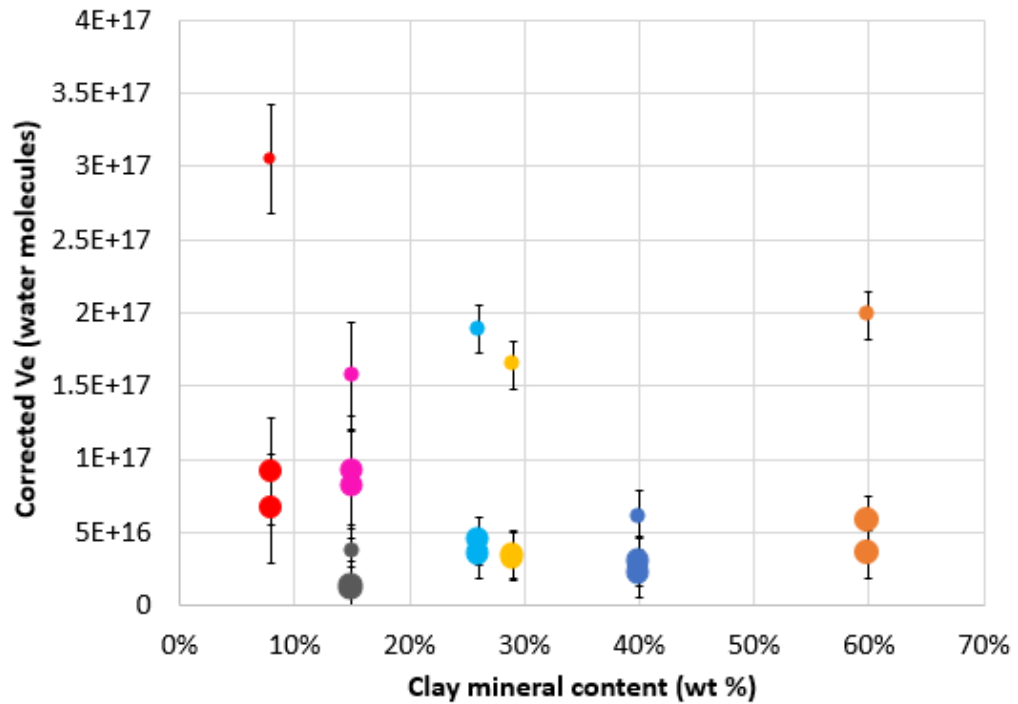


Figure 4.30 Clay mineral content effect on the corrected imbibed water volume (V_e). Corrections for anhydrite content and induced fracture volume have been applied. Point size is proportional to the particle size. The smallest particle size (200 μm) behaves differently in all the samples.

Figure 4.31 shows the relationship between the anhydrite content and V_e with the respective correction for clay mineral and induced fracture volume. Similar to Figure 4.30, point size is proportional to the particle size for each sample. The 200 μm samples for all the formations show values outside of the error margin, resulting in high values for V_e .

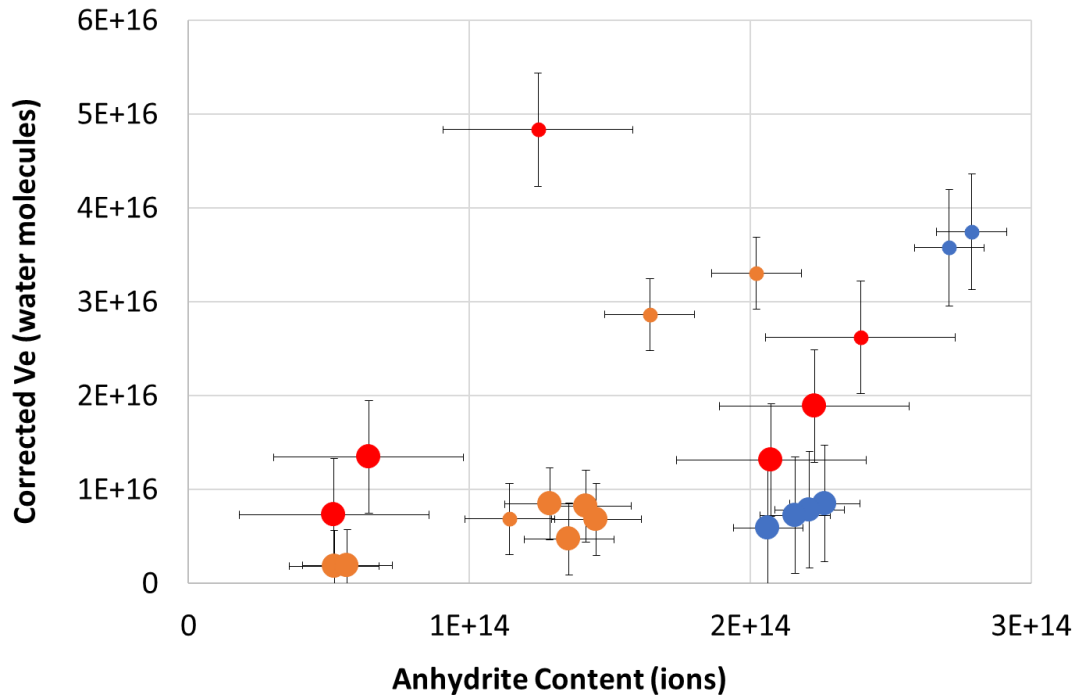


Figure 4.31 Anhydrite content effect in the corrected imbibed water volume (V_e). Corrections include clay mineral content and induced fracture porosity have been applied. Point size is proportional to the particle grain size. It can be observed how the smallest grain behaves different compare with the other particle sizes.

To understand this result, thin sections and laser particle size distribution data were used. Figure 4.32 shows a thin section for the 200 μm particle size in sample B(60) from the Bossier Formation. Abundant, very fine material is present between the larger particles. This fine material will impact both, imbibition and conductivity, but data suggests that imbibition is affected to a greater level. In contrast, in the 500 μm and 700 μm thin sections for sample B(60), these fine particles are not observed. (See Figure 4.33 and 4.34).

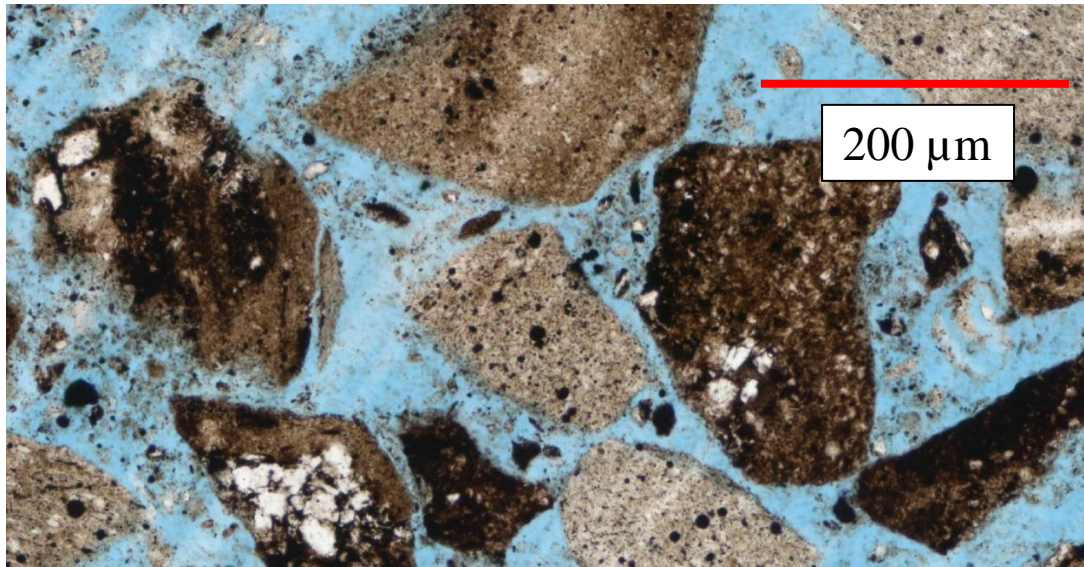


Figure 4.32 Bossier Formation Thin Section, B(60)_{200µm} sample. Abundant fine material is observed between the particles.

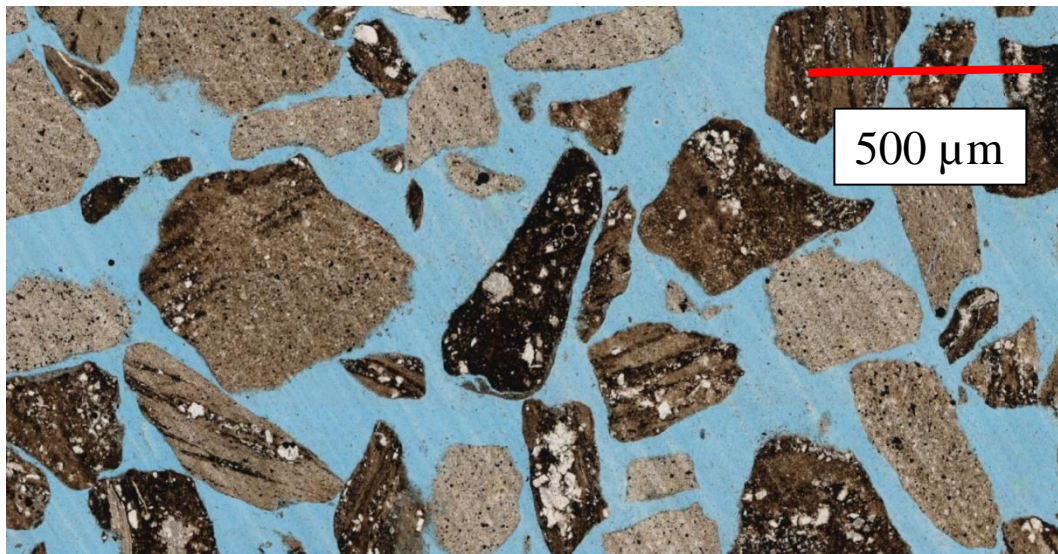


Figure 4.33 Bossier Formation Thin Section, B(60) 500µm sample. The fine particles observed in the smallest particle size are not present.



Figure 4.34 Bossier Formation Thin Section, B(60)700µm sample. Similar to the previous image, the fine particles observed in the smallest particle size are not present. Scale bar is the size of the particle size, in this case 700 µm.

A similar condition was observed in the Haynesville samples (Figures 4.35 and 4.36) and in the La Luna Formation (Figures 4.37 and 4.38). In the 200 µm samples, fine material is observed between the particles and it is not present in any samples for the larger particle sizes.

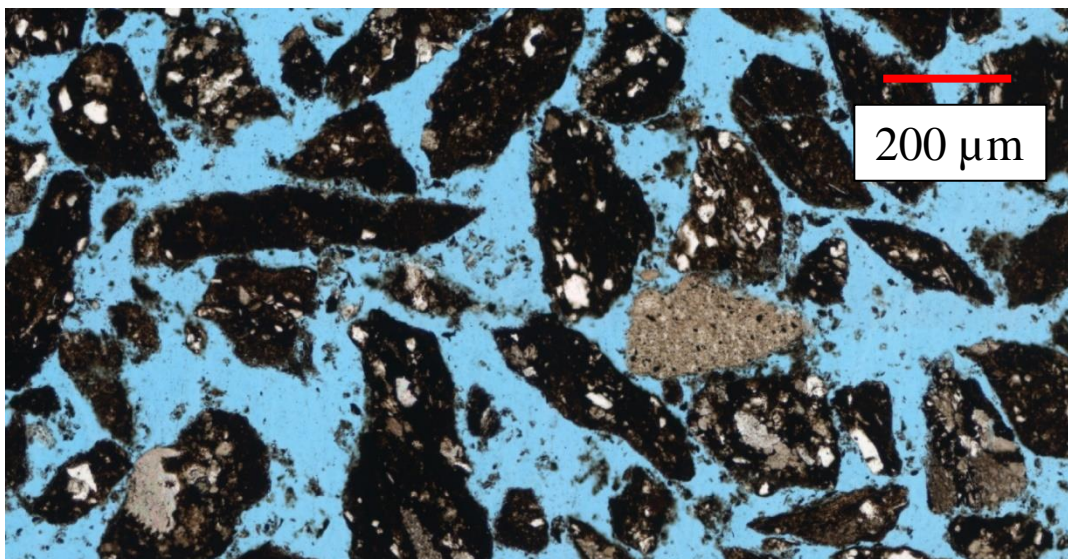


Figure 4.35 Haynesville Formation Thin Section, H(26)200µm sample. Fine material is observed between the particles.

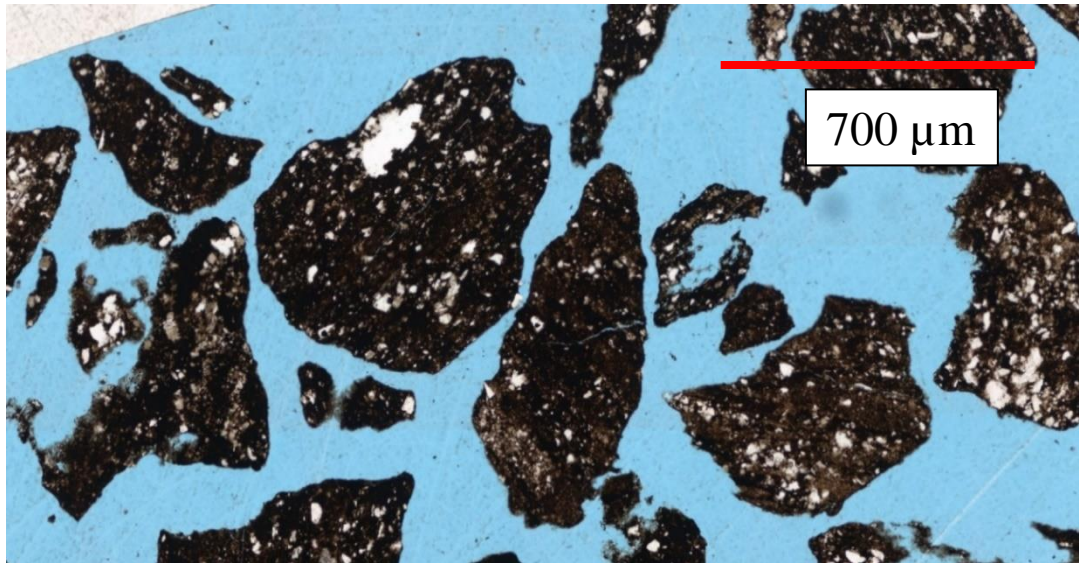


Figure 4.36 Haynesville Formation Thin Section, H(26)700 μ m sample. The fine particles observed in the smallest particle size are not present.

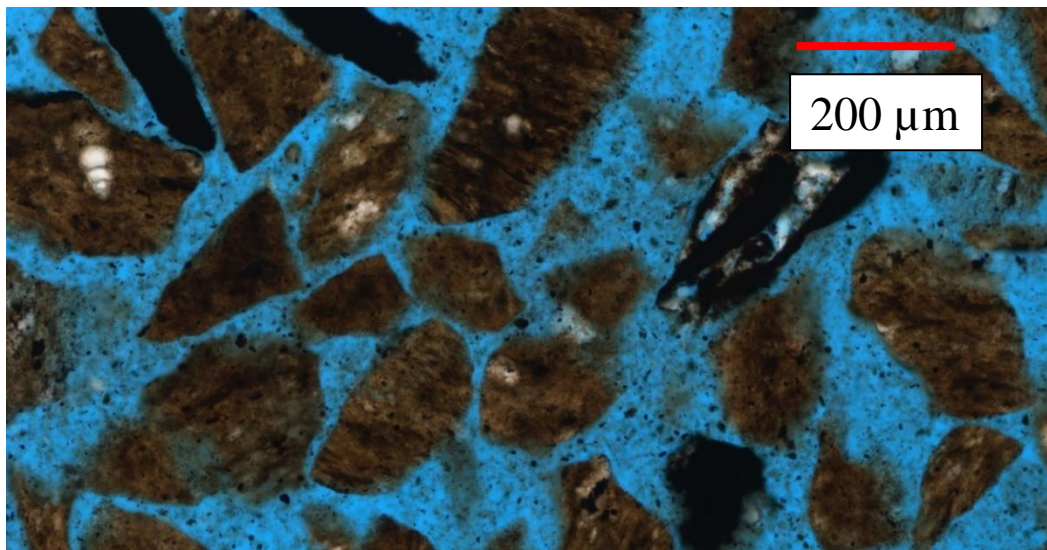


Figure 4.37 La Luna Formation Thin Section, LL(15)_{200 μ m} sample. Fine material is observed between the particles.

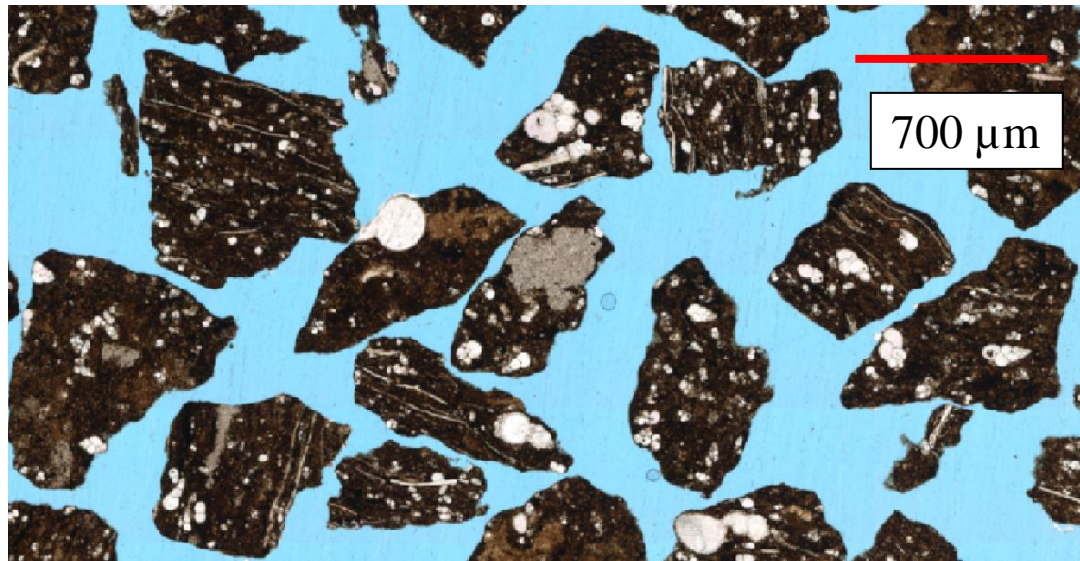


Figure 4.38 La Luna Formation Thin Section, LL(15)_{700µm} sample. The fine particles observed in the smallest particle size are not present in the coarser size fractions.

In the methodology section, the particle size distributions were shown. Based on that, the finest size fraction was excluded from the research due to its bimodal distribution, (a predominantly unimodal distribution was observed for the other sizes) (See Figure 4.38). This suggested a problem with the sieving procedure, in which very fine material is present, and adheres to the sieve mesh. The fines were included when the ground material was retrieved from the sieve. Although the magnitude is smaller than for the 106 – 90 µm sample, a bimodal distribution can also be observed in the 212-106 µm sample (see the red circle in Figure 4.38).

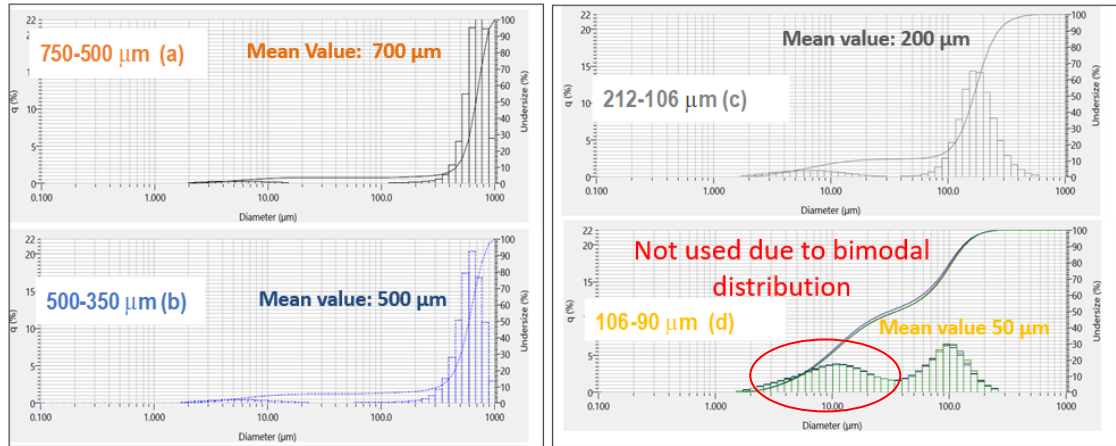


Figure 4.38 Laser particle size distribution for the particle sizes used in the study. The 106 – 90 μm size range was not used in the research due to the bimodal distribution observed in the data. A similar, although less volumetrically important, bimodal distribution is observed in the 212-106 μm .

Modifications to the sieving process are required in order to eliminate this small material. Wet sieving can be used to reduce adhesion of small particles to the mesh, however, due to the objectives of our research, wet sieving of the samples was not an option. In future studies sieving should be conducted in several steps, washing and drying the mesh between each step. A correction for the volume of this fine material must be applied, based on the surface area occupied by this material in each thin section. This will be the subject of future work and for this discussion, the 200 μm sized sample will not be considered for the V_e evaluation.

Figure 4.39 shows the corrected V_e and the clay mineral content with the smallest particle sizes removed. Assuming a direct proportionality, three different relationships between V_e and clay mineral content are observed, one for each formation. Alternatively, two relationships can be applied if the Haynesville and Bossier Formations are evaluated together. Imbibition increases with clay mineral content at different rates for each formation. Figure 4.40 illustrates the corrected V_e and the anhydrite content with the smallest particle size samples removed.

Similar to the clay mineral volume, three different relationships are observed, one for each formation. Imbibition increases with anhydrite content at different rates by formation.

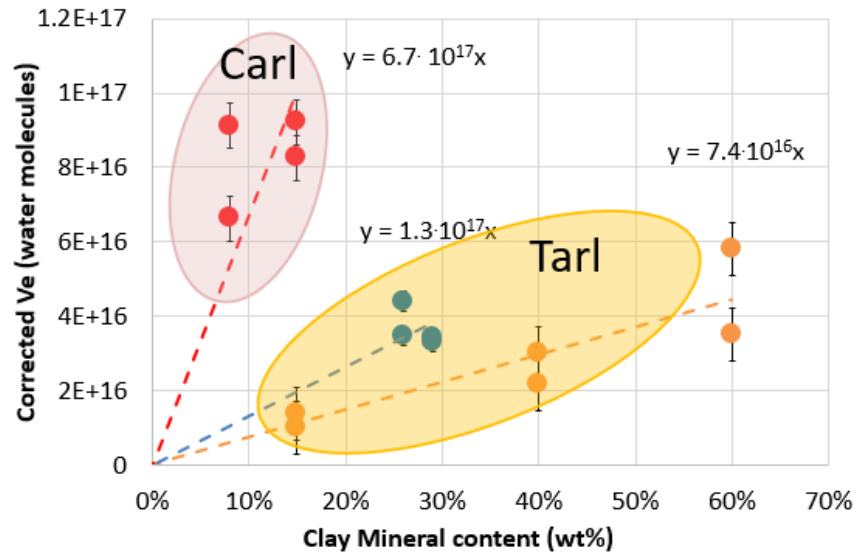


Figure 4.39 Corrected V_e as a function of clay mineral content with the smallest particle size samples removed. Imbibition increases with clay mineral content, at different rates for each formation, although the Haynesville and Bossier could be considered together. The terminology CARL and TARL are from Milliken, (year).

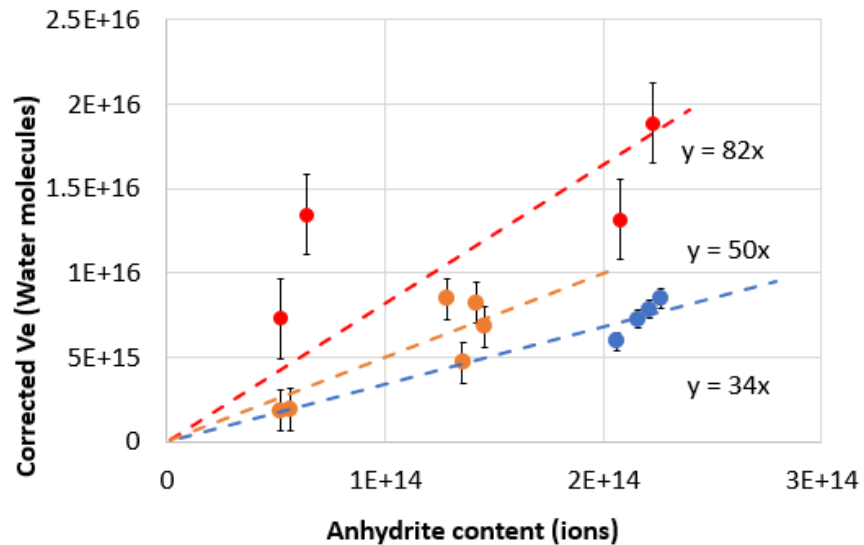


Figure 4.40 Corrected V_e and the anhydrite content with the smallest particle sized samples removed. Imbibition increases with anhydrite content, at different proportions for each formation.

4.5. In situ salinity calculation

Total salinity in the supernatant fluid was calculated by using the data from the imbibition experiments (total final salinity estimated from conductivity), the reported total porosity, and reported water saturation values from core analysis measurements. This information was available only for the Bossier and Haynesville Formations. Additionally, ICP (inductively coupled plasma ion detection) analyses were performed to identify the ionic species present, which allows us to correct the final salinity for the presence of salt minerals (anhydrite). Total dissolved salinity estimates were obtained as follows

$$V_p = \left(\frac{M_t}{\rho g} \right) * \phi \quad , \quad \text{Eq. 10}$$

$$V_{rw} = \frac{W_{vi}}{V_p} \quad , \quad \text{Eq. 11}$$

$$\text{and} \quad \text{Total_Dissolved_Salinity} = C_e * V_{rw} \quad , \quad \text{Eq. 12}$$

where V_p (cc) is the pore volume, M_t (g) is the total material mass used in the experiment, ρg is grain density (g/cc), Φ is porosity, V_{rw} is water volume ratio, W_{vi} (cc) is initial water volume, and C_e (ppm) is the final salinity in the sample, estimated from conductivity. Total salinity estimates were then used to formulate four scenarios for in – situ salinities (Table 3.5).

Table 3.5. Summary for in situ salinities with the assumptions made on each scenario.

In situ salinity values (kppm) and assumptions					
B(60)	B(15)	B(40)	H(26)	H(29)	Assumptions
227	135	176	216	210	Anhydrite is not precipitated in situ and 100% water saturation
446	291	524	999	857	Anhydrite is not precipitated in situ and present day water saturation
82	83	56	56	55	Anhydrite is precipitated in situ and 100% water saturation
161	177	168	260	223	Anhydrite is precipitated in situ and present day water saturation

Figure 4.41 shows the four scenarios formulated for the Bossier Formation, where the water saturation and the estimate of in situ salinity varies. Scenario a): Assumes that anhydrite is not precipitated in situ (i.e. anhydrite precipitation occurred after core acquisition as a function of surface dehydration) and that the entire porosity is 100% water saturated. Reasonable in situ salinity values, on the order of 220 kppm are obtained, however, this implies that gas stripping of water vapor during gas expulsion from the source rock did not occur. Upper bound scenario (b): If present-day water saturation and 100 % final salinity are used (assumes anhydrite was not precipitated in situ) a salinity of 450 kppm is obtained, which is higher than halite saturation at in situ conditions. Because halite precipitation was not observed in the cores, it is not considered physically possible. Lower bound scenario (c): If a correction for dissolved anhydrite is made (assuming anhydrite precipitation occurred in situ) and 100% water saturation is assumed a lower bound of 112 kppm is obtained. Finally, a scenario (d), which we believe is the correct approach, in which the present-day water volume from Dean Stark and the anhydrite correction (%) are applied to obtain an estimated pore fluid salinity of 160 kppm. This scenario is analogous to the Dean Stark Crush and Leach procedure used to report salinity values of 200 kppm for the Haynesville Formation, by Ramirez, 2011. The difference is that in Ramirez, 2011, they estimate the salinity required to correct the measurements only using the measured Cl^{-1} present in the supernatant fluid, and do not include other mineral salts, such as anhydrite. Because the leach time was only 48 hours, all precipitated halite may not have been recovered (our experiments required on the order of one month to equilibrate). Figures 4.42 and 4.43 shows the results from the other samples in the Bossier Formation, B(40) and B(15). Comparing the scenarios for the three different samples, in scenario a) values vary from 135 Kppm to 220 Kppm, this can be translated, assuming an in-situ temperature of 200 °C, as R_w values between 0.018 to 0.024 ohm – m. Scenario b) has estimated pore fluid salinities higher than halite saturation. Because halite precipitation was not observed in the samples, this scenario is not

physically reasonable. Finally, scenario d) shows values that vary from 160 to 180 Kppm, which will provide 0.019 to 0.021 ohm – m.

For the Haynesville Formation, which is deeper than Bossier Formation (figure 4.42), the same four scenarios were considered. Values between 230 and 260 Kppm were obtained in scenario d, which equate to an R_w that ranges between 0.016 ohm – 0.015 ohm-m. For the La Luna Formation, not enough information is available to make the estimate (no Dean Stark measurements are available). Estimates of in situ salinity for the La Luna re the subject of ongoing work.

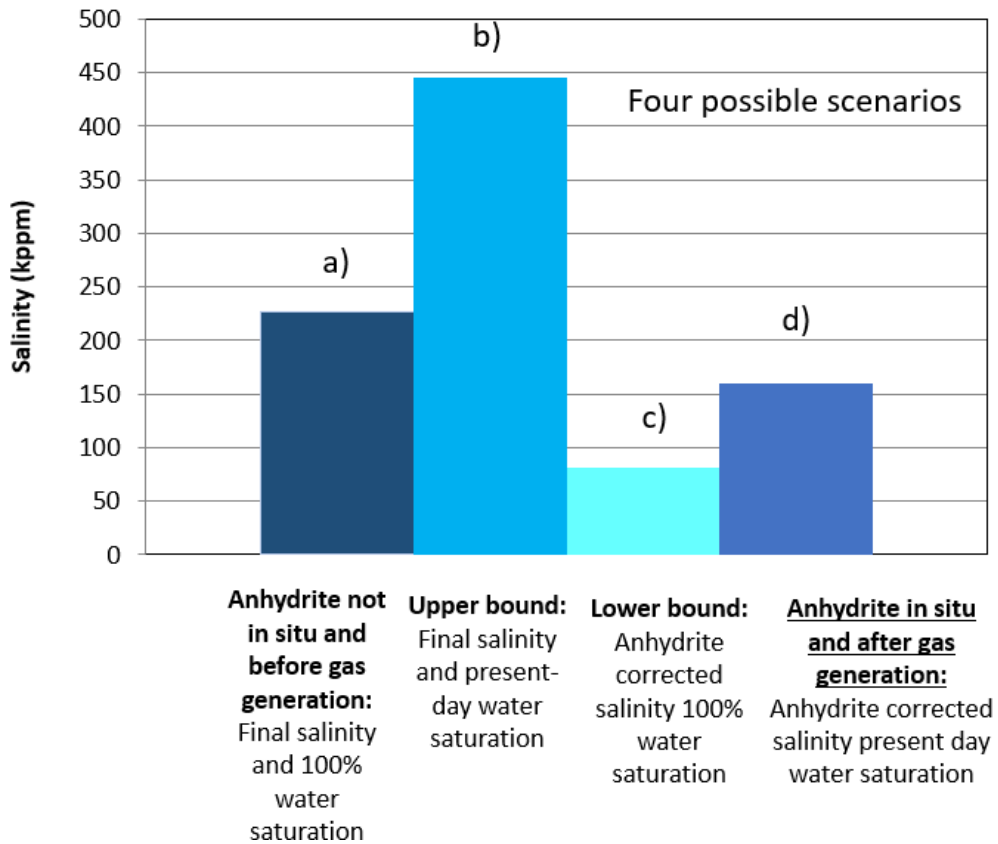


Figure 4.41 B(60) In situ salinity calculation results for different scenarios using a) 100% water saturation and 100 % imbibition final salinity, b) present day water saturation and 100 % imbibition final salinity c) 100% water saturation and 36% imbibition final salinity (removing ions sourced from anhydrite dissolution), and d) present day water saturation and 36% imbibition final salinity.

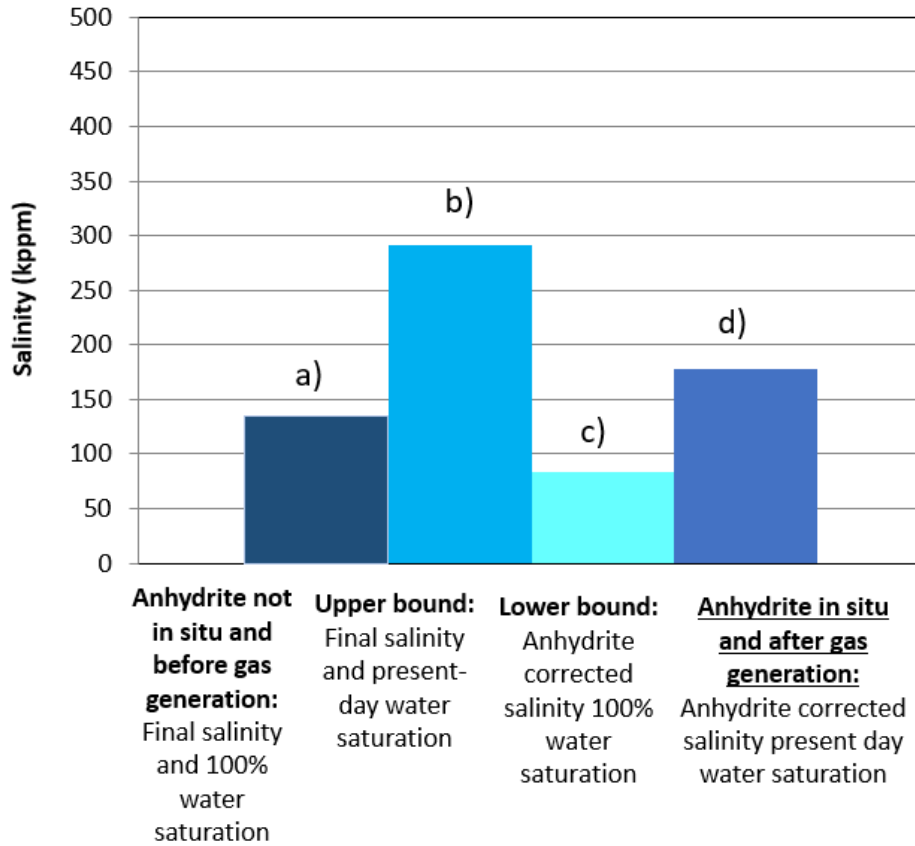


Figure 4.41 B(15) In situ salinity calculation results for different scenarios using a) 100% water saturation and 100 % imbibition final salinity, b) present day water saturation and 100 % imbibition final salinity c) 100% water saturation and 61% imbibition final salinity (removing ions sourced from anhydrite dissolution), and d) present day water saturation and 61% imbibition final salinity.

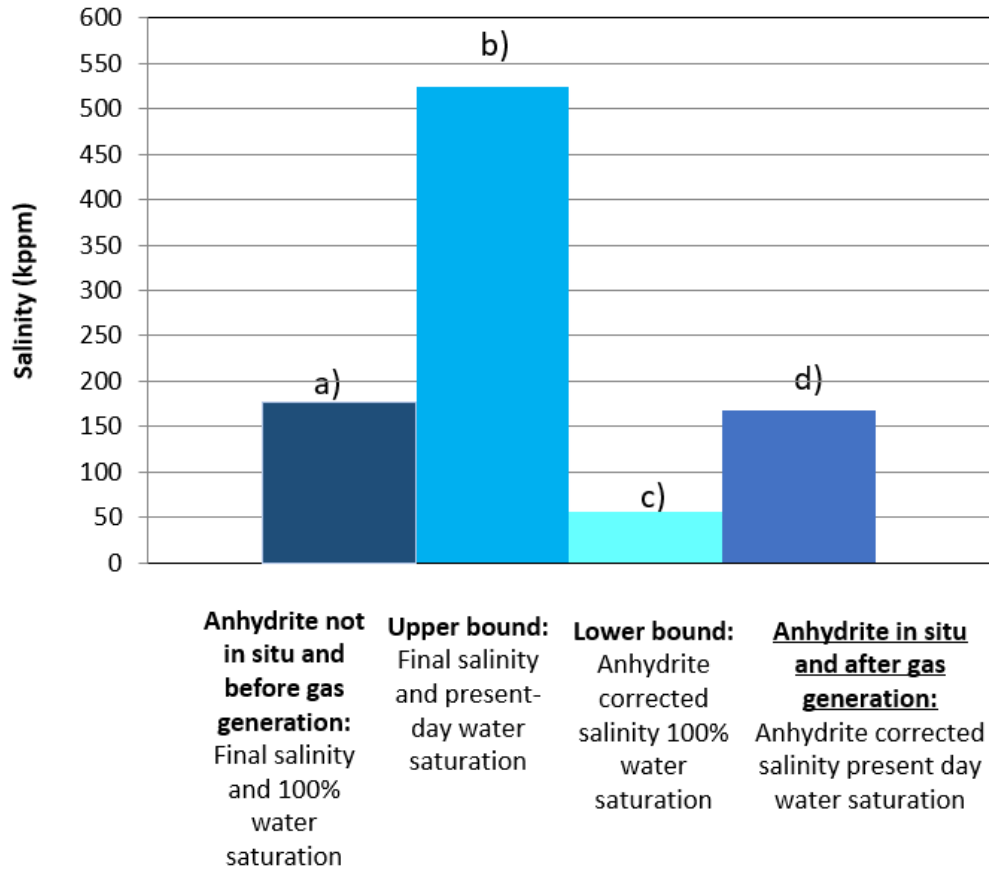


Figure 4.41 B(40) In situ salinity calculation results for different scenarios using a) 100% water saturation and 100 % imbibition final salinity, b) present day water saturation and 100 % imbibition final salinity c) 100% water saturation and 32% imbibition final salinity (removing ions sourced from anhydrite dissolution), and d) present day water saturation and 32% imbibition final salinity.

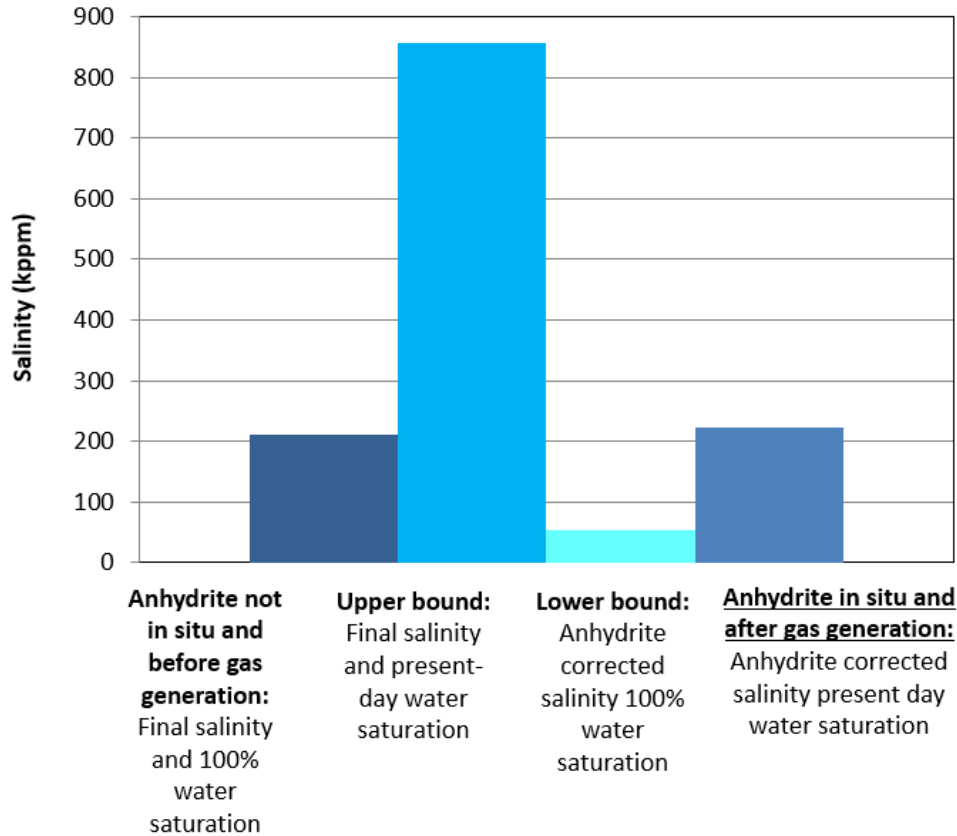


Figure 4.42 Haynesville Formation In situ Salinity Estimation. In situ salinity calculation results for different scenarios using a) 100% water saturation and 100 % imbibition final salinity, b) present day water saturation and 100 % imbibition final salinity c) 100% water saturation and 26% imbibition final salinity (removing ions sourced from anhydrite dissolution), and d) present day water saturation and 26% imbibition final salinity.

The combination of spontaneous imbibition experiments and chemical analysis of the supernatant fluid is a valid approach for deriving in situ salinity and therefore, water resistivity values for shale gas reservoirs. Finally, with these values, Dean Stark porosity can be appropriately corrected for salt content. The approach more commonly used in the industry is to correct the porosity assuming a water salinity of 30 kppm, which is typically too low for these reservoirs.

CHAPTER 5. CONCLUSIONS

This study reports the results of spontaneous imbibition experiments performed on full diameter core samples from shale gas reservoirs. Seven different samples, selected from 89 feet of core, were used. Samples were selected so that varying clay mineral content, porosity, permeability and water saturation were studied. Each sample was crushed to three different particle sizes for testing. This approach was motivated by the absence of time dependent flowback water samples. The spontaneous imbibition experiments were considered analogues to the injection of fresh water during stimulation and the results analogous to the resulting high salinity and low load recovery on these reservoirs.

A spontaneous imbibition-based model developed to indicate the source of high flowback water salinity in the Bossier, Haynesville and the La Luna Formations suggests that two mechanisms are present: anhydrite (salt) dissolution and interaction with clay mineral surfaces, a function of the cation exchange capacity. Anhydrite, observed precipitated between clay platelets contributes substantially to imbibition water salinity in the Bossier Formation. Fracture fill is more common in the La Luna Formation and likely is the main reason for its high flowback water salinity.

An imbibed water model was developed (in volume and in time) and provides a promising technique for estimating organic porosities in shale gas reservoirs. When corrected for the volume of dissolved salt and the volume of induced fractures formed during sample preparation, the difference between the imbibed water volume and as-received Boyle's Law porosities are in good agreement with estimates of organic matter hosted porosity from oil imbibition and image analysis studies. Results also suggested that at this level of maturation, approximately 1.4-2.5% R_o , organic pores remain oil wet. The imbibed water volume will not be affected by organic matter hosted porosity.

The imbibed water volume model suggests that a total porosity correction, particularly in high carbonate content formations, should be applied to routine GRI measurements, due to induced fractures created when crushing the sample. The volume of these induced microcracks formed during sample preparation increases as a function of particle size, and carbonate content and was observed to be greatest in the particle size most often used for crushed rock measurements using the GRI (Gas Research Institute) protocol. A recommendation is to use NMR measurements, pre and post Boyle's law porosity measurement, which will provide a good estimate of the volume of those induced fracture pores.

The results of imbibition/ion expulsion experiments can be used to generate estimates of in situ pore fluid salinities for interpretation of electrical logs. A scenario was developed to determine the present day in-situ salinity. This uses the as received, present-day water saturation (from Dean Stark) and the final equivalent NaCl salinity corrected for anhydrite dissolution. The estimated in-situ salinities in the Bossier and Haynesville Formations are 170 kppm and 220 kppm respectively. . This estimate of in situ salinity will allow the Dean Stark porosity to be appropriately corrected for salt content, instead of using an assumed value (typically 30 kppm).

The original concept of a permeability model was based on literature results suggesting a possible relationship between imbibition and diffusion coefficients. Although particle size dependence was originally observed in the water imbibition data, data analyses suggests that this observation resulted from two effects associated with sample preparation. Anhydrite (or precipitated salt) becomes concentrated in the finer size fractions. This results from the mechanical properties of the salts (cleavage and hardness) causing them to break more easily during sample preparation. In addition, the retention of very fine material that adheres to the sieve mesh as mesh size decreases, which was included when the ground material was retrieved

from the sieve, resulted in increasing volumes of imbibed fluid. When these effects are removed from the data, no grain size dependence on the conductivity, nor on the imbibition results was observed. This suggests the absence of a characteristic length, which is a well-established condition for diffusion processes.

Additionally, results showed that as clay mineral content increases, the time required to reach equilibrium decreases, which is also not a condition expected for a diffusion-controlled process. For these reasons, as well as a lack of confidence in the GRI methodology used to estimate permeability in the samples, a permeability model was not obtained, and will be the subject of future work.

The experimental approach, combining water and oil imbibition with ion expulsion experiments, and detailed sample and brine characterization can be used to gain an understanding of the high flowback salinity and low load recovery in the Bossier, Haynesville and La Luna Formations. The experimental results provide insight into:

- **Mineralogy:** Imbibition experiment salinity and the imbibed water volume can be used as a proxy for mineralogy. High maturity, carbonate rich mudrocks (La Luna Formation) and high maturity clay mineral rich mudrocks (Bossier and Haynesville Formation) can be differentiated by using this information. Carbonate rich formations with high precipitated salt content (in the La Luna Formation, anhydrite), will provide high salinity flowback and exhibit high volumes of imbibed water. High clay mineral content formations, will provide a high salinity flowback, with low to moderate imbibed volumes. When salt dissolution occurs in clay mineral rich formations, higher volumes of water will be imbibed, and the resulting flow back salinity will be higher.

- **Rate of change of spontaneous imbibition salinity:** Results of this work suggest that the rate at which the ions are expelled during the imbibition experiment, depends on the clay mineral content and the precipitated salt volume. The rate of change in salinity is faster and less complicated than the rate at which water is imbibed. The imbibition rate is a function of clay mineral content and relative connectivity (percolation) through the rock volume, the volume of precipitated salts and their distribution, and on the mineral dissolution rate. The spontaneous imbibition salinity is suggested to vary as a function of clay mineral content and could provide an indication of relative brittleness or fracability.
- **Total Porosity:** Comparison of the Boyle's Law total porosity measurements, and the imbibed water total porosity from the experiments, suggests that water was not imbibed into the organic matter hosted pore-system. This measurement required a correction for the volume of induced fractures and dissolved salts. As the water wet porosity system increases, salinity and imbibed volume increases. The proportion of induced fracture porosity was observed to be a function of carbonate content in both terrigenous argillaceous mudrocks and calcareous mudrocks.

The water wet porosity system increases as the clay mineral content increases, resulting in an increase in both supernatant fluid salinity and imbibed volume (lower load recovery). In formations for which salt dissolution is the rate limiting step, as observed in the La Luna Formation, imbibed volume and flow-back salinity will both increase as the volume of precipitated salt increases. Imbibed water volume is a function of total porosity, and the volume of mineral

hosted (water wetting) pores present in the rock. This includes predominantly clay mineral associated porosity, pores created by salt dissolution and the induced porosity created by the crushing of the sample during sample preparation.

- The Cation Exchange Capacity (CEC) of the clay minerals influences the salinity of flowback water in shale gas reservoirs. Measurements on different particle size aliquots for the different formations tested, suggest that CEC does not vary with grain size. This is supported by the results of X-Ray diffraction analysis performed on the various particle size aliquots. As clay mineral content increases, and CEC increases, imbibition salinity and imbibed water volume increase.

REFERENCES

1. Aguilera, R. "Flow Units: From Conventional to Tight-Gas to Shale-Gas to Tight-Oil to Shale-Oil Reservoirs." SPE, 2014.
2. Aguilera, R. "Flow units: From Conventional to Tight Gas to Shale Gas reservoirs." SPE Paper 132845. Trinidad y Tobago Energy Resources conference, 2010.
3. Akbarabadi, M. "Nano tomography of the Spontaneous Imbibition in Shale." Unconventional Resources Technology Conference, 2015.
4. Ambrose, Susan A. "How Learning Works: Seven Research-Based Principles for Smart Teaching." 2010.
5. Al-Arfaj, M., Al-Osail, M., & Sultan, A. "Monitoring Imbibition of Water into Shale Pore System: State of the Art." Society of Petroleum Engineers, 2017.
6. Alqahtani, A., "Quantification of Total Organic Carbon Content in Shale Source Rocks: An Eagle Ford Case Study." Paper URTeC 1921783, presented at the URTeC, 2014.
7. Ambrose, R.J., Hartman, R.C., Diaz-Campos, M., Akkutlu, I.Y., Sondergeld, C.H. "Shale gas-in-place calculations Part I: New pore-scale considerations." SPE Journal 17 (1).
8. Asadi, M., Woodroof, R.W., Malone, W.S., and Shaw. "Monitoring Fracturing Fluid Flowback With Chemical Tracers: A Field Case Study. Paper SPE 77750 presented at the SPE Annual Technical Conference and Exhibition, 2002.
9. Asadi, M. "Post-Frac Analysis Based on Flowback Results Using Chemical Frac-Tracers." International Petroleum Technology Conference, 2008.

10. Ballard, T. J, “Fundamentals of Shale Stabilization: Water Transport Through Shales.” Society of Petroleum Engineers, 1994.
11. Bearinger, D. “Message in a Bottle.” SPE/AAPG/SEG Unconventional Technology Conference, 2013.
12. Bennion, D.B. “Formation Damage Processes Reducing Productivity of Low Permeability Gas Reservoirs.” SPE. Low permeability reservoirs Symposium, 2000.
13. Behar, F., Beaumont, V., Penteado, H.L., De, B. “Rock-Eval 6 technology: performances and developments oil & gas science and technology.” Rev. IFP 56 (2), 111–134. 2001.
14. Bissada, K.K, L.W. Elrod, C.R. Robison, L.M. Darnell, H.M. “Energy Exploration & Exploitation.” Vol. 11, No. 3/4, SPECIAL ISSUE: Hydrocarbon Exploration, pp. 295-328. 1993.
15. BP Tissot, “Petroleum Formation and Occurrence. A new approach to oil and gas exploration.” 1978.
16. Blauch, M. “Marcellus Shale Post-Frac Flowback Waters - Where is All the Salt Coming from and What are the Implications?” SPE 125740, 2009.
17. Boyer, C., “Producing gas from its source.” Oilfield Review 1 (3), 36–49. 2006.
18. Bust, V.K., Majid, A.A., Oletu, J.U., Worthington, P.F. “The Petrophysics of Shale Gas Reservoirs.” Technical. 2011.
19. Bustin, R.M., “Impact of Shale Properties on Pore Structure and Storage Characteristics.” SPE 119892, presented at the SPE Shale Gas Production Conference, 2008.

20. Campos, J., Hilchie, D. "The Effects of Sample Grinding on Cation Exchange Capacity Measurements." 1980.
21. Carman, P.S., Lant, K., "Making the case for shale clay Stabilization." SPE 139030, SPE Eastern Regional Meeting, Morgantown, 2010.
22. Chakraborty, N., & Karpyn, Z. T. "Gas Permeability Evolution with Soaking Time in Ultra Tight Shales." Society of Petroleum Engineers, 2015.
23. Clarkson. L, "Case Study: Production Data and Pressure Transient Analysis of Horseshoe Canyon CBM Wells." The Journal of Canadian Petroleum Technology 48: 27- 38, 2009.
24. Clarkson,C., Beierle, J., "Integration of Micro seismic and Other Post-Fracture Surveillance with Production Analysis: A Tight Gas Study." SPE Unconventional Gas Conference, 2010.
25. Curtis, John. "Fractured shale-gas systems." AAPG Bulletin, 2002
26. Daniels, J.L. "Contacting more of the Barnett shale through an integration of real-time micro seismic monitoring, petrophysics, and hydraulic fracture design." In Proceedings of the SPE Annual Technical Conference and Exhibition, 2007.
27. Dehghanpour, H, 2012. "Liquid intake of organic shales." Energy & Fuels, 26, 5750-5758.
28. Dehghanpour, H., "Spontaneous Imbibition of Brine and Oil in Gas Shales: Effect of Water Adsorption and Resulting Microfractures." Energy & Fuels, 2013.
29. Ding, M., Kantzas, A., & Lastockin, D. "Evaluation of Gas Saturation During Water Imbibition Experiments." Petroleum Society of Canada, 2013.

30. Dressel, P.E., and Rose, A.W, “Chemistry and Origin of Oil and Gas Well Brine in Western Pennsylvania.” Open file report, 2010.
31. Dogan, A.U., Dogan, M., Onal, M., Sarikaya, Y., Aburub, A., AND Wurster, D.E., “Baseline studies of the Clay Minerals Society source clays: specific surface area by the Brunauer Emmett Teller (BET) method: Clays and Clay Minerals”, v. 54, p. 62–66. 2006.
32. Emmanuel, S., Ague, J.J., and Walderhaug, O., “Interfacial energy effects and the evolution of pore size distributions during quartz precipitation in sandstone”: *Geochimica Acta*, v. 74, p. 3539–3552. 2010.
33. Engelder, T., “Capillary tension and imbibition sequester frack fluid in Marcellus gas shale: Proceedings of the National Academy of Sciences of the United States of America”, v. 109, no. 52, 2012
34. Fan, Li. “Understanding Gas Production Mechanism and Effectiveness of Well Stimulation in the Haynesville Shale Through Reservoir Simulation.” SPE, 2010.
35. Fisher, M.K. “Optimizing Horizontal Completion Techniques in the Barnett Shale Using Micro Seismic Fracture Mapping.” SPE Annual Technical Conference, 2004.
36. Frantz, J.H. “Evaluating Barnett Shale Production Performance Using an Integrated Approach.” Paper SPE 96917 presented at the SPE ATCE Conference, Dallas, Texas, USA. 2005.
37. Frantz, J.K. and Jochen, V. “Shale Gas White Paper.” Schlumberger Marketing Communications, 2005.

38. Fakcharoenphol, P. "The effect of Osmotic Pressure on Improve Oil Recovery from Fractured Shale Formations." SPE, URTEC, 2014.
39. Folk, R.L, "Petrology of Sedimentary Rocks": Austin, Texas, Hemphill Publishing Company, 182 p. 1980.
40. Gdanski, R. "Numerical Study of PDL-Induced Fracture-Face Damage using a Fracturing Mimicator." SPE. 2010.
41. Gdanski, R. D. "Modeling the Impact of Capillary Pressure Reduction by Surfactants." Society of Petroleum Engineers, 2017.
42. Ghanbari, E. "Flowback Volumetric and Chemical Analysis for Evaluating Load Recovery and Its Impact on Early-Time Production." SPE. URTEC, 2013.
43. Ghanbari, E., Xu, M., Dehghanpour, H., & Bearinger, D. "Advances in Understanding Liquid Flow in Gas Shales." Society of Petroleum Engineers, 2014.
44. G.T. Phillipe, "On the depth, time and mechanism of petroleum generation." 1968.
45. Hammes, U., S. H. Hamlin, and T. E. Ewing, "Geologic analysis of the Upper Jurassic Haynesville Shale in east Texas and west Louisiana": AAPG Bulletin, v. 95, no. 10, p. 1643–1666, 2011.
46. Haluszczak, L. "Geochemical evaluation of flowback brine from Marcellus gas wells in Pennsylvania." Applied Geochemistry, 2013.
47. Hamblin, Anthony P. "The" shale gas" concept in Canada: a preliminary inventory of possibilities." Geological Survey of Canada, 2006.
48. Handy, L. L. "Determination of Effective Capillary Pressures for Porous Media from Imbibition Data." Society of Petroleum Engineers, 1960.

49. Hayes, T., 2009. "Sampling and analysis of water streams associated with the development of Marcellus shale gas." Report by Gas Technology Institute, for the Marcellus Shale Coalition, 2009.
50. Holditch, S. "Factors Affecting Water Blocking and Gas Flow from Hydraulically Fractured Gas Wells." 1979.
51. Holditch, S., Royer, J.J., "Unconventional Resource Handbook: Evaluation and Development." Elsevier.
52. Huang, Y. "Effect of coal mining on vegetation disturbance and associated carbon loss." Environmental Earth Science, 2014.
53. Hu, Q., "Pore Accessibility and Connectivity of Mineral and Kerogen Phases in Shales." Unconventional Resources Technology Conference, 2014
54. Hunt, J. "Petroleum Geology and Geochemistry." 1996.
55. Jarvie, D., R. J. Hill, T. E. Ruble, and R. M. Pollastro, 2007, "Unconventional shale-gas systems: the Mississippian Barnett Shale of north-central Texas as one model for thermogenic shale-gas assessment." AAPG Bulletin, v. 91, no. 4, p. 475–499, 2007.
56. Jayakumar, 2011. "Impact of Uncertainty in Estimation of Shale Gas Reservoir and Completion Properties on EUR Forecast and Optimal Development Planning: A Marcellus Case Study." SPE Reservoir Evaluation & Engineering., 2012.
57. Johnston, C.T., "Probing the nanoscale architecture of clay minerals: Clay Minerals", v. 45, p. 245–279. 2010
58. Johnson, W. L. and Linke, W. A., 1977, "Some Practical Applications to Improve Formation Evaluation of Sandstones in the Mackenzie Delta." Presented at the 6th

Formation Evaluation Symposium of Canadian Well Logging Society in Calgary, 1977.

59. Johnson, M.D., Pechiney, J.J., Warren, M.N., Woodroof, R.A., Leonard, R.S., and Moore, C.P. "Using Completion Diagnostics to Optimize Completion Designs in Several Horizontal Shale Plays." Paper SPE 166488 presented at the SPE Annual Technical Conference and Exhibition, 2013.
60. Jorden and F. Campbell "Well logging I. Rock properties Borehole Environment, mud and temperature logging." SPE.
61. Keller, G. "Elastic, Mechanical, And Electrical Properties of Low-porosity Rocks." Society of Petrophysicists and Well-Log Analysts, 1981.
62. King, G.E., "Hydraulic fracturing 101: What every representative, environmentalist, regulator, reporter, investor, university researcher, neighbor, and engineer should know about estimating frac risk and improving frac performance in unconventional oil and gas wells", Paper SPE 152596 presented at Society of Petroleum Engineers Hydraulic Fracturing Technology Conference, 2012.
63. Klimchouk, A. "Dissolution and Conversions of Gypsum to Anhydrite." National Academy of Science of Ukraine. Research Gate. April 2000.
64. Kuru, E. "Drainage Against Gravity: Factors Impacting the Load Recovery in Fractures." SPE - URTEC.2013, 2013.
65. Li, X.-C F.-C., Watson, A.T. "Adsorption Studies of Natural Gas Storage in Devonian Shales." SPE Formation Evaluation 26632, 1995.
66. Loucks, R.G., R.M. Reed, S.C. Ruppel, and D.M. Jarvie. "Morphology, genesis, and distribution of nanometer-scale pores in siliceous mudstones of the Mississippian

- Barnett Shale.” v. 79/12, p. 848-861, 2009.
67. Loucks, R.G., “Spectrum of pore types and networks in Mudrocks and a Descriptive Classification for matrix related Mudrock pores.” AAPG Bulletin 96 (6), 1071–1098. 2012.
68. Lu, J., Ruppel, S.C. “Organic matter pores and oil generation in the Tuscaloosa marine shale.” AAPG Bulletin 99 (2), 333–357. 2015.
69. Luffel, D.L., Guidry, F.K., Curtis, J.B. “Evaluation of Devonian Shale with New Core and Log Analysis Methods.” SPE, 21297, JPT, 1192–1197. 2012.
70. Ma, Y.Z. “Uncertainty analysis in reservoir characterization and management.” Ma, Y.Z., LaPointe, P.(Eds.), Uncertainty Analysis and Reservoir Modeling, AAPG Memoir 96. 2011.
71. Ma, Y.Z., “Integrated reservoir modeling of a Pinedale tight-gas reservoir in the greater Green river Basin, Wyoming.” In: Ma, Y.Z., LaPointe, P. (Eds.), Uncertainty Analysis and Reservoir Modeling, AAPG Memoir 96, pp. 89–106. 2011.
72. Macquaker, J.H.S., Keller, M.A., and Davies, S.J., “Algal bloom and “marine snow” : mechanisms that enhance preservation of organic carbon in ancient fine-grained sediments.” Journal of Sedimentary Research, v. 80, p. 934–942. 2010.
73. Marks, L., Viewpoint: “What are the resolution limits in electron microscopes?” Physics, v. 6, p. 82. 2013.
74. M. Economides. “Petroleum Production System”. Second Edition, 2013.
75. Mark A Parker, Dan Buller, James Erik Petre, Douglas Troy Dreher. “Haynesville shale-

- petrophysical evaluation.” In SPE Rocky Mountain Petroleum Technology Conference. Society of Petroleum Engineers, 2009.
76. Makhanov, K., Dehghanpour, H., & Kuru, E. “Measuring Liquid Uptake of Organic Shales: A Workflow to Estimate Water Loss During Shut-in Periods.” Society of Petroleum Engineers, 2013.
77. Makhanov, K. “An Experimental Study of Spontaneous Imbibition in Horn River Shales.” 2012.
78. Mahadevan, J. “Impact of Capillary Suction on Fracture Face Skin Evolution in Water blocked Wells.” SPE. Hydraulic Fracturing Technology Conference, 2009.
79. Makhanov, K. “Measuring Liquid Uptake of Organic Shales: A Workflow to Estimate Water Loss During Shut-in Periods.” SPE. URTEC, 2013.
80. McIntosh, J.C., “Geochemical and isotopic composition of Appalachian Basin brines: Origin of salinity and fingerprints of fluid reservoirs: Geological Society of America Abstracts with Programs”, v. 44, no. 7, p. 337, 2012.
81. Merry, H. and Ehlig-Economides, “Model for a Shale Gas Formation with Salt-Sealed Natural Fractures.” SPE, 2015.
82. Meyer. B.I., “Identification of source rocks on wireline by density/resistivity and sonic transit time/resistivity crossplot.” 1984.
83. Milliken, K, “A compositional classification for grain assemblages in fine grained sediments and sedimentary rocks.” Bureau of Economic Geology, Jackson School of Geosciences. University of Texas at Austin, Texas 78759, USA. 2014.
84. Milliken, K.L., Papazis, P.K., Day-stirrat, R.J., and Dohse, C., “Carbonate lithologies

- of the Barnett Shale, in Breyer, J., ed., *Shale Reservoirs—Giant Resources for the 21st Century.*” American Association of Petroleum Geologists, Memoir 97, p. 290–321.
85. Milliken, Kitty. “A Compositional Classification for Grain Assemblages in Fine-Grained Sediments and Sedimentary Rocks.” *Journal of Sedimentary Research*, 2014.
 86. Montgomery, “*Hydraulic Fracturing: History of an Enduring Technology.*” *Journal of Petroleum Technology*, 62, 2010.
 87. Ning, X., Fan, J., Holditch, S.A., and Lee, W.J. “The measurement of Matrix and fractures Properties in naturally Fractured cores.” Paper SPE 25898. *Low permeability Reservoirs Symposium*, 1993.
 88. Pritz, M.E., Kirby, C.S. “Geochemical investigation of Marcellus Shale natural gas hydrofracturing waters.” *Geol. Soc. Am. Abstr. Prog.*42 (1), 121, 2010.
 89. Parmar, J. “Unstable Displacement: A Missing Factor in Fracturing Fluid Recovery.” SPE, 2012.
 90. Passey, Q., Creaney, S., Kulla, J., Moretti F. and Stroud, J. “A practical model for organic richness from porosity and resistivity logs.” *The American Association of Petroleum Geologists Bulletin*. 74(12): 1777- 1794, 1990.
 91. Passey, Q.R. “From Oil-Prone Source Rock to Gas-Producing Shale Reservoir, Geologic and Petrophysical Characterization of Unconventional Shale-Gas Reservoirs.” Paper SPE 131350 presented at the CPS/SPE International Oil and Gas Conference and Exhibition, Beijing, China. 2010.
 92. Penny, G.S., Pursley, J.T. “Field Studies of Drilling and Completion Fluids to Minimize Damage and Enhance Gas Production in Unconventional Reservoirs.” SPE 107844,

- presented at European Formation Damage Conference, 2007.
93. Peters, K.E., Cassa , M.R., 1994. “Applied source rock geochemistry.” In: Magoon, L.B., Dow, W.G. (Eds.), *The Petroleum System—From Source to Trap*: Tulsa, Okla., American Association of Petroleum Geologists Memoir 60, pp. 93–117. 1994.
 94. *Petroleum geology of the Bakken Formation, Williston basin, North Dakota and Montana* . Montana Geology Society. F.F. Meissner. 1978.
 95. Pope, C.D., Palisch, T.T., Lolon, E., Dzubin, B., and Chapman, M.A. 2010. “Improving Stimulation Effectiveness: Field Results in the Haynesville Shale.” Paper SPE 134165 presented at the SPE Annual Technical Conference and Exhibition, 2010.
 96. Pritz, M.E., Kirby, C.S., “Geochemical investigation of Marcellus Shale natural gas hydrofracturing waters.” *Geol. Soc. Am. Abstr. Prog.*42 (1), 121. 2010.
 97. Rezaee, R, “Fundamentals of Shale Reservoirs.” *Energy Information Administration Bulletin*, 2015.
 98. Ritter, U. “*Fractionation of petroleum during expulsion from kerogen.*” *Journal of Geochemical Exploration* , 2003.
 99. Rowan. “Radium Content of Oil- and Gas-Field Produced Waters in the Northern Appalachian Basin (USA): Summary and Discussion of Data.” U.S Department of the Interior, 2011.
 100. Rokosh, Dean. “Geochemical and Geological Characterization of the Duvernay and Muskwa Formation in Alberta.” 2010.
 101. Rowan, E.L., Engle, M.A., Kraemer, T.F., Schroeder, K.T., Hammack, R.W., and Doughten, M.W., “Geochemical and isotopic evolution of water produced from Middle

- Devonian Marcellus shale gas wells, Appalachian basin, Pennsylvania: American Association of Petroleum Geologists Bulletin”, v. 99, no. 2, p. 181–206, 2015.
102. Rushing, J.A., Newsham, K.E., Blasingame, T.A. “Rock Typing - Keys to Understanding Productivity in Tight Gas Sands.” Paper SPE 114164 presented at the SPE. 2008.
103. Sakhaee-Pour, A., & Bryant, S. “Gas Permeability of Shale. Society of Petroleum Engineers”, 2012.
104. Schieber, J., Southard, J., and Thaisen, K., “Accretion of mudstone beds from migrating floccule ripples”: Science, v. 318, p. 1760–1763, 2007.
105. Schieber, J., Southard, J.B., Kissling, P., Rossman, B., and Ginsburg, R., “*Experimental deposition of carbonate mud from moving suspensions: importance of flocculation and implications for modern and ancient carbonate mud deposition.*” Journal of Sedimentary Research, v. 83, p. 1025–1031. 2013.
106. Stoneburner, R., “The Haynesville Shale: What we have learned in the first two years.” SIPES Quarterly, v. 46, no. 3, 7 p, 2010.
107. Soeder, D.J., Randolph, P.L., and Matthews, R.D., 1986, “Porosity and Permeability of Eastern Devonian Gas Shale: Chicago, Illinois, Institute of Gas Technology”, prepared for U.S. Department of Energy under contract DE-AC21–83MC20342, 1986.
108. Song, Y. “The concept and the accumulation characteristics of unconventional hydrocarbon resources”, 2015.
109. Sullivan, R.; Woodroof, R.; Steinberger-Glaser, A.; Fielder, R.; Asadi, M. 2004. “Optimizing fracturing fluid cleanup in the Bossier Sand using chemical frac tracers

- and aggressive gel breaker deployment.” Society of Petroleum Engineers annual technical conference and exhibition, 2004.
110. Stewart, B.W., Chapman, E., Capo, R.C., and Schroeder, K., “Origin of brines, salts and carbonate from shales of the Marcellus Formation: Evidence from geochemical and Sr isotope study of sequentially extracted fluids: Applied Geochemistry”, v. 60, p. 78–88, 2015.
 111. Tissot, B.P., Welte, D.H. “Petroleum Formation and Occurrence.” Springer-Verlag. 1984.
 112. Thompson, J.W., Fan, L., Grant, D., Martin, R.B., Kanneganti, K.T. “An Overview of Horizontal Well Completions in the Haynesville Shale.” Paper SPE 136875 presented at the Canadian Unconventional Resources and International Petroleum Conference, 2010.
 113. Torres, E. “Unconventional Resources Assessment of La Luna Formation in the Middle Magdalena Valley Basin, Colombia”, 2012.
 114. Treybal, R.E., “Mass Transfer Operations”, McGraw Hill, 1955.
 115. Tourtellot, H.A. “Origin and Use of the word Shale.” Am.J. Sct, Bradley Vo, 558- A.
 116. Twenhofel. “Silurian Strata of Notre Dame Bay and Exploits Valley, Newfoundland.” GSA Bulletin, 1937.
 117. Van Krevelen, D.W. “Coal: Typology-Chemistry-Physics-Constitution.” Elsevier Science, Amsterdam. 1961.
 118. Ursula Hammes, H Scott Hamlin, and Thomas E Ewing. “Geologic analysis of the Upper Jurassic Haynesville Shale in east Texas and west Louisiana.” AAPG bulletin,

- 95(10): 1643–1666, 2011.
119. Wang, G., and T. R. Carr, “Marcellus Shale lithofacies prediction by multiclass neural network classification in the Appalachian Basin: Mathematical Geosciences”, v. 44, p. 975–1004, 2012.
120. Wang, J.J., Raham, S.S., 2015. “An Investigation of Fluid Leak-off Due to Osmotic and Capillary Effects and its Impact on Micro-fracture Generation during Hydraulic Fracturing Stimulation of Gas Shale.” Paper SPE-174392-MS presented at the EUROPEC, 2015.
121. Wasaki, A., & Akkutlu, I. Y. “Permeability of Organic-Rich Shale.” Society of Petroleum Engineers, 2015.
122. Waxman, M. H. and Smits, I. J. M., 1968, "Electrical Conductivities in Oil-Bearing Shaly Formation Sands." Presented as paper SPE 1863-A at SPE 42nd Annual Fall Meeting, 1967.
123. Woodroof, R.A., Jr.; Asadi, M.; Leonard, R.S.; Rainbolt, M. 2003a. “Monitoring fracturing fluid flowback and optimizing fracturing fluid cleanup in the Bossier Sand using chemical frac tracers.” Society of Petroleum Engineers annual technical conference and exhibition, 2003.
124. Woodward, H.P, “Devonian of West Virginia: West Virginia Geological Survey Report” V-15, 655 p., 1943.
125. Yang, L, “New Method for Inferring the Mean Pore Size of Shale Using Imbibition-Diffusion Data”, 2017.
126. Yang, L., Liu, D., Ge, H., Shen, Y., Li, C., & Zhang, K. “Experimental Investigation

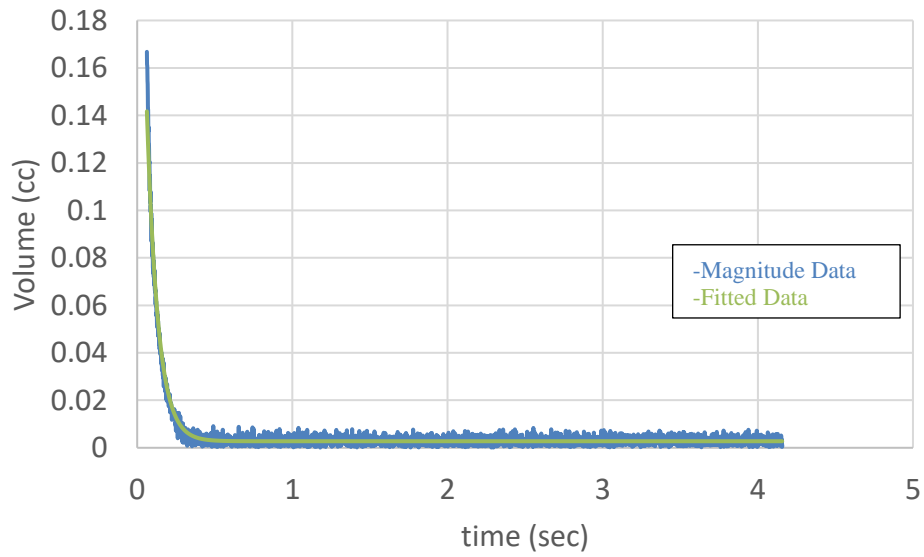
- on the Effects of Flow Resistance on the Fracturing Fluids Imbibition into Gas Shale”, 2014.
127. Zhang, M. “Numerical and Experimental Analysis of Diffusion and Sorption Kinetics Effects in Marcellus Shale Gas Transport”, 2019.
128. Zhang, B. “Direct Determination of Surface Relaxivity in Isolated Kerogen by Pulsed”, 2007.
129. Zhou, Z. “Experimental and Numerical Study on Spontaneous Imbibition of Fracturing Fluids in the Horn River Shale Gas Formation”, 2016
130. Zolfaghari, S. Flowback Chemical Analysis: An Interplay of Shale-Water Interactions, 2015.
131. Zolfaghari, S. “Understanding the Origin of Flowback Salts: A Laboratory and Field Study.” Society of Petroleum Engineers, 2014.

APPENDIX

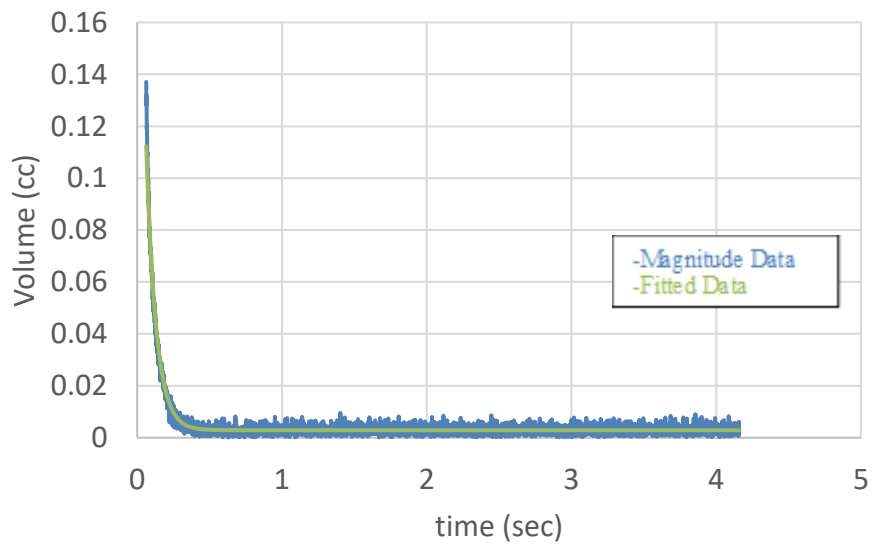
Free Induction Decay (FID) Data (Pre-Spontaneous Imbibition Experiment)

Bossier Formation

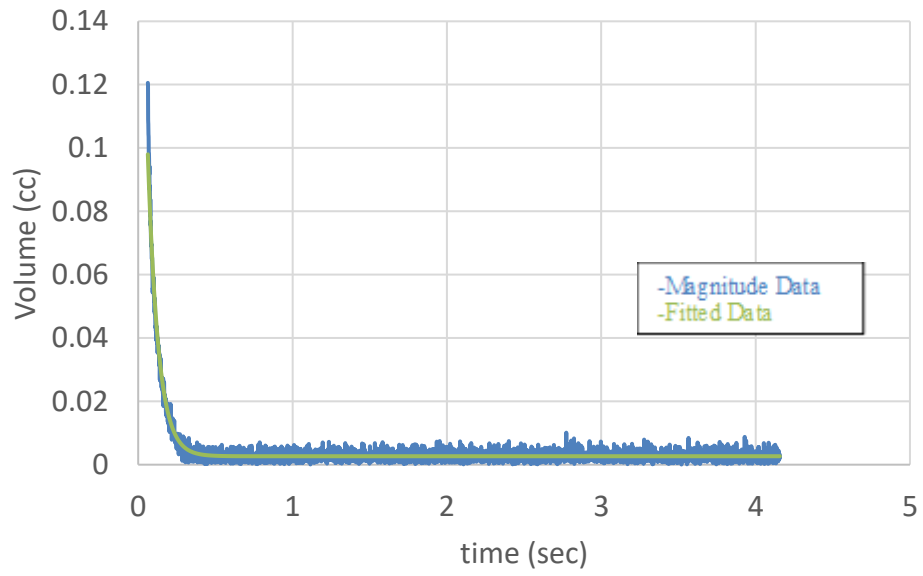
$B(60)_{700\ \mu\text{m}}$



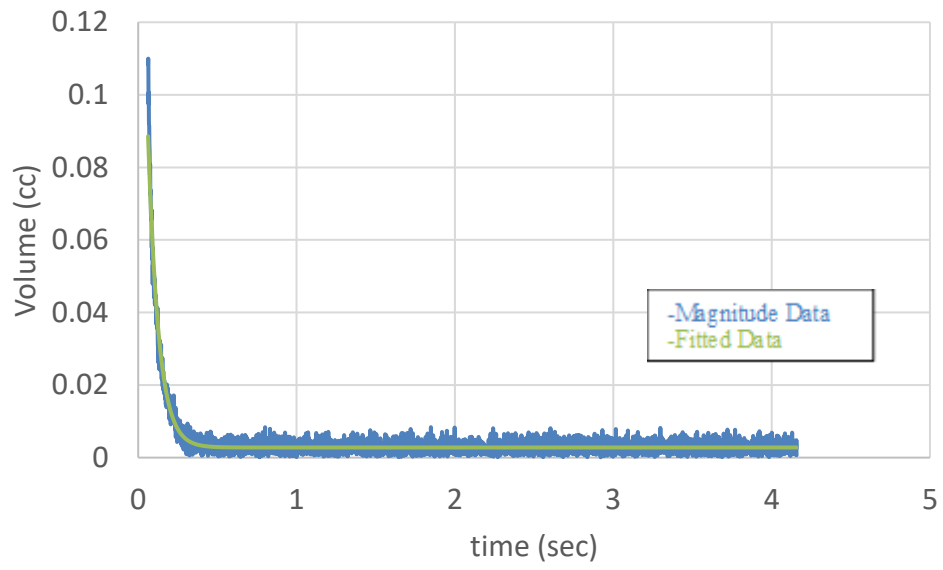
$(B60)_{500\ \mu\text{m}}$



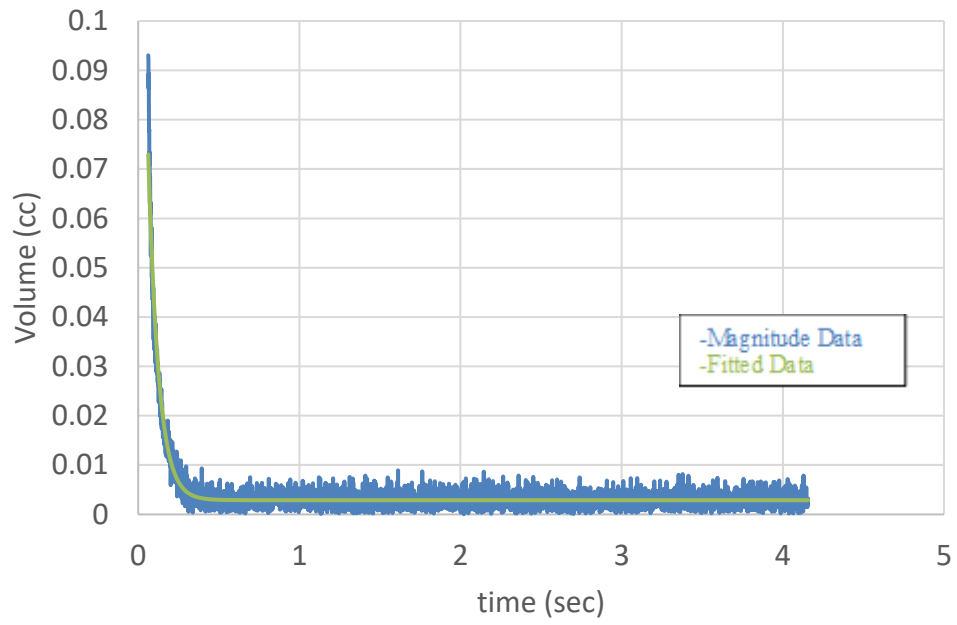
B(60)_{200 μm}



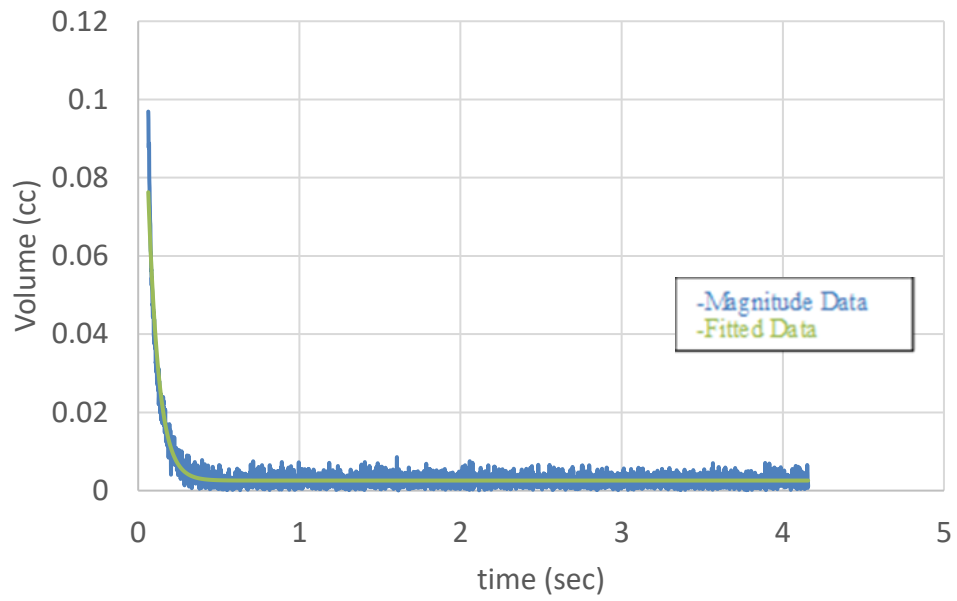
B(40)_{700 μm}



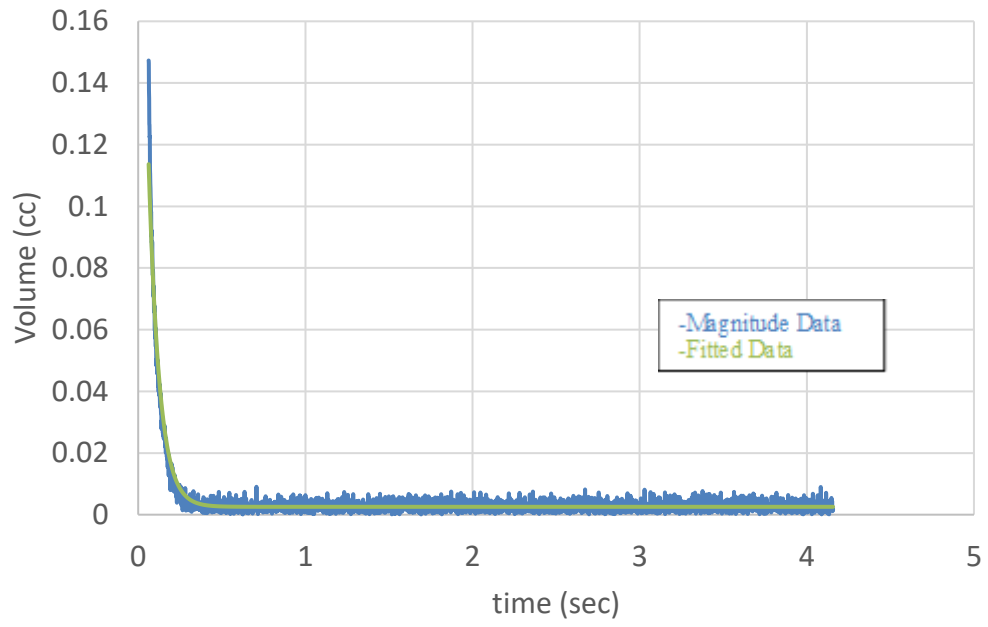
B(40)_{500 μm}



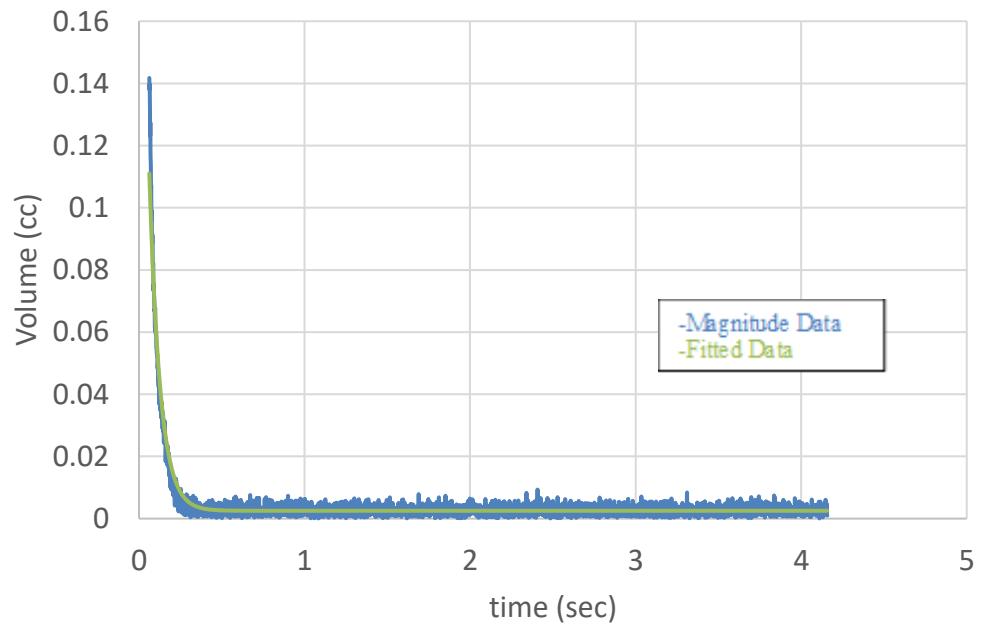
B(40)_{200 μm}



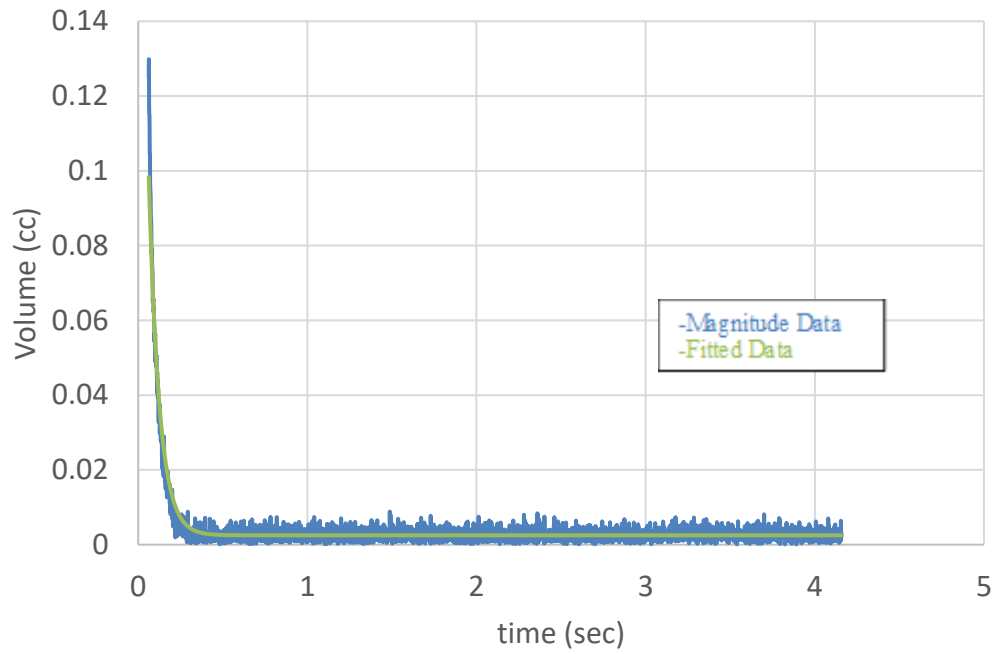
B(15)_{700 μm}



B(15)_{500 μm}

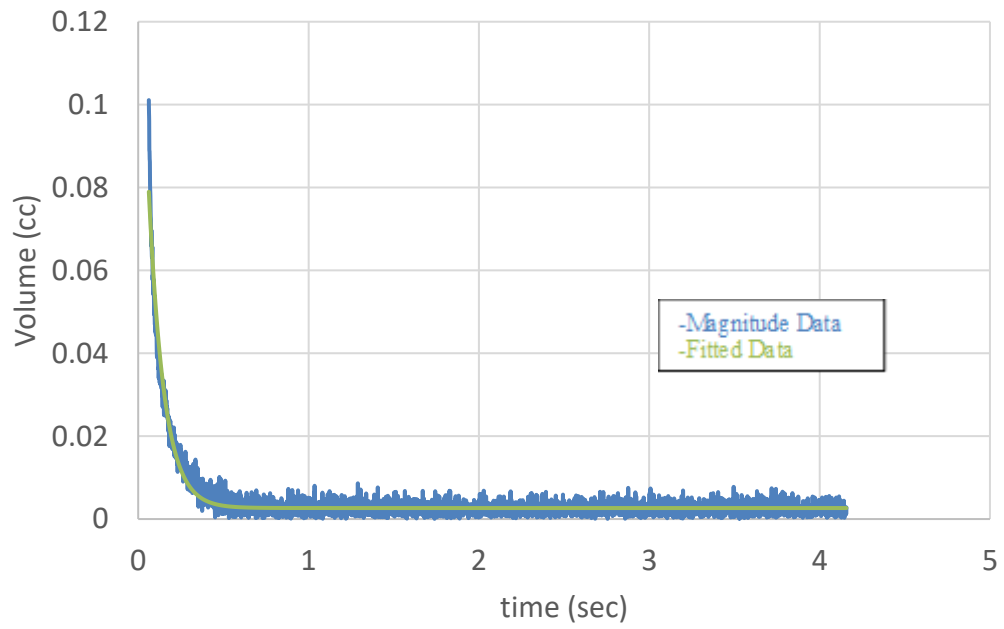


B(15)_{200 μm}

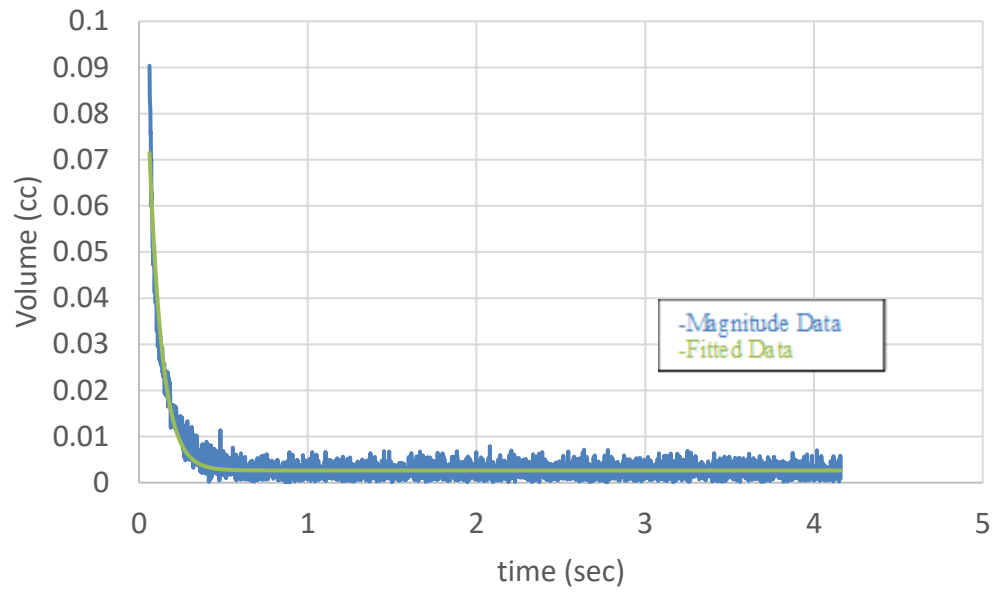


Haynesville Formation

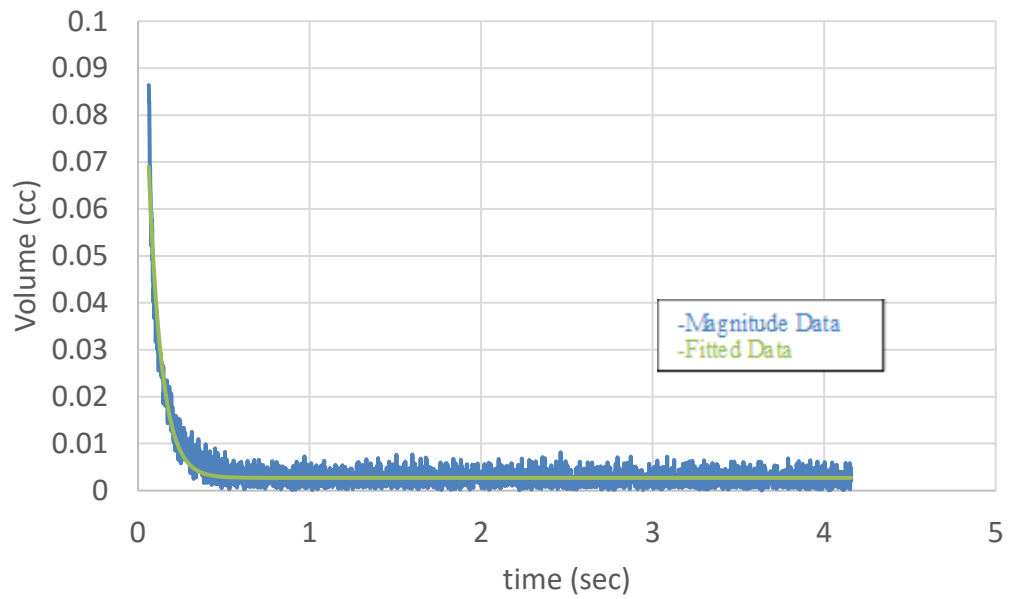
H(26)_{700 μm}



H(26)_{500 μm}

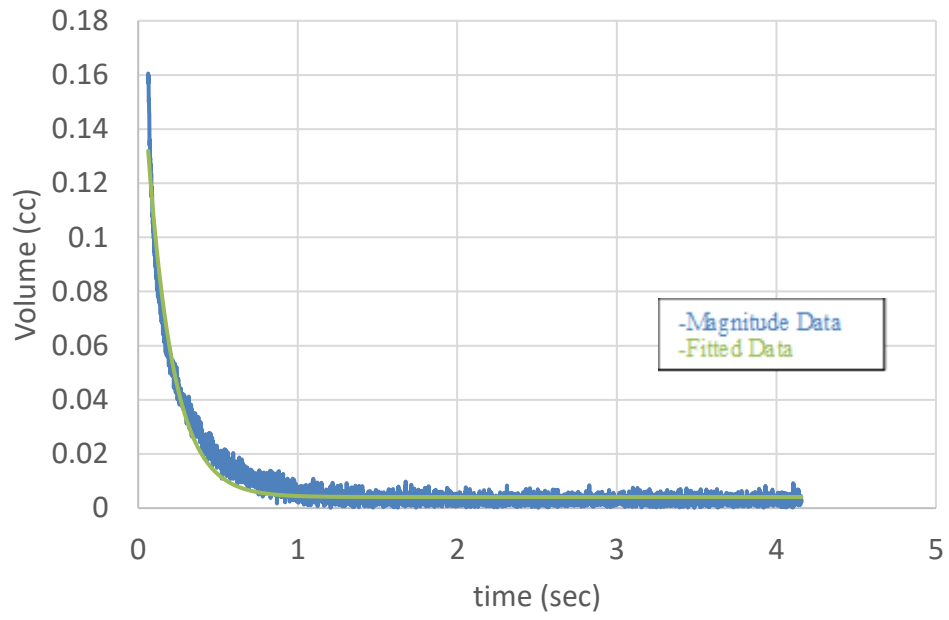


H(26)_{200 μm}

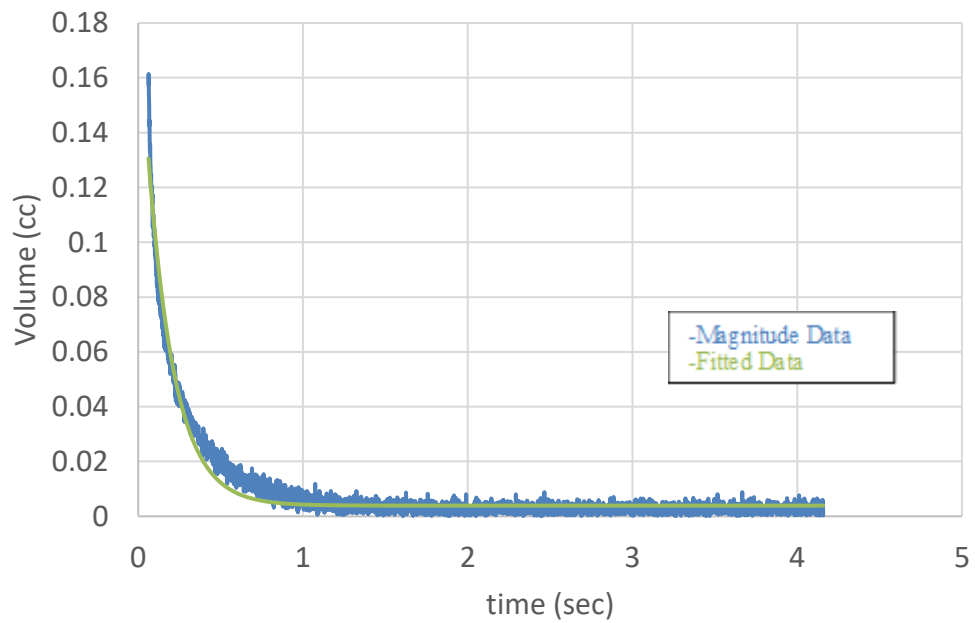


La Luna Formation

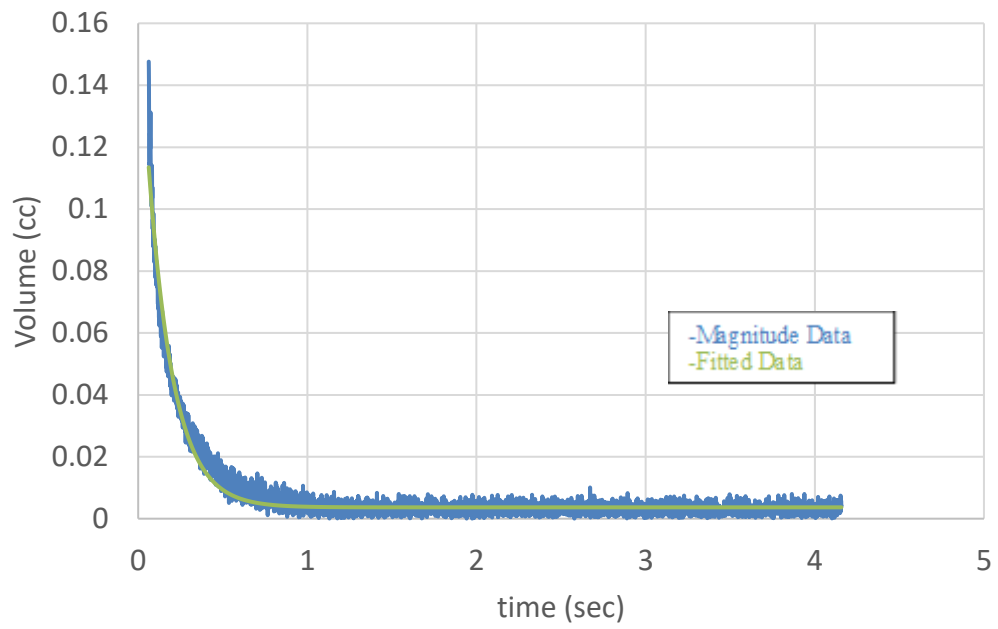
LL(15)_{700 μm}



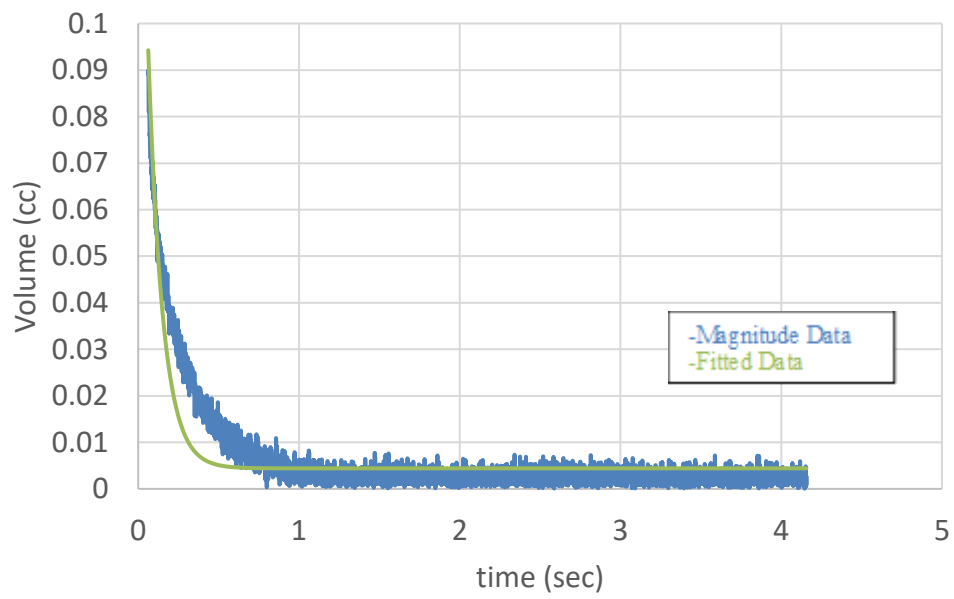
LL(15)_{500 μm}



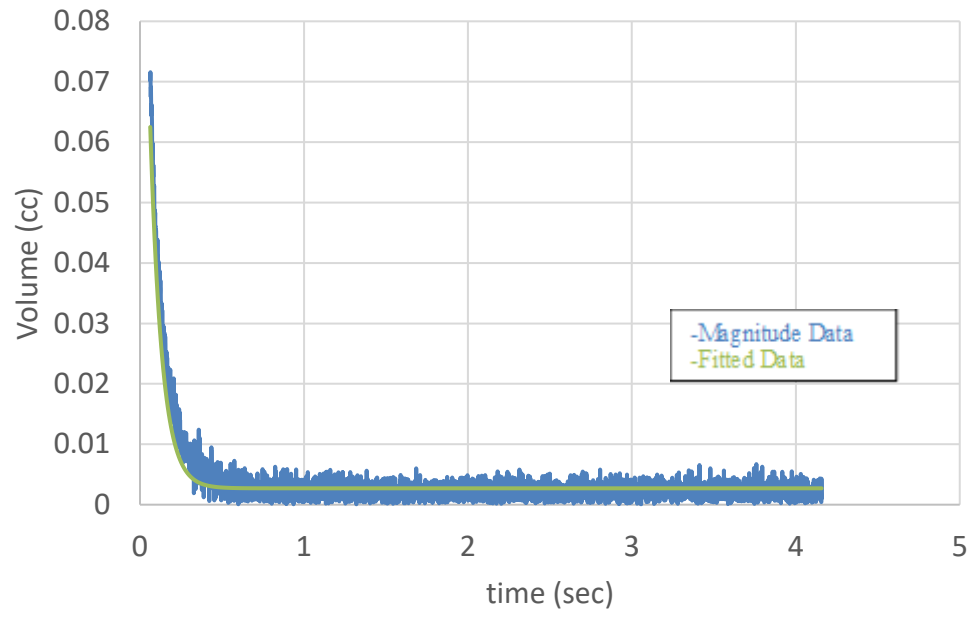
LL(15)_{200 μm}



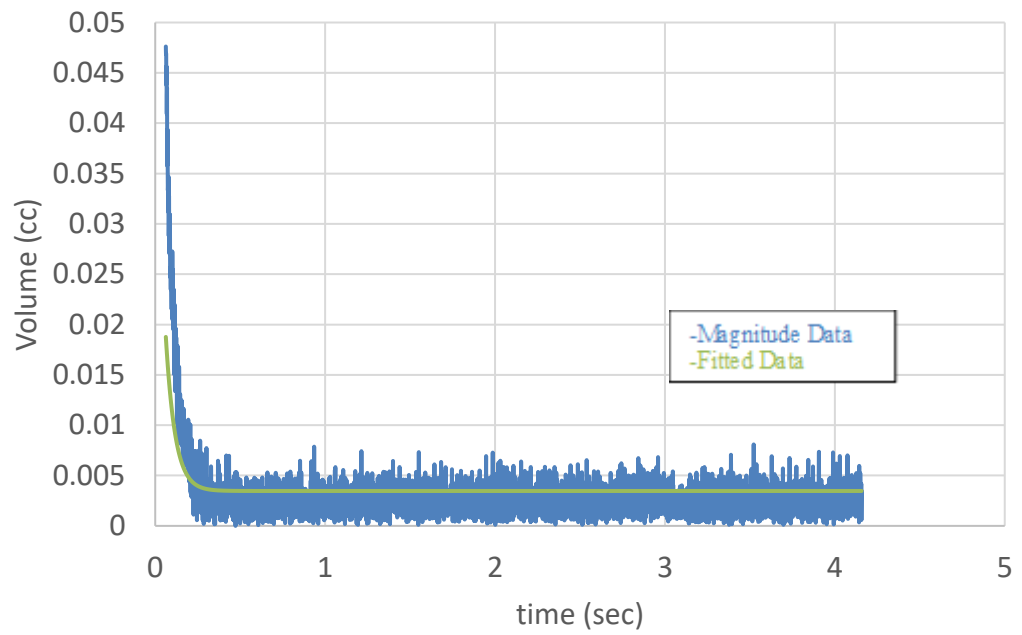
LL(8)_{700 μm}



LL(8)_{500 μm}



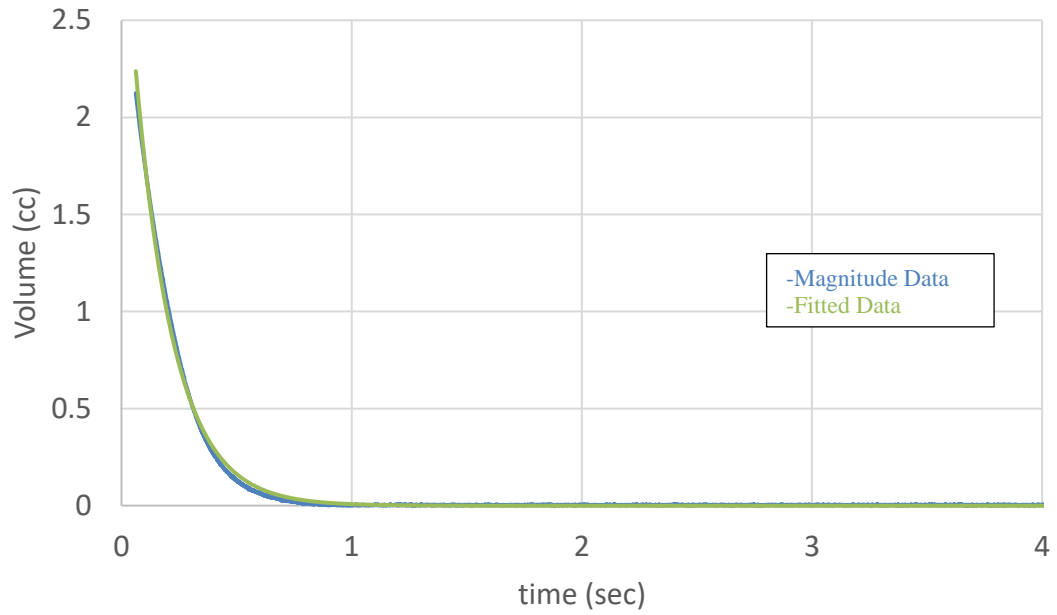
LL(8)_{200 μm}



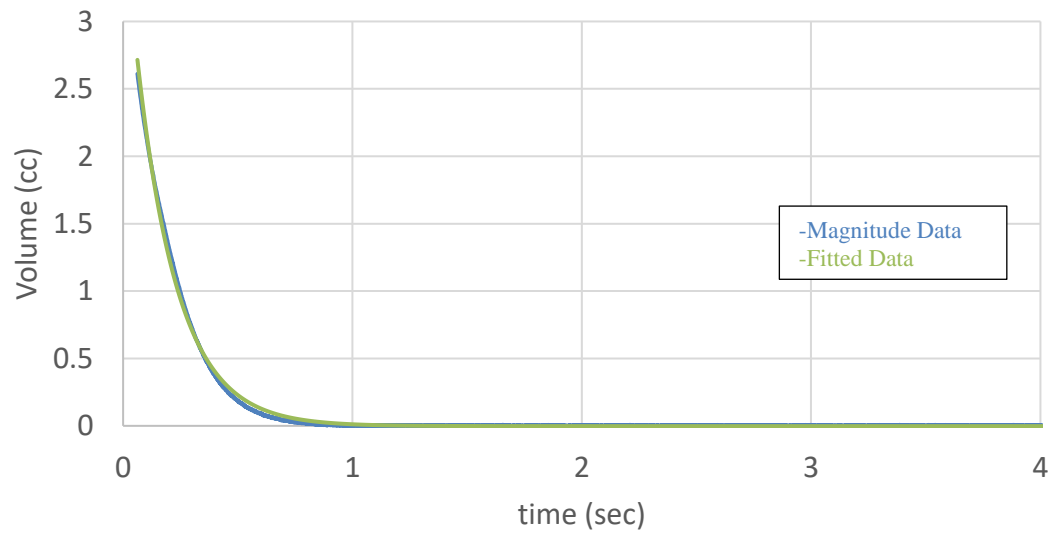
Free Induction Decay (FID) Data (Post-Spontaneous Imbibition Experiment)

Bossier Formation

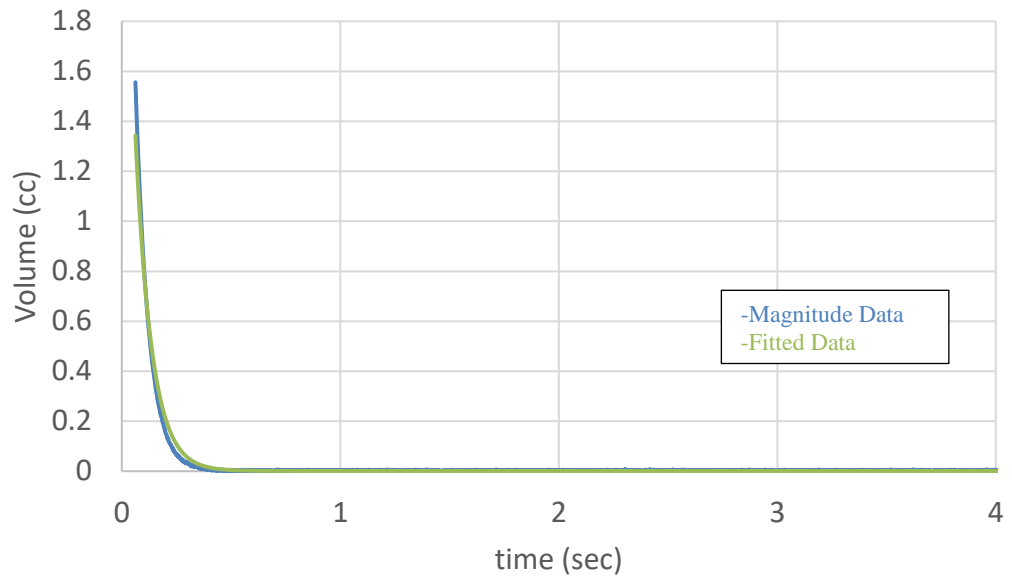
$B(60)_{700\ \mu\text{m}}$



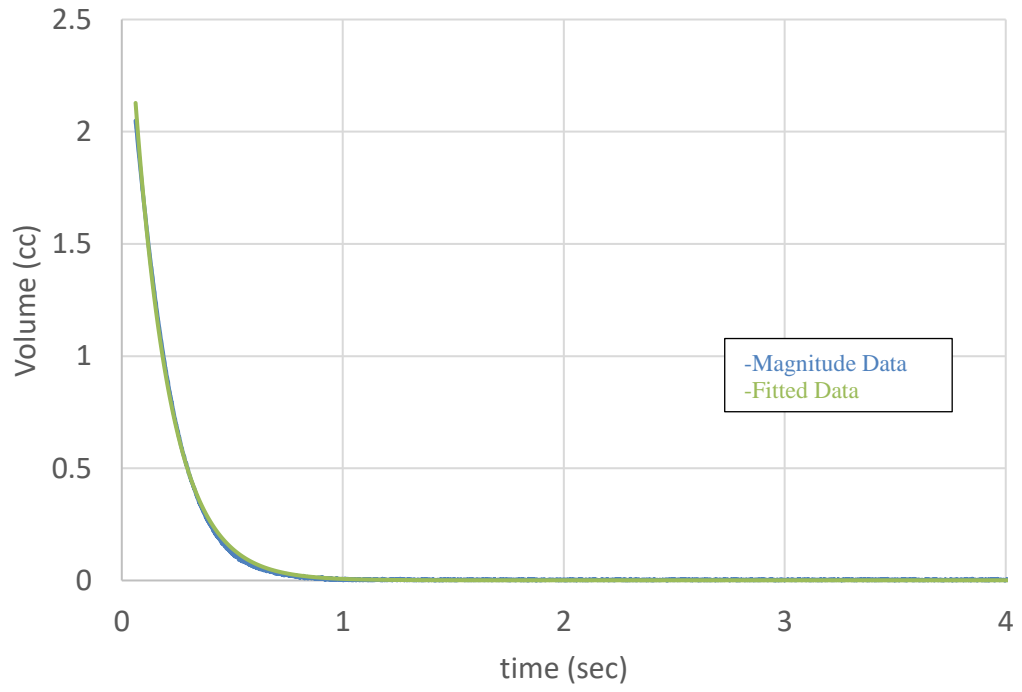
$B(60)_{500\ \mu\text{m}}$



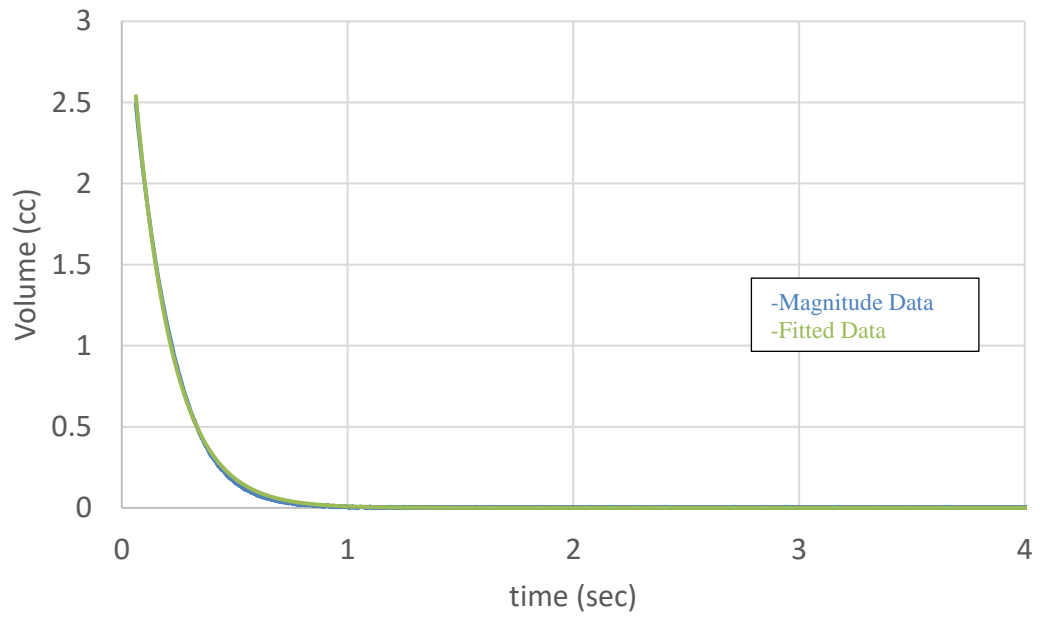
B(60)_{200 μm}



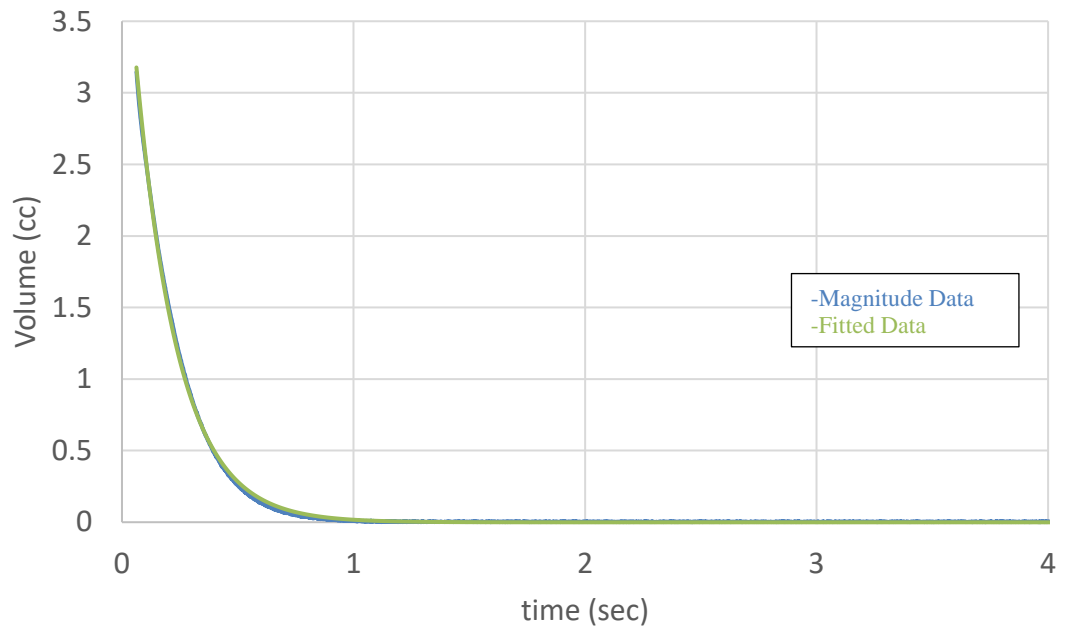
B(40)_{700 μm}



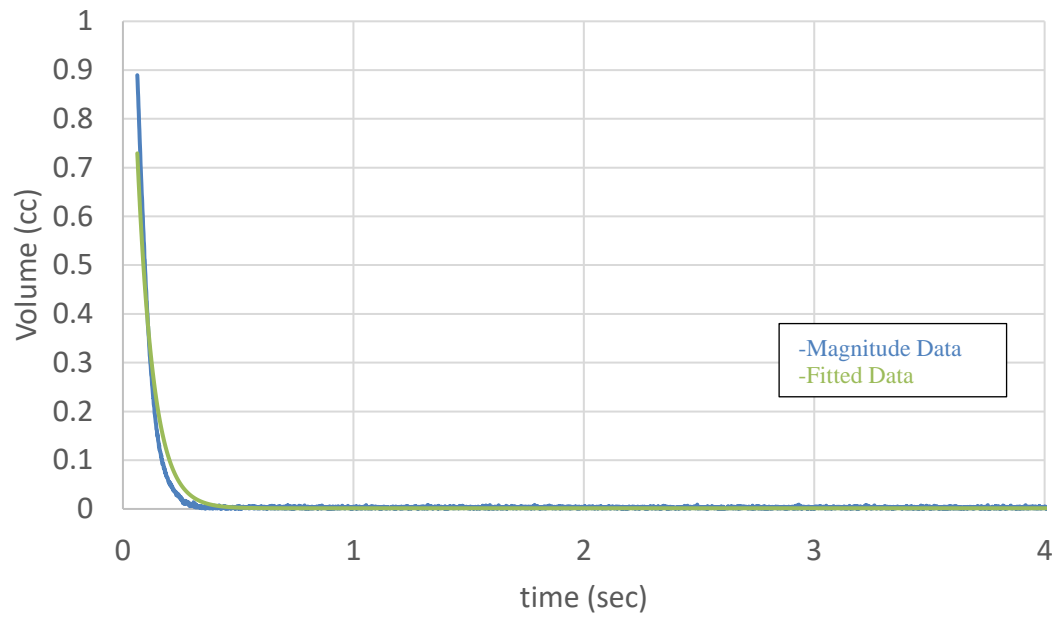
B(40)_{500 μm}



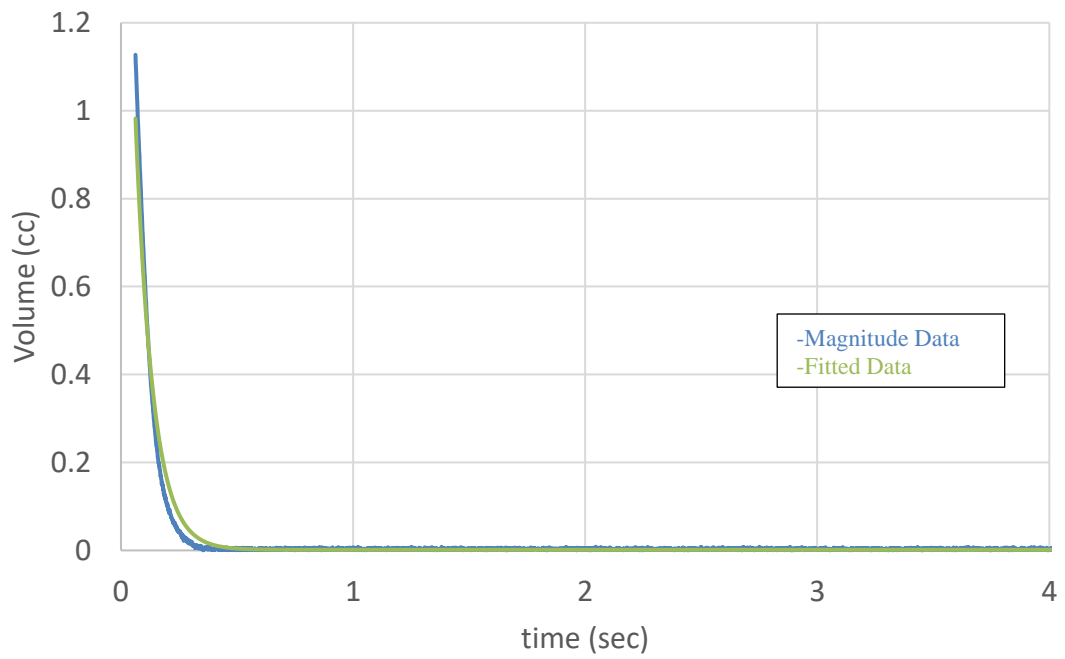
B(40)_{200 μm}



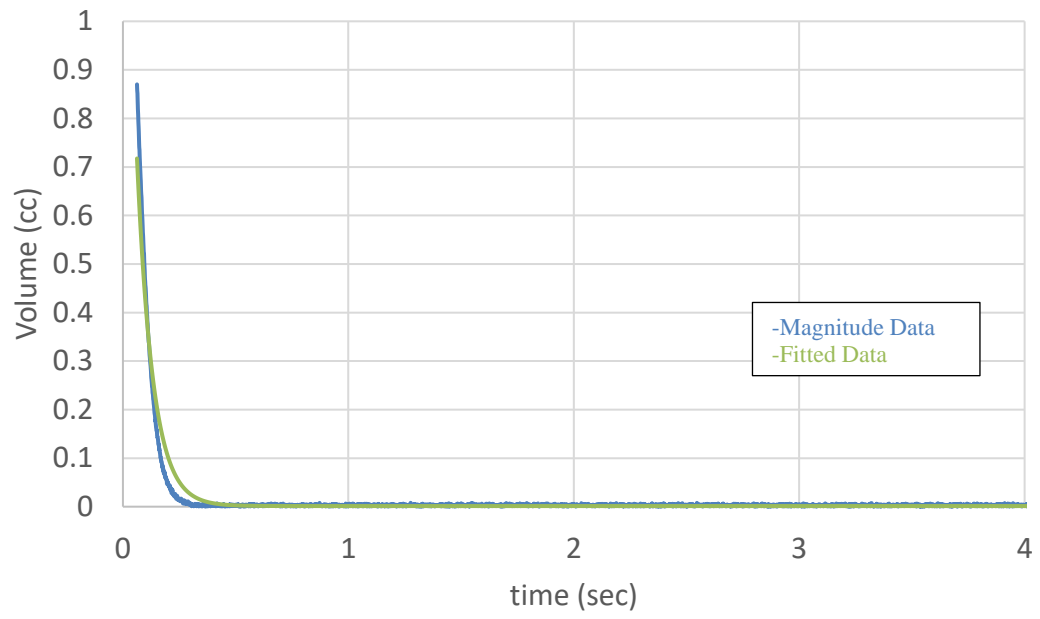
B(15)_{700 μm}



B(15)_{500 μm}

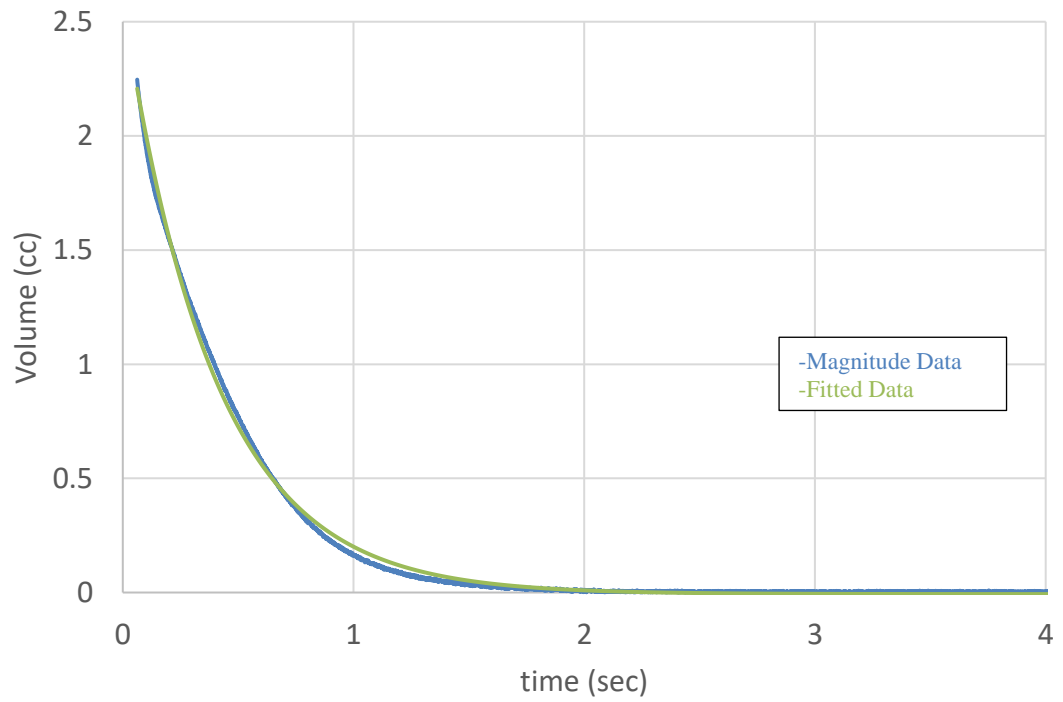


B(15)_{200 μm}

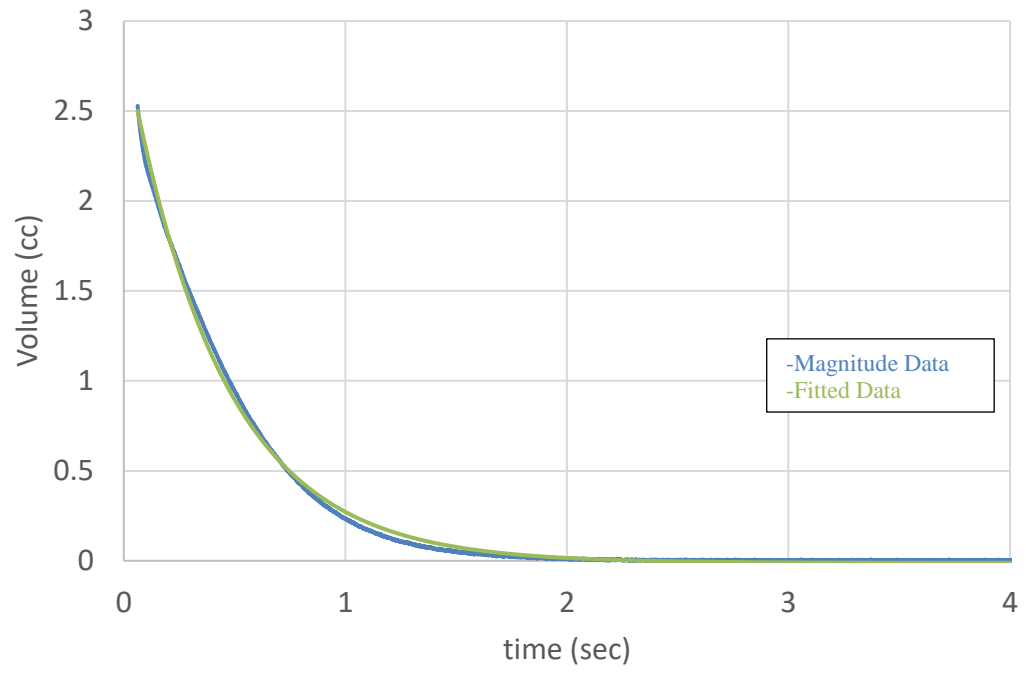


Haynesville Formation

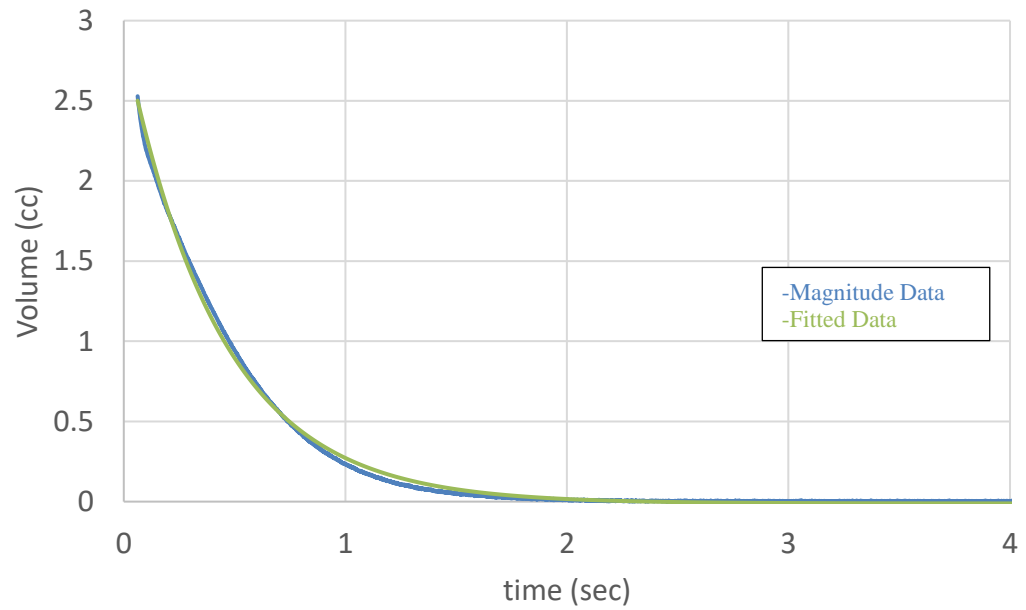
H(26)_{700 μm}



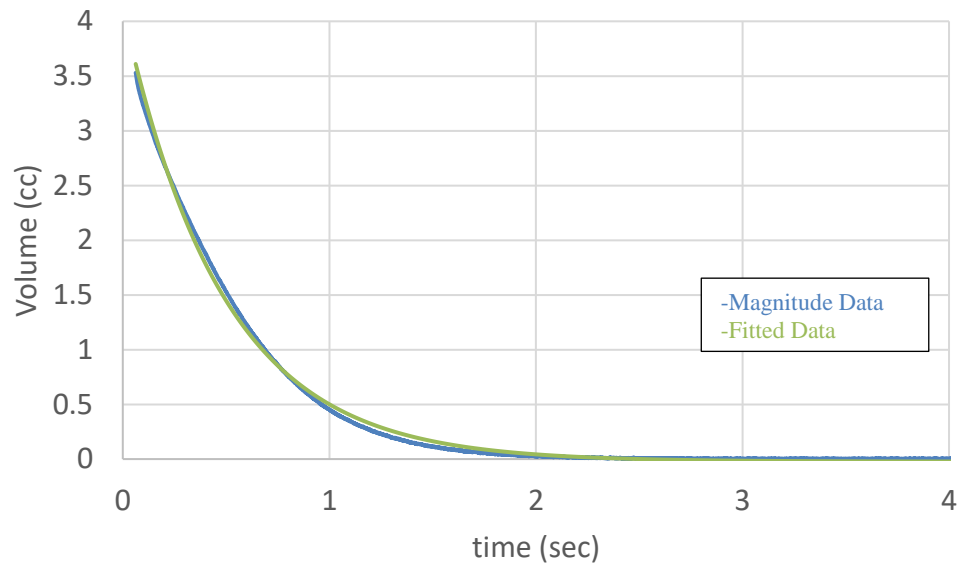
H(26)_{500 μm}



H(26)_{500 μm}

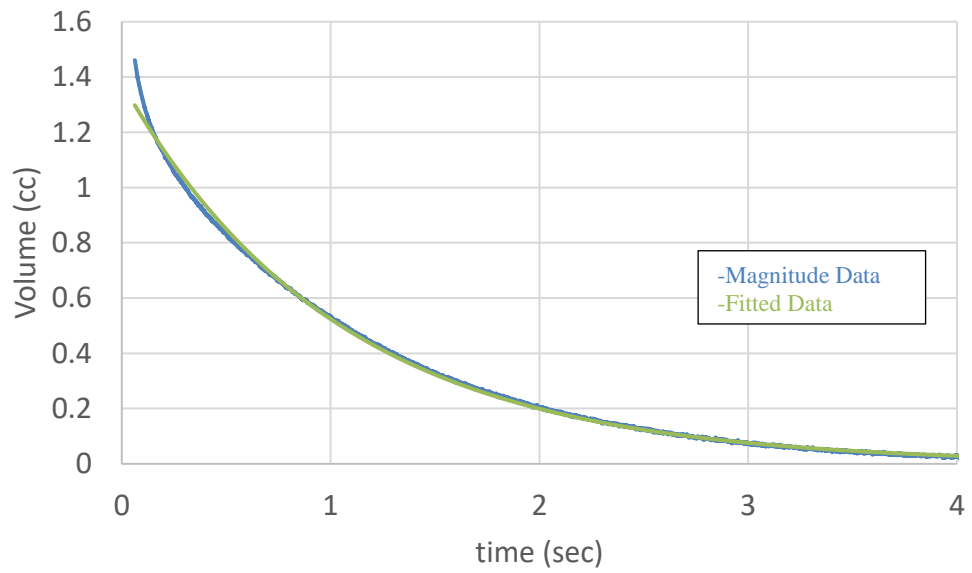


H(26)_{200 μm}

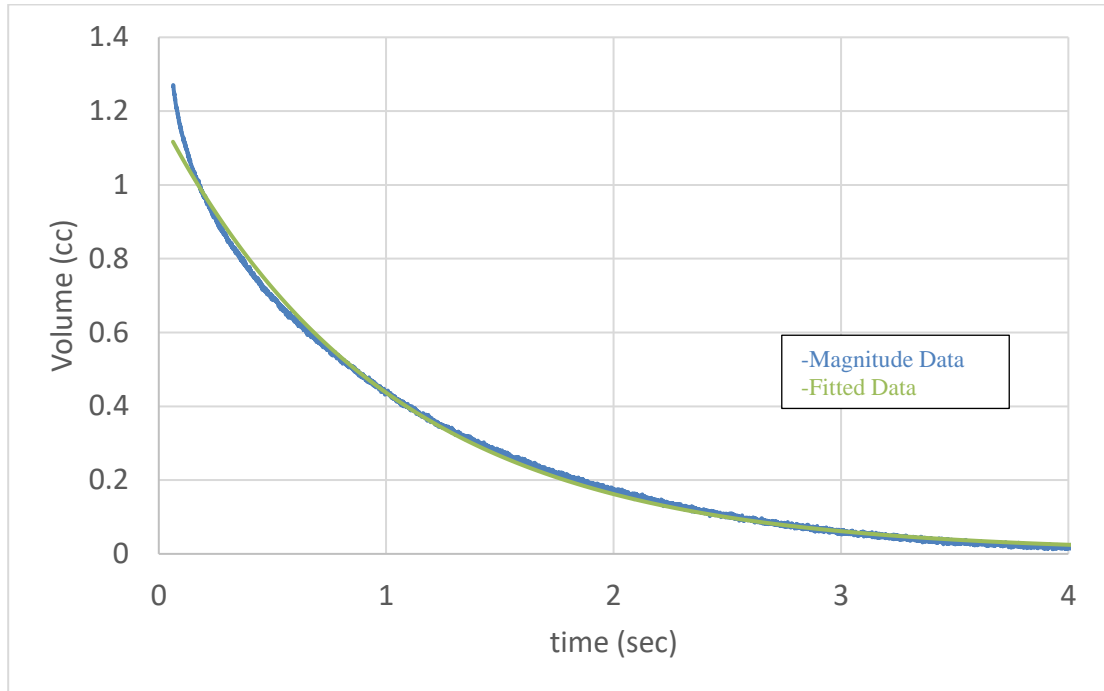


La Luna Formation

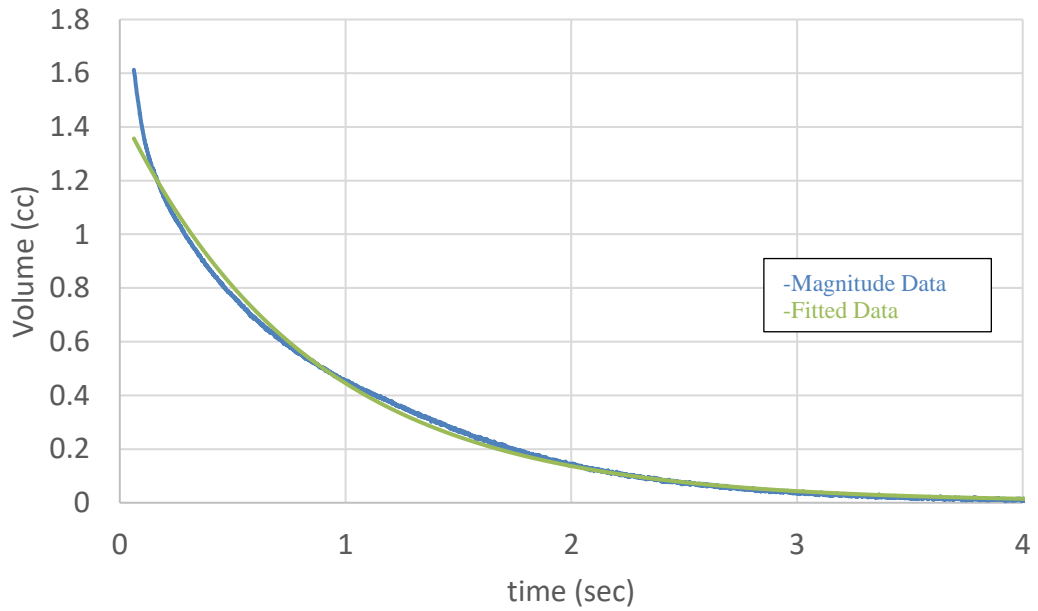
LL(15)_{700 μm}



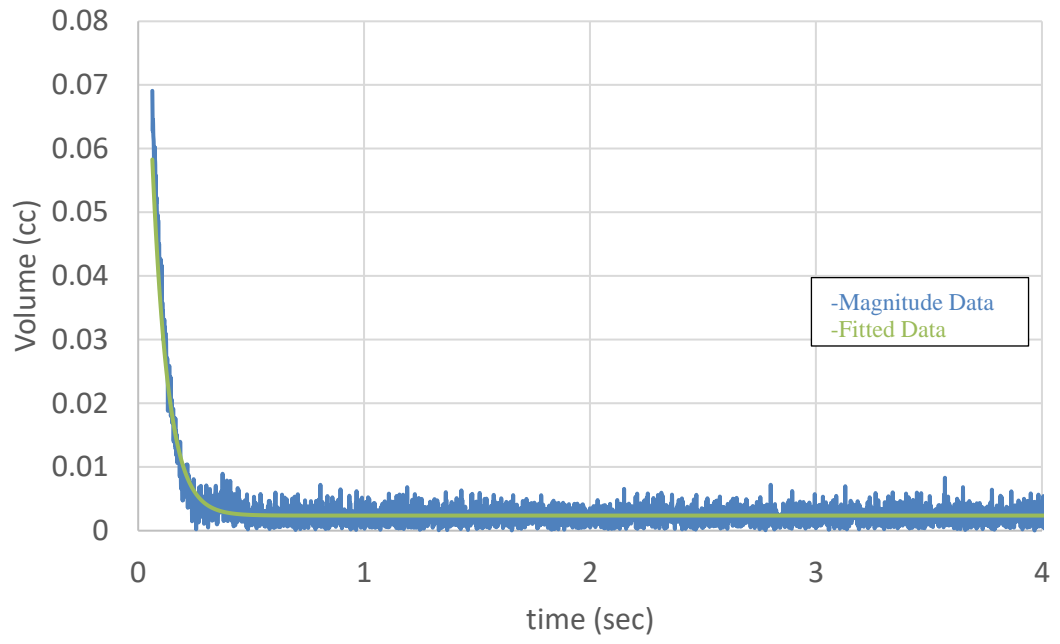
LL(15)_{500 μm}



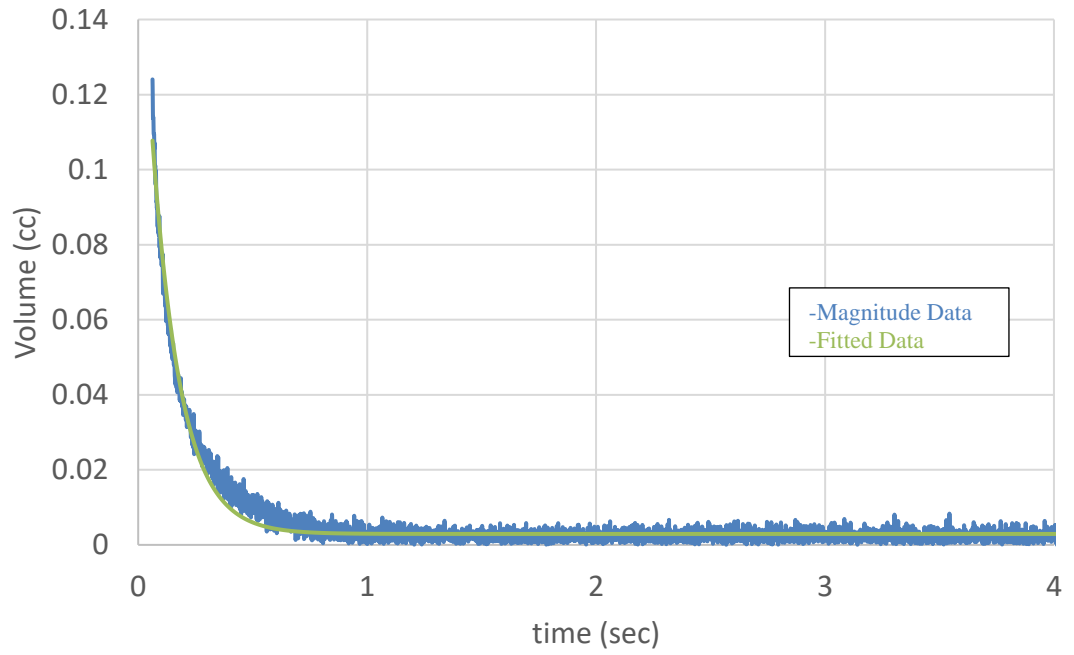
LL(15)_{200 μm}



LL(8)_{700 μm}



LL(8)_{500 μm}



LL(8)_{200 μm}

